1–10 Myr-old Low Mass Stars and Brown Dwarfs in Nearby Star Forming Regions

Thesis by

Catherine L. Slesnick

In Partial Fulfillment of the Requirements

for the Degree of

Doctor of Philosophy

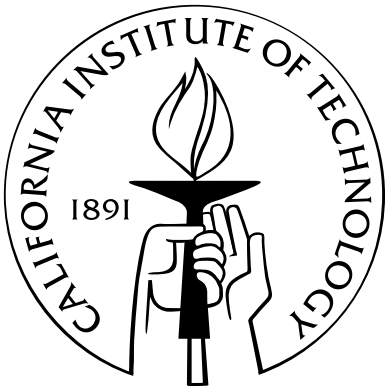

California Institute of Technology

Pasadena, California

2008

(Defended July 31, 2007)

Dedication

I dedicate this thesis to the 2001–2002 inhabitants of 05 Robinson,
and to Rim, who clearly knew what she was doing.

Acknowledgements

The list of people without whom this thesis would not have been possible is long, and I will try to be brief.

First and foremost, I would like to thank my advisor, Lynne Hillenbrand, who is primarily responsible for my growth as a scientist during the past six years. I could not have asked for a better advisor, and I feel fortunate to have been able to work with someone for whom I have such deep respect both scientifically and personally. Thank you for being my advisor when I needed it, and my collaborator the rest of the time, for knowing when to guide me, and when to allow me to find my own way.

I consider myself an unusually fortunate grad student to have had not one, but two amazing advisors. Most of my work at Caltech has been done in close collaboration with John Carpenter. Unfortunately for John, he had an office right down the hall from mine, so my seemingly endless stream of questions flowed his way first. Yet, he always listened, ever patiently, offered me a gentle shove in the right direction and then told me to find the rest of the way myself. From John I have learned the great value of meticulousness, of being able to explain every detail of my science. Thank you for your kindness, and for always making time to listen to my questions, no matter how busy you were.

My experience at Caltech has changed my life in so many ways. Not only will I earn my PhD at Caltech, but also I met my future husband in the Robinson hallway. Francis O'Donovan, you are the light, love, and inspiration of my life. Everything I do, including writing this thesis, is more worthwhile knowing that I will be spending the rest of my life with you.

I am grateful for entering Caltech with a fabulous group of classmates, Stuartt Corder, Melissa Enoch, Laura Hainline, Margaret Pan, Milan Bogosavljevic, and Elina Brobeck, without whose support, camaraderie, and comic relief I would never have made it through the first year of grad school.

I owe a huge thank you to my parents, Frank and Sue Slesnick, and my brother Tim Slesnick for all their encouragement during my time at Caltech, and throughout my life. The three of you continue to inspire me, both through your everyday actions and through the support you give to me. And Mom, thank you for keeping me to my word and not letting me drop out of grad school before I had stuck it out at least a year and a half.

I am forever indebted to my good friend Karen Girard, without whose encouragement I would have never run 26.2 miles, and without whose cooking Francis and I surely would have died of malnutrition during the two months prior to our defense.

I appreciate the time and effort contributed to bettering my thesis by members of my defense committee, Mike Brown, Lynne Hillenbrand, Anneila Sargent, Judy Cohen, and John Carpenter, every one of whom graciously bent their schedules to allow my defense to proceed in a timely manner. Robinson is fortunate to have a fantastic group of system administrators, Patrick Shopbell, Anu Mahabal and Cheryl Southard, who keep the building running smoothly, and who have been invaluable to me throughout my six years of computer use at Caltech.

This work could not have been possible without the help and support from the Palomar Observatory staff. I have spent a total of 47 nights observing at Palomar during my six years at Caltech, every one of them made more enjoyable by the delicious cooking and overall friendliness of Dipali and Rose. I am particularly thankful to Dipali, who spent many of her free afternoons taking me hiking in the hills and swimming in the ponds near the observatory. Jean Mueller and Karl Dunscombe have been fantastic company and support to me during my many long nights at the telescope, and were very kind to not complain at my attempting to lay the telescope on its side while observing the southern USco OB association, time and time again. I would like to thank Rick Burruss and Jeff Hickey for keeping the instruments

running smoothly. The Quest-2 surveys were made possible by the Quest-2 collaboration, including David Rabinowitz, Ashish Mahabal, Anne Bauer, Jonathan Jerke, Eilat Glikman, and George Djorgovski.

I was fortunate to be a part of a wonderful group of researchers, including Stan Metchev, Adam Kraus, Russel White, Greg Herczeg, Josh Eisner, and Scott Dahm, with whom I've had many insightful conversations over the years. I am grateful to Phil Massey who, to a large extent, is responsible for my ending up where I am today writing this thesis, and who has stuck with our friendship through the ups and the downs over the past eight years. I owe thanks to Steve Strom for taking an interest in my work, and to my early astro mentors, including Patrick Huggins, Steven Majewski, Bob Donahue and Sallie Baliunas. I would like to thank Wal Sargent, for always saying hello when he saw me in the hallway, Nick Scoville, for coming to visit me in the hospital after I had surgery, and Re'em Sari, for holding my hand while I was learning to scuba dive and I was scared.

I am blessed to be surrounded by so many good friends, who keep me smiling through even the hardest of times. To Melissa Enoch, whom I've sat next to for six years, and Laura Hainline, who is the only person I know that is capable of being as outraged as I can be, thank you for always being there for me. Brian and Danielle Cameron have set me on the road to becoming a wine snob and provided me with countless hours of good times and good friendship. I will forever appreciate Stuartt Corder and Jennifer Edwards for inspiring me to become a reverend and allowing me to officiate at their wedding. I thank my office-mate Milan Bogosavljevic, for introducing me to dunja and sharing with me his home country of Serbia. I am grateful to countless unmentioned people, both inside and outside of Caltech, whose friendship and laughter have made my experience during the past six years more enjoyable. The Caltech Astronomy department is home to a great group of grad students, postdocs, faculty and staff, whose doors are always open.

Abstract

My thesis research has focused primarily on identifying and characterizing pre-main sequence stars in nearby star-forming regions. To this end, I carried out wide-field ($\sim$150–250 deg^2) optical photometric and spectroscopic surveys in and near the star forming regions of Taurus and Upper Scorpius.

In Taurus, the aim of my optical photometric/spectroscopic survey was specifically to probe for a population of intermediate-age pre-main sequence stars outside of the young subclusters that are known to contain most of the young Taurus population. From this work I found tens of young ($\sim$1–3 Myr) and intermediate-age ($\sim$5–10 Myr) stars both near the known Taurus population and to the east, but relatively few pre-main sequence stars of any age to the west. I argued that the new pre-main sequence stars identified far from Taurus can not have originated from the vicinity of the 1–2 Myr-old subclusters and I proposed instead that they comprise a new, previously undiscovered region of recent star formation.

In USco, the aim of my optical photometric/spectroscopic survey was to probe beyond previously explored regions to identify large numbers of 5 Myr-old low mass stars. From the spectroscopic data I have discovered 145 low mass members of USco. Using Monte Carlo simulations I showed that, taking into account known observational errors, the observed age dispersion for the low mass population in USco is consistent with all stars forming in a single burst $\sim$5 Myr ago. I also derived the first spectroscopic mass function for USco that extends into the substellar regime and compared results to similar mass functions derived for stars in four other young clusters and associations.

Contents

List of Figures

List of Tables

Chapter 1

Motivation

Current observational evidence indicates that a significant fraction of stars are born in groups (i.e., clusters or associations) within giant molecular clouds (e.g., Gomez et al. 1993, Lada & Lada 1995, Carpenter 2000, Lada & Lada 2003). As such, understanding young star forming groups plays an important role in advancing our knowledge of the universe. Key questions that can be addressed by studying star-forming groups include the following: (1) What is the timescale of star formation within a single molecular cloud compared to the lifetime of that cloud? Most nearby regions of recent star formation are found to contain only very young stars ($\lesssim$1–2 Myr) whereas molecular clouds, from which those stars are born, are thought to have lifetimes on the order of >10 Myr. We do not yet understand how to reconcile these two seemingly inconsistent results. (2) How and why do molecular clouds contract at particular sites to form stellar clusters and associations? It is suspected that formation of massive stars in one region can trigger star formation in a neighboring region (e.g., Brown 1996). What is not understood is how the processes of triggered vs. independent star formation will affect (if at all) the end result of the star forming group. (3) What determines whether a particular site of star formation will become a sparse T association, an OB association, or a bound cluster? (4) What role, if any, does stellar birth environment have on determining the observed spectrum of stellar masses within a star forming region? The answer to this question requires detailed comparisons of the initial mass function (IMF) across many different star forming regions. Because current stellar theory predicts that the evolution of an individual

star is dictated almost entirely by its stellar mass, understanding the IMF and its possible variations is of extreme importance in star formation theory. (5) Does a young star's external environment affect the lifetime of its primordial circumstellar disk? High stellar densities and possible UV excess emission present in large star forming clusters could affect the lifetimes of circumstellar disks and thus, the capability of cluster members to form planetary systems.

Of particular interest for examining the above questions are the low mass populations associated with recent star formation. Studies of low mass ($M \lesssim 1$ $M_\odot$) pre-main sequence (hereafter PMS) stars offer distinct advantages over studies of associated higher mass stars for the primary reason that there are many more low mass stars to examine. An average star forming group containing $\sim$500 $M_\odot$ worth of stars (Lada & Lada, 2003) will contain $\sim$1000 stars, only $\sim$5% of which will have $M > 1$ $M_\odot$. The sheer numbers of low mass stars in these regions allow statistical studies not possible when considering only the high mass populations. Furthermore, we might expect lower mass stars to be more susceptible to environmental influences. Newly formed low mass stars have correspondingly lower mass circumstellar disks (Scholz et al. 2006, Andrews & Williams 2005), which are more easily photoevaporated in the presence of an external radiation field (e.g., Adams et al. 2004). Lower mass stars also are more sensitive to dynamical interactions with surrounding stars than their higher mass neighbors (Adams et al., 2006). Thus, studies of the low mass members within a star forming group will better reflect any effects caused by differences in birth environment than will studies of only the high mass members.

For my thesis, I sought to address some of the aforementioned unanswered questions relating to star formation in clusters and associations. The specific goals of my thesis are fourfold:

1) To identify low mass PMS stars and brown dwarfs in a variety of different star forming environments using a combination of imaging and spectroscopic techniques.

2) To determine the possible existence of a population of intermediate-age PMS stars ($\sim$5–10 Myr) associated with the young ($\sim$1 Myr) Taurus members. My goal in this region is specifically to address the length of time stars have been forming in

Taurus compared to the assumed lifetime of the associated molecular cloud.

3) To examine mass functions for clusters and associations in different environments. I concentrate on the low mass end and attempt to discern if environment plays a substantial role in determination of the IMF.

4) To probe the evolution of circumstellar material around substellar objects during the first 5 million years.

1.1 Star Formation in Clusters and Associations

Our working knowledge of how isolated stars are born is not substantially different from the view put forth by Shu et al. (1987) in their seminal paper "Star Formation in Molecular Clouds: Observations and Theory." In this work Shu et al. (1987) proposed a fourstage process to star formation, shown as a, b, c, and d in figure 1.1. In this picture, star formation begins with slowly rotating cloud cores inside molecular clouds (a) which become unstable, and collapse dynamically forming a protostar with a disk embedded inside the molecular cloud (b). During this stage, the protostar accretes material from the surrounding disk and envelope until it has accumulated enough mass to begin driving a stellar wind which channels itself along the rotational poles (c). In the fourth phase (d) of the Shu et al. (1987) model, the surrounding stellar envelope has dissipated and the system has evolved into a classical T Tauri star with a circumstellar disk.

However, as discussed above, most stars do not form in isolation, they form in clusters and associations that share a common parental molecular cloud. Thus, understanding how stars form in groups, rather than in isolation, is crucial to understanding the formation of a 'typical' star. Unlike formation of a single isolated star, multiple star-forming protostellar cores must undergo significant fragmentations (Lada & Lada, 2003). The physics behind this process is not well understood. Various theoretical models have been proposed (e.g., Myers 1998); however, because protostellar clusters are still deeply embedded in molecular gas and dust, corresponding observational evidence from the earliest stages of stellar group formation is difficult to accrue.

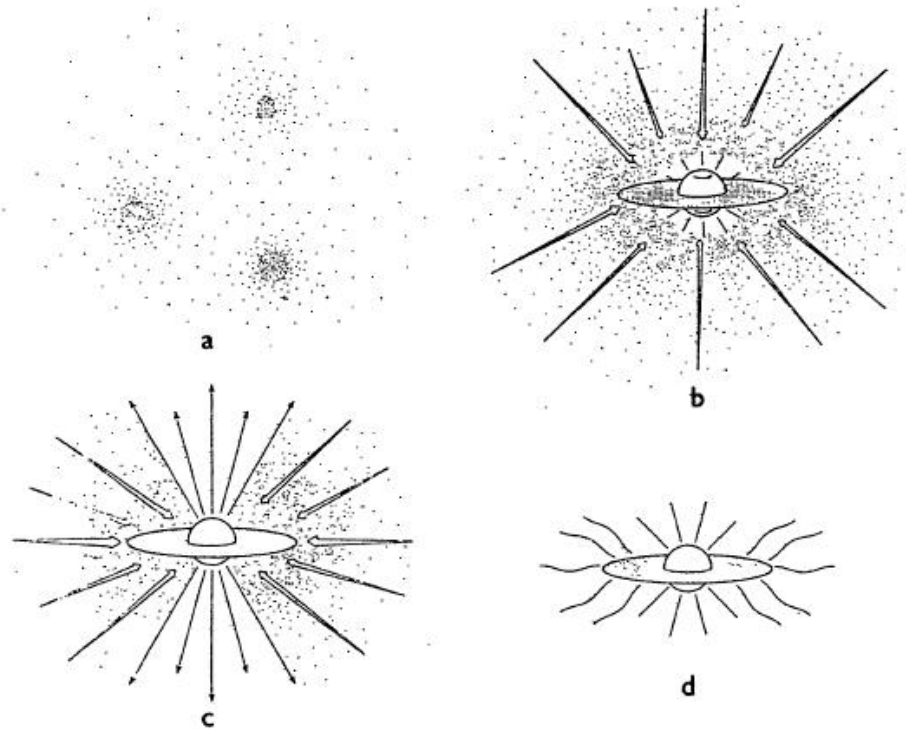

Figure 1.1 Figure 7 of Shu et al. (1987) illustrating the four stages of star formation.

Observations of the end results of these process, i.e., resultant young stellar groups, however, are more readily made using traditional optical and near-infrared observing techniques. In particular, from observations of mass, age and spatial distributions of different regions at different stages of evolution, we can begin to piece together the picture of how stars within those regions formed and what role birth environment may have played in this process.

The first issue that must be addressed in this matter is to understand that not all stellar groups are the same. They come in many different flavors, the most common of which (and those that will be discussed in this work) are described below.

Young stellar clusters. In its most general definition, a star cluster is a group of stars that is gravitationally bound. This fact implies that young clusters either have densities $\rho_* \geq 1$ $M_\odot$ pc^{-3} and thus remain stable against galactic tidal forces (Bok, 1934) and interactions with giant molecular clouds (Spitzer, 1958), or are still deeply embedded in primordial molecular gas and dust that binds them together. I have used

the term 'young stellar cluster' to differentiate the clusters that will be discussed in this work from globular clusters, which are a fundamentally different type of stellar cluster and not relevant to the discussion at hand. Young star clusters can come in a large variety of shapes and sizes and can range up to densities as high as $\sim 10^4$ stars pc^{-3}. An example of a young stellar cluster is the Orion Nebula Cluster (ONC; figure 1.2, top) which contains $\sim$3500 stars within a radius of $\sim$2.5 pc. The ONC is an example of an embedded cluster in that it still retains much of its surrounding molecular gas and dust, rendering only $\sim$50% of its population observable at visible wavelengths. The ONC is centrally concentrated with the most massive stars found preferentially within $<$0.3 pc from the cluster center (Hillenbrand, 1997).

Stellar associations. Groups of stars formed out of the same molecular cloud which are not gravitationally bound to each other are called stellar associations. Because stellar associations have inherently low stellar densities ($\rho_* \lesssim 1$ M$_\odot$ pc^{-3}), members are often hard to identify among the considerable field star population that lies along the same line of site. The low densities of a stellar association implies that it cannot live more than $\sim$200 Myr before tidal interactions with giant molecular clouds pull the association apart (Spitzer, 1958). In general, associations can contain as few as ten to as many as several hundred members. Stellar associations are further subdivided dependent on their stellar content and spatial distribution. I discuss several specific examples.

OB associations - OB associations are characterized by a substantial fraction of O- and B-type stars. Often, they start out their lives as loosely bound stellar clusters; however, the high mass stars blow out any gas and dust associated with the star forming region within the first few megayears, leaving the stars unbound. OB associations are, by definition, still very young because their massive OB members do not live longer than $\sim$1–10 Myr. An example of an OB association is the Upper Scorpius OB association (figure 1.2, bottom) which contains 120 known Hipparcos members, including 49 B-type stars and the pulsar remnant of a massive O star that exploded as a super novae $\sim$1.5 Myr ago.

T associations - A T association contains a large fraction of low mass T Tauri-type

Figure 1.2 Top: Inner region of the Orion Nebula Cluster imaged in the near infrared (1–5 μm) with the VLT. The central concentration of bright blue high mass stars is clearly visible in the center of the cluster. Bottom: Palomar Sky survey plate of part of the Upper Scorpius OB association. The brightest star visible is π Sco, a B1V-B2V spectroscopic binary member of Upper Sco.

stars and very few, if any, high mass stars. The nearest example is the Taurus-Auriga T association located ∼140 pc from the sun. Taurus contains >100 known members, most with M <1 $M_{\odot}$.

Moving groups - Broadly speaking, all associations are moving groups in that their stellar constituent has a common origin and moves together through space. In a more narrow view, when one speaks of young moving groups, such as TW Hya, Beta Pic or AB dor, she is generally referring to small groups of very nearby (<50 pc) stars. The moving groups that we can observe are thought to be the remnants of small-scale star forming events that produced a few dozen stars which have since drifted apart. Members can be identified by common space motions that can be traced back to a common point of origin. Because moving groups contain so few stars spread over a large area on the sky, we can identify only those that are our close neighbors.

Common properties to all young stellar clusters and associations is that members share a common parental molecular cloud, and hence, a common birth environment. They contain statistically significant samples of stars within a relatively small volume of space, and thus can be used to test theories of stellar evolution.

1.2 Observational Challenges to Observing Nearby Star Forming Regions

Observational studies of nearby young clusters and associations have found, in almost every case, that star formation within a molecular cloud takes place on short timescales (1–2 Myr). For example, Carpenter (2000) carried out a statistical star count survey of the Perseus, Orion A, Orion B, and Mon R2 molecular clouds using the 2 Micron All Sky Survey (2MASS). From this work he found no evidence for a large fraction of stars substantially older than previously known young members in any region. Another example can be found in the study by Palla & Stahler (2000). This work derived ages for nine young star-forming regions by placing known members of each association onto an HR digram. In eight of the nine regions they find

only a small fraction of each association is contained in stars older than ∼4 Myr, with the dominant component consisting of very young, 1–2 Myr-old stars.

The large numbers of very young stars and apparent lack of more evolved post T-Tauri stars (∼3–10 Myr-old star; hereafter PTTSs) in star forming regions contrasts with ages of a tens of megayears (e.g., Blitz & Shu 1980) inferred for molecular clouds, because it implies that star-formation takes place for only a small fraction of the cloud lifetime. If that were true, and a typical cloud lifetime is ∼10 Myr but it is only actively forming stars for ∼2 Myr, we would expect to see >4× more quiescent (i.e., not currently star forming) giant molecular clouds than active star-forming clouds. However, the observed result is that there exist ∼2× more active than quiescent giant molecular clouds (Ballesteros-Paredes & Hartmann, 2007). This problem has been discussed in the literature for almost three decades, and is commonly known as the 'Post T-Tauri Star Problem' (Herbig, 1978).

One explanation for these results that has received renewed interest in recent years is that the lifetime of molecular clouds is much shorter than previously accepted. Such could be the case if, for example, molecular cloud formation occurs due to large-scale flows in the ISM driven by global stellar winds and supernovae (Hartmann et al., 2001). An alternative explanation for the apparent lack of older stars in molecular clouds is that such objects have been missed in previous surveys. Most techniques (e.g., strong Hα emission or infrared excess detection) to identify pre-main-sequence stars emphasize characteristics associated with optically thick, circumstellar accretion disks that may last for only a few million years (e.g., Briceño et al. 2001). Thus, if one wishes to probe for PTTSs associated with the young, ∼1 Myr-old population in Taurus, or to study low mass stars associated with the ∼5 Myr-old Upper Scorpius OB association (Preibisch et al., 2002) or the ∼11 Myr-old Beta Pic moving group (Ortega et al., 2004), such techniques will not garner a full census of the population.

Observable magnetic activity in young stars will last well beyond disk dissipation timescales up to at least the ∼115 Myr age of the Pleiades (Marino et al., 2003). Activity signatures are observable through several means, most notably photometric variability, X-ray emission, and UV excess detection. X-ray emission in particular

is known to be particularly strong in pre-main sequence stars from very young ages through >100 Myrs and several authors (e.g., Neuhaeuser et al. 1995, Wichmann et al. 1996) have attempted to identify higher mass (A–G type) PTTSs near the young, 1 Myr-old subclusters in Taurus using the ROSAT All Sky Survey. These observations revealed a population of Lithium-rich (indicating that they are younger than ∼100 Myr) stars widely dispersed across the cloud. However, neither X-ray emission nor Li measurements are capable of distinguishing whether a star at these spectral types is 1, 10 or 100 Myr-old and the origin of these stars and their relation to Taurus is still debated (Briceno et al., 1997). Further, due to sensitivity limits of X-ray observations, attempting to search for the existence of a low mass (K- and M-type stars) population of PTTSs in this manner is impractical.

One of the most efficient methods of identifying low mass members of young stellar clusters and associations in an unbiased manner (i.e., regardless of their circumstellar evolutionary state) is through optical and near-infrared imaging surveys. Young, nearby low mass PMS stars still undergoing contraction will be systematically more luminous than older stars of the same mass. When photometric monitoring observations are available, PMS stars can also be identified through photometric variability caused by the presence of large, cool spots produced from magnetic activity. A major challenge faced by studies seeking to use photometry to identify and assess properties of young stellar clusters and associations is that the group must be relatively nearby if one wishes to probe the entire mass range of its population, down to substellar-type members. However, most young stellar groups within ∼300 pc are low density associations, and hence occupy a large area on the sky. Limitations in telescope time and instrument fields of view necessitate that most surveys are constrained to small-area observations that often focus only on small subclusters known to contain very young stars. If a more evolved population of low mass stars exists in these associations, in 5–10 Myr it likely would have dispersed away from active star-forming regions and probing stars only within small subclusters does not necessarily reflect properties of the association as a whole. Thus, understanding how stars form within a given molecular cloud and what role, if any, birth environment plays in shaping the resul-

tant stellar group requires large scale, large instrument field of view efforts. For my thesis, I sought to undertake such surveys in two nearby star forming regions.

1.3 Thesis Overview

My thesis utilized the Quest-2 camera on the Palomar 48-inch telescope. The Quest-2 camera offers a strong advantage for studies of young nearby stellar clusters and associations because it has a *very* large field of view ($\sim$15 deg^2). Thus, using the Quest-2 camera I was able to map several hundred square degrees of sky in a single night. The work presented here concentrates on two nearby star-forming regions, Taurus and Upper Scorpius (hereafter USco). Detailed motivations for selecting to survey these two particular associations is given in chapters 4 and 5. Broadly speaking, Taurus and USco are among the nearest star forming regions to the Sun ($\sim$140 pc), and thus we can examine even the faintest and lowest mass members. Taurus ($\sim$1 Myr) is a sparsely populated T association composed predominantly of low mass stars. The more evolved ($\sim$5 Myr) region of Upper Sco is a well-known OB association with $>$100 high mass Hipparcos members. Specific survey areas were selected to target both known regions of recent star formation and areas well beyond those previously studied. The goal in USco is to better constrain the mass and spatial distributions of low mass association members, and in Taurus is to search for a possible distributed population of intermediate-age ($\sim$5–10 Myr) PMS stars associated with known young ($\sim$1 Myr) subclusters.

The survey presented here consists primarily of data taken at Palomar Observatory, as discussed in chapters 2– 5. Initial photometric observations were made during 12 nights of observing with the Quest-2 camera on the Samuel Oschin Schmidt 48-inch Telescope. The observations encompassed an area of $\sim$250 deg^2 near the Taurus Molecular Clouds in the northern hemisphere, and $\sim$150 deg^2 in the southern OB association of Upper Scorpius. A detailed description of the Quest-2 camera and of spatial areas observed is given in chapter 2, where I also overview photometric data reduction and analysis. In chapter 3, I combine the Quest-2 optical photometry with

2MASS near-infrared magnitudes to select candidate PMS stars. These candidates must then be observed spectroscopically to confirm signatures of youth and measure spectral types. The follow-up spectroscopic program consisted of 20 nights of observations on the Palomar 200-inch telescope using the Double Spectrograph, and 5 nights of observations at the Cerro Tololo Intra-American Observatory using the Hydra multi-fiber spectrograph.

In chapter 4, I describe results from photometric and spectroscopic observations in Taurus. I identify 42 new low mass PMS stars spread over $\sim 35^o$ in and near the Taurus molecular clouds. Based on assessment of the spatial and proper motion distributions for this population, I argue that new PMS stars identified far from the clouds cannot have originated near the known young stellar subclusters, but instead represent a newly-identified region of recent star formation. Chapter 5 is a discussion of similar results from the observations in USco. I identify 145 PMS stars from this work including 56 brown dwarfs. From analysis of all spectroscopically observed PMS candidates compared to those determined to be association members, I conclude that, within the area surveyed, USco's low mass population shares a common spatial distribution with the high mass members, and find no evidence for spatial segregation.

Chapters 6 and 7 present discussions of follow-up analysis from the survey in USco. In chapter 6 I assess the observed age spread for low mass stars and brown dwarfs as derived from an HR diagram. I derive the first spectroscopic mass function for USco that extends into the substellar regime, and compare results in this region to those I derived previously for the ONC, as well as to results from the literature for other young regions. Chapter 7 presents mid-infrared observations taken with the *Spitzer Space Telescope* for 27 substellar members of USco identified in my thesis. In chapter 8, I discuss ongoing and future directions for this work, and in chapter 9, I give a brief summary of all results.

Part I:
New Observations

Chapter 2

Photometric Surveys of Taurus and Upper Scorpius Using Quest-2: The Saga

Results from my thesis work center around identification and analysis of large numbers of new young and intermediate-age PMS stars in the two nearby star forming regions of Taurus and USco. This work required multiple types of observations, starting with large photometric surveys carried out using the Quest-2 camera on the Palomar 48-inch telescope. All of the new PMS stars presented in this work were first identified as candidate young objects based on their optical Quest-2 colors and magnitudes, and later confirmed from spectroscopic analysis to be bona fide PMS stars.

As part of my work with the Quest-2 data, I built a PSQL database which allowed me to easily store, organize, and access the data, and a C++/PSQL software package for data calibration and manipulation. In total, my survey consists of $UBRI$ observations of $\sim$250 deg^2 near Taurus and $\sim$150 deg^2 near USco. Twelve separate scans were observed of the entire survey field near Taurus, and 24 scans were observed of the central $\sim$60 deg^2 of the field in USco. Motivations for observing specific areas in each region are described in chapters 4 & 5. A detailed discussion of PMS star candidate selection is reserved for chapter 3. In this chapter, I describe the Quest-2 camera and give an abbreviated description of the processes required to reduce and calibrate the data.

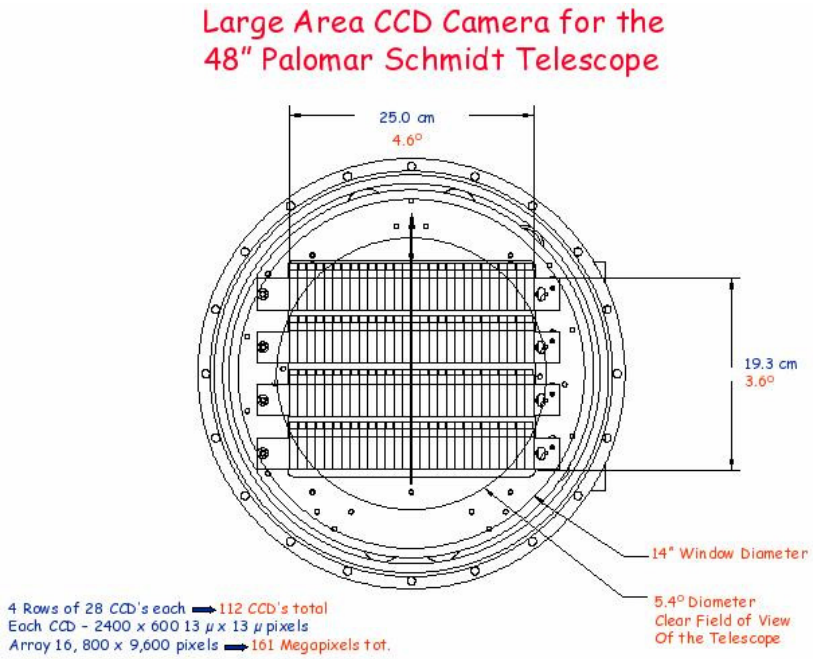

Figure 2.1 Layout of CCDs in the Quest-2 camera. Image taken from http://hepwww.physics.yale.edu/quest/large-camera.html.

2.1 Quest-2 Camera and Yale Reduction Pipeline

All photometric data were taken with the Quest-2 Camera (Rabinowitz et al., 2003) on the 48-inch Samuel Oschin Schmidt Telescope at Palomar Observatory. The Quest-2 Camera is a large-area mosaic of 112 CCDs arranged in 4 rows by 28 columns (see figure 2.1). Each of the four rows views the sky through a separate filter, in this case, UBR or I. The CCDs are 600 $\times$ 2400 pixels with a scale of $\sim$0.8"/pixel. In total, the camera covers a $3.6^o \times 4.6^o$ field of view, but taking into account gaps between rows and chips, the total on-sky coverage is 9.4 deg^2. The data were observed in driftscan mode in which any given patch of sky is observed over the entire 2400-pixel width of four separate CCDs (1 per filter) in one of the 28 columns. Charge is continuously read out of each CCD throughout the observation and the final data product is a strip of uniform width in declination and time-dependent length in right ascension that has been imaged in four filters.

In Taurus, one strip covering the RA range $40^o \lesssim \alpha \lesssim 90^o$ and spanning 4.6^o

in declination centered on δ=22.5^o was observed twice per night on the nights of 27–30 November 2003 and 4–5 December 2003 for a total of 12 scans of the same portion of the sky. This spatial area includes the young regions of L 1536 and L 1529, as well as the Pleiades open cluster (α=57^o, δ=24^o). In USco, three scans, centered at $\delta = -15.7^o, -19.5^o, -23.3^o$, were each observed between RA of 15h46m and 16h36m. The scan centered at $\delta = -19.5^o$ was observed 3–4 times per night on seven consecutive, photometric nights between 20 and 26 June 2004. The other two scans were observed once each during this period. The CCDs are less sensitive in the U-band than anticipated and very few source detections were obtained in either region. I therefore exclude the U data from the remainder of this discussion. In addition, 14 of the 84 B, R, I CCDs have failed since installation due to bad connections or faulty chips, rendering the spatial coverage within each survey region non-uniform.

When operated in driftscan format, the Quest-2 camera generates ∼50 GB of raw, compressed data in a single night. To efficiently process such a large volume of data, the Quest-2 Collaboration (Rabinowitz et al., 2003) has developed automated data reduction software (Andrews, 2003) referred to below as the 'Yale pipeline.' Each of the CCDs is treated as a separate instrument during reductions. I will therefore explain the procedure only for a single chip. The software first performs the basic bias subtraction and flat-fielding. The bias level for a given column of the CCD is computed by median-combining 25 rows in the overscan region. Dark subtraction and flat-fielding cannot be carried out using the standard techniques of pointed observations. Instead, skyflat and dark driftscans were taken on the first night of observations in both regions. Each such scan is first divided into 240 separate 600 × 10 pixel segments. These segments are median-combined using the IRAF IMSUM task to remove cosmic rays (darks) or stars (skyflats). The resulting 600x10 pixel image is then averaged into a single row of 600 pixels using the IRAF BLKAVG task. The averaged dark and flat rows are subtracted and divided respectively from each row of data.

For a given CCD, the Yale pipeline divides a drift scan into discrete frames 2048

pixels in length. After pre-processing, the pipeline generates a point-spread function (PSF) for each frame which it uses to detect sources and generate PSF photometry. It registers detections from all four filters and generates an astrometric solution from the USNO-A2 catalog. The Yale pipeline then measures aperture photometry for all objects through a square aperture of half-width 3.5 pixels. The final data product I received was a catalog containing positions and instrumental magnitudes (both PSF and aperture) for each source detected in this manner.

2.2 Post-"Yale Reduction Pipeline" Pipeline

My first task on this project was to build a database to hold the data given to me, some 200 million detections from $\sim$400 deg^2 of sky. Thus, in total, the Yale catalogs contained $\sim$440,000 detections per deg^2 or 120 detections per arcmin^2 down to a magnitude of $\sim$20 (see §2.3 for more details). To put this number into perspective, the Hubble Deep Field detected $\sim$230 objects per arcmin^2 to a magnitude of $\sim$30, 13$\times$ fainter than my survey limit. As I quickly figured out, the source of the anomalously high number of objects detected in my data largely originated from the methods employed during initial processing of the driftscans. The Yale pipeline is efficient at processing a very large amount of data relatively quickly. However, the pipeline is not designed to be efficient at identifying bona fide astronomical sources. Most of the CCDs that comprise the Quest-2 camera are of *engineering grade* rather than science grade. As a result, they have many more cosmetic defects than those used in typical scientific instruments. The Yale pipeline does not sufficiently account for these defects and thus identifies many CCD artifacts as astronomical sources. This problem is compounded by the fact that the detection algorithm was written to find very faint quasars and therefore uses a low detection threshold which identifies even low signal-to-noise detections as candidate sources.

The third, and dominating source of spurious detections requires explanation of the method that is used by the Yale pipeline to detect sources. For a given frame, a PSF is generated by stacking postage cutouts of individual stars. However, because

the pipeline does not first reject faint, crowded or false detections, the frame PSFs are often odd-shaped, and do not adequately represent the PSF of the data. Each star on a given frame is fit with this PSF and then subtracted. Any residuals due to imperfect PSF subtraction (most often due to odd PSFs rather than odd data) are then refit and subtracted again. The process repeats until no residuals are left. Thus, this process produces not only (often) erroneous PSF photometry, but also many extra detections for each star. The combined result of these decisions is that the data catalogs I received were dominated by 'junk' detections, i.e., catalog entries that did not correspond to real sources. The majority of the extra sources originated from single stars that the pipeline decided were two (or more depending on the brightness of the star).

None of the above facts are documented, and thus, it took a non-trivial amount of time (on the order of 6 months) to determine 1) that most of the sources in the catalog were not real, and 2) from where the false detections originated. Once both of these facts had been established, the question became how to get around the problem. The Yale pipeline establishes a detection in one filter and then forces photometry in the other three, regardless of whether the original source is a bona fide star as opposed to a 'junk' source or an artifact. Thus, requiring detections in multiple filters as a way to weed out junk sources at this stage was not effective. Instead, I took advantage of the fact that repeated monitoring observations were taken.

2.2.1 Source Matching

In sum, I took 12 scans of the entire survey field near Taurus, and 24 scans of the central $\sim$60 deg^2 of the field in USco, where one 'scan' refers to a single driftscan observation of the area. I matched detections between scans within a 0.8" radius and computed new coordinates for each source by averaging together coordinates from individual scans. The typical astrometric RMS deviation about the mean was $\sim$0.13". For occasions where multiple sources were detected within a single scan, the source closest (in RA and DEC) to detections of the same star in other scans was

chosen as the real source and a 'confusion' flag was inserted into the catalog indicating that the source was either a projected multiple ($a \lesssim 110$ AU in projected distance), or adjacent to one or more bogus detections. This step produced catalogs containing $\sim$8 and $\sim$15 million sources in USco and Taurus, respectively. Of those, $\sim$60% in each region of multiple observations were single detections with no counterparts on other scans and were eliminated from further consideration.

2.2.2 Calibration to the Sloan System

Deriving calibrations capable of converting the Quest-2 photometry to a standard system is significantly more complicated that it is for general point and track observations taken with single CCD cameras. Because the data are taken in driftscan format, the flux from each star has traveled across 2400 separate pixels on a given CCD before being read out. Because each CCD functions as an independent detector, calibrations must be derived for each of the 112 CCDs separately. Many of the CCDs have been found to be highly non-linear, and spectral response is known to vary from pixel-to-pixel across each detector. Both gain levels and linearity have been found to vary as a function of time. Thus, in order to calibrate the data in a truly robust manner, observations of standard stars would need to have been taken at several places on each of the 112 CCDs throughout my observations. Taking such observations was not realistically feasible. Below I describe the procedure I used to calibrate the Quest-2 data to a photometric system *close to* that used by the Sloan Digital Sky Survey (York et al., 2000). I chose to calibrate to Sloan data because, at the time, it was the largest optical imaging survey that significantly overlapped area surveyed with the Quest-2 camera. However, because the calibration data was not observed at the same time as was my survey data (see below), and the gain and linearity are known to be time variable, it is not possible to transform the Quest-2 magnitudes exactly into Sloan photometry.

I matched a subset of data taken by the Quest-2 collaboration (Rabinowitz et al., 2003) in a different part of the sky ($-2.5^o \lesssim \delta \lesssim 2.5^o$, $120^o \lesssim \alpha \lesssim 240^o$) to data from

Sloan. For each of the Quest-2 CCDs, I computed a conversion from Quest-2 to Sloan magnitudes in the form of:

$$r = a_R + b_R \times R_{Quest} + c_R \times Row + d_R \times (R-I)_{Quest}$$

$$i = a_I + b_I \times I_{Quest} + c_I \times Row + d_I \times (R-I)_{Quest}$$

$$g = a_B + b_B \times B_{Quest} + c_B \times Row + d_B \times (B-R)_{Quest},$$

where a_X, b_X, c_X, d_X are constants and '*Row*' refers to a row of pixels (perpendicular to the drift scan direction) on the CCD. Only stars with both Sloan and Quest-2 photometric uncertainties of < 0.1 mag, and instrumental Quest-2 magnitudes $11.5 < R, I < 19$ and $14 < B < 21$ were used to derive the calibrations to avoid saturated and faint sources with systematically larger uncertainties than those present for the bulk of the population. Constants were computed every 0.75 mag (b_X), 50 pixels (c_X) and 0.2 mag in color (d_X) and determined in an iterative manner for each equation above until each constant changed by <0.0005 mag for at least 3 iterations.

Derived coefficients are shown in figures 2.2–2.8. Many CCDs do not have calibrations either because that CCD is not functioning properly, or because the corresponding CCD required to compute color terms is not functioning properly. Figure 2.2 shows the zeropoint applied to the transformations for each chip plotted as a function of instrument column (i.e., 1–28). Each filter (i.e., row 1–4) is shown as a different symbol. Zeropoints (a_X terms) are negative for all CCDs discussed here. Figures 2.3 & 2.4 illustrate that most CCDs are not linear (b_X coefficients) and CCD sensitivity is a function of magnitude that decreases for brighter stars. Row (pixel on the CCD) coefficients (c_X; figures 2.5 & 2.6) in general are not large. The 'wave-like' pattern seen for CCDs in column 14 occurs because the each filter is actually in parts, which join in the middle of the CCDs in column 14. By far the largest and most structured calibration terms are the color coefficients (d_X) shown in figures 2.7 & 2.8. These figures illustrate that the reddest stars are systematically fainter than the bluest stars by as much as 0.5 magnitudes.

Average values for each constant are given in the second column of table 2.1, along with the full range covered by all 28 CCDs in a particular filter (column 3 of table 2.1). Constants listed correspond to coefficients in the calibration equations given above.

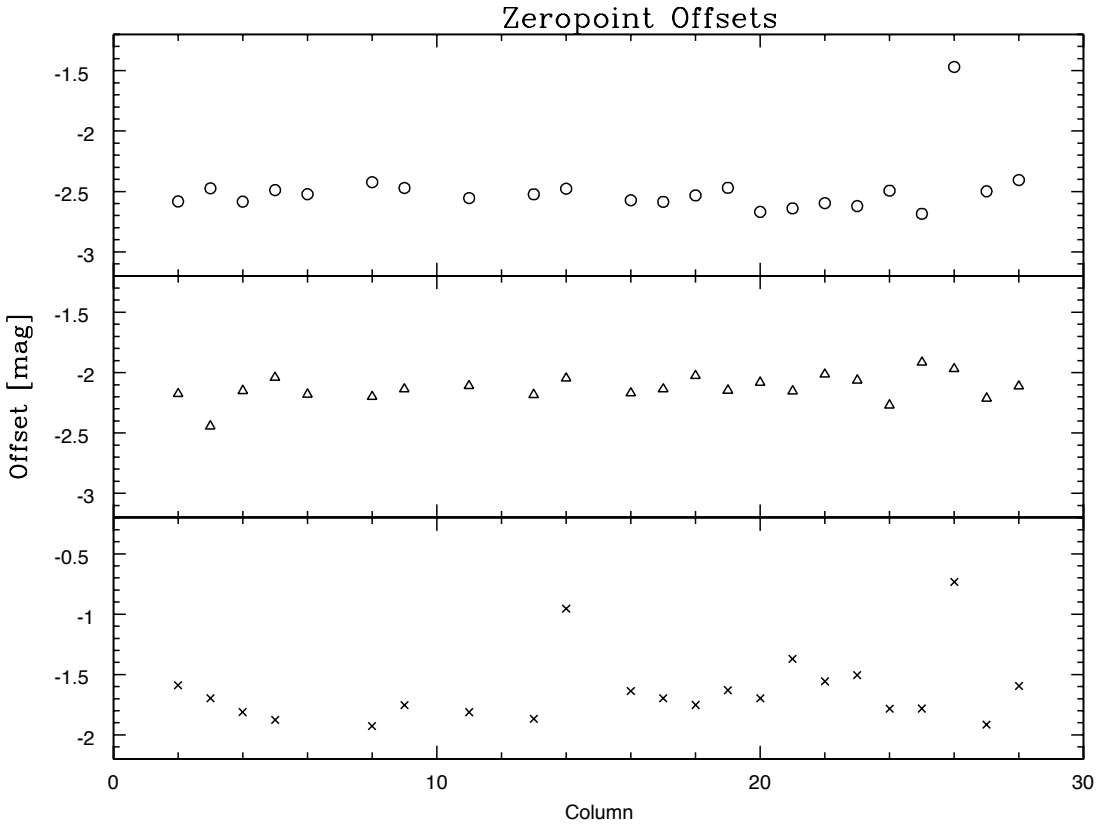

Figure 2.2 Calibration terms (a_X values) shown for individual CCDs, plotted as a function of instrument column (i.e., 1–28). Each filter (i.e., row 1–4) is shown as a different symbol. Symbols are as follows: circles represent R–band terms, triangles represent I–band terms, and x's represent B–band terms. Many CCDs do not have calibrations either because that CCD is not functioning properly, or because the corresponding CCD required to compute color terms is not functioning properly.

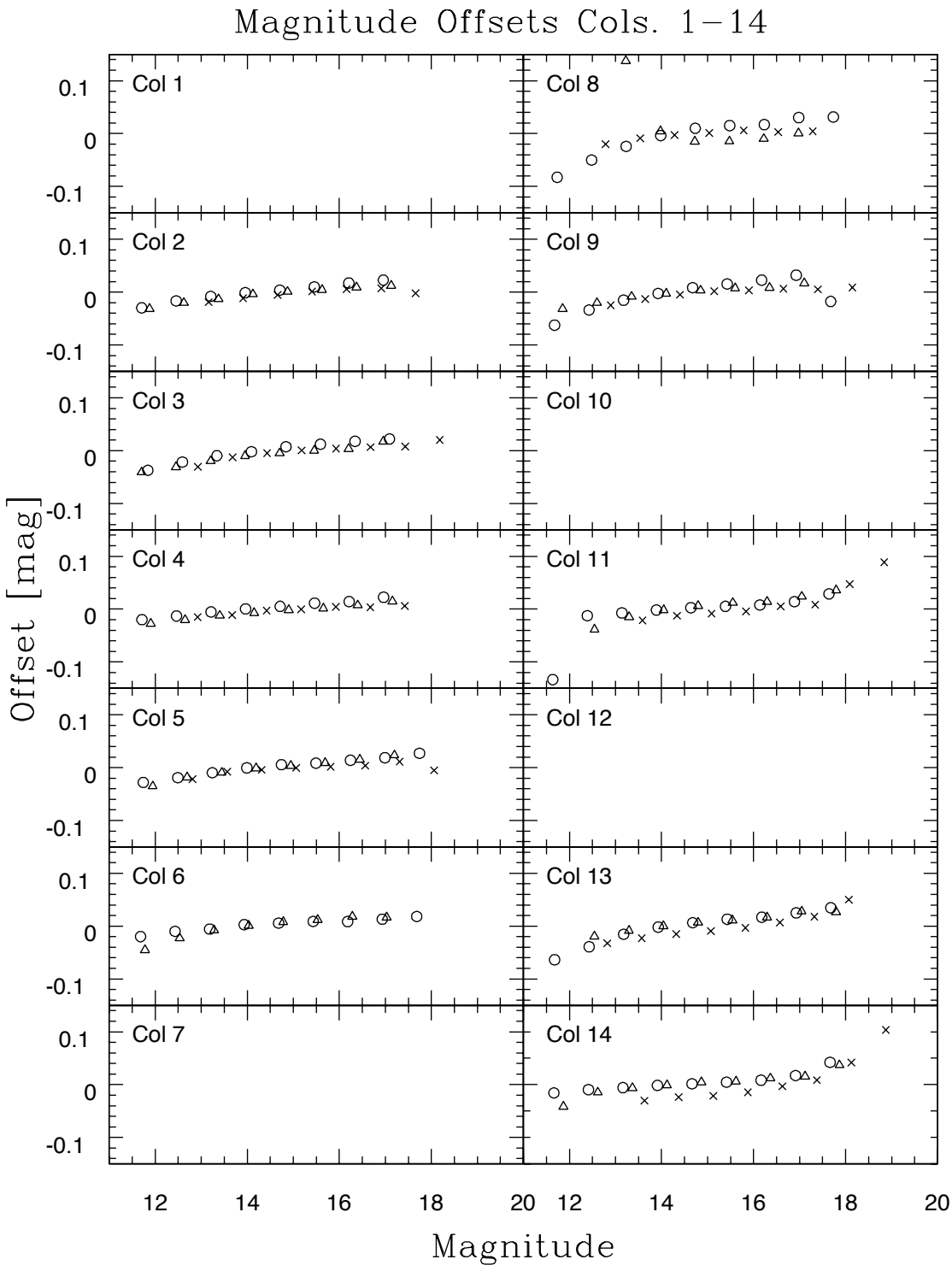

Figure 2.3 Calibration terms (b_X values) for each column (1–14) computed as a function of magnitude. Symbols are as follows: circles represent R–band terms, triangles represent I–band terms, and x's represent B–band terms. Many CCDs do not have calibrations either because that CCD is not functioning properly, or because the corresponding CCD required to compute color terms is not functioning properly.

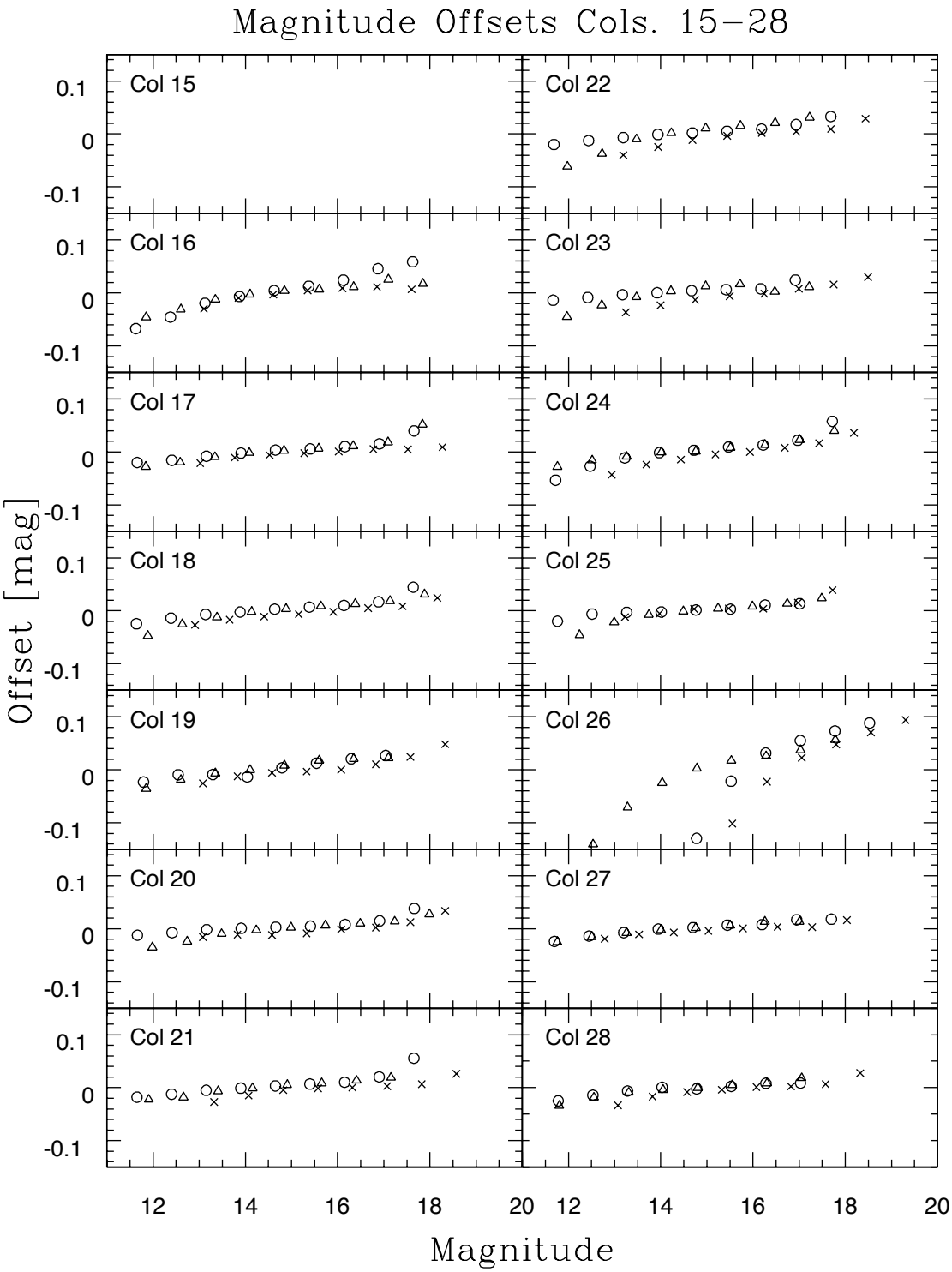

Figure 2.4 Calibration terms (b_X values) for each column (15–28) computed as a function of magnitude. Symbols are as follows: circles represent R–band terms, triangles represent I–band terms, and x's represent B–band terms. Many CCDs do not have calibrations either because that CCD is not functioning properly, or because the corresponding CCD required to compute color terms is not functioning properly.

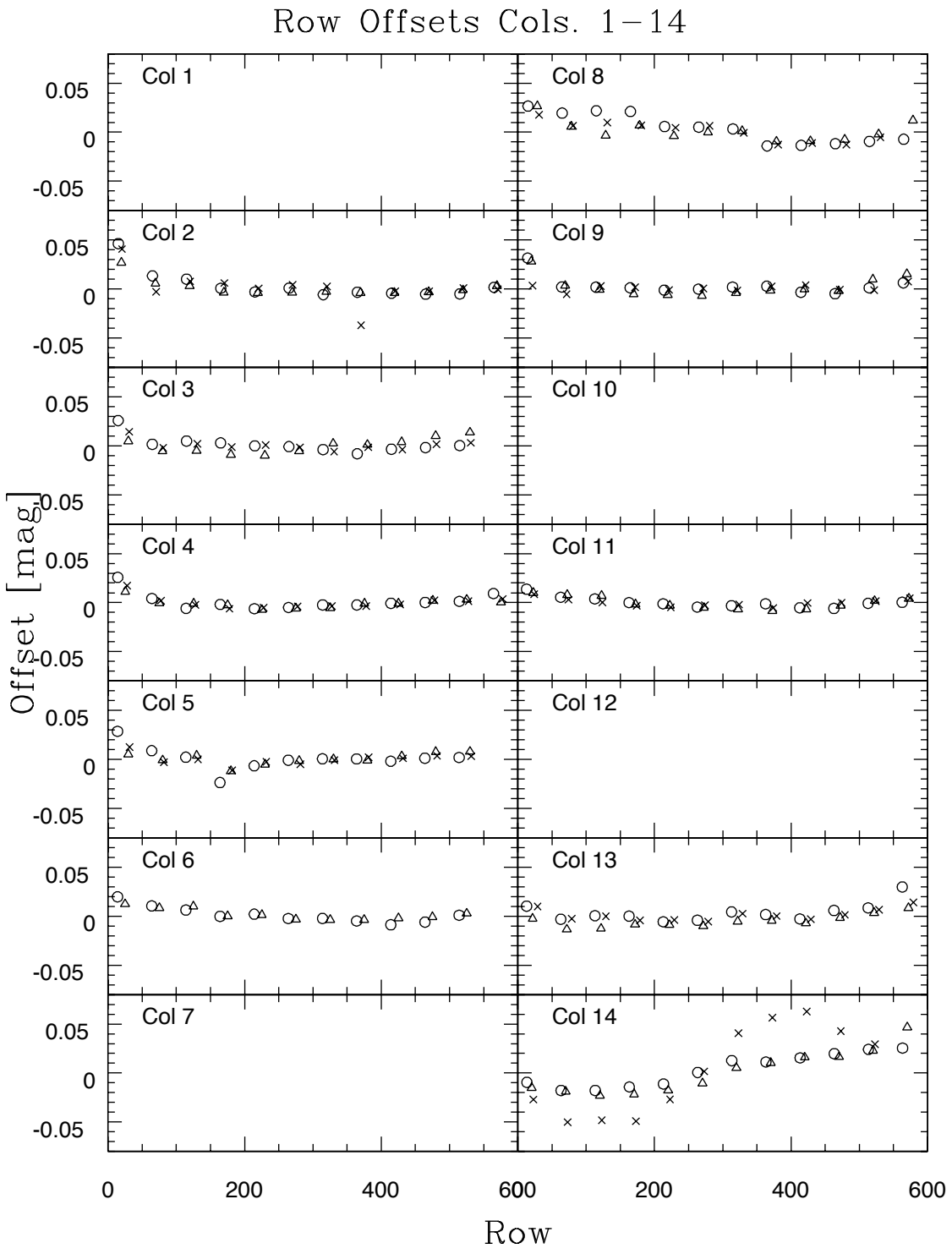

Figure 2.5 Calibration terms (c_X values) for each column (1–14) computed as a function of position on the CCD (i.e., row 0–600). Symbols are as follows: circles represent R–band terms, triangles represent I–band terms, and x's represent B–band terms. Many CCDs do not have calibrations either because that CCD is not functioning properly, or because the corresponding CCD required to compute color terms is not functioning properly.

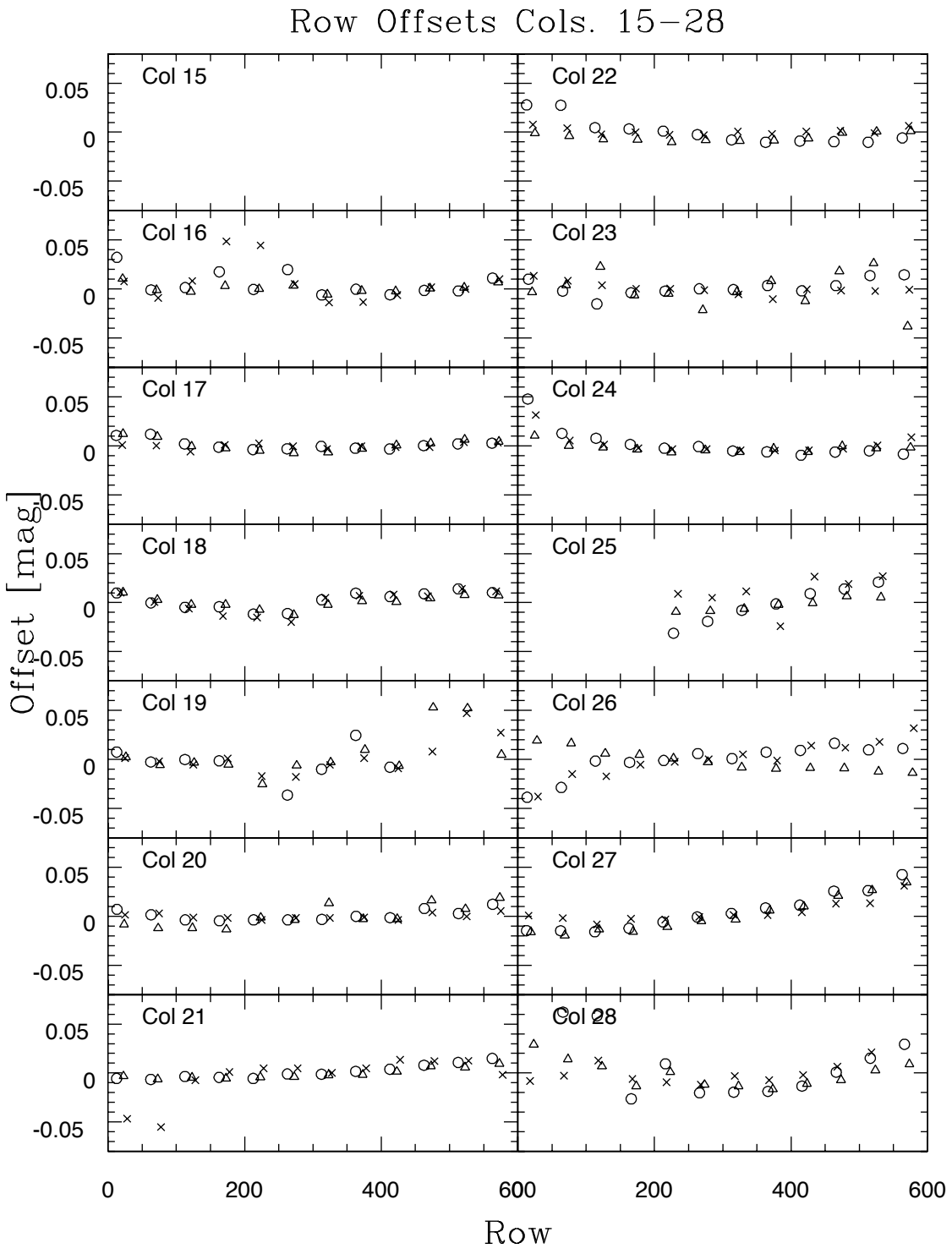

Figure 2.6 Calibration terms (c_X values) for each column (15–28) computed as a function of position on the CCD (i.e., row 0–600). Symbols are as follows: circles represent R–band terms, triangles represent I–band terms, and x's represent B–band terms. Many CCDs do not have calibrations either because that CCD is not functioning properly, or because the corresponding CCD required to compute color terms is not functioning properly.

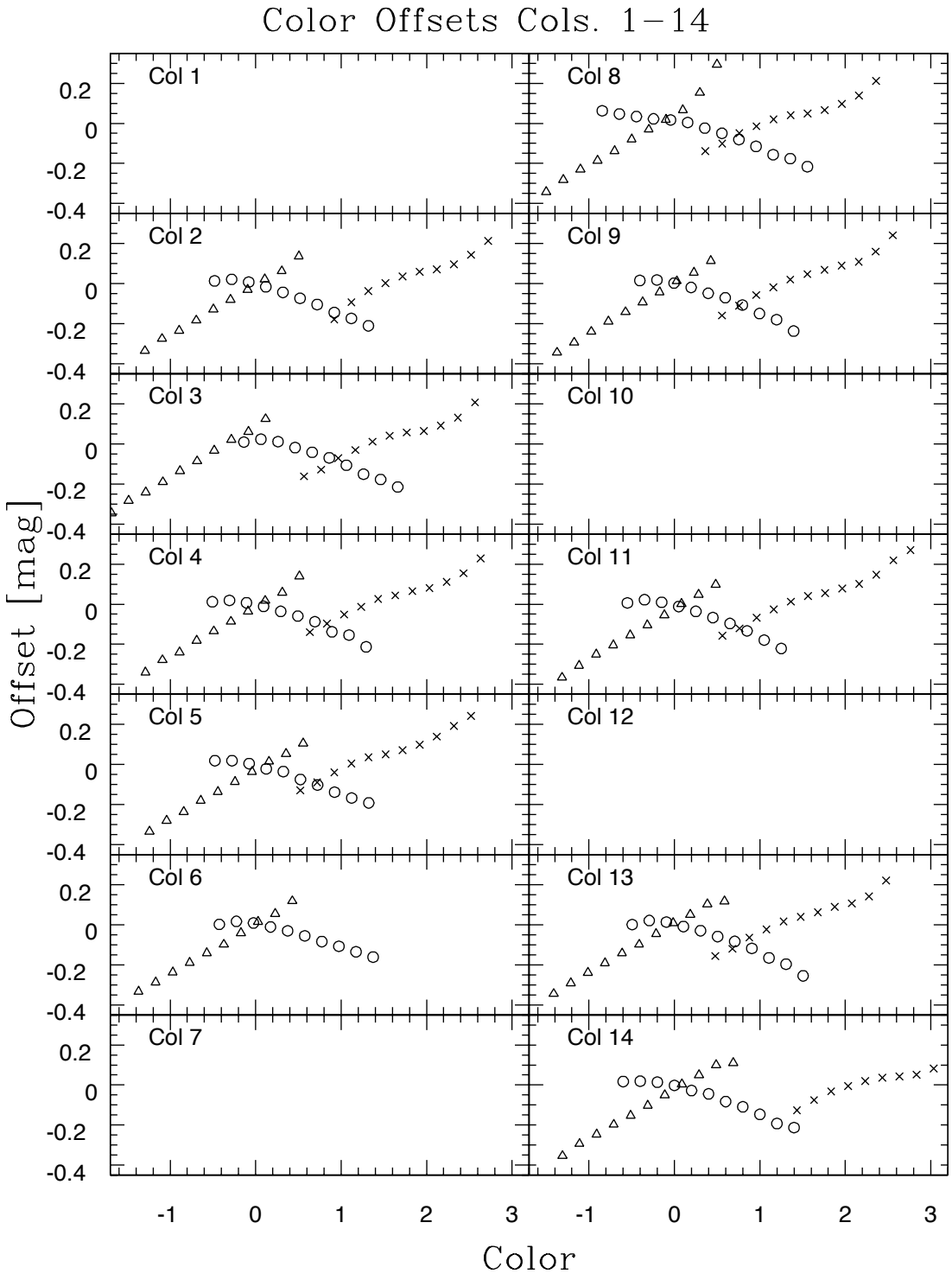

Figure 2.7 Calibration terms (d_X values) for each column (1–14) computed as a function of color. Symbols are as follows: circles represent R–band terms computed from $R - I$ colors, triangles represent I–band terms computed from $I - R$ colors, and x's represent B–band terms computed from $B - R$ colors. Many CCDs do not have calibrations either because that CCD is not functioning properly, or because the corresponding CCD required to compute color terms is not functioning properly.

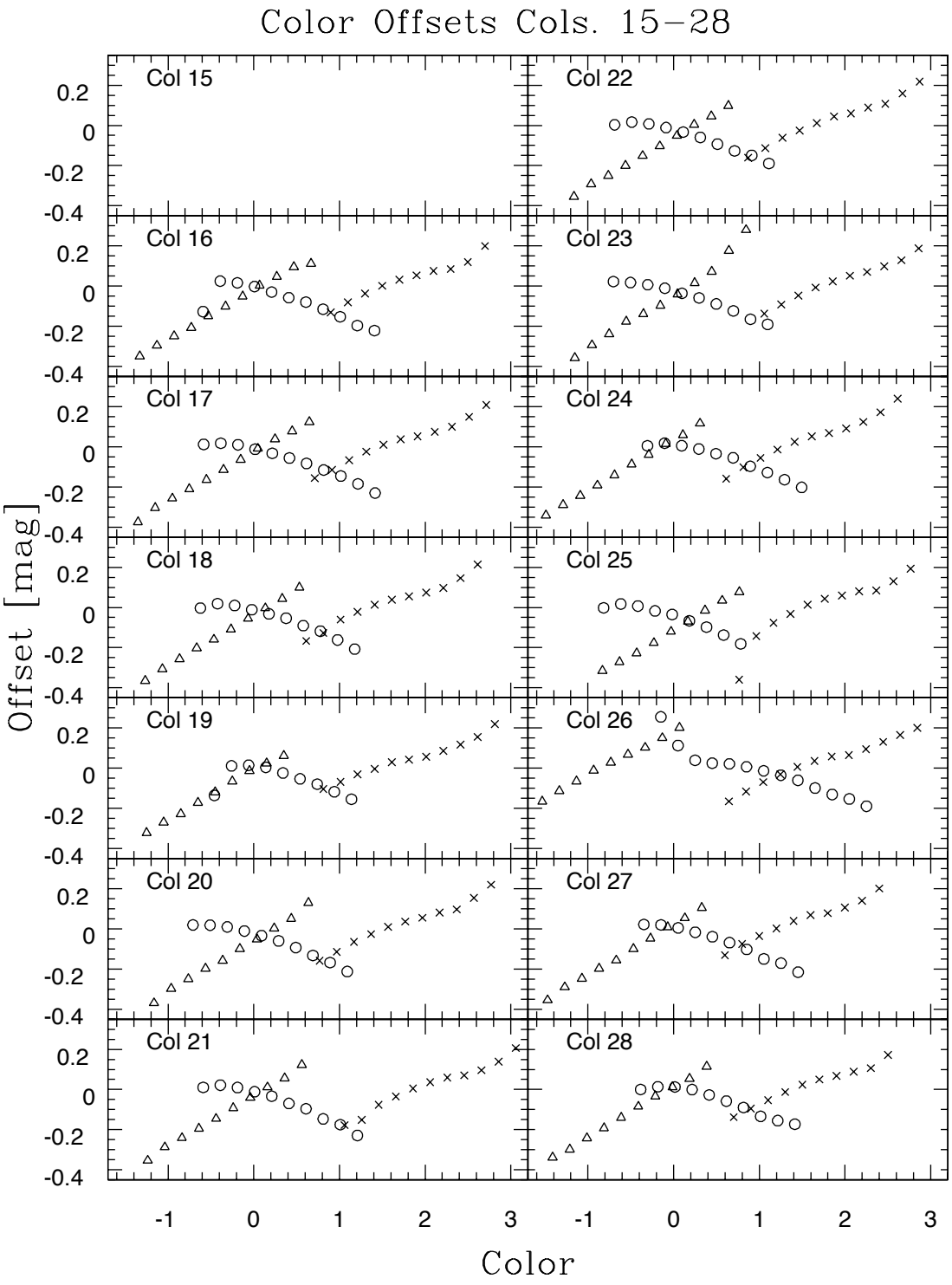

Figure 2.8 Calibration terms (d_X values) for each column (15–28) computed as a function of color. Symbols are as follows: circles represent R–band terms computed from $R - I$ colors, triangles represent I–band terms computed from $I - R$ colors, and x's represent B–band terms computed from $B - R$ colors. Many CCDs do not have calibrations either because that CCD is not functioning properly, or because the corresponding CCD required to compute color terms is not functioning properly.

Table 2.1. Calibration constants for Quest-2–to–Sloan conversions

constant	<value>[a]	full range[a,b]	$< \sigma >$[a]	<nstars>
a_R	-2.49	-2.68 – -1.46	0.06	14717
a_I	-2.12	-2.44 – -1.91	0.05	14735
a_B	-1.63	-1.92 – -0.73	0.06	8933
b_R	-0.01	-1.03 – 0.08	0.13	1653
b_I	0.00	-0.34 – 0.25	0.11	1708
b_B	0.00	-0.54 – 0.10	0.10	1121
c_R	0.00	-0.08 – 0.25	0.13	1234
c_I	0.00	-0.03 – 0.05	0.11	1238
c_B	0.00	-0.05 – 0.06	0.08	753
d_R	-0.06	-0.25 – 0.25	0.14	1399
d_I	-0.10	-0.37 – 0.42	0.10	1408
d_B	0.02	-0.72 – 0.26	0.09	802

[a]Value given is in magnitudes.

[b]'Full range' refers to the minimum and maximum value of each coefficient across all 28 CCDs within a given filter.

Often the range for a single coefficient is quite large, ∼0.5–1 mag, even when the average term is close to zero. This point is illustrated explicitly in figures 2.2–2.8. Also given in table 2.1 is the average sigma for each constant and the average number of stars that went into computing a given constant. In general, average sigmas listed are representative of all CCDs excepting the R & B CCDs in column 26 for which an unreliable cable causes inconsistent measurements and large non-linearity problems.

I applied the derived calibrations to the Taurus and USco instrumental magnitudes by linearly interpolating between values in each parameter for the appropriate CCD's coefficients. Outlier calibration points arising from noisy data at faint magnitudes or chip edges were identified and not applied to the catalog data. To account for differences in airmass between the Yale calibrator scans and USco scans, I applied the first order linear extinction terms as derived by Fukugita et al. (1996), 0.09, 0.08, & 0.18 for *rig* respectively, and assumed an average airmass of $Z = 2$ for all USco driftscans. The Taurus scans were taken at low air mass similar to that of the

calibrator scans, and no airmass correction was applied.

2.2.3 Night-to-Night Calibrations

I accounted for small atmospheric transparency changes during the night and between nights by applying a photometric offset to every scan in both regions as a function of RA. In Taurus, the data were taken primarily under non-photometric conditions. Thus, because some of the data were taken through thick clouds ($\geq$2 mag of extinction), most faint sources were not detected in all 12 scans. In Taurus, I thus chose the 'best' (i.e., most photometric) scan, taken on 27 Nov 2003, to define the photometric reference system. I selected a subset of $\sim$100,000 stars from the source catalog that were detected in at least 6 of 12 scans (including the 'best' scan used as a reference) and had no neighbors within 5". For each such star I computed the difference between the reference magnitude and the magnitude measured in an individual scan. The data in USco were taken under good conditions. Here, I selected a subset of calibrator stars from the source catalog that were detected in at least 20 out of 24 of the monitoring scans, and had no neighbors within 5". For each star and filter an average magnitude of all detections was calculated along with the difference between that average magnitude and the magnitude measured on each individual scan.

In both regions, for every chip and scan I created a catalog of offsets by stepping through in RA every 25 (USco) or 5 (Taurus) calibrator stars and calculating a median offset value. An example is shown in figure 2.9. Due to the highly structured nature of transparency changes that occurred while the Taurus data were taken, it was necessary to compute a finer grid of offsets. Average scan-to-scan offset values for a single CCD were 0.23 mag in i, 0.20 mag in r, and 0.10 mag in g in Taurus, and were much lower ($\pm$0.001 mag in all three filters) in USco. The average range of offsets within a single CCD-scan combination were 1.07 mag in i, 1.23 mag in r, and 1.11 mag in g for Taurus, and 0.05 mag in i, 0.07 mag in r, and 0.07 mag in g for USco. I applied these offsets to the entire dataset as a function of RA and CCD chip by linearly interpolating between values in RA. Because the data span $\sim$5 deg in Dec

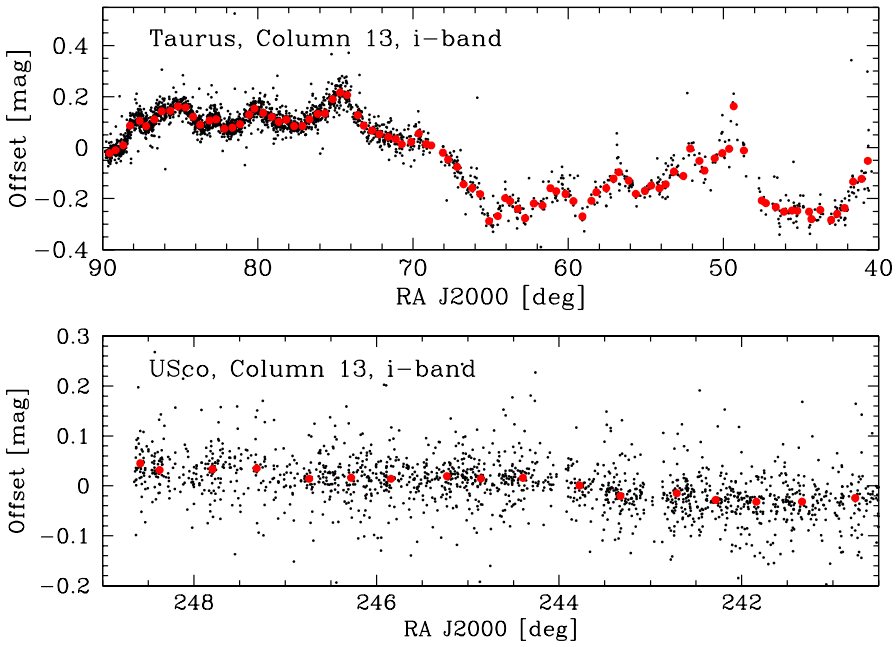

Figure 2.9 Example of calibrations computed to account for transparency changes during the night and from night to night. In both panels, black points represent stars extracted from the catalog meeting the selection criteria outlined in §2.2.3. Large red points represent median values computed every 25 (USco) or 5 (Taurus) stars. Due to the highly structured nature of transparency changes that occurred while the Taurus data were taken, it was necessary to compute a very fine grid of offsets in this region.

per driftscan, offsets as a function of declination were also computed. However, upon examination, I found no systematic structure in the offsets as a function of declination and thus, only the RA offset was necessary.

The high (δ =-15.7^o) and low (δ =-23.3^o) declination scans in USco do not have repeated observations and overlap only the top and bottom 0.8 deg of the monitoring (repeated) scans (δ =-19.5^o) in that region. For these driftscans I calculated a scan offset as a function of RA using the same procedure outlined above but averaging together all columns of overlap with the mid-declination scans, rather than chip by chip. I find this procedure to produce magnitudes consistent with those derived from the multiple-scan region at the $< \Delta mag > = 0.2\%$ (r), 0.03% (i), and 3.8% (g) levels for objects in the overlap region. The observed differences in $< \Delta mag >$ between the three filters directly correlates to the observed differences in the average matched magnitude; i.e., the average matched g magnitude is $\sim$1 mag fainter than the average matched i magnitude, and thus, $< \Delta g >$ is systematically larger than $< \Delta i >$.

2.3 Precision, Accuracy, and Completeness

For each source in the Taurus region and in the central declination strip in the USco region, final stellar magnitudes were computed by averaging together calibrated, transparency-corrected instrumental magnitudes corresponding to the same source on-sky. I can thus use photometry from the monitoring scans to assess the relative precision of the photometric data by computing for each star the RMS deviation of individual measurements about the final, averaged magnitude. I find the photometric precision to be highly CCD dependent, owing to the fact that the 112 CCDs are of varying quality. In the left panels of figure 2.10, I show computed RMS deviations as a function of magnitude in the USco region for four different CCDs. In each plot, RMS data is shown for any star that was detected in more than half of the monitoring scans, i.e., more than 12 times. The top left panel shows repeatability for one of the best CCDs, which have average RMS values from $\sim$0.02–0.03 mag for stars brighter than gri $\sim$18, to $\sim$0.08 mag for stars fainter than this value (i.e., 18 to $\sim$20–21 mag).

The second panel from the top represents repeatability for a CCD of typical quality, with similar average RMS values of ∼0.02–0.03 mag at the bright end but higher average values of ∼0.09–0.1 at the faint end. I find nine CCDs to be of poor quality with average RMS values of ∼0.12–0.18 for faint stars. An example of such a CCD is shown in the third panel from the top. The bottom panel shows repeatability for one CCD within an anomalous column that is known to produce highly unstable magnitudes. The corresponding panels on the right show data taken on with the same CCDs in the Taurus survey for stars observed in at least half (>6) of the scans in that region. Due to bad weather at the time these data were taken, the data are of poor repeatability even after calibration, but could possibly be used to identify very high amplitude variables.

Figure 2.11 shows the similar data to that shown in the left panels of figure 2.10, but for $r - i$ color. In this case the data represent the difference of magnitudes from two different CCDs within a column. I find both color repeatability and the distribution of observed colors to be highly column dependent, as would be expected given the differences observed between CCDs in figure 2.10.

The accuracy of the absolute photometry is harder to quantify. While I have accounted for relative extinction due to weather within the dataset, I am not able to account for zero point shifts between the Taurus/USco drift scans and the scans used to derive the Quest-2–to–Sloan calibrations. Despite this fact, comparison of the average $r - i$ color for the calibrated Quest-2 photometry agrees to ∼0.01 mag with the average $r - i$ color of the Sloan data used to derive the calibrations. Therefore, while I cannot claim the photometry is on a standard Sloan g, r, i system, it should be fairly closely aligned with Sloan.

From histograms of all detections (figure 2.12) for the *rig* filters, I find a peak in number of objects detected at $r \sim 20$ mag, $i \sim 19.5$ mag, and $g \sim 20$ mag for the USco data. In Taurus, my photometric survey was slightly shallower (by ∼0.5 mag) due to challenges produced from bad weather. Figures 2.13–2.15 show detection histograms of each CCD individually for data taken in the USco region. The completeness turnover for all CCDs as an ensemble within the row containing

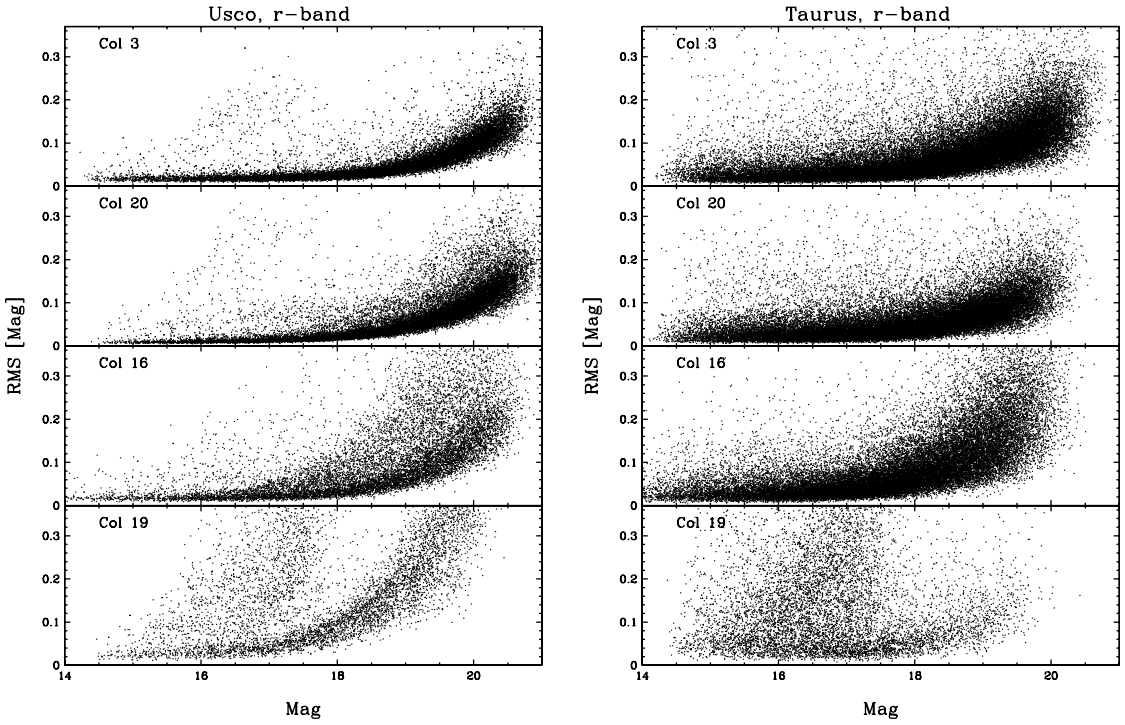

Figure 2.10 Panels on the left show computed RMS deviations as a function of magnitude in the USco region for four different CCDs. RMS data is shown for any star that was detected in more than half of the monitoring scans, i.e., more than 12 times. Each magnitude is the average of all measurements and the corresponding RMS values represent the deviation of individual measurements about that average. The top left panel shows repeatability for one of the best CCDs, the second panel represents repeatability for an average CCD, and the third panel from the top shows repeatability for one of the worst CCDs. The bottom panel shows repeatability for one CCD within an anomalous column that is known to produce highly unstable magnitudes. The corresponding panels on the right show data taken on with the same CCDs in the Taurus region. Due to bad weather at the time these data were taken, the data are of poor repeatability even after calibration.

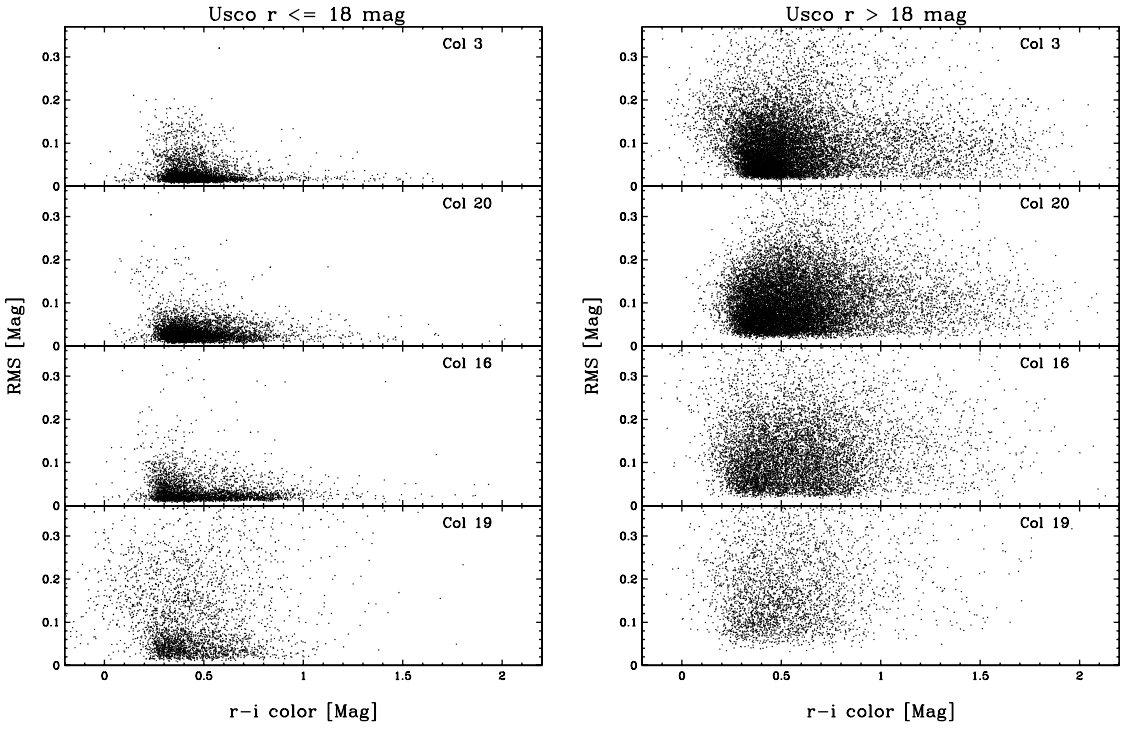

Figure 2.11 Computed RMS deviations as a function of $r-i$ color in the USco region for bright (left panel) and faint (right panel) stars in four different columns. RMS data is shown for any star that was detected in more than half of the monitoring scans, i.e., more than 12 times in both r and i CCDs within a column. Each magnitude is the average of all measurements and the corresponding RMS values represent the deviation of individual measurements about that average. Panels are as described in figure 2.10.

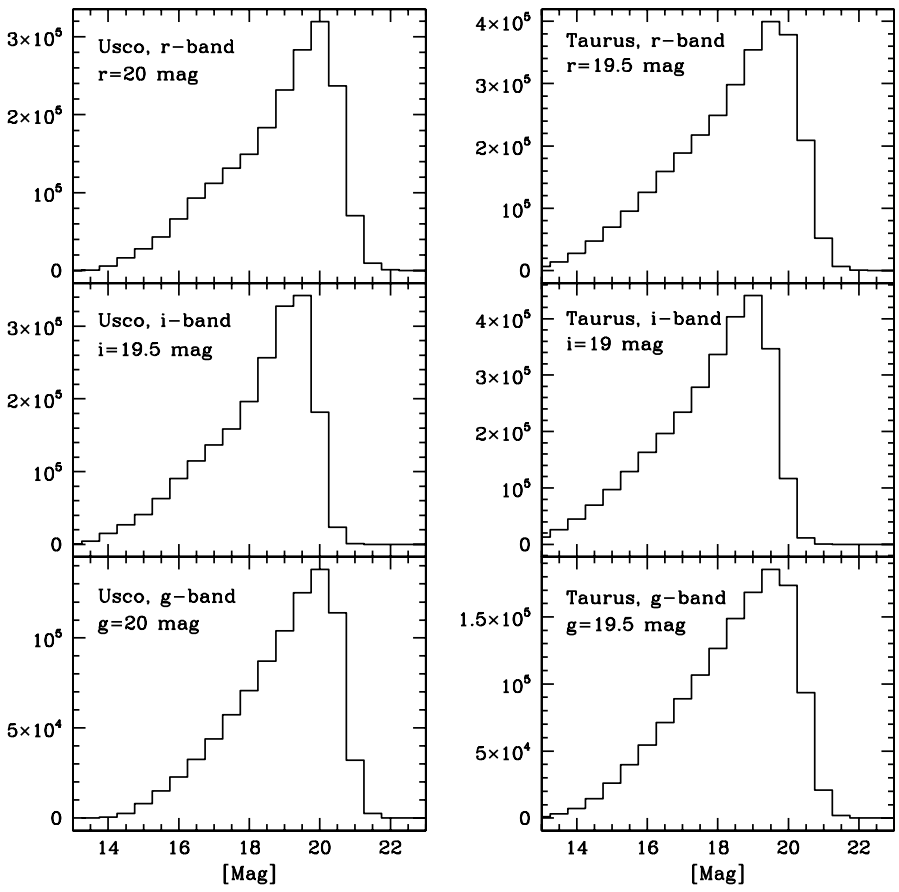

Figure 2.12 Number of individual stars in each region as a function of magnitude. Data have been binned by 0.5 mag. Approximate histogram peaks are given in each panel.

that CCD (i.e., all 28 columns in a single filter) is shown in each panel as a dotted line. Data in figures 2.12–2.15 have been binned by 0.5 magnitudes. The histogram peak, saturation points and CCD sensitivity varies between CCDs. However, in general, I find the peak of the histograms for individual CCDs corresponds to that found for the ensemble average in that filter. Noted exceptions are that CCDs in columns 19 and 25 (in all filters) and column 16 in the g filter are not as sensitive as most of the other CCDs, due to electronic/detector unreliability, and the histograms for CCDs in column 26 (all filters) have a different profile shape than most others. The histograms for the r and i CCDs in column 28 have the same shape as for the other r and i CCDs, however, many fewer sources were detected.

2.4 Summary of Quest-2 Photometric Survey

The final source catalogs contains optical photometry for $\sim$3 million sources within the $\sim$250 deg^2 Taurus survey region and $\sim$2 million sources in the $\sim$150 deg^2 USco region. In both regions, some or all of the stars have repeated monitoring observations. In this chapter I detail source matching among the repeated observations and account for night-to-night transparency changes. I also convert the data such that they are closely aligned with the standard Sloan gri system. In the next chapter (chapter 3), I present photometric diagrams (color-color and color-magnitude), and explain how I use these data combined with follow-up spectroscopic observations to identify PMS stars.

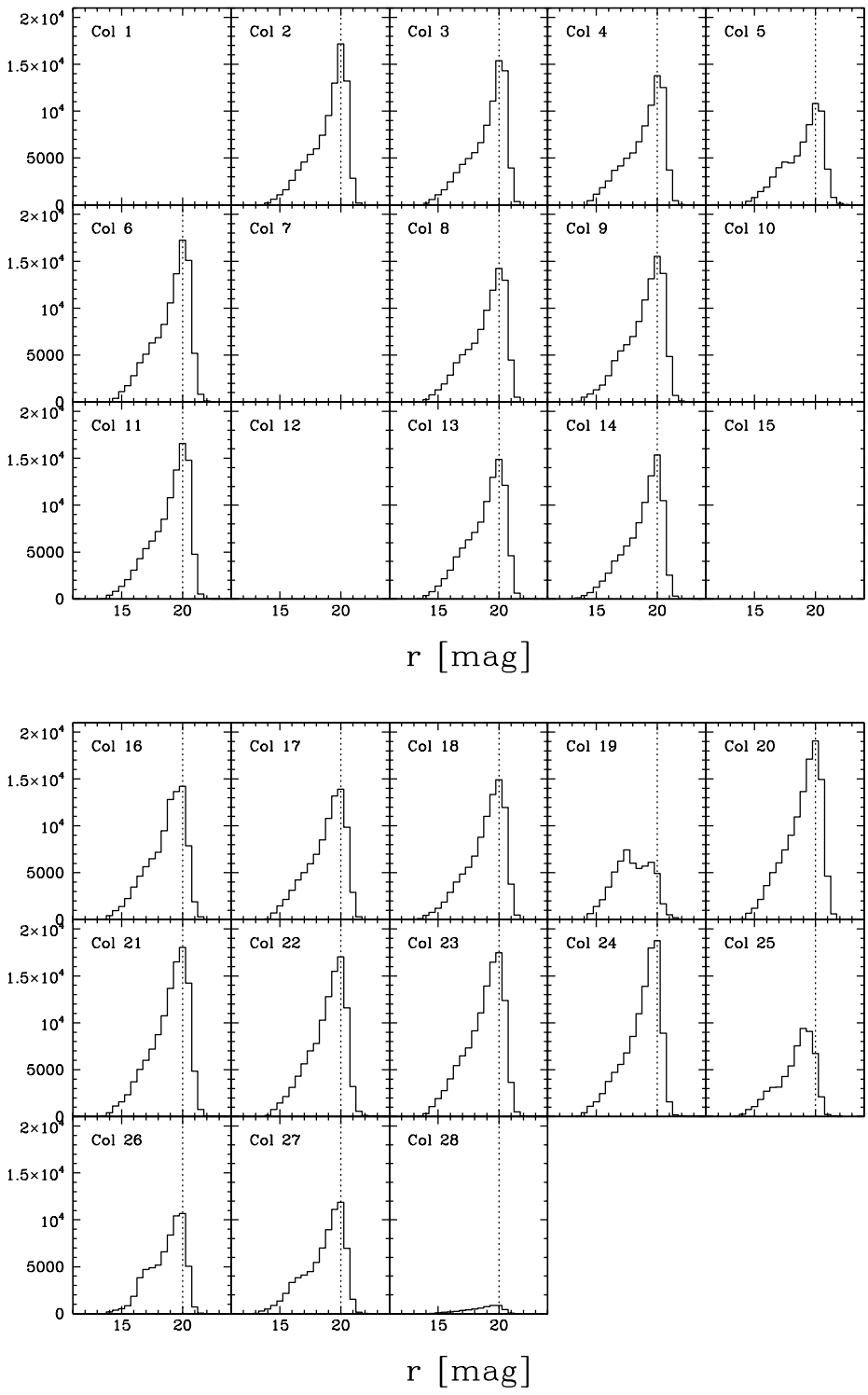

Figure 2.13 Number of detections as a function of magnitude in the USco survey for individual CCDs. The completeness turnover for all CCDs in the r filter as an ensemble is shown in each panel as a dotted line at r=20 mag. Variations in completeness, saturation point, and sensitivity can be seen between CCDs. Blank panels correspond to CCDS that have either failed since installation, or do not have derived calibrations (see §2.2.2).

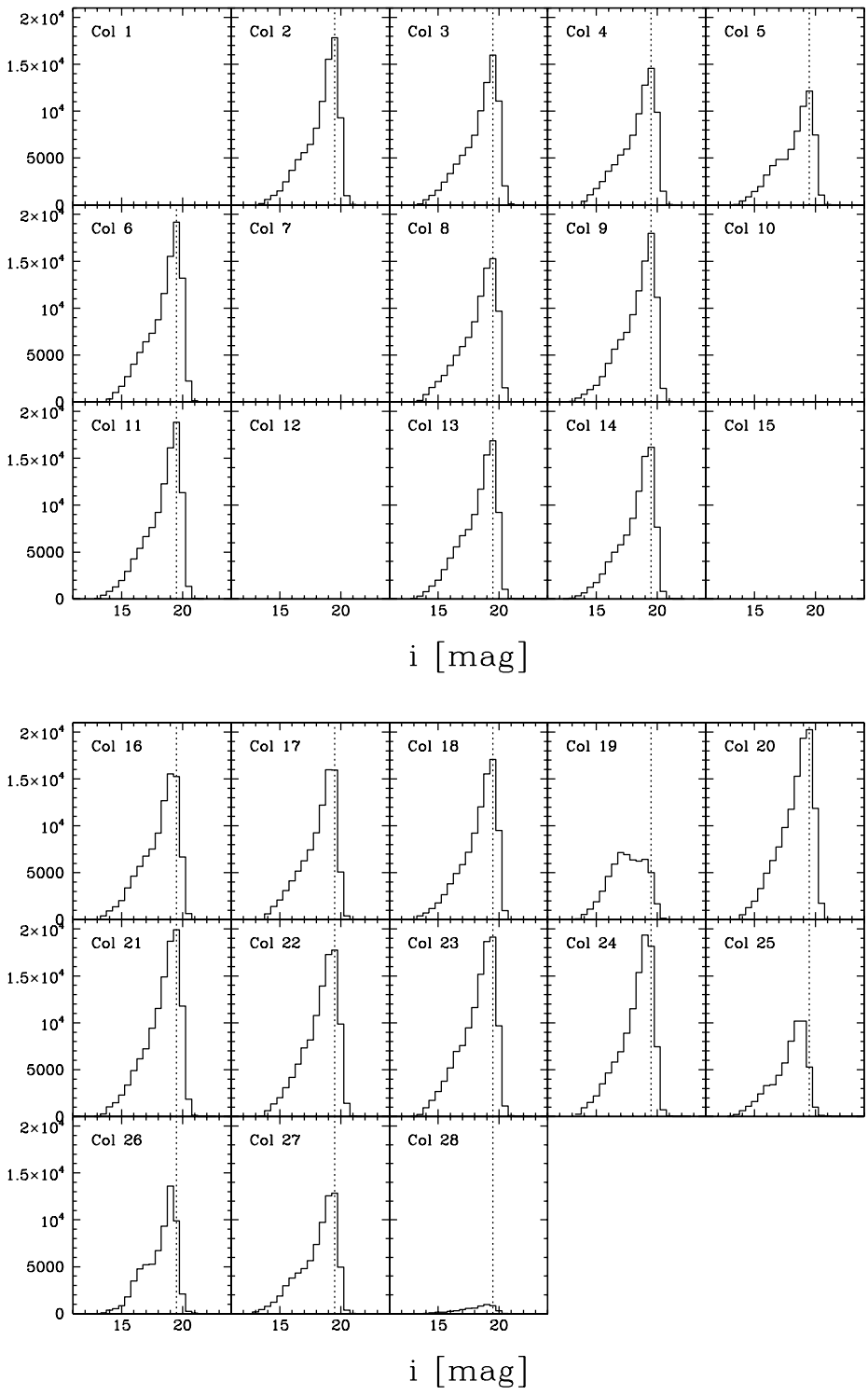

Figure 2.14 Number of detections as a function of magnitude in the USco survey for individual CCDs. The completeness turnover for all CCDs in the i filter as an ensemble is shown in each panel as a dotted line at i=19.5 mag. Variations in completeness, saturation point, and sensitivity can be seen between CCDs. Blank panels correspond to CCDS that have either failed since installation, or do not have derived calibrations (see §2.2.2).

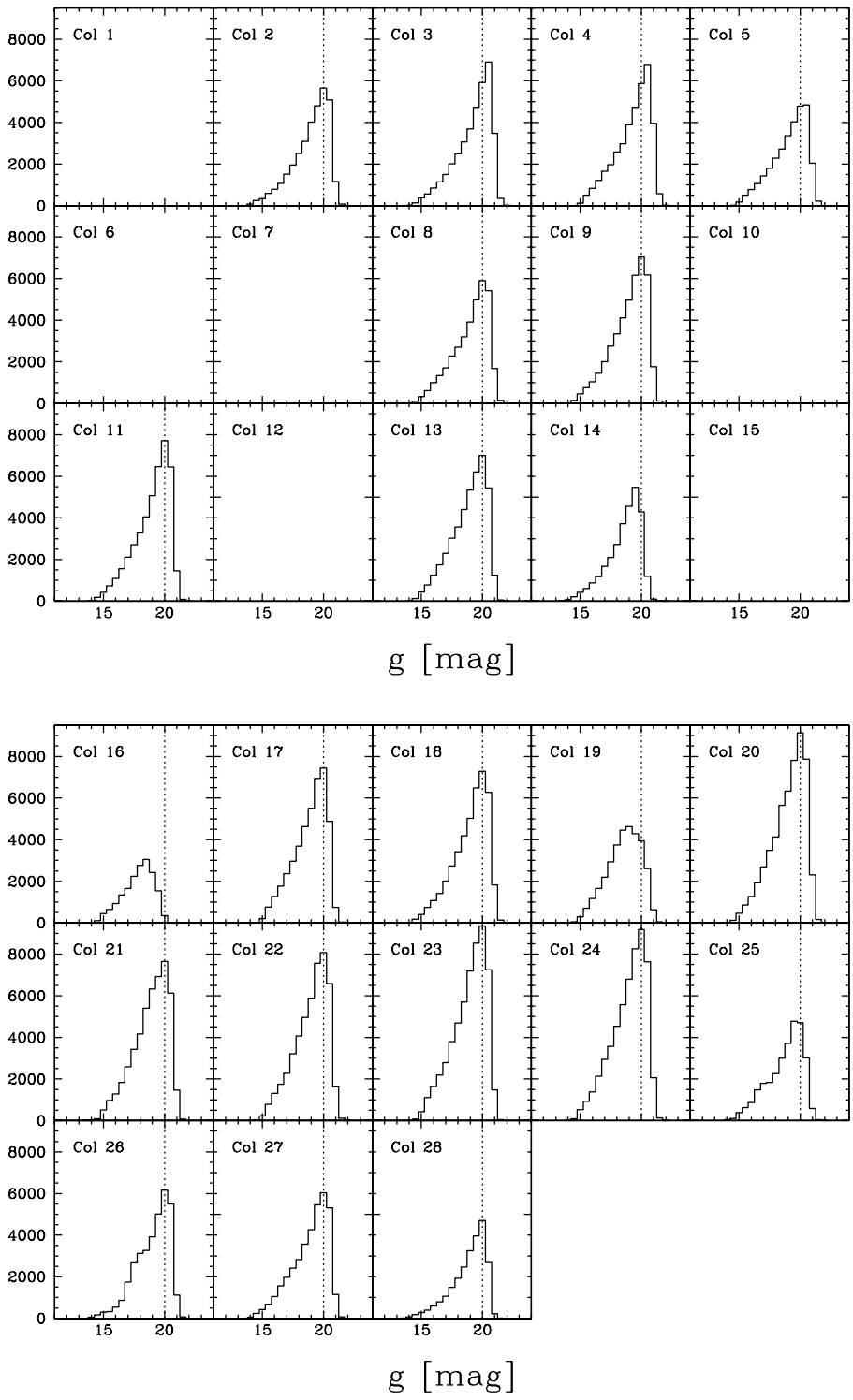

Figure 2.15 Number of detections as a function of magnitude in the USco survey for individual CCDs. The completeness turnover for all CCDs in the g filter as an ensemble is shown in each panel as a dotted line at g=20 mag. Variations in completeness, saturation point, and sensitivity can be seen between CCDs. Blank panels correspond to CCDS that have either failed since installation, or do not have derived calibrations (see §2.2.2).

Chapter 3

Optical Spectroscopic Surveys of Photometrically Selected Pre-Main Sequence Star Candidates

The full Quest-2 photometric catalogs contain ∼2 million and ∼3 million stars with measurable and calibratable $r/i/g$ photometry in USco and Taurus, respectively, and encompass a total of ∼400 deg^2 of sky. All stars in Taurus and ∼1/3 of the stars in USco have been monitored over a period of 6 or 7 nights comprised in total of 12 (Taurus) or 24 (USco) individual observations. Photometric precision between observations ranges from ∼0.02 mag to >0.1 mag dependent upon the brightness of the star and with which of the 112 CCDs it was observed. These catalogs have the potential to produce a large variety of science, and my thesis work only begins to scratch the surface of the data.

For the purpose of my thesis, I am interested primarily in using the Quest-2 optical photometry to identify young pre-main sequence (PMS) stars. Nearby young stars still undergoing contraction are systematically more luminous than their main-sequence counterparts, and thus occupy a sequence in an optical color-magnitude diagram (CMD) that is correspondingly brighter than the sequence occupied by most of the field stars. However, the position of a star in a color-magnitude diagram is dependent on mass, age, extinction, distance, and the possible presence of a circumstellar disk. Unless these parameters can be measured through independent observations (which in most cases is not yet possible), membership of individual stars cannot be

determined. Thus, generally speaking, photometry alone is insufficient for identifying young stars on an individual basis. For a survey such as the one discussed here, which covers a very large spatial extent (hundreds of square degrees) and seeks to identify members of low stellar-density associations, field star contamination will be large and statistical estimates concerning the extent and characterization of the field star population must be derived. Thus, mass, age or spatial distributions derived for these associations from photometry alone represents only statistically probable distributions, which may or may not accurately represent the association.

Follow-up spectroscopic observations of potential PMS stars identified photometrically *can* confirm membership for individual association members and uniquely determine a star's extinction and possible disk excess, thus allowing placement of a star on an HR diagram from which mass and age can be derived. In this chapter I detail my follow-up spectroscopic program, including the criteria used to select candidate PMS stars from the photometric data. The spectroscopic program was carried out using telescopes in both the northern (Palomar Observatory) and southern (Cerro Tololo Intra-American Observatory) hemispheres, and took place during a total of 25 nights of observing. For both the Palomar and the Cerro Tololo data, I discuss the observations, reduction, and analysis, detailing association membership confirmation and spectral type classification methods.

3.1 PMS Star Candidate Selection

The full (junk-free) catalogs contain ∼2 million and ∼3 million stars in USco and Taurus, respectively, most of which are field stars. To produce a reliable list of candidate PMS stars, I applied several constraints to the source catalogs with the aim of using colors and magnitudes to isolate bona fide PMS stars. The first criterion imposed on the Quest-2 data was to require stars be detected at both the r– and i– bands, thus ensuring optical color information be present for candidate selection. I rejected all objects which had a 'confusion' flag in the catalog indicating that more than one detection was made on a single scan within 0.8" (see §2.2.1). This requirement has

the disadvantage of excluding a priori any star with a close binary companion ($\lesssim$110 AU away in projected distance) capable of being resolved in my survey ($\gtrsim$20 AU away in projected distance). However, the implications of this constraint are relatively insignificant for the samples of low mass stars and brown dwarfs I will be discussing, as separations for low mass binary systems are predominantly observed to be small ($\lesssim$ 20 AU; cf. Kraus et al. 2006 and references therein) and would not be resolvable with Quest-2.

I matched the entire dataset to the 2MASS All Sky Catalog (Skrutskie et al., 2006) using a 2" matching radius. Average offsets between Quest-2 and 2MASS coordinates were +0.2" in RA and +0.04" in Dec. I considered stars to be potential PMS candidates only if they had a corresponding 2MASS detection. This criterion biases the final catalogs against faint blue objects to which 2MASS is not sensitive. However, because I am interested only in the reddest 1% of objects in either region (see below for details), and those bright enough to be observed spectroscopically ($r \lesssim$ 20 mag), this bias does not affect candidate selection in practice. Figure 3.1 shows contour optical color-magnitude diagrams of all Quest-2 sources (black) and those with 2MASS detections (green) in both USco (left) and Taurus (right). As can be seen, the red side of the color-magnitude diagram brighter than $r \sim 20$ is not substantially affected by excluding objects without a 2MASS detection. Figure 3.2 shows the converse data. Black contours represent $K_S, H - K_S$ data for all 2MASS point sources within the USco survey region; green contours represent 2MASS sources with Quest-2 detections. This figure illustrates that the Quest-2 sources are an unbiased representation of the 2MASS data in this region, excepting the bright end for which the Quest-2 photometry saturates.

The final USco and Taurus source catalogs from which PMS candidates were selected contained ∼600,000 and ∼1.1 million stars, respectively, with $riJHK_S$ magnitudes (and g, when detected) and no neighbors within 0.8". From these datasets, I selected candidate PMS stars based on their colors and magnitudes indicating they could be young, low mass PMS stars. I used three levels of selection criteria. In each of figures 3.3– 3.5, objects which meet the selection criteria outlined below are shown

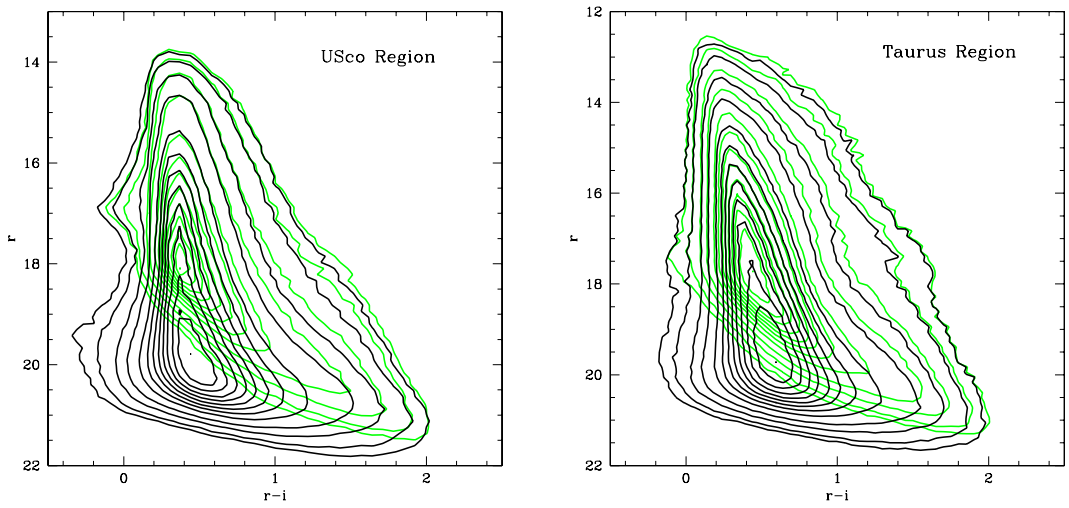

Figure 3.1 Optical color-magnitude diagrams of all Quest-2 sources (black) and those with 2MASS detections (green) in USco (left) and Taurus (right). For both black and green contours, data are represented at 90% to 10%, 5%, 2%, & 1% of the peak level.

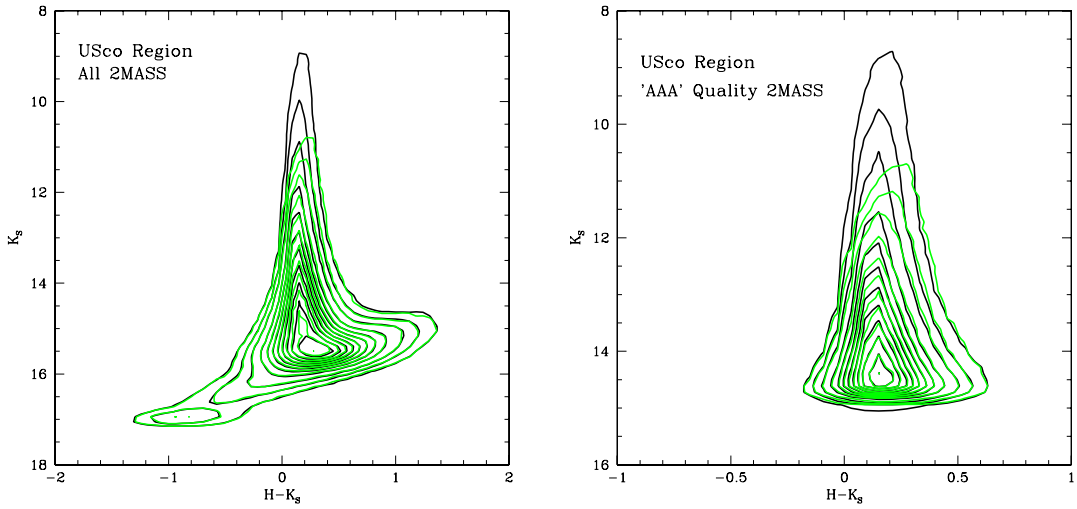

Figure 3.2 2MASS color-magnitude diagrams of all 2MASS point sources within the USco survey region (black), and those with Quest-2 detections (green). For both black and green contours, data are represented at 90% to 10%, 5%, & 2% of the peak level. Left and right panels show respectively all 2MASS sources, and only those with 'good' 2MASS photometry (quality flag 'A') in all three JHK_S-bands. Note the differences in both color and magnitude ranges between right and left panels. Note also the faint blue bump in the left-hand panel which corresponds to stars with poor quality 2MASS photometry (see Skrutskie et al. 2006).

as discreet points. Candidates observed spectroscopically at Palomar (§3.2) or Cerro Tololo (§3.3) metting all of the selection criteria outlined below are shown as large magenta and blue points, respectively.

Because Quest-2 was a new instrument at the time these observations were taken, the reduction software has undergone several iterations resulting in the photometric data being re-reduced several times. Therefore, I did not derive the calibrations from Quest-2 instrumental magnitudes to (approximate) Sloan magnitudes until after most of the follow-up spectroscopy had been observed. I was reluctant to choose candidates based on the colors and magnitudes that correspond to particular optical isochronal ages as such isochrones would be specific to a particular filter set. Thus, I felt a selection based on relative optical colors and magnitudes within each survey region would provide the most consistent and unbiased selection. For the spectroscopic observations presented here, I considered as potential candidate PMS stars all sources red-ward of a linear approximation of the 1% data contour in an $r, r-i$ CMD (see figure 3.3).

Near-infrared photometry were also considered during selection of PMS star candidates. In figure 3.4 I show a near-infrared color-color diagram. Solid lines represent the dwarf (bottom line) and giant (top line) loci. The dashed line represents the classical T Tauri star locus as defined by Meyer et al. (1997). Beyond this point I considered only objects which had 'good' 2MASS photometry (quality flag 'A') in all three JHK_S-bands. Any star with $J-H, H-K_S$ colors consistent with those expected for background giants [$(J-H) > 0.6(H-K_S)+0.6$ or $(J-H) > 1.69(H-K_S)+0.29$] was excluded.

After applying the above selection criteria I identified ∼2350 and ∼4800 photometrically selected candidate PMS stars in USco and Taurus from a total of ∼400 deg^2 of sky. As discussed at the start of this chapter, due to interstellar extinction and distance effects, optical and near-infrared colors and magnitudes alone are not a unique indicator of youth. Therefore, it is necessary to obtain spectroscopic follow-up observations for all photometrically selected candidates to determine an object's spectral type and confirm the presence of spectral features indicative of youth. Because

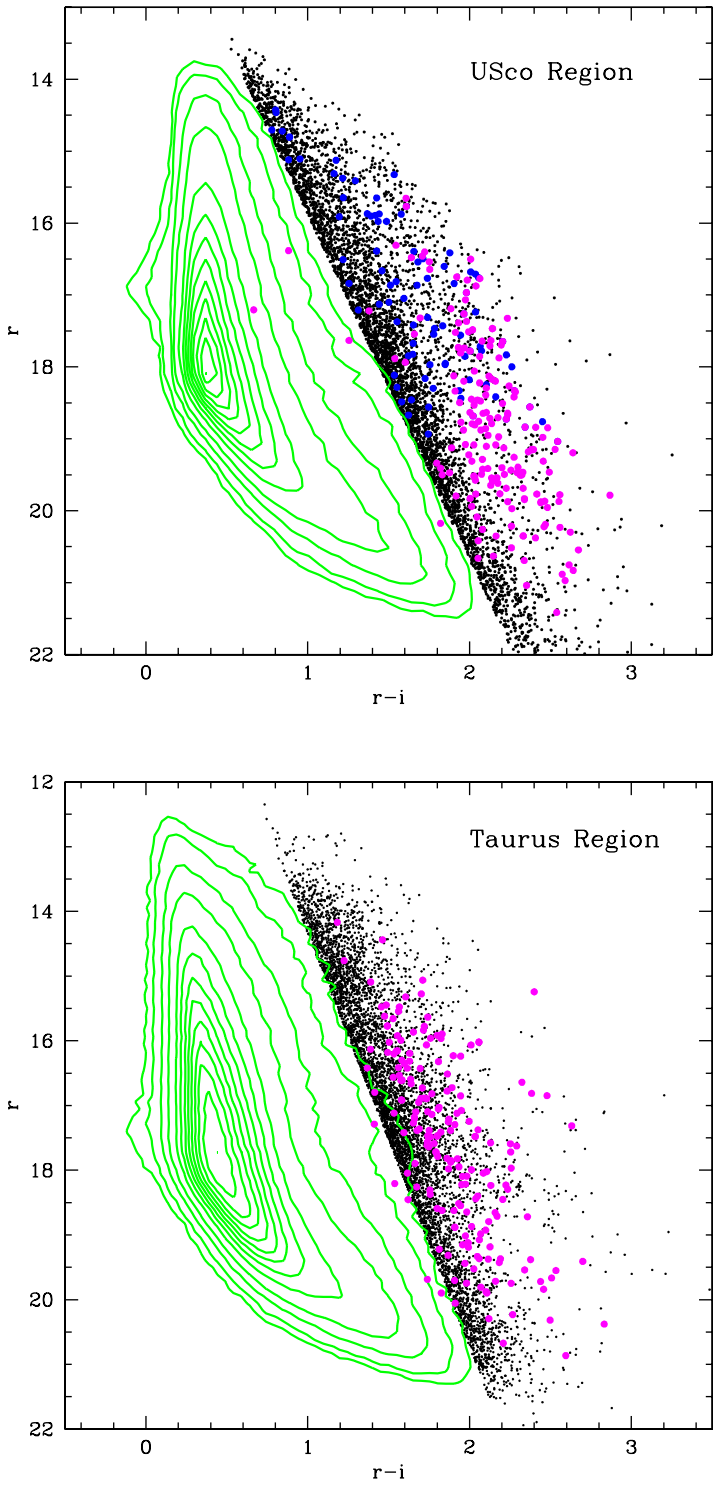

Figure 3.3 Optical color-magnitude diagram of all Quest-2 sources in final USco and Taurus catalogs with $riJHK_S$ detections. Contours represent data at 90%–10%, 5%, 2%, and 1% of the peak level. Objects red-ward of a linear approximation of the 1% contour are shown as discrete points. Objects for which I have spectral data taken at Palomar (magenta) or CTIO (blue) are shown as large symbols.

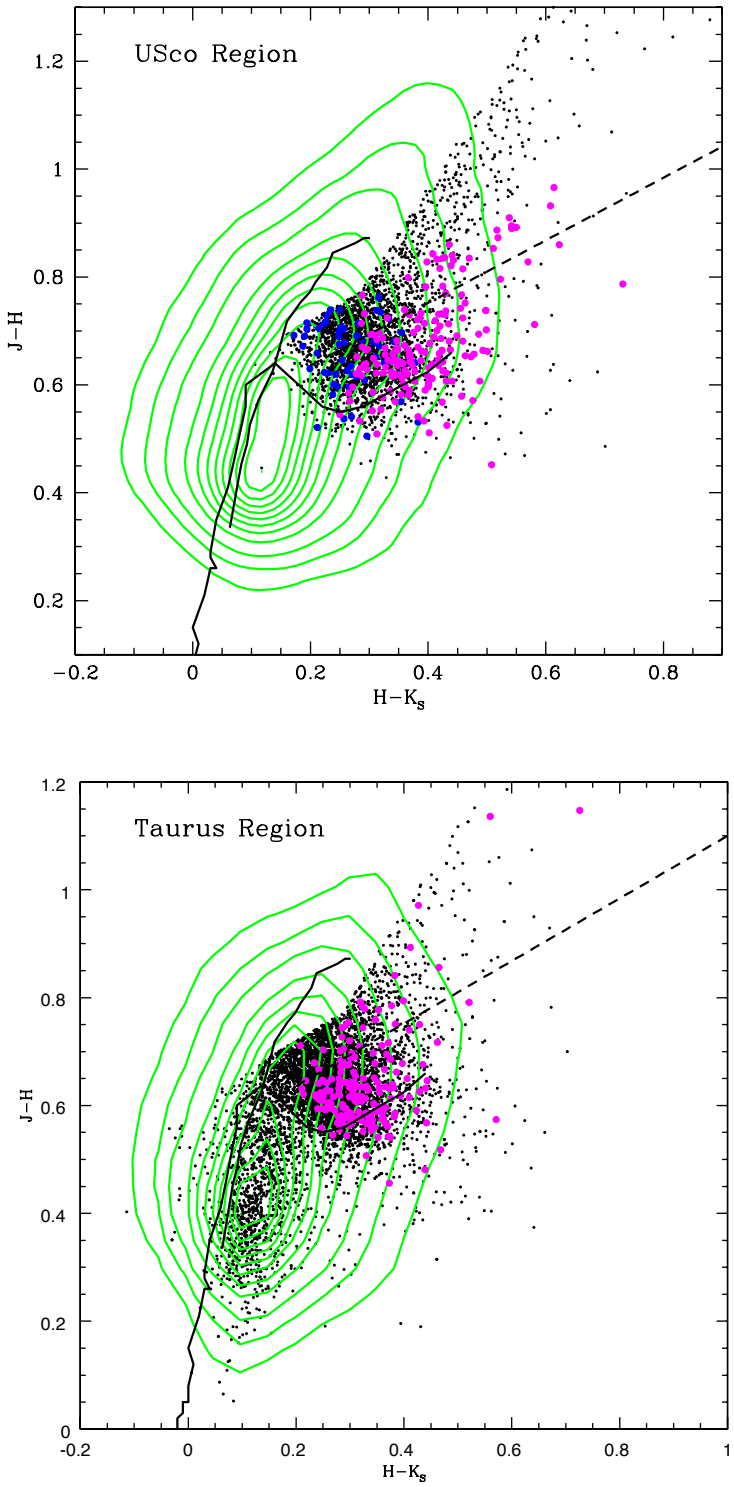

Figure 3.4 2MASS $J-H, H-K_S$ color-color diagram for all data in USco and Taurus represented as contours at 90% to 10%, 5% and 2% of the peak level. Shown as discreet points are all objects that appear red-ward of the 1% data contour in an optical CMD and that do not have colors consistent with those of background giants. Solid lines are dwarf zero-age main sequence (O5–M8) and giant loci (G0–M7). The dashed line represents the classical T Tauri locus as defined by Meyer et al. (1997). Spectroscopic targets presented here are shown as large circles.

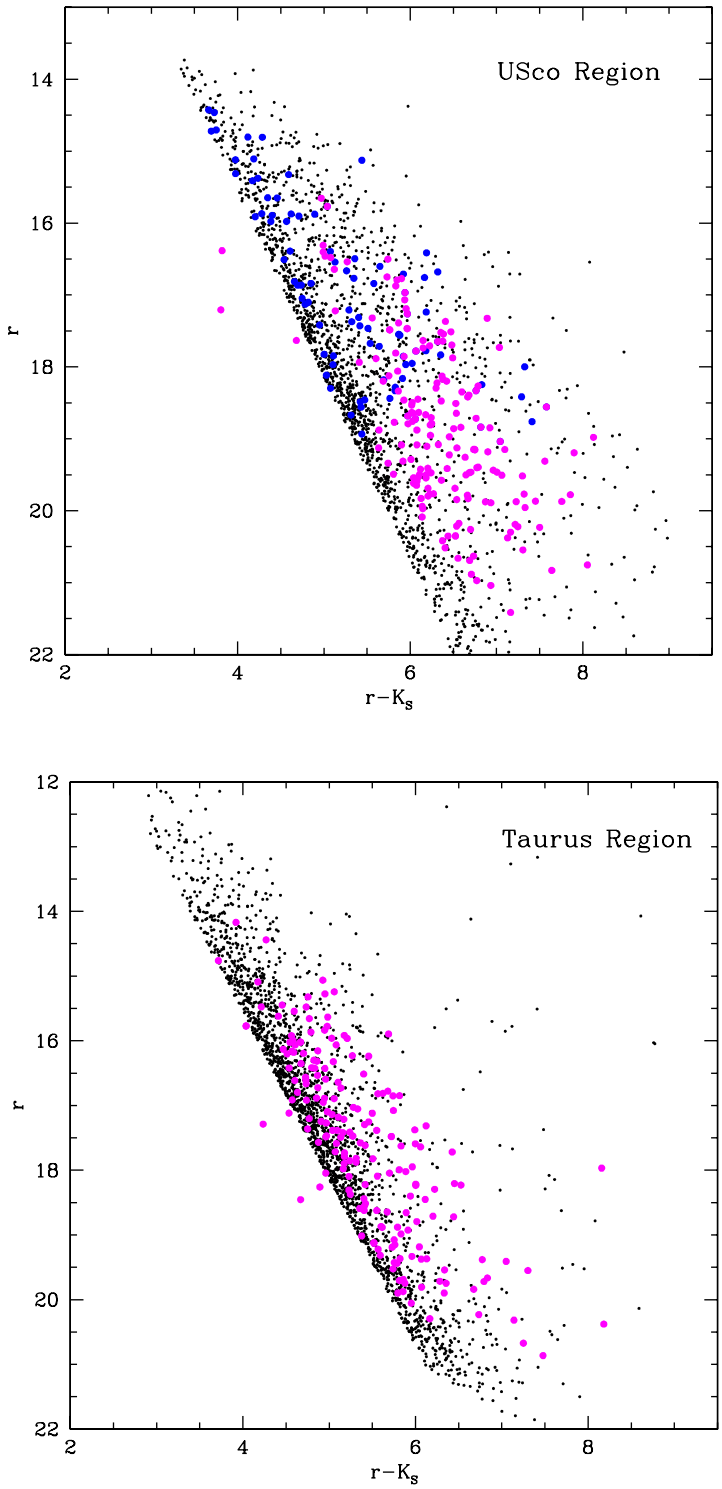

Figure 3.5 $r, r - K_S$ color-magnitude diagram for the stars that meet optical and near-infrared selection criteria shown in Figures 3.3 & 3.4 and which appear red in $r - K_S$. Spectroscopic targets presented here are shown as large circles.

it was not possible to observe all the candidates spectroscopically, I chose to focus my efforts on candidates red in $r - K_S$ first, specifically targeting new very low mass stars and brown dwarfs. Thus, I narrowed my candidate list to include only stars satisfying $r < 2.57(r - K_S - 3) + 13$ as shown in figure 3.5. Photometry for seven of the spectral targets (three in USco and four in Taurus) has changed significantly since the spectroscopic observations were taken such that they would no longer be considered candidates. All such objects were determined to be field dwarfs based on their spectra (see chapters 4 and 5).

Although g–band data was not used in the selection criteria, ∼50% of the candidates in each region have a g detection. Figure 3.6 shows an $(r - i)$ vs. $(g - r)$ color-color diagram for all data with r, i, g detections and 2MASS detections. Data meeting the selection criteria outlined above with a detection in the g–band are shown as discrete points. Of the candidates we observed spectroscopically, ∼70% in Taurus and ∼35% in USco have a g–band detection.

3.2 Palomar Spectroscopy

Once candidate PMS stars were selected, I pursued spectroscopic follow-up observations both at Palomar Observatory (USco and Taurus) in the northern hemisphere, and at Cerro Tololo Inter-American Observatory (CTIO; USco only) in the southern hemisphere. In total, the spectroscopic data were taken during five different observing runs comprised of 20 nights at Palomar and 5 nights at CTIO. In this section I present the Palomar data, and in §3.3 I present data taken at CTIO.

Moderate-resolution spectra of 190 candidate PMS candidates in Taurus were taken with the Double Spectrograph on the Palomar 200-inch telescope on the nights of Dec. 9–11 2004 and Nov. 23–27 2005. In USco, I observed 167 objects with the same telescope and instrument during the nights of June 8–12 2005, May 16–19 2006, and June -1-2 2006. All data were taken with the red side of the spectrograph through either the 1.5" or the 2" slit using a 5500 Å dichroic and a 316 lines mm^{-1} grating blazed at 7500 Å. This set-up produced wavelength coverage from 6300 to

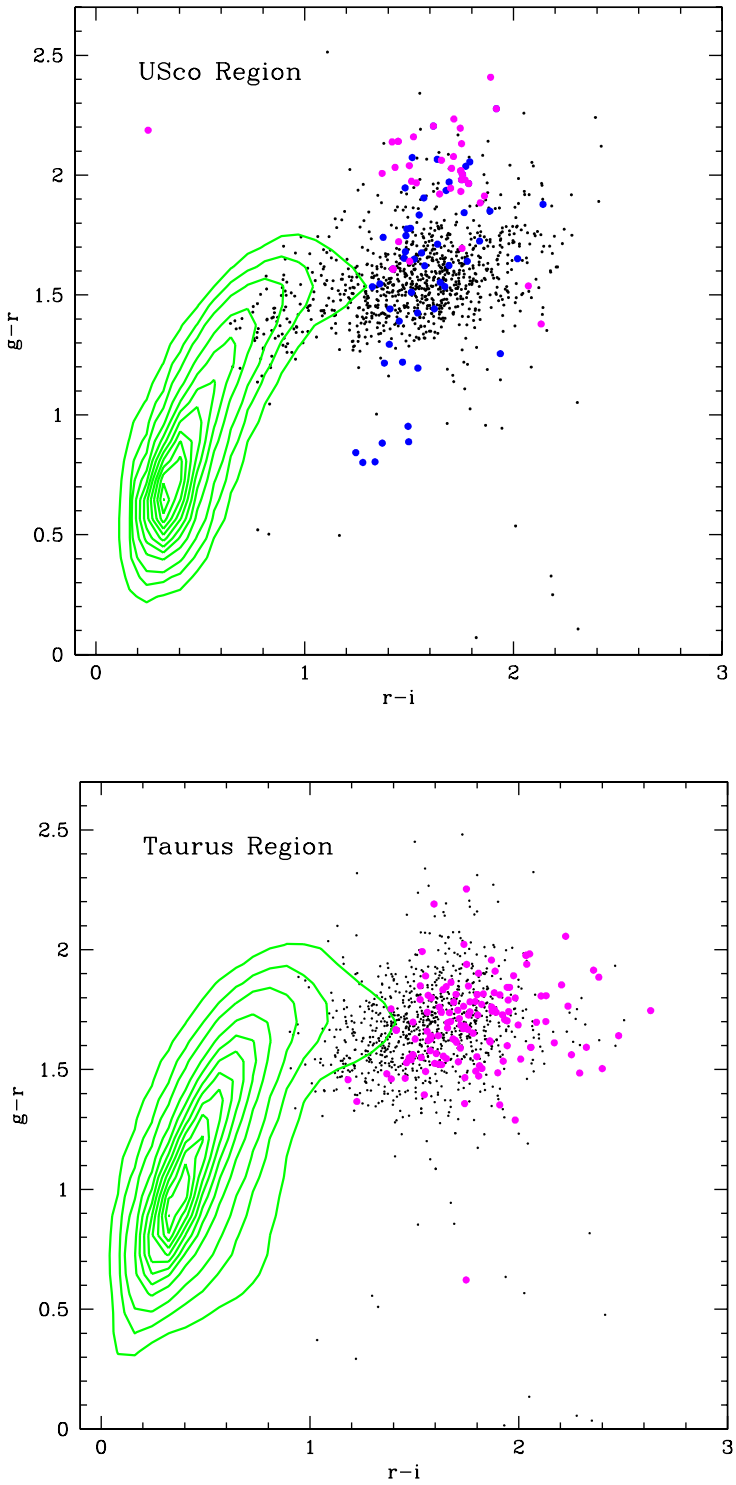

Figure 3.6 Optical $r-i, g-r$ color-color diagram for all data in USco and Taurus with 2MASS detection represented as contours at 90% to 10%, 5% and 2% of the peak level. Shown as discreet points are objects that meet all of the selection criteria outlined in §3.1. Spectroscopic targets presented here are shown as large circles.

8825 Å at a resolution of R ∼1250. Typical exposure times were 300–900 sec, and up to 1800 sec for the faintest targets (r ∼21). Spectrophotometric standard stars (Massey et al., 1988) were observed throughout each night for flux calibration. All sources were processed, extracted and calibrated using standard IRAF tasks.

In addition to my program targets, I also observed a range of spectral main sequence standards (K5-L3), giant standards (K7-M9), previously identified Taurus objects (K3-M7.25; Briceño et al. 2002, Luhman 2004b) and previously identified USco objects (K3–M8; Preibisch & Zinnecker 1999, Ardila et al. 2000, Martín et al. 2004). I observed several members of the Hyades (∼650 Myr; Lebreton et al. 2001), Pleiades (∼115 Myr; Basri et al. 1996), AB Dor (∼75–150 Myr; Luhman et al. 2005), Beta Pic (∼11 Myr; Ortega et al. 2004) and TW Hya (∼8 Myr; de la Reza et al. 2006) associations. Together, these observations provide a very broad range of standards in both spectral type (temperature) and surface gravity (age).

3.2.1 Temperature Classification

Figure 3.7 shows spectra for dwarf stars of spectral types M3, M6 & M8. The dominant molecular absorption features present are attributed to titanium oxide (TiO). These features increase in strength from mid-K through ∼M7 spectral types at which point TiO absorption begins to decrease. Vandium oxide (VO) absorption starts to dominate spectra by early-L types. I have defined or adopted from the literature several band indices to measure the strength of the TiO absorption features. I find two in particular to be diagnostic. TiO-7140 measures the strength of TiO λ7140 Å absorption compared to a continuum band at λ7035 Å (Wilking et al., 2005). This index is defined as TiO-7140=$F_{\lambda7140}/F_{\lambda7035}$ with bandwidths of 50 Å. TiO-8465 is a new index I created (TiO-8465=$F_{\lambda8465}/F_{\lambda8415}$ with bandwidths of 20 Å) to measure the strength of TiO λ8465 Å absorption compared to a continuum band at λ8415 Å. In Figure 3.7, light and dark shaded regions respectively show location of the TiO and continuum bands used in my analysis.

The left side of figure 3.8 shows a plot of TiO-8465 vs. TiO-7140 for observed

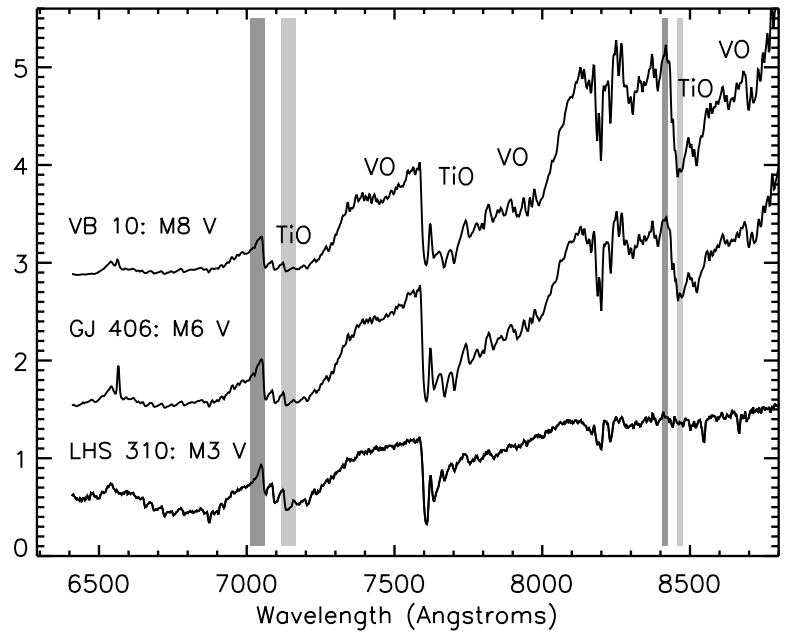

Figure 3.7 Spectra for M3, M6, and M8 type dwarf stars. Dominant TiO and VO features are labeled. Light and dark shaded regions respectively show location of the TiO and continuum bands used in spectral classification.

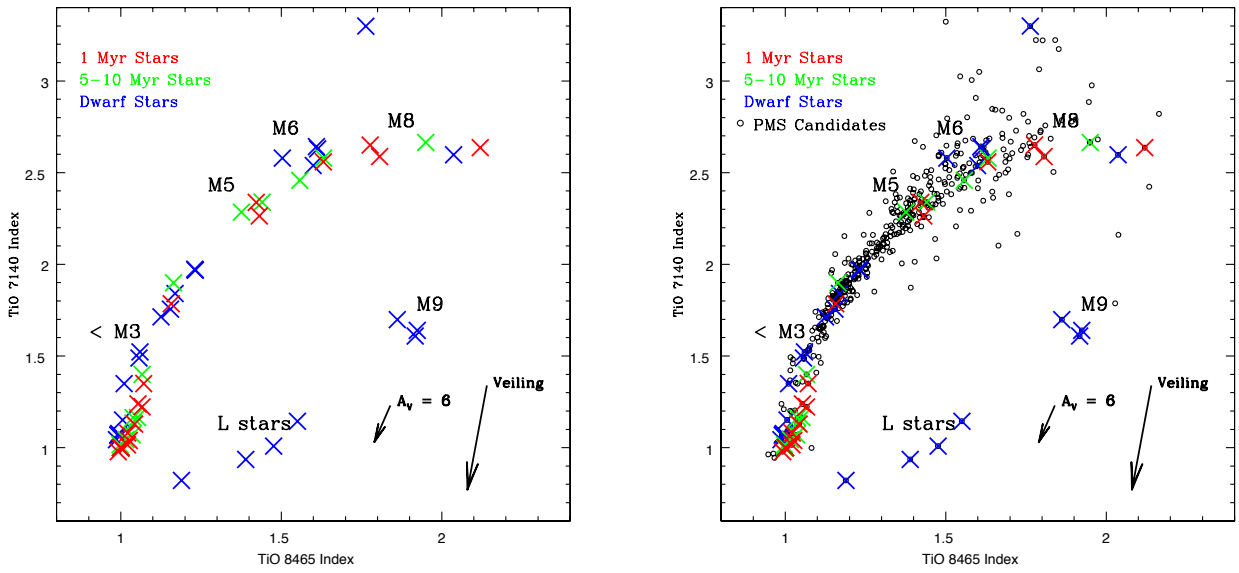

Figure 3.8 Temperature-sensitive TiO-7140 vs. TiO-8465 indices. Blue X's represent measured indices for field dwarfs and members of the Hyades (∼650 Myr), Pleiades (∼115 Myr) and AB Dor (∼75–150 Myr) associations. Green X's show measured indices for intermediate-age spectral standards from Beta Pic (∼11 Myr), TW Hya (∼8 Myr), and Upper Sco (∼5 Myr). Red X's show measured indices for young Taurus members (∼1–2 Myr). In the right panel, black symbols are measured indices for Quest-2 PMS candidates. The effects of extinction and veiling are shown as vectors (see §3.2.3). This diagram is useful for classifying stars with spectral types M3-L3.

spectral standards. Blue X's are measured indices for dwarf stars and members of the Hyades, Pleiades, and AB Dor (ages $>$ 75 Myr). Green X's are measured indices for members of TW Hya, Beta Pic and known members of Upper Sco (ages 5–10 Myr), and red X's are measured indices for known Taurus members (ages ∼1–2 Myr). This diagram is useful for classifying stars with spectral types M3–L3. No significant age dependence exists between measured TiO indices of older stars (blue) and young (red) or intermediate-age (green) PMS standard stars. In the right side of figure 3.8, black circles represent measured indices for program sources in Taurus and USco. The measurements predominantly follow the locus determined by the spectral standards. Specific outliers are discussed in detail in chapters 4 & 5.

Spectral types were determined first from quantitative analysis using an object's

measured TiO indices. More weight was given to the value of the TiO-8465 index which I find particularly insensitive to the effects of reddening and veiling (§3.2.3). However, using the TiO indices alone I can not uniquely recover spectral types for the dwarf and PMS standard stars. This ambiguity is due in part to uncertainties in published spectral types and in part to systematic differences between spectral classification schemes of different authors. Therefore, it was necessary to examine each spectrum by eye and use the information from the entire spectral range in final type determination. All program spectra were thus compared visually to a large grid of standard spectra. Typical revisions to the quantitative spectral types were at the level of $\lesssim$1 subclass.

3.2.2 Surface Gravity Classification

In addition to determining spectral types, it was also necessary to determine which of the candidates are bona fide PMS stars. Because low mass young stars are still undergoing contraction to the main sequence, they have systematically lower surface gravity than their older main sequence star counterparts. I therefore use surface gravity to roughly define stellar age. Several diagnostics of surface gravity exist in this wavelength regime which can be assessed in low and moderate resolution spectra. The three most prominent features are due to Na I (λ8183 & λ8195 Å) and K I (λ7665 & λ7699 Å) doublets, and CaH molecular absorption at $\lambda\lambda$6975 Å. Figure 3.9 shows a sequence of three M6 standard stars: a high-gravity main-sequence star (GJ406), a 5 Myr intermediate-gravity USco object (DENIS-P16007.5-181056.4) and a 1 Myr low-gravity Taurus object (MH05). Gravity sensitive absorption features are labeled and increase in strength with increasing stellar age and gravity. The location of Li and Hα lines are also shown.

To assess surface gravity quantitatively, I have developed a gravity-sensitive index to measure the strength of the Na I doublet, defined as Na-8190=$F_{\lambda 8189}/F_{\lambda 8150}$ with bandwidths of 30 Å. Figure 3.10 shows a plot of the gravity-sensitive Na-8190 index as a function of the temperature-sensitive TiO-8465 index for all stars earlier than

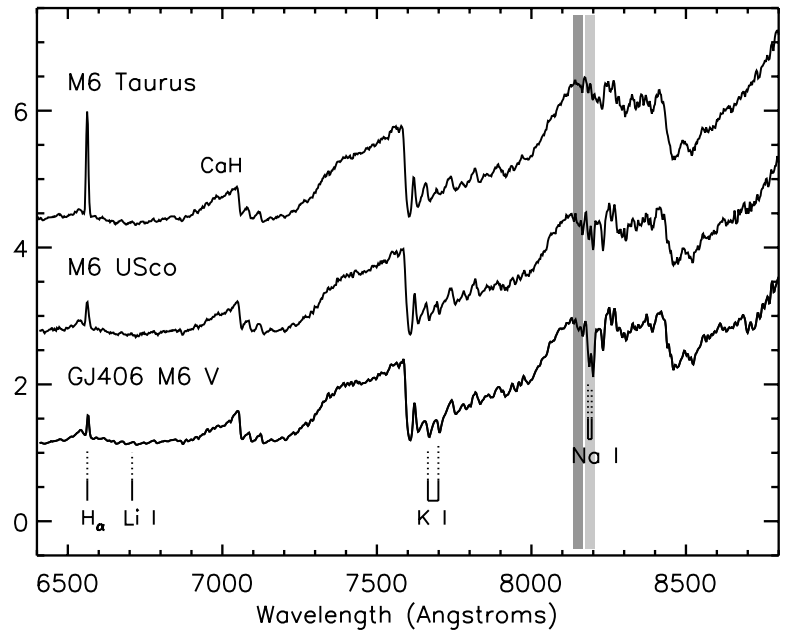

Figure 3.9 Sequence of three M6 stars: a high-gravity main-sequence star (GJ406), a 5 Myr intermediate-gravity USco object (DENIS-P16007.5-181056.4) and a 1 Myr Taurus object (MH05). Gravity- sensitive absorption features are labeled and increase with increasing stellar age and gravity. Light and dark shaded regions respectively show location of the Na I and continuum bands used in surface gravity analysis.

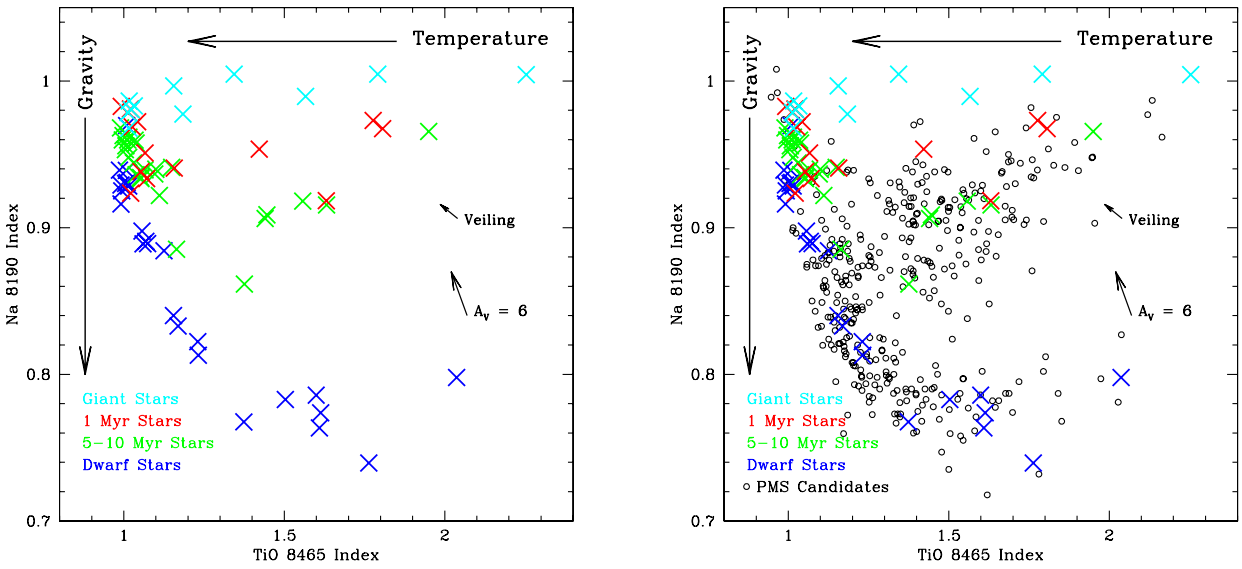

Figure 3.10 TiO-8465 index vs. the gravity sensitive Na-8190 index. Symbols are as in figure 3.8 with the addition of cyan X's which represent measured indices for giant standard stars. Objects with higher surface gravity have more Na I absorption present in their spectra and thus, a smaller Na-8190 index. In the right panel, black symbols are measured indices for Quest-2 PMS candidates. As in figure 3.8, the effects of veiling and extinction are shown as vectors (see §3.2.3).

M9. On the left is shown measured indices for spectral standards. Colors are as in figure 3.8 with the addition of cyan X's for giant stars.

I find the Na-8190 index to be a robust diagnostic that clearly separates low, intermediate and high gravity stars for spectral types later than M2 and earlier than M9. Objects with spectral types outside of this range do not exhibit substantial Na I absorption. Measured Na-8190 indices for ∼100 Myr Pleiades stars are indistinguishable from those for dwarfs at similar spectral types (see chapter 4 for more details). In figure 3.10, black symbols in the right-hand panel show measured indices for program PMS star candidates in USco and Taurus. A large fraction of the candidate PMS objects in both regions have measured Na-8190 indices consistent with their having surface gravity less than that of field dwarfs at similar spectral types. Gravity signatures in all candidate PMS star spectra were additionally verified visually. Discussion

on results for the individual associations is reserved for chapters 4 & 5.

3.2.3 Extinction and Veiling

While most of the known low mass Taurus members have low extinction ($A_V \sim 1$; e.g., Kenyon et al. (1994)), and hot OB stars have dispersed much of the dense gas and dust within the USco association, the quantitative indices used in classification can be affected by interstellar reddening and this fact must be taken into account during classification. I first derived an approximate, qualitative A_V measurement for each star by visually dereddening its spectrum until its slope matched that of a standard star of the same spectral type. I find that almost all of the PMS stars newly identified from their surface gravity signatures have $A_V < 1$ based on spectral slope from λ6300 to 8825 Å. For the stars in the USco survey, more precise extinction values are derived from each object's spectral type and colors in chapter 5, and in all cases I find agreement to within one magnitude of my visual estimate.

To assess the effect reddening has on my quantitative classification indices I artificially reddened all standard stars by A_V=10 mag, the maximum extinction inferred from large-beam dust measurements towards my survey region in USco excluding the young ρ Ophiuchus molecular cloud core (Schlegel et al., 1998). I measured index strengths for artificially reddened spectra and find average index shifts of -0.1 for TiO-7140 and -0.04 for TiO-8465. As can be seen from Figure 3.8, index shifts at this level are not sufficient to affect my quantitative temperature determination from TiO indices at the 0.5 subclass level. Ten magnitudes of extinction could affect the Na-8190 index by an average shift of -0.05. However at a level of reddening more consistent with actual measured values for new USco members ($A_V \lesssim 2$; table 5.1), I find a much more moderate shift of -0.01 which would not be sufficient to make a dwarf star look like a PMS star for objects between M2 and M9. In Taurus, the maximum extinction within my survey region as inferred from large-beam dust maps (Schlegel et al. 1998) is A_V=6 mag. Results of reddening the standards by this amount are shown for a typical M5 star on figures 3.8 & 3.10. Reddening at this level, in addition

to not shifting the spectral indices by a significant amount to affect classification, can be easily identified upon visual assessment of a spectrum's overall slope.

I must also consider the effects of veiling at optical/UV wavelengths which may occur in the presence of either excess hot emission from an accretion shock or excess thermal emission from dust grains in a circumstellar disk. In both cases the excess emission veils (decreases) the strength of the molecular absorption features used in classification and will cause a star to be systematically classified too hot (early) in spectral type. The veiling index is defined as $r_\lambda = F_{\lambda,ex}/F_{\lambda,ph}$, where "ex" indicates excess and "ph" indicates photosphere. I tested several scenarios to determine the existence and magnitude of any bias in the spectral types attributable to veiling. The maximum shift produced from these experiments is shown in figures 3.8 and 3.10.

First, I added to all spectra a T_{eff}=1400 K blackbody consistent with a cool disk around a low mass star or brown dwarf at a veiling level of r_K=0.6, corresponding to the median near-infrared veiling value for K7-M0 classical T Tauri stars (Meyer et al., 1997). Theoretically, the Wein tail of such a blackbody could affect my spectral indices around 0.8μm. I remeasured indices for veiled standard spectra and found, as expected, excess thermal emission from a cool disk has very little effect on optical spectra. Next, I investigated the effects of veiling from a hot accretion shock. I used a value of r_{6500}=0.6, equivalent to the average optical veiling value for late K and early M stars (White & Hillenbrand, 2004). I added a T_{eff}=8000 K blackbody at this level to all standard spectra and rederived the spectral classification indices. I additionally experimented by adding a continuum excess of constant flux at the r_λ=0.6 level, shown by White & Hillenbrand (2004) to be more consistent with observations than a hot blackbody. In both cases, the strength of the TiO-7140 index decreases substantially while the change in the TiO-8465 and Na-8190 indices are much smaller. For this reason, I rely primarily on the TiO-8465 index for temperature classification and believe my surface gravity assessment from the Na-8190 index to be robust to effects of veiling.

3.3 Cerro Tololo Spectroscopy

Additional spectra of PMS star candidates in USco were taken at Cerro Tololo Inter-American Observatory (CTIO) using the Hydra multifiber spectrograph on the Blanco 4-m telescope during the nights of 2005 July 24–28. In total, 26 fields were observed with the Site2k×4k CCD through the KPGLF grating. The setup provided wavelength coverage from ∼6300 to 8660 Å at a resolution of 1.15 Å/pixel.

My strategy for prioritizing stars was first to place as many fibers as possible on stars meeting the criteria outlined in §3.1, thus providing a sample of candidates analogous to those observed at Palomar. Remaining fibers were placed on stars meeting one or more of the criteria outlined in §3.1, but not all three. For the practical requirements of the Hydra observations, stars were assigned to either 'bright' fields (corresponding to $r \lesssim 16.5$) or 'faint' fields (corresponding to $16.5 \lesssim r \lesssim 18.5$). Exposure times ranged from 900 to 1800 sec for bright fields (dependent on weather conditions) and were set at 2700 sec for faint fields. In total, 10 bright and 16 faint fields were observed during the 5 nights. At each fiber configuration I observed a comparison lamp spectra and a quartz lamp spectra to allow determination of the dispersion solution and throughput correction during data reduction. Biases and dome flats were taken each afternoon with all working fibers put in the 'large circle' configuration. Milk flats (see below) were taken once during the observing run.

3.3.1 Image Processing

All frames were first pre-processed (bias correction and trimming) using CCDPROC. Milk flats were obtained on the second afternoon of observing. This type of observation is an exposure of the daytime sky and is taken through a plate of milky glass placed between the output of the fibers and the spectrograph camera. The purpose of such an observation is to allow removal of pixel-to-pixel variations from the data without having to worry about fiber placement. A spectral response image was created by smoothing in both X and Y directions. The original milk flat was then divided by the spectral response image to create an image with a value of 1.0 everywhere except

where pixel-to-pixel variations exist. All data and calibration frames were divided by the this image.

Subsequent data reduction was done using the IRAF dohydra task. All data for a given night were divided by the dome flat taken that afternoon. Individual fiber-to-fiber throughput corrections (which change for each configuration) were made by dividing each object frame by the corresponding quartz lamp spectra taken in the same fiber configuration. Wavelength calibration was done by matching each object spectrum to the lamp spectrum taken with the same fiber during the lamp exposure taken for that specific configuration.

3.3.2 Sky Subtraction

For each field, a single sky spectrum was made using the sky generating tasks within dohydra. Typically, ∼5–20 fibers were placed on sky during each observation. The task first allows rejection of any anomalous sky spectra which may have inadvertently fallen on a star or a clump of nebulosity. Remaining sky spectra were averaged together using a 3-sigma clipping algorithm. The hydra field of view is large, 40' on a side. While much of the nebular material has been dispersed by hot stars in USco, in places a significant amount remains such that the sky level was not constant across the entire field. Thus, I found subtraction of a single sky spectrum for all spectra within a field often produced insufficient sky subtraction in that for a given spectrum, all sky lines would be systematically over- or under-subtracted. To correct this problem, for each object spectrum and for the sky spectrum I computed the flux in a single sky line chosen to be towards the center of the spectrum at ∼7316 Å and to be sufficiently isolated that is was not blended with any other sky or stellar lines. I then scaled each object spectrum such that the flux computed for its central sky line matched that of the sky spectrum and then subtracted the sky spectrum. I found, in general, this procedure produced satisfactory results.

3.3.3 Classification

Spectral observations taken through fibers produce flux that varies as a function of wavelength dependent on the the fiber configuration, i.e., how the relevant fiber is bent and stretched to place it into position on the star. Thus flux correction of fiber data is inherently very difficult to do because it is not practical to observe a calibrator star through every fiber at every configuration. Thus, I was not able to flux-correct the hydra spectra in an analogous manner to the Palomar data and therefore could not use the quantitative spectral indices (which rely on flux-corrected spectra) to aid in classification. During observations, my primary targets set around UT 6:00 and I used the remaining hours to observe individual standard stars. I took a range of known dwarf stars and giant stars (spectral types K0–M8). In addition, I observed known intermediate-age PMS members of the ∼30 Myr-old Tucanae Hor association (Mamajek et al., 2004) with early M spectral types. Spectra of previously identified K0–M8-type USco members were observed in the primary fields along with program candidates. Though the overall spectral shape is not meaningful because the spectra are not flux corrected, the depth of absorption and emission features is not substantially affected. All spectra of candidate PMS stars were thus classified by hand through comparison to each other and to standard stars observed with hydra.

In total, the hydra observations yielded ∼1150 spectra (of varying quality). I first classified all of the spectra into broad categories. Approximately 450 were determined to be mid K- to M-type stars based on the presence of TiO molecular absorption in their spectra, and a lack of Hα absorption (though Hα can be seen in emission). The largest constituent of the spectral sample (∼650 stars) were intermediate-type stars with spectral types late F through early K. These stars are characterized by a lack of TiO molecular absorption but the presence of Ca II triplet (λ8498, λ8542 ,λ8662 Å) and Hα atomic absorption. Absorption from and the Ba II, Fe I, Ca I blend at λ6497 Å begins to appear at late F/early G types and increases in strength compared to Hα absorption through K spectral types. The remaining stars were determined to have spectral types A-F with deep Hα and Ca II triplet absorption but noticeably

lacking any absorption at the λ6497 Å blend. I saw no evidence of He absorption in any of the spectra and thus concluded that my survey did not probe B- or O-type stars. Thus far, I have derived detailed (at the $\sim$0.5 subclass level) classifications from these data only for those stars whose colors and magnitudes meet all of the selection criteria outlined in §3.1. I discuss these results in chapter 5 along with results from the Palomar spectral observations. The remaining stars are predominantly earlier than spectral type$\sim$M2, and are discussed in more detail in chapter 8.

3.4 Summary of Candidate Selection and Spectroscopic Observations

In this chapter I combine the Quest-2 optical photometry with 2MASS near-infrared magnitudes and select candidate PMS stars and brown dwarfs based on their systematic high luminosities above the main sequence and red infrared colors. I present follow-up optical spectral observations taken at either Palomar or CTIO for several hundred candidates in Taurus and USco, and detail temperature and surface gravity classifications of stars based on spectral features. In the next two chapters I discuss implications of survey results in specific regions.

Chapter 4

A Distributed Population of Low Mass Pre-Main Sequence Stars near the Taurus Molecular Clouds[1]

In this chapter, I present a driftscan survey covering a $\sim 5^o \times 50^o$ region toward the Southern portion of the Taurus-Auriga molecular cloud. Data taken in the B, R, I filters (converted to g, r, i photometry) with the Quest-2 camera on the Palomar 48-inch telescope were combined with 2MASS near-infrared photometry to select candidate young stars. Follow-up optical spectroscopy of 190 candidates led to identification of 42 new low mass PMS stars with spectral types M4-M8, of which approximately half exhibit surface gravity signatures similar to known Taurus stars while the other half exhibit surface gravity signatures similar to members of the somewhat older Upper Sco, TW Hya and Beta Pic associations. The pre-main sequence stars are spread over $\sim 35^o$, and many are located well outside of previously explored regions. From assessment of the spatial and proper motion distributions, I argue that the new pre-main sequence stars identified far from the clouds cannot have originated from the vicinity of the 1–2 Myr-old subclusters which contain the bulk of the identified Taurus members, but instead represent a newly-identified area of recent star-formation near the clouds.

[1] A modified version of this chapter has been published previously as Slesnick, Carpenter, Hillenbrand, & Mamjek 2006, AJ, 132, 2665.

4.1 Motivation

The Taurus-Auriga molecular cloud complex has, for decades, been considered the quintessential example of low density, isolated star formation. This fact along with the proximity of Taurus (140 pc) and its position in the northern hemisphere has caused Taurus to be one of the most often studied star-forming regions. Several authors (e.g., Briceño et al. 1999, Luhman 2000, Briceño et al. 2002, Luhman et al. 2003a, Luhman 2004b, Guieu et al. 2006) have used optical/near-infrared/X-ray imaging to identify young star candidates within the clouds. Follow-up optical spectroscopy of photometrically selected candidates can distinguish members of Taurus from foreground or background field interlopers. These studies found the Taurus population is clustered into several loose aggregates (Gomez et al., 1993), and is predominantly very young ($\sim$1–2 Myr; e.g., Briceño et al. 1998, Hartmann 2000). Thus far, no conclusive evidence has been established for a widespread population of older stars within or near the cloud (Briceño et al., 1999).

The phenomenon of short timescale (1–2 Myr) clustered star-formation is not unique to Taurus but has been found in almost all other nearby young associations (e.g., Carpenter 2000, Palla & Stahler 2000). The large numbers of very young stars and apparent lack of more evolved (5–10 Myr-old) objects in star forming regions contrasts with ages of a few tens of megayears (e.g., Blitz & Shu 1980) inferred for molecular clouds. Either star-formation takes place for only a small fraction of the cloud lifetime, or molecular clouds themselves live only a few megayears (e.g., Hartmann et al. 2001).

An alternative explanation for the apparent lack of older stars in molecular clouds is that such objects have been missed in previous surveys. Limitations in telescope time and instrument fields of view have constrained most previous deep imaging surveys in Taurus (e.g., Briceño et al. 1999, Luhman 2000) to small areas focused on the subclusters (each $\sim$1 pc wide) known to contain most of the young members. Assuming a mean velocity dispersion of $\sim$2 km/s (Hartmann et al., 1986), a putative population of 5–10 Myr old stars in Taurus could travel up to $\sim$20 pc (8 deg) away

from its birth site.

Several studies (e.g., Neuhaeuser et al. 1997, Wichmann et al. 1996) have attempted to use the ROSAT All Sky Survey (RASS) with spectroscopic follow-up to identify G–mid K-type post T-Tauri Stars (stars with ages ∼3–10 Myr; PTTSs) far from the current Taurus members. These observations revealed a distributed population of lithium-rich stars (indicating that they are younger than ∼100 Myr) that are widely dispersed across the cloud and beyond. However, because both the decay of x-ray emission and the depletion of lithium occur slowly for G–type stars with ages <100 Myr, these data alone cannot discriminate whether the RASS-selected stars represent a 1 Myr-old or 10 Myr-old Taurus population, or a 100 Myr-old population that originated elsewhere. Consequently, the origin of these stars and their relation to Taurus is still controversial (e.g., Briceno et al. 1997). The largest optical/near-infrared imaging survey to date that searched for Taurus members is that of Luhman (2006) who used a combination of USNO and 2MASS magnitudes to find young brown dwarfs within a 15×15 deg^2 region centered on the known 1 Myr-old subclusters. The survey was aimed specifically at identifying young brown dwarfs with colors and magnitudes similar to known ∼1 Myr-old substellar Taurus members and was not targeted at finding older objects or comparably aged low mass stars. My survey includes regions beyond previously studied parts of the cloud, and is ideally suited to find slightly more evolved association members if they exist as counterparts to the young population.

4.2 Observations

I have used the Quest-2 camera to complete a new optical B, R, I (converted to g, r, i) imaging survey of ∼250 deg^2 near the Taurus molecular clouds. The specific survey area was chosen to include both well-known subclusters of stars (L 1536 and L 1529) and regions beyond previously studied parts of the cloud. Details of the photometric survey were given in chapter 2. My primary goal in Taurus is to search for and characterize a possible distributed population of pre-main sequence (PMS) stars

within and surrounding the clouds. In chapter 3, I combined the Taurus photometric data with 2MASS J, H, K_S photometry to select candidate young stars, and presented newly obtained spectral data for 190 of these candidates.

All spectral analysis was performed as outlined in chapter 3. Figure 4.1 shows measured indices for all PMS star spectral candidates observed in the Taurus region. In the left panel, two outliers (SCH J0429595+2433080 and SCH J0518028+2327126) sit below the primary sequence of data points. Both objects are confirmed to be young stars with strong Hα emission (indicating that the star is likely still accreting; see §5.3.3) and I attribute their position in the left panel of figure 4.1 to a small amount of veiling present in their spectra (see §3.2.3). In the right side of figure 4.1 measured indices for PMS candidates have been divided into three groups based on their surface gravity: circles represent objects with surface gravity lower (i.e., younger in age) than the Upper Sco association, triangles indicate objects with intermediate surface gravity comparable to the Upper Sco, TW Hya and Beta Pic associations, and black X's indicate field stars (see §4.3).

One difficulty in interpreting the right panel of figure 4.1 directly is that the Na-8190 index is contaminated by telluric features. The Taurus spectral data were taken at systematically lower airmasses than many of the spectral standards. As a result, a program star with intermediate gravity signatures observed at low airmass will have a lower Na-8190 index than an intermediate gravity standard of the same spectral type observed at high airmass. This effect causes a discrepancy between the positions of the green X's and the triangles in the right panel of figure 4.1.

Figure 4.2 shows a section of the spectra which highlights the Na I (8183 and 8195 Å) absorption feature for dwarf, intermediate, and low gravity stars of the same spectral type. Both GJ 866 and USco CTIO 53 (the dwarf and intermediate-gravity stars) were observed at high airmass whereas MHO 7 (the low gravity Taurus member) was observed at low airmass. Telluric absorption (8161–8282 Å) seen in the spectra of GJ 866 and USco CTIO 53 affects both the continuum band and Na I band causing systematically high measurements of the Na-8190 index. However, the three spectra can be clearly distinguished through visual inspection of the NaI line strengths. Thus,

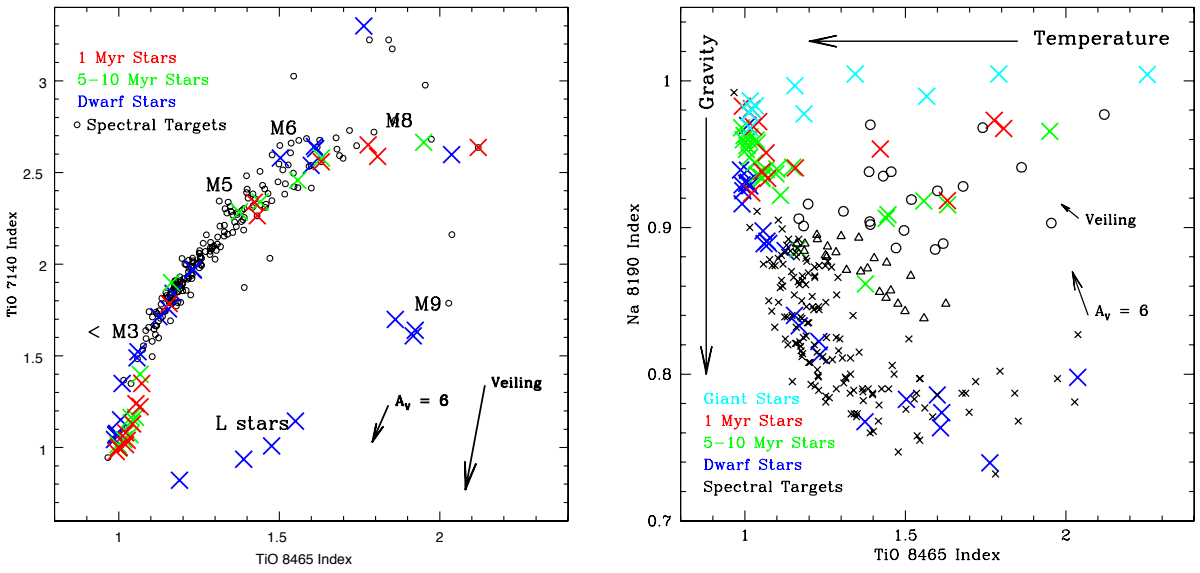

Figure 4.1 The left panel shows temperature-sensitive TiO-7140 vs. TiO-8465 indices; the right panel shows the TiO-8465 index vs. the gravity sensitive Na-8190 index. In both panels, blue X's represent measured indices for field dwarfs and members of the Hyades (∼650 Myr), Pleiades (∼115 Myr) and AB Dor (∼75–150 Myr) associations. Green X's show measured indices for intermediate-age spectral standards from Beta Pic (∼11 Myr), TW Hya (∼8 Myr), and Upper Sco (∼5 Myr). Red X's show measured indices for young Taurus members (∼1–2 Myr). Cyan X's which in the right panel represent measured indices for giant standard stars. In both panels, the effects of extinction and veiling are shown as vectors (see §3.2.3). Black symbols are measured indices for Taurus PMS candidates. In the right panel, these symbols are divided into three groups based on inferred surface gravity: circles represent objects with surface gravity lower (i.e., younger in age) than the Upper Sco association, triangles indicate objects with intermediate surface gravity comparable to the Upper Sco, TW Hya and Beta Pic associations, and black X's indicate field stars.

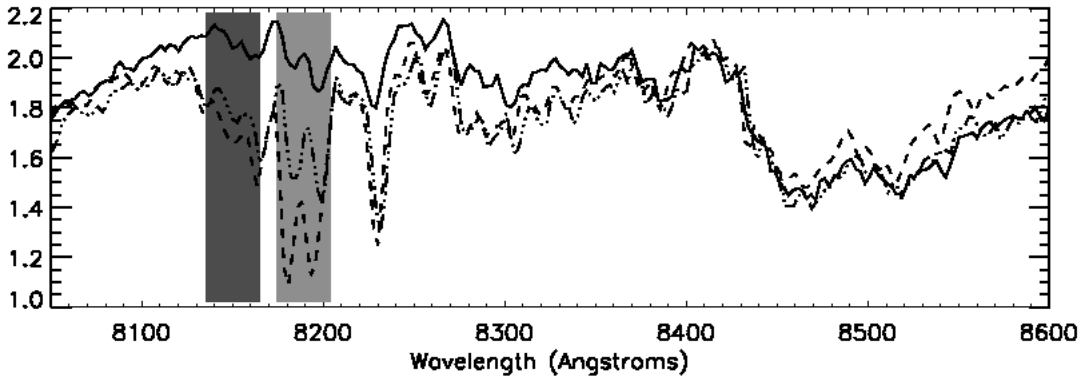

Figure 4.2 Section of the optical spectrum highlighting the surface gravity sensitive Na I doublet (8183 and 8195 Å). The dashed spectrum is an M5V star (GJ 866; Kirkpatrick et al. 1991), the dotted-dashed spectrum is an M5 Upper Sco member (USco CTIO 53; Ardila et al. 2000), and the solid spectrum is an M5 Taurus member (MHO 7; Briceño et al. 1998). Light and dark shaded regions show the respective locations of the Na I and the continuum bands used in constructing the Na-8190 index. All spectra have been normalized at 8410 Å near the temperature-sensitive TiO (8465 Å) molecular absorption band. Both GJ 866 and USco CTIO 53 were observed at high airmass and telluric absorption (8161-8282 Å) affects both the continuum band and Na I band, causing systematically high measurements of the Na-8190 index. However, gravity signatures in the three spectra can be distinguished clearly through visual inspection of the line strengths.

I used the quantitative indices as a rough guide only, and all final gravity classification was done by eye.

Table 4.1. Measured quantities for new PMS stars near Taurus

ID[a]	g	r	i	J[c]	H[c]	K_S[c]	TiO-7140	TiO-8165	Na-8195	SpType[d]	$W(H\alpha)$ [Å]	Age[e]
SCH J0325332+2426581	18.0	16.4	14.7	12.34	11.72	11.47	2.02	1.30	0.89	M4.5	-10	int
SCH J0359099+2009362	19.8	18.0	16.1	13.47	12.89	12.53	2.32	1.42	0.85	M4.75	-7	int
SCH J0400220+2232382	–	18.4	16.3	13.45	12.76	12.45	2.23	1.36	0.87	M4.75	-6	int
SCH J0400279+2031593	20.0	18.2	16.1	13.14	12.56	12.23	2.54	1.49	0.84	M5.75	-16	int
SCH J0407246+2332554	18.4	16.7	14.8	12.77	12.06	11.85	1.69	1.16	0.88	M4	-6	int
SCH J0407350+2237396	18.6	16.8	15.0	12.16	11.60	11.25	2.38	1.51	0.86	M5	-16	int
SCH J0412433+2055306	–	20.3	17.8	14.24	13.53	13.17	2.97	1.95	0.90	M8	-15	int
SCH J0416272+2053093[b]	18.6	16.8	14.9	12.05	11.47	11.11	2.26	1.43	0.93	M5	-5	young
SCH J0420068+2432267	17.5	16.1	14.6	12.42	11.87	11.59	1.84	1.18	0.88	M4	–	int
SCH J0420491+2327370	18.3	16.7	14.9	12.07	11.39	11.09	2.03	1.25	0.88	M4.25	-8	int
SCH J0426452+2131408	19.3	17.8	15.8	13.19	12.64	12.31	2.23	1.38	0.87	M4.75	-8	int
SCH J0427074+2215039	–	17.7	15.4	12.27	11.64	11.29	2.64	1.74	0.96	M6.75	-18	young
SCH J0429595+2433080[b]	–	17.9	15.7	11.68	10.53	9.81	1.87	1.39	0.97	M5.5	-71	young
SCH J0431191+2335048[b]	–	20.3	17.5	13.50	12.71	12.19	2.63	2.12	0.97	M8	-32	young
SCH J0433131+2025200	–	19.1	17.0	14.20	13.46	13.14	2.36	1.40	0.87	M5	-12	int
SCH J0434454+2308035	20.2	18.2	16.0	12.80	12.02	11.70	2.31	1.45	0.93	M5.25	-11	young
SCH J0438001+2327167	19.7	18.0	15.9	13.27	12.66	12.34	2.41	1.45	0.85	M5.25	-15	int
SCH J0438163+2326404	17.7	16.2	14.3	11.80	11.24	10.96	2.24	1.38	0.93	M4.75	-7	young
SCH J0438586+2336352	18.4	16.8	14.3	11.97	11.36	11.03	2.03	1.19	0.91	M4.25	-15	young
SCH J0438587+2323596	19.1	17.5	15.3	12.49	11.93	11.59	2.62	1.68	0.92	M6.5	-14	young
SCH J0439016+2336030	16.7	15.2	12.8	11.33	10.59	10.18	2.41	1.60	0.92	M6	-62	young
SCH J0439064+2334179	19.0	17.3	14.6	12.09	11.53	11.19	2.78	1.86	0.94	M7.5	-8	young
SCH J0439410+2304262	–	19.1	17.1	14.41	13.81	13.46	2.09	1.31	0.87	M4.5	-12	int
SCH J0439507+2133564	–	19.7	17.5	14.43	13.80	13.43	2.67	1.62	0.84	M6	-8	int

Table 4.1 (cont'd)

ID[a]	g	r	i	J[c]	H[c]	K_S[c]	TiO-7140	TiO-8165	Na-8195	SpType[d]	$W(H\alpha)$ [Å]	Age[e]
SCH J0440534+2055473	18.8	17.1	15.1	12.48	11.88	11.62	2.32	1.44	0.87	M5.	-11	int
SCH J0502377+2154050	19.2	17.4	15.6	13.16	12.53	12.20	1.99	1.25	0.88	M4.25	-10	int
SCH J0506466+2104298	18.1	16.5	14.6	12.05	11.40	11.11	2.43	1.51	0.91	M5.25	-14	young
SCH J0516021+2214530	17.4	15.9	14.1	11.67	11.13	10.75	2.25	1.39	0.90	M5	-10	young
SCH J0516058+2236152	19.1	17.2	15.6	13.29	12.59	12.30	1.88	1.18	0.88	M4	-8	int
SCH J0518028+2327126	18.6	17.2	15.3	12.99	12.32	11.88	2.03	1.47	0.88	M5	-21	young
SCH J0522333+2439254	18.9	17.0	15.2	12.75	12.04	11.72	2.18	1.38	0.90	M4.75	-7	young
SCH J0522335+2439197	19.2	17.2	15.3	12.79	12.14	11.79	2.10	1.30	0.91	M4.5	-8	young
SCH J0523020+2428087	18.1	16.4	14.8	12.60	11.92	11.61	1.78	1.16	0.90	M4	-3	int
SCH J0523500+2435237	–	18.7	16.6	13.81	13.14	12.77	2.63	1.61	0.88	M6	-18	young
SCH J0531021+2333579	17.5	16.0	14.0	12.28	11.64	11.39	1.79	1.18	0.90	M4	-5	int
SCH J0531026+2334022	17.6	16.0	13.9	12.26	11.58	11.35	1.83	1.22	0.89	M4	-5	int
SCH J0532021+2423030	19.9	18.2	16.2	13.69	13.06	12.80	2.50	1.44	0.85	M5	-19	int
SCH J0533363+2102276	17.4	15.8	14.2	11.93	11.32	11.07	2.05	1.28	0.88	M4.5	-7	int
SCH J0534480+2243142	18.2	16.6	15.0	12.83	12.18	11.93	1.94	1.22	0.89	M4.25	-6	young
SCH J0536190+2242428	17.7	16.3	14.5	12.13	11.53	11.27	2.17	1.35	0.89	M4.75	-12	int
SCH J0537385+2428518	17.8	16.2	14.2	11.66	11.06	10.78	2.44	1.49	0.89	M5.25	-14	young
SCH J0539009+2322081	19.1	17.6	15.3	12.68	12.10	11.79	2.53	1.59	0.88	M6	-16	young

[a]Object IDs given in J2000 coordinates.

[b]Three of the PMS objects discussed in this work were previously identified in the literature: SCH J0429595+2433080 (Guieu et al. 2006), SCH J0431191+2335048 (Luhman 2006), and SCH J0416272+2053093 (Wichmann et al. 1996)

[c]Near-infrared photometry taken from 2MASS.

[d]Spectral type uncertainties are ±0.5 subclasses.

[e]An age of 'int' indicates the star exhibited surface gravity-sensitive spectral features consistent with those of 5–10 Myr-old stars. Stars labeled 'young' have gravity signatures that indicate the star is only 1 to a few Myr-old.

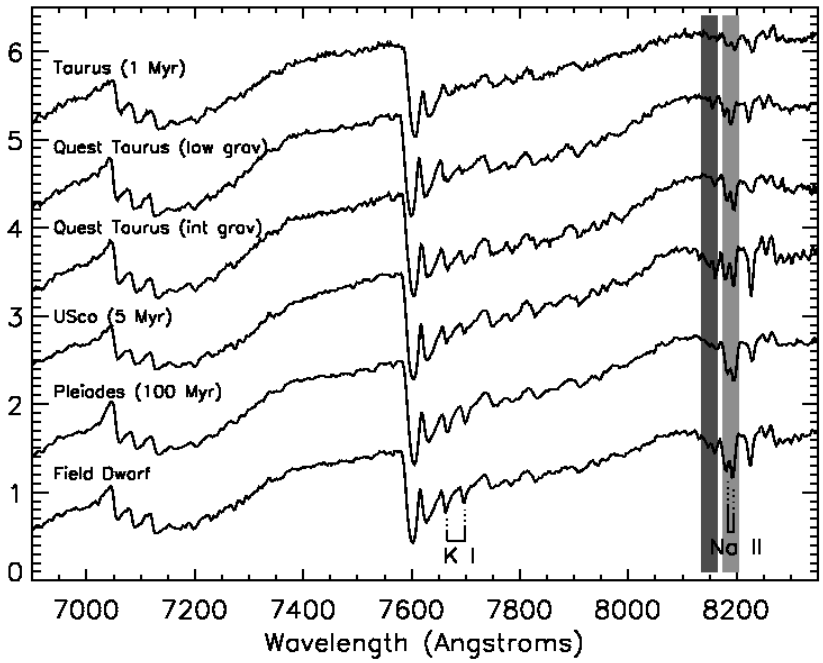

Figure 4.3 Spectra of M4/M4.5 stars presented in order of decreasing surface gravity (bottom to top). Spectra shown are of a field dwarf, a 115 Myr Pleiades object, a 5 Myr Upper Sco member, a new Quest-2 Taurus candidate identified to have Upper Sco-type intermediate gravity, a new Quest-2 Taurus candidate identified to have low gravity, and a 1 Myr Taurus star. Surface gravity sensitive features include the K I doublet (7677 Å) and the Na I doublet (8189 Å).

4.3 Discussion

For the remainder of this analysis, objects with surface gravity features weaker than those of the intermediate-age standards are considered by me to have low gravity; objects with gravity features similar to those exhibited by the intermediate-age standards are considered to have intermediate gravity. Based on this classification scheme I identify 42 new PMS stars (see table 4.1). Within the 42 new PMS stars, I identify 19 objects to have spectral features which indicate lower surface gravity than members of Upper Sco (∼5 Myr). Most of the new low gravity objects have inferred gravities as low as those similarly inferred for known 1–2 Myr Taurus members. Of these 19 objects, three were previously identified in the literature: SCH J04295950+2433080 (Guieu et al., 2006), SCH J04311908+2335048 (Luhman, 2006)

and SCH J0416272+2053093 (Wichmann et al., 1996). I additionally identify 23 objects that have intermediate-strength surface gravity features consistent with those observed in Upper Sco, TW Hya and Beta Pic stars. In figure 4.3 I present spectra of M4/M4.5 stars shown in order of decreasing surface gravity and decreasing Na I and K I absorption (bottom to top). All spectra of observed stars as old as AB Dor or the Pleiades ($\sim$100 Myr) appear identical to those of dwarf stars. Therefore, the intermediate-age population in Taurus is likely significantly younger than $\sim$100 Myr, although the exact upper bound on the age of this population is unknown due to lack of comparison stars with ages between 10 and 100 Myrs. This interpretation may also apply to three objects identified by Luhman (2006) which were found to have gravity intermediate between Taurus and dwarf stars and presumed in that study to be $\sim$100 Myr-old due to lack of comparison stars with ages between those of Taurus members and field dwarfs. Hereafter I refer to the low gravity objects as "young" and the intermediate gravity objects as "intermediate-age." In the color-magnitude and color-color diagrams (figure 3.3 and figure 3.4), candidates for which I have obtained spectral data are shown as large symbols. Photometric and spectral data for new PMS stars are given in table 4.1. Table 4.2 contains magnitudes and spectral index measurements for PMS candidates spectroscopically determined to be field dwarfs.

Understanding the relationship of the newly-identified PMS population to the known Taurus members requires distances to the new PMS stars which I can not determine based on the current data set. If I assume they are located at the distance of Taurus, the derived ages from an HR diagram are $\sim$1–10 Myr, and the intermediate-age stars tend to have systematically lower derived luminosities than the young stars at a given spectral type. While these relative ages are consistent with those derived from surface gravity analysis, a range of distances could yield similar luminosity segregation results. In lieu of distance measurements, I constrain the origin of the PMS objects identified in this work by assessing the projected spatial distribution and kinematics of the new young and intermediate-age stars in relation to the known Taurus population.

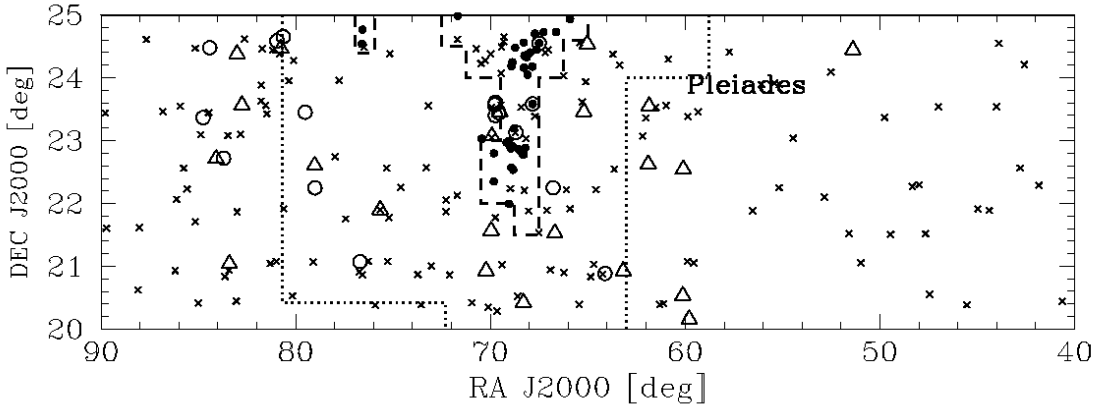

Figure 4.4 Spatial area of the imaging survey shown with previously known low mass Taurus members (filled circles; see text for references). Dashed lines indicate the boundary of previous deep CCD imaging surveys aimed at identifying new 1 Myr-old association members. Dotted lines indicate the boundary a 5 Myr old star with velocity 2 km/s could have traveled from any of the known subclusters. Open circles and triangles represent new low and intermediate-gravity stars identified from this work. Black X's show spectral candidates determined to be field dwarfs. The location of the Pleiades cluster (α=57 deg, δ=24 deg) is indicated.

4.3.1 Spatial Distribution of New PMS Stars

The new young and intermediate-age stars are distributed throughout the survey region, and many are located well beyond regions previously explored for young PMS stars. Figure 4.4 shows the location of spectroscopically observed Quest-2 candidates, along with known low mass Taurus members from the literature (Briceño et al. 2002, Guieu et al. 2006, Hartmann 2002, Luhman et al. 2003a, Luhman 2004b, Luhman 2006). The region that has been previously studied for low mass stars using deep optical/near-infrared imaging with spectroscopic follow-up (Briceño et al. 2002, Guieu et al. 2006, Luhman 2000, Luhman et al. 2003a, Luhman 2004b) is indicated, as is the Pleiades association. Based on comparison with CO maps of the region (Dame et al., 2001), while some objects do lie in projection near molecular gas, I see no systematic correlation between the spatial distribution of the new PMS stars and the CO emission.

To assess whether the new PMS stars are associated with the known concentrations of Taurus members or whether they are more uniformly distributed, I show in

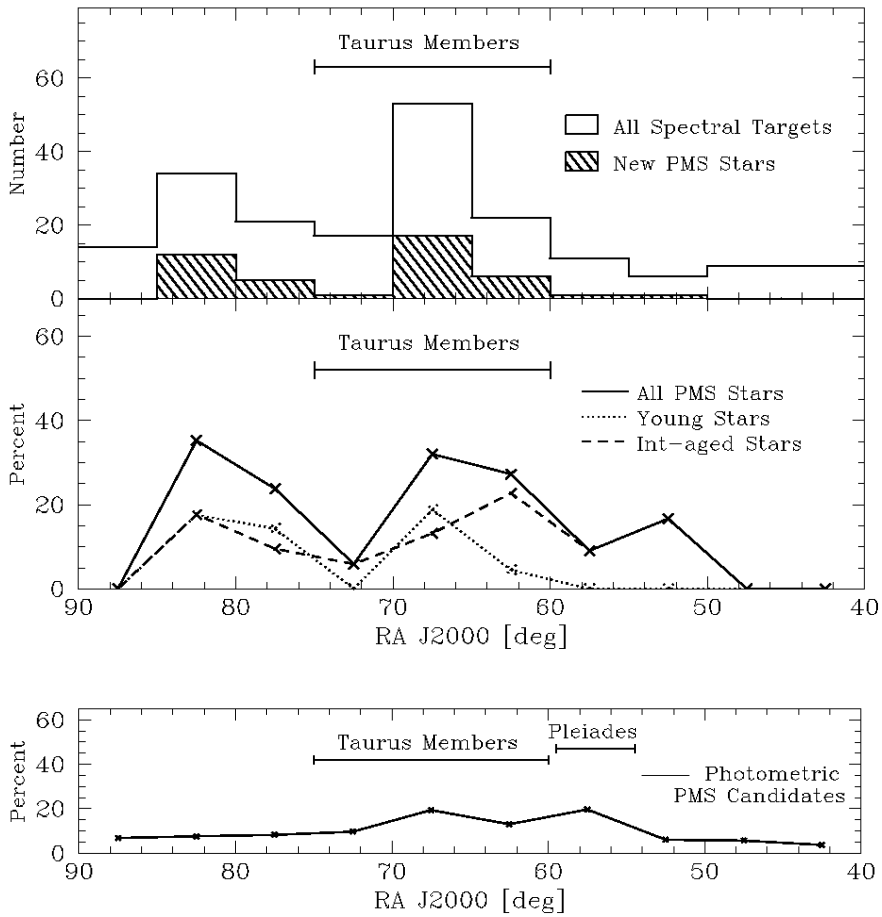

Figure 4.5 Top panel shows, as a function of RA, histograms for the total number of stars observed spectroscopically (open histogram) and those that were determined to be PMS stars (hatched histogram). Middle panel indicates the percentage of spectroscopically observed objects classified as PMS stars (solid line), and separately the percentage determined to be young (dotted line) or intermediate-age (dashed line) stars based on spectroscopic signatures of surface gravity. The RA range containing 98% of known low mass Taurus members is shown. Bottom panel shows the percentage of the ∼1800 photometric PMS candidates which fall at a given RA.

figure 4.5 a histogram of the RA values for all sources with spectra presented here and for those sources confirmed as PMS objects. In the middle panel I present the percentage of spectroscopically observed objects determined to be PMS stars. These can be compared to the RA range that contains 98% of the known low mass Taurus members (Briceño et al. 2002, Guieu et al. 2006, Hartmann 2002, Luhman et al. 2003a, Luhman 2004b, Luhman 2006). The bottom panel shows the percentage of the 1800 photometric candidates (see §3.1) located within a given RA range.

I note two spatial concentrations of new PMS stars: one near the known Taurus members at $\alpha \approx 68^o$, and a second in the eastern portion of the cloud centered around $\alpha \approx 82^o$. In figure 4.4 I indicate the approximate boundary within which a 5 Myr star with velocity 2 km/s relative to Taurus could have traveled from any of the known Taurus subclusters. Some of the young objects newly identified here are located well beyond this region. Assuming an age of <5 Myr as derived from surface gravity analysis, if these new young stars originated in the known star-forming subclusters they must, therefore, have arrived at their current positions at relatively high velocities.

An alternative, and perhaps more likely scenario is that I have identified a previously unknown area of recent star-formation outside of the current dense cloud complex. To further quantify the new PMS population and assess this possibility, I divide my PMS stars into 3 groups: those that lie in the same RA range as 98% of the known Taurus sample ($60^o \leq \alpha \leq 75^o$), those that are east ($\alpha > 75^o$) and those that are west ($\alpha < 60^o$) of this RA range. I find that of the 190 spectral candidates, 2/33 (6%) are confirmed to be PMS stars in the western region, 23/89 (26%) in the central region, and 17/68 (25%) in the eastern region. Spectroscopic confirmation rates of 25% in the east and only 6% in the west are contrary to the isotropic distribution I would expect to observe if these stars had been dispersed from the central regions. Using the two-tailed Fisher Exact test I compute a probability of ∼3% that the observed eastern and western distributions could have been drawn from the same population. I can therefore conclude with 97% confidence that the distributed PMS stars were not randomly dispersed from the known 1–2 Myr-old Taurus population. Instead, I suggest that they likely represent a population that is not associated with

the currently visible areas of the dense Taurus-Auriga molecular cloud complex.

4.3.2 Proper Motion Analysis

A primary goal of my large-area survey is to search for and characterize any PMS stars that might exist far from the ∼1–2 Myr-old subclusters in Taurus. Having identified several tens of such stars, I can use proper motion information to further study the characteristics of this spectroscopically selected sample.

I extracted USNO-B1.0 proper motions[2] (Monet et al., 2003) for 141 of the 190 objects with spectra. Figure 4.6 shows histograms of the α and δ proper motion components for new young and intermediate-age PMS targets and for stars classified as field dwarfs. Because proper motions listed in the USNO catalog are relative rather than absolute (i.e., the proper motions of background stars have not been accounted for), it was necessary to extract similarly derived USNO proper motions of known Taurus members for comparison rather than using more accurate values listed in the literature (e.g., Frink et al. 1997). The bottom panels of figure 4.6 show histograms of USNO proper motions for 160 previously known Taurus members and for 58 Hipparcos-selected Pleiades members (Robichon et al., 1999).

The proper motions of the PMS stars appear strongly correlated (independent of RA) and distinct from the proper motions of Pleiades members, whereas the spectroscopic field dwarfs exhibit a very broad distribution of proper motions. These results indicate that the newly identified PMS population is not associated with the Pleiades and is not a collection of random field stars. Further, the PMS stars farthest from the known Taurus population do not exhibit systematically higher proper motions, as would have been expected if they had been ejected from the current star-forming regions, giving further evidence that I have identified a new region of relatively recent

[2]I define an object to have a measured USNO proper motion if it has either a non-zero proper motion or a non-zero proper motion uncertainty in the USNO-B1.0 Whole Sky catalog (Monet et al., 2003). This cut biases my analysis against objects with intrinsically small (proper motion <2 mas/yr) but well-measured (uncertainty < 2 mas/yr) proper motions which will be listed with μRA=0, μDec=0, μRA_err=0 and μDec_err=0. However, because the USNO proper motion measurements are rounded to the nearest mas/yr and non-measurements are not indicated, I am unsure when a measured proper motion uncertainty of zero refers to a very small uncertainty vs. a non-detection. Therefore, I feel this is a necessary, if conservative, selection criteria.

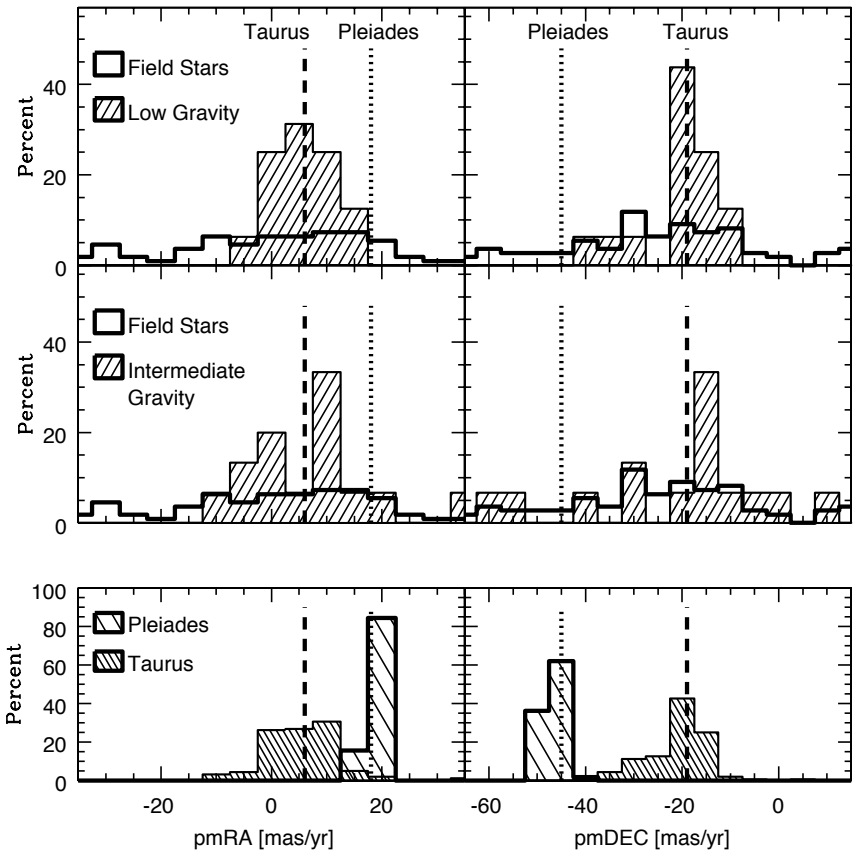

Figure 4.6 Histograms of proper motions extracted from the USNO-B1.0 catalog. In the top and middle panels, open histograms represent proper motions for stars which were spectroscopically determined to be field dwarfs; hatched histograms represent proper motions for new young (top) and intermediate-age (middle) PMS targets. In the bottom panels the light hatched histogram shows USNO-B1.0 proper motions for a sample of Pleiades members; the dark hatched histogram shows equivalent data for the sample of known Taurus members indicated in figure 4.4. All histograms have been normalized for ease of comparison and average values for Taurus and the Pleiades are shown in all panels. Data have been binned by 5 mas/yr. The average measured uncertainty for new PMS candidates is 4 mas/yr.

star-formation within the eastern regions of the clouds. The young sample in particular appears to have proper motions consistent with Taurus. A possible interpretation of these data is that the new PMS objects in the central regions are associated with the known Taurus population and the new PMS objects farther away were formed out of molecular material sharing a similar velocity and distance to that forming the current 1 Myr-old population. However, typical USNO proper motion uncertainties are large ($\pm$4 mas/yr), and the Taurus data themselves exhibit a large spread (bottom panels of figure 4.6). Therefore, a more detailed kinematic study of these objects is necessary before a definitive conclusion about their origin can be drawn (§4.5).

4.4 A New Distributed Population and the PTTS Problem

There has been much debate over the last few decades as to whether there exists a population of 3–10 Myr old post T-Tauri stars associated with the current 1–2 Myr old Taurus members. Spectroscopic follow-up studies of RASS-selected sources have identified a widespread population of stars in the vicinity of Taurus (e.g., Neuhaeuser et al. 1997, Wichmann et al. 1996), but the distances, ages, and origins of these stars remain controversial. Measures of x-ray emission and lithium equivalent widths are consistent with any ages from $\sim$1 to 100 Myr for these objects, and the nearly uniform spatial distribution of this population is consistent with its originating from a number of sources other than Taurus (e.g., Briceno et al. 1997). I have compared the spatial location of the new PMS sources identified here to the distribution of RASS sources in the area (e.g., Guillout et al. 1998) and find no correlation between areas of dense x-ray sources detected in the RASS and the newly identified stars in the eastern part of my survey region.

Besides X-ray emission, an efficient method of identifying nearby older PMS stars over a large area is through optical and near-infrared imaging combined with spectroscopic follow-up observations. Surface gravity signatures present in optical spec-

tra of late-K and M stars offer the advantage of clearly distinguishing young and intermediate-age PMS stars from 75–100 Myr-old stars. Considering the large number of imaging/spectroscopic surveys in the Taurus region, a natural question to ask is, how were the PMS stars presented here not discovered prior to my survey?

The primary reason these objects were not identified in earlier work is that I have searched much farther away from the clouds than most previous photometric/spectroscopic studies. The large-area work by Luhman (2006) probed only as far east as $\alpha \approx$5 hr and did not extend to the large number of newly discovered PMS stars in the eastern portion of my survey at $\alpha >$80 deg. Additionally, my survey occupies a unique range in color/magnitude space. Low mass stars discovered in early CCD surveys (e.g., Briceño et al. 2002) are saturated in the Quest-2 data. More recent surveys (e.g., Luhman 2004b, Guieu et al. 2006, Luhman 2006) have been concerned primarily with finding new brown dwarfs with spectral types $\geq$M6, which will be predominantly fainter and redder than the candidates discussed here. Indeed, comparison of USNO-$I2$ and 2MASS-J, H, K_S photometry for the Quest-2 PMS candidates to those selected in the Luhman (2006) study reveals that the Quest-2 candidates are systematically bluer. Despite the large overlap in area ($\sim$50 deg^2), the only observed candidate in my survey with spectral type $\geq$M6 selected as a candidate via the Luhman (2006) criteria is the one star (SCH J04311908+2335048) which our two works both identified. It is unlikely that the intermediate-age objects found in this work, which are predominantly bluer than the young objects (see figure 3.3), would have been selected as candidate Taurus members in any of the previous optical studies.

While I have discovered a new distributed population of both young and intermediate-age stars, I do not at this time claim that these objects represent the 'missing' post T-Tauri stars in Taurus. The spatial distribution of the PMS stars identified far from the known members is not consistent with those stars being associated with the Taurus subclusters. Additionally, the fact that the proper motions for the new young stars located tens of degrees away are consistent with known Taurus members implies that they were not ejected at high velocities from the current star-forming regions. Because my dataset is not complete either spatially or in magnitude/color

space (due to difficulties with weather and calibration), I cannot assess the full extent of this new population. Rather, I note that its existence hints there may be many more as-yet undiscovered PMS objects waiting to be identified in and surrounding the Taurus clouds.

4.5 Future Work

Radial velocities from high resolution spectra for all 42 new PMS stars combined with more robust proper motion measurements derived from existing catalogs will allow me to compute a 3D U, V, W velocity for each object over a range of distances. In addition, lithium equivalent widths can help confirm the youth of the new PMS sample which is currently based on NaI and KI line strengths. While lithium depletion occurs slowly over >100 Myr for G type stars and is therefore not suitable for distinguishing PTTSs from 100 Myr objects at these temperatures, for K to mid-M type stars that are fully convective, lithium depletion occurs over much faster timescales ($\sim$10 Myr; e.g., D'Antona & Mazzitelli 1994), and is a more robust indicator of youth. Finally, I emphasize that the new PMS population of 42 stars and a spectroscopic confirmation rate of $\sim$20% implies that several hundred similar young and intermediate-age PMS stars may be present in my larger photometric database.

Table 4.2. Measured quantities for candidates spectroscopically confirmed as field dwarfs near Taurus

ID[a]	g	r	i	J[c]	H[c]	K_S[c]	TiO-7140	TiO-8165	Na-8195
SCH J02423426+20262686[b]	17.3	–	14.4	12.53	11.98	11.69	1.55	1.07	0.87
SCH J02471836+22171512	–	20.2	17.9	14.58	13.94	13.49	3.17	1.85	0.76
SCH J02502040+24124969	18.4	16.5	14.9	12.55	11.94	11.63	1.98	1.22	0.81
SCH J02511084+22335835	17.8	16.1	14.7	12.52	11.90	11.66	1.84	1.16	0.86
SCH J02553616+24324815	19.2	17.3	15.5	12.82	12.18	11.83	2.28	1.35	0.77
SCH J02560113+23322159	19.2	17.5	15.4	13.13	12.55	12.21	2.11	1.26	0.78
SCH J02573373+21531119	17.0	15.4	13.9	11.58	11.03	10.74	1.84	1.14	0.84
SCH J02595189+21544806	18.8	17.1	15.5	13.00	12.36	12.07	2.03	1.25	0.82
SCH J03020861+20231122	17.3	15.7	14.0	11.68	11.05	10.79	2.06	1.25	0.88
SCH J03075903+23322049	17.6	16.0	14.0	12.31	11.74	11.46	1.71	1.10	0.84
SCH J03094953+20331863[b]	–	–	17.2	14.33	13.80	13.40	2.51	1.51	0.82
SCH J03103858+21311454	–	19.3	17.1	14.17	13.59	13.23	2.49	1.54	0.79
SCH J03115647+22180844	17.4	15.9	14.1	11.63	11.06	10.74	2.00	1.24	0.81
SCH J03132170+22162027	–	17.8	15.9	13.39	12.85	12.50	2.26	1.35	0.81
SCH J03174808+21303385	–	19.6	17.1	13.82	13.20	12.83	3.22	1.84	0.78
SCH J03190120+23221434	17.7	16.1	14.5	12.40	11.79	11.49	1.89	1.18	0.81
SCH J03235205+21031471	–	19.3	17.2	14.38	13.81	13.37	2.60	1.53	0.78
SCH J03262127+21311647	19.9	18.2	16.5	14.22	13.61	13.36	2.03	1.25	0.80
SCH J03300514+24052826	19.3	17.3	15.3	12.38	11.75	11.38	2.53	1.59	0.78
SCH J03312473+22060010	17.7	16.0	14.3	11.86	11.28	10.98	2.07	1.28	0.82
SCH J03374928+23022559	19.3	17.4	15.7	13.33	12.79	12.52	2.16	1.27	0.81
SCH J03403619+23533219	–	16.6	15.0	12.77	12.15	11.87	1.91	1.19	0.84
SCH J03404340+22150722	16.4	17.9	15.9	13.14	12.56	12.18	2.66	1.53	0.75
SCH J03414241+23545753	–	19.8	17.7	14.68	14.09	13.73	2.45	1.47	0.82
SCH J03441969+23534558	–	19.3	17.2	14.34	13.65	13.30	2.09	1.29	0.82
SCH J03461023+21525651	–	19.8	17.7	14.62	13.93	13.56	2.72	1.79	0.80
SCH J03505739+24244507	20.0	18.3	16.6	14.06	13.49	13.12	2.34	1.31	0.79
SCH J03571934+23273777	19.5	18.0	16.4	13.98	13.40	13.08	1.85	1.21	0.85
SCH J03581419+21030390	18.8	17.0	15.1	12.24	11.66	11.33	2.20	1.36	0.79
SCH J03592666+23230761	17.1	15.6	13.8	11.51	10.91	10.65	1.89	1.19	0.80
SCH J03593125+21044985	–	20.8	18.2	14.47	13.75	13.38	2.68	1.97	0.79
SCH J04032860+24175096	19.4	17.4	15.4	12.65	12.09	11.75	2.33	1.34	0.77
SCH J04032860+24175096	19.4	17.4	15.4	12.65	12.09	11.75	2.32	1.45	0.80
SCH J04035482+23334369	–	18.8	16.8	14.20	13.59	13.26	2.31	1.34	0.77
SCH J04042706+20243026	16.8	15.2	13.5	11.21	10.59	10.32	1.90	1.19	0.82
SCH J04051322+20233680	18.8	17.0	15.4	12.99	12.41	12.12	1.98	1.25	0.87
SCH J04055922+23314683	20.3	18.4	16.4	14.03	13.34	13.03	1.98	1.23	0.78

Table 4.2 (cont'd)

ID[a]	g	r	i	J[c]	H[c]	K_S[c]	TiO-7140	TiO-8165	Na-8195
SCH J04080508+23213945	18.1	17.4	15.7	13.25	12.68	12.35	2.28	1.36	0.78
SCH J04084314+23042360	–	19.5	17.1	14.03	13.57	13.20	3.02	1.54	0.75
SCH J04132997+24121104	19.7	17.8	15.9	13.64	12.90	12.61	1.63	1.08	0.84
SCH J04143471+22324170	18.0	16.2	14.7	12.36	11.77	11.47	1.82	1.14	0.79
SCH J04145027+24223723	18.4	16.7	15.0	12.47	11.90	11.59	1.93	1.22	0.79
SCH J04165655+20523604	–	19.3	17.0	13.66	13.03	12.60	2.59	1.68	0.78
SCH J04181857+22132340	17.7	15.8	14.0	11.17	10.54	10.20	2.38	1.41	0.77
SCH J04184558+21015469	20.1	18.2	16.2	13.14	12.53	12.21	2.43	1.44	0.79
SCH J04192264+20500801	18.4	16.7	15.3	13.13	12.45	12.16	1.57	1.10	0.87
SCH J04202448+23561330	–	20.6	18.4	14.60	13.85	13.42	2.16	2.03	0.82
SCH J04210820+23370654	19.9	18.6	16.6	13.89	13.31	12.97	2.48	1.39	0.78
SCH J04213745+24333974	–	19.1	17.1	14.35	13.72	13.39	2.40	1.40	0.76
SCH J04214590+20234439	–	19.7	17.2	13.94	13.34	12.92	2.72	1.71	0.79
SCH J04233635+21545582	18.4	17.0	15.3	12.99	12.35	12.11	1.88	1.17	0.81
SCH J04242298+22130276	18.5	17.0	15.2	12.70	12.06	11.74	1.79	1.16	0.88
SCH J04245196+20540815	19.2	17.7	15.9	13.44	12.80	12.55	1.81	1.15	0.85
SCH J04245748+24020200	–	19.4	16.7	13.37	12.73	12.35	3.22	1.78	0.73
SCH J04273712+20563907	20.0	18.2	16.0	13.08	12.45	12.07	2.54	1.52	0.78
SCH J04280637+24265280	19.8	17.6	15.8	12.97	12.00	11.58	1.34	1.03	0.91
SCH J04281979+21532986	18.5	16.9	15.2	12.86	12.29	12.02	2.00	1.20	0.79
SCH J04284465+24241965	20.3	18.4	16.2	13.35	12.73	12.33	2.64	1.50	0.77
SCH J04300382+21320646	20.2	18.5	16.6	14.06	13.45	13.13	2.27	1.33	0.84
SCH J04304952+23231579	–	20.2	18.1	15.27	14.69	14.12	1.78	1.16	0.88
SCH J04320885+21525117	17.8	16.3	14.7	12.54	11.89	11.67	1.85	1.17	0.82
SCH J04324101+23020399	20.1	18.2	16.6	13.45	12.31	11.75	0.94	0.96	0.99
SCH J04330156+22123664	–	18.8	16.9	14.21	13.44	13.08	1.93	1.19	0.86
SCH J04333877+23320263	–	18.6	16.4	13.86	13.09	12.76	1.84	1.16	0.88
SCH J04342548+20313479	18.6	16.8	15.1	12.73	12.08	11.83	1.95	1.21	0.87
SCH J04345291+23073158	19.6	17.6	15.8	13.31	12.51	12.20	1.66	1.11	0.86
SCH J04345328+23073237	–	19.1	17.1	14.66	13.98	13.60	1.76	1.26	0.82
SCH J04345328+23073237	–	19.1	17.1	14.66	13.98	13.60	1.80	1.17	0.83
SCH J04345328+23073237	–	19.1	17.1	14.66	13.98	13.60	1.81	1.16	0.83
SCH J04355509+22142525	–	18.3	16.5	14.03	13.36	13.07	1.99	1.25	0.87
SCH J04371222+24390300	–	18.6	16.7	14.05	13.54	13.07	2.29	1.38	0.79
SCH J04371755+24343438	17.8	16.1	14.6	12.50	11.83	11.59	1.73	1.11	0.89
SCH J04373727+21013612	17.1	15.6	14.1	12.07	11.46	11.21	1.81	1.15	0.86
SCH J04374450+24292963	–	19.7	17.4	14.46	13.83	13.39	2.67	1.56	0.77

Table 4.2 (cont'd)

ID[a]	g	r	i	J[c]	H[c]	K_S[c]	TiO-7140	TiO-8165	Na-8195
SCH J04374507+24043707	18.0	16.1	14.6	12.24	11.53	11.28	1.73	1.11	0.87
SCH J04374892+23341428	–	19.4	17.2	14.59	13.98	13.67	2.30	1.33	0.77
SCH J04383805+20171185	18.4	16.5	15.0	12.80	12.12	11.83	1.81	1.16	0.89
SCH J04385768+21463160	17.6	16.0	14.5	12.34	11.76	11.47	1.89	1.19	0.86
SCH J04394466+23315824	18.2	16.6	14.3	12.47	11.88	11.53	1.92	1.22	0.79
SCH J04394606+23025115	18.3	16.5	14.9	12.65	11.95	11.67	1.70	1.13	0.88
SCH J04395425+24230090	–	19.7	17.7	15.08	14.28	13.88	1.81	1.13	0.82
SCH J04402568+20205742	19.5	17.7	15.9	13.54	12.92	12.61	1.99	1.21	0.84
SCH J04410309+24164674	19.6	17.4	15.8	13.42	12.63	12.26	1.36	1.01	0.90
SCH J04415604+24135000	–	19.2	17.4	14.76	14.00	13.65	1.66	1.11	0.86
SCH J04425645+24275227	–	19.6	17.9	15.14	14.29	13.82	1.53	1.07	0.85
SCH J04434744+20251637	–	18.9	16.8	13.97	13.32	13.01	2.59	1.47	0.74
SCH J04464506+24364027	19.8	18.0	15.9	13.07	12.49	12.13	2.42	1.54	0.79
SCH J04464799+22075523	20.6	18.8	16.9	14.23	13.60	13.27	2.30	1.39	0.76
SCH J04482247+20514344	20.6	18.7	16.3	13.30	12.68	12.27	2.68	1.67	0.78
SCH J04490551+22031618	19.2	17.5	15.8	13.36	12.76	12.50	2.03	1.23	0.84
SCH J04490646+21522093	17.4	15.9	14.3	12.21	11.59	11.35	1.87	1.17	0.83
SCH J04520656+21002458	19.7	17.9	16.1	13.78	13.09	12.81	1.86	1.17	0.86
SCH J04524307+23332126	18.9	17.2	15.2	13.20	12.61	12.34	1.91	1.17	0.81
SCH J04531153+22341775	17.4	15.6	14.1	11.78	11.16	10.88	1.98	1.22	0.80
SCH J04541393+20230789	–	19.0	17.0	14.55	14.07	13.63	2.16	1.33	0.78
SCH J04545348+20521016	19.6	17.8	15.9	13.48	12.90	12.56	2.21	1.32	0.81
SCH J04582402+22151391	–	19.7	17.7	14.81	14.21	13.86	2.41	1.55	0.83
SCH J05003897+24225824	19.1	17.4	15.5	13.08	12.54	12.17	2.15	1.32	0.78
SCH J05005117+21462825	–	19.5	17.4	14.76	14.11	13.78	2.30	1.41	0.76
SCH J05010346+21043879	17.9	16.4	15.0	12.83	12.16	11.88	1.61	1.11	0.88
SCH J05011746+22335209	–	17.8	16.2	13.76	13.01	12.72	1.79	1.19	0.87
SCH J05023772+21540495	19.2	17.4	15.6	13.16	12.53	12.20	2.01	1.23	0.87
SCH J05033707+20230742	–	19.3	17.3	14.72	14.00	13.54	2.08	1.29	0.86
SCH J05050345+21044447	16.5	15.0	13.7	11.77	11.20	10.91	1.59	1.08	0.87
SCH J05055623+24291071	18.0	16.4	14.8	12.52	11.87	11.59	1.92	1.21	0.86
SCH J05061752+20514348	17.3	15.7	14.2	12.59	12.01	11.73	1.78	1.13	0.83
SCH J05061752+20514348	17.3	15.7	14.2	12.59	12.01	11.73	1.74	1.12	0.82
SCH J05065480+20542499	16.9	15.4	13.9	11.85	11.24	10.99	1.86	1.19	0.87
SCH J05094454+21452199	–	18.5	16.7	14.29	13.64	13.23	1.86	1.17	0.86
SCH J05110235+23574031	–	16.2	14.6	12.60	11.95	11.69	1.83	1.16	0.82
SCH J05115260+22444103	16.9	15.4	14.0	12.10	11.47	11.26	1.71	1.13	0.89

Table 4.2 (cont'd)

ID[a]	g	r	i	J[c]	H[c]	K_S[c]	TiO-7140	TiO-8165	Na-8195
SCH J05162541+21040800	19.1	17.4	15.7	13.36	12.80	12.49	2.09	1.29	0.81
SCH J05202425+24163845	–	20.0	18.1	15.40	14.51	14.10	1.74	1.14	0.87
SCH J05204088+20314071	18.5	16.8	15.1	12.90	12.28	12.03	2.02	1.21	0.86
SCH J05212398+23572292	–	19.0	17.0	14.39	13.72	13.32	2.35	1.42	0.79
SCH J05222623+21545792	18.5	16.9	15.3	13.19	12.59	12.34	1.91	1.21	0.84
SCH J05232027+24230192	20.2	18.5	16.5	14.05	13.46	13.09	2.20	1.31	0.79
SCH J05240100+21045046	17.2	15.5	13.9	11.81	11.23	10.95	1.85	1.18	0.82
SCH J05244136+24263530	18.8	17.2	15.5	13.29	12.73	12.43	1.92	1.20	0.80
SCH J05251535+21023971	–	19.5	17.0	13.29	12.63	12.24	1.78	2.02	0.78
SCH J05255410+23254047	–	18.6	16.7	14.26	13.51	13.21	1.74	1.09	0.87
SCH J05260810+23333802	–	19.4	17.4	14.78	14.03	13.65	1.79	1.15	0.82
SCH J05265150+24274728	19.2	17.3	15.7	13.29	12.59	12.29	1.77	1.17	0.86
SCH J05270113+23530238	–	19.8	18.0	15.32	14.48	14.10	1.59	1.12	0.83
SCH J05270681+23374776	–	19.8	17.7	15.03	14.30	14.02	2.39	1.39	0.78
SCH J05302983+24370854	18.8	17.1	15.3	13.05	12.40	12.10	2.07	1.30	0.81
SCH J05311984+23060478	17.6	15.9	14.4	12.21	11.65	11.41	1.85	1.19	0.83
SCH J05320030+21515747	16.8	15.3	13.7	11.50	10.87	10.56	1.97	1.21	0.79
SCH J05321214+20264183	17.6	15.9	14.2	11.85	11.23	10.93	2.08	1.28	0.79
SCH J05334071+20560298	18.1	16.6	15.0	12.88	12.25	12.01	1.87	1.19	0.83
SCH J05335346+23045373	19.4	17.7	15.9	13.51	12.93	12.64	2.05	1.25	0.84
SCH J05343049+20502794	16.1	14.7	13.5	11.88	11.26	11.04	1.48	1.05	0.87
SCH J05375244+23264770	15.9	14.4	12.9	11.00	10.41	10.17	1.65	1.09	0.83
SCH J05393117+23054477	19.3	17.3	15.6	13.27	12.65	12.34	2.07	1.25	0.78
SCH J05400118+20250873	18.9	17.2	15.3	12.94	12.36	12.04	2.14	1.30	0.79
SCH J05403786+24281777	–	18.9	16.9	14.17	13.49	13.15	2.38	1.46	0.80
SCH J05403868+21423466	19.1	17.3	15.6	13.44	12.94	12.61	2.01	1.23	0.84
SCH J05422003+22134842	15.6	14.1	12.9	11.14	10.51	10.25	1.49	1.10	0.90
SCH J05430011+22335091	–	19.3	17.4	14.69	14.03	13.72	2.34	1.47	0.84
SCH J05433937+23330204	18.6	16.8	14.4	12.14	11.50	11.19	2.27	1.36	0.78
SCH J05442656+22035440	18.5	16.9	15.3	13.11	12.48	12.18	1.90	1.17	0.85
SCH J05444476+20555487	18.7	16.8	15.1	12.85	12.22	11.94	2.01	1.25	0.78
SCH J05471468+23274615	–	19.8	17.3	14.18	13.46	13.16	2.57	1.69	0.77
SCH J05503959+24364706	19.2	17.5	15.8	13.57	12.99	12.69	2.11	1.28	0.85
SCH J05520649+21365149	18.9	17.2	15.8	13.89	13.30	13.05	1.64	1.11	0.85
SCH J05522087+20372913	19.9	18.0	16.1	13.74	13.15	12.86	2.06	1.27	0.87
SCH J05585296+21362200	20.2	18.4	16.8	14.71	14.15	13.78	1.74	1.31	0.87
SCH J05590744+23263037	18.6	17.1	15.5	13.50	12.86	12.58	1.69	1.12	0.88

Table 4.2 (cont'd)

ID[a]	g	r	i	J[c]	H[c]	K_S[c]	TiO-7140	TiO-8165	Na-8195

[a]Object IDs given in J2000 coordinates.

[b]Two faint candidates observed during the first spectroscopic observing run before the final photometric calibrations were finished do not have *r*-band photometry.

[c]Near-infrared photometry taken from 2MASS.

Chapter 5

A Large-Area Search for New Brown Dwarfs and Low Mass Stars in Upper Scorpius[1]

I present a wide-field photometric survey covering ∼150 deg^2 toward the Upper Scorpius OB association. Data in the BRI bands (converted to gri) taken with the Quest-2 camera on the Palomar 48-inch telescope were combined with the 2MASS JHK_S survey and used to select candidate pre-main sequence stars. Follow-up spectroscopy with the Palomar 200-inch telescope and the CTIO 4-m telescope of 243 candidate late-type members identified 145 stars that have surface gravity signatures consistent with association membership. Twelve of the 145 PMS stars identified exhibit Hα emission sufficient for accretion. From the optical/near-infrared photometry and derived spectral types, I construct an HR diagram for the new members and find 56 likely brown dwarfs, more than doubling the known substellar population of the Upper Scorpius OB association. From analysis of all observed PMS candidates compared to those determined to be association members, I conclude that the northern part of USco's low mass population shares a common spatial distribution with the high mass members, and find no evidence for spatial segregation.

[1]A modified version of this chapter has been published previously as Slesnick, Carpenter, & Hillenbrand 2006, AJ, 131, 3016. The current work has been updated to reflect new spectral observations taken after the time of original publication.

5.1 Motivation

The Upper Scorpius OB Association (USco) is the closest (145 pc; de Zeeuw et al. 1999) young OB association to the Sun with 120 known high mass Hipparcos stars. At an age of ∼5 Myr (Preibisch et al., 2002), this cluster is at an intermediate age between very young star forming regions and older open clusters where samples are sparser and studies of processes such as circumstellar disk dissipation are critical. Recent mid-infrared work by Mamajek et al. (2004) and Silverstone et al. (2006) indicates that by ∼10 Myr dust is removed from the inner few AU of circumstellar disks for $\gtrsim$85% of stars, whereas ∼80% of young 1 Myr stars in Taurus still retain their disks at these radii (Kenyon & Hartmann 1995; Skrutskie et al. 1990). This evolution in circumstellar material corresponds to the stage when planets are thought to be forming. Meteoritic evidence suggests the timescale for dissipation of our own solar system's nebula was on order of $\sim 10^7$ yr (Podosek & Cassen, 1994). Further, discovery of ^{60}Fe in meteorites argues that short-lived radionuclides were injected into the solar system's early protoplanetary disk from the explosion of a nearby supernovae (Desch & Ouellette 2005; Tachibana & Huss 2003). This evidence strongly suggests that our solar system was formed in an OB association similar to USco. Therefore, if we are to understand our own earth's origins, we must study the evolution of OB association members during planet-building stages.

A major difficulty faced by studies of the USco region is that the Hipparcos members alone span >200 deg^2 on the sky. Obtaining a complete census of the association's low mass population is thus a formidable task as one must identify faint objects over a very large spatial region. While there exist several techniques to identify young stars not associated with molecular gas, many of them are also accretion diagnostics. For example, a common method is to search for strong Hα emission (Ardila et al., 2000) produced in outflow or accretion flows (see §5.3.3), or near-infrared excess emission associated with warm inner accretion disks. While accretion can terminate over a wide range in age (1–10 Myr), the median lifetime of optically thick accretion disks is closer to 2–3 Myr (Haisch et al. 2001; Hillenbrand 2005). Therefore, surveys to look

for accretion signatures alone will not garner a full census of a 5 Myr association.

Enhanced chromospheric and coronal activity can last well beyond accretion timescales. This activity is linked with X-ray emission (Ku & Chanan 1979; Feigelson & Decampli 1981) though the exact cause of this phenomenon is still not fully understood (Preibisch et al., 2005). Many previous large-scale efforts in USco have successfully utilized Einstein data (Walter et al., 1994) or the ROSAT All Sky Survey (RASS; Preibisch et al. 1998; Preibisch & Zinnecker 1999) to identify hundreds of low and intermediate mass association members. However, neither the Einstein observations nor the RASS were sensitive enough to detect faint X-ray emission from the lowest mass stars and brown dwarfs.

Recently, deep, multicolor imaging surveys combined with spectroscopic follow-up have proved successful in identifying both the youngest classical T Tauri-type objects and more evolved very low mass stars and brown dwarfs in a variety of young regions. Young PMS objects still undergoing contraction towards the main sequence are redder and more luminous than their main sequence counterparts. Spectroscopic follow-up observations allow assessment of surface gravity diagnostics which can be used to distinguish young PMS stars from reddened field dwarfs and background giants. Previous imaging and spectroscopic surveys in USco include work by Preibisch et al. (2001) and Preibisch et al. (2002) who selected candidate association members based on optical magnitudes and colors obtained from photographic plates in the United Kingdon Schmidt Telescope survey fields. Their spectroscopic survey of 700 candidates over 9 deg^2 using the 2dF multifiber spectrograph yielded 166 new PMS stars based on the presence of lithium in their spectra. Martín et al. (2004) selected candidate young objects from the DENIS I, J survey and obtained spectra of 36 targets. Of these 28 were confirmed to be new low mass association members based on surface gravity diagnostics. Ardila et al. (2000) used R, I, Z photographic photometry to identify candidate members within an 80'×80' area of the association. Spectroscopic data were obtained for 22 candidates, 20 of which were determined to exhibit Hα emission indicating possible membership. Thus far, over 300 low mass (M <0.6 M$_\odot$) members have been identified in USco through X-rays, Hα emission,

photometry and/or spectroscopy. However most searches have been limited to small subregions or bright objects. Given the USco upper IMF, and assuming the high and low mass objects share the same spatial distribution, Preibisch et al. (2002) estimate the entire USco region should contain >1500 young, low mass objects with M <0.6 $M_{\odot}$, most of which are yet to be discovered.

5.2 Observations

Building on previous work in this region, I have completed a large-area optical *gri* photometric survey of ∼150 deg^2 in and near USco. Details of the photometric survey were given in chapter 2. My primary goal in USco is to significantly expand the number of known intermediate-age, ∼5–10 Myr-old low mass stars and brown dwarfs. Identifying large samples of objects at this age is critical for our understanding of early stellar evolution and planet formation. Usco is the ideal region to conduct such a survey because it contains the largest (>1500 objects) nearby (<300 pc) population of low mass intermediate-age PMS stars, most of which have not yet been uncovered. In chapter 3, I combined the Quest-2 photometric data with 2MASS JHK_S photometry to select candidate PMS stars, and presented newly obtained spectral data for 243 candidates discussed here. These candidates represent all stars observed at either Palomar or CTIO which meet all of the selection criteria outlined in §3.1.

All spectral analysis was carried out as outlined in chapter 3. Figure 5.1 shows spectral indices for 167 PMS spectral candidates in the USco region observed at Palomar. In the left panel I find fourteen outliers to sit below the main locus of data points. In all cases, the star is confirmed to exhibit low gravity signatures (§3.2.2) and I attribute the position in figure 5.1 to a small amount of veiling or reddening present in its spectra (§3.2.3). As shown in the right panel of figure 5.1, a large fraction (∼65%) of the candidate objects have measured Na-8190 indices consistent with their having surface gravity less than that of field dwarfs at similar spectral types. Note that because both program stars and most standard stars were observed at similar high airmasses in this region, there does not exist a systematic shift in the Na-8190

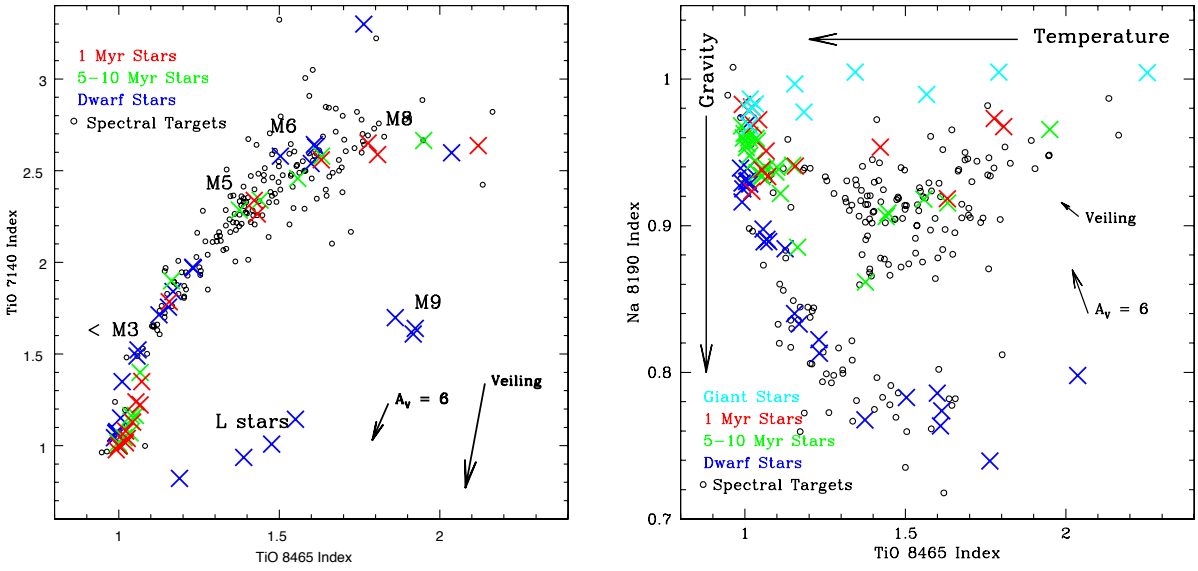

Figure 5.1 The left panel shows temperature-sensitive TiO-7140 vs. TiO-8465 indices; the right panel shows the TiO-8465 index vs. the gravity sensitive Na-8190 index. In both panels, blue X's represent measured indices for field dwarfs and members of the Hyades (∼650 Myr), Pleiades (∼115 Myr) and AB Dor (∼75–150 Myr) associations. Green X's show measured indices for intermediate-age spectral standards from Beta Pic (∼11 Myr), TW Hya (∼8 Myr), and Upper Sco (∼5 Myr). Red X's show measured indices for young Taurus members (∼1–2 Myr). Cyan X's in the right panel represent measured indices for giant standard stars. In both panels, black symbols are measured indices for USco PMS candidates observed at Palomar. The effects of extinction and veiling are shown as vectors (see §3.2.3).

index between the two populations as was the case in Taurus (chapter 4).

Of the 243 objects with spectra presented here, 76 were observed with the hydra multifiber spectrograph on the 4-m telescope at CTIO. These spectra have not been flux calibrated due to the intrinsic difficulties with this process for spectra taken through fibers. Thus, I cannot use quantitative index measurements for spectral classification, and all spectra were classified visually in relation to each other and to spectral standards taken during the observing run.

Table 5.1 lists optical and near-infrared 2MASS photometry, measured spectral indices (for Palomar spectra), spectral types and Hα equivalent widths for all USco

members discovered in my work. Seventeen of the 145 PMS stars identified here have been previously discussed in the literature, including 12 with previous spectral type determinations. When present, an alternative ID and spectral type is also given.

Table 5.1. Measured quantities for new PMS stars in USco

ID[a]	g	r	i	J[c]	H[c]	K_S[c]	TiO-7140	TiO-8165	Na-8195	SpType[d]	$W(H\alpha)$ [Å]	Otherid/Sptype
SCH J15560497-21064632		20.19	17.72	14.12	13.41	12.97	2.88	1.94	0.94	M7	-16.5	DENIS-P J155605.0-210646/M7[e]
SCH J15561978-24232936		18.17	16.18	13.36	12.74	12.48				M4.5	-9.2	
SCH J15574757-24441236	19.02	17.37	15.81	12.98	12.36	12.05				M4	-8.8	
SCH J15582337-21515908[b]	18.71			12.24	11.59	11.28	2.21	1.36	0.94	M4.75	-9.4	
SCH J15582566-18260865	19.59	18.17	16.03	12.92	12.20	11.79	2.55	1.57	0.92	M6	-20.2	
SCH J15583162-24025411		18.05	16.02	13.16	12.51	12.20	1.95	1.25	0.93	M4.5	-7.6	
SCH J15584812-21413426	20.23	18.53	16.50	13.48	12.87	12.51	2.39	1.42	0.87	M5.5	-10.8	
SCH J15594802-22271650		19.83	17.49	14.24	13.56	13.16	2.78	1.90	0.93	M7.5	-15.2	
SCH J15595868-18365205		19.15	16.76	13.43	12.76	12.40	2.48	1.53	0.91	M5.5	-14.8	
SCH J16002669-20563190	20.00	18.33	16.39	13.46	12.89	12.50				M4.5	-16.6	UScoCTIO 112/M5.5[h]
SCH J16014156-21113855	19.05	17.54	15.76	12.74	12.04	11.68				M4	-79.2	
SCH J16014768-24410152		19.08	16.92	13.87	13.27	13.00	2.44	1.45	0.86	M5	-16.0	
SCH J16024143-22484204		18.29	16.19	13.04	12.42	11.99	2.48	1.56	0.91	M5.5	-18.4	UScoCTIO 102[h]
SCH J16024576-23045102	18.91	17.46	15.32	12.46	11.84	11.50	2.33	1.38	0.87	M5	-9.6	[PBB2002] USco J160245.7-230450/M6[f]
SCH J16033470-18293060	19.38	17.63	15.50	12.51	11.83	11.48	2.21	1.38	0.91	M5	-36.6	DENIS-P J160334.7-182930/M5[e]
SCH J16034029-23352386		16.39	14.74	12.26	11.62	11.32				M4	-5.3	
SCH J16035651-23572517	19.91	18.43	16.49	13.60	13.01	12.67				M4.5	-10.3	
SCH J16040453-23463795	17.19	15.76	14.15	11.74	11.04	10.73	1.81	1.20	0.93	M4	-4.0	
SCH J16044303-23182620		19.50	17.17	13.81	13.19	12.85	2.72	1.79	0.90	M6.5	-18.0	UScoCTIO 1102[h]
SCH J16051829-17562092	17.07	15.65	14.04	11.64	10.98	10.68	1.66	1.11	0.93	M4	-5.4	
SCH J16053077-22462016		19.47	17.17	13.78	13.18	12.78	2.84	1.65	0.89	M6	-17.8	
SCH J16054416-21550566		16.79	14.80	11.90	11.28	10.94	2.35	1.40	0.90	M5	-9.4	
SCH J16060391-20564497		19.43	17.18	13.52	12.90	12.47	2.77	1.89	0.95	M7	-159.0	DENIS-P J160603.9-205644/M7.5[e]
SCH J16072239-20115852	19.27	17.73	15.76	12.70	12.02	11.58	2.37	1.48	0.93	M5.5	-14.2	[PBB2002] USco J160722.4-201158/M5[f]

Table 5.1 (cont'd)

ID[a]	g	r	i	J[c]	H[c]	K_S[c]	TiO-7140	TiO-8165	Na-8195	SpType[d]	$W(H\alpha)$ [Å]	Otherid/Sptype
SCH J16072640-21441727		20.21	17.95	14.66	14.02	13.67	2.36	1.64	0.88	M6	-10.7	
SCH J16075565-24432714		18.68	16.66	13.83	13.13	12.71	2.13	1.46	0.90	M5.5	-47.3	
SCH J16075850-20394890		19.12	16.91	13.59	12.95	12.58	2.47	1.53	0.89	M6	-14.9	
SCH J16081081-22294303		17.55	15.61	12.61	11.99	11.67				M5	-49.0	
SCH J16083646-24453053	16.64	15.32	13.79	11.59	10.94	10.73				M3.5	-12.0	
SCH J16083658-18024994		18.41	16.14	12.78	12.21	11.75	2.59	1.75	0.93	M6.5	-16.6	
SCH J16084058-22255726	19.78	18.29	16.52	14.09	13.46	13.22				M4	-2.6	
SCH J16084170-18561077	19.44	17.69	15.50	12.22	11.58	11.21	2.55	1.60	0.92	M6	-10.1	[PBB2002] USco J160841.7-185610/M6[f]
SCH J16085870-24493641	18.02	16.54	14.86	12.31	11.66	11.41				M4	-7.1	
SCH J16090451-22245259		19.03	16.49	13.01	12.36	11.99	2.75	1.81	0.95	M7	-17.1	
SCH J16090511-24262843		15.87	14.29	11.96	11.26	10.98				M4	-5.9	
SCH J16090771-23395430	18.57	17.06	15.09	12.08	11.44	11.13	2.30	1.39	0.92	M5	-15.7	
SCH J16090883-22174699	19.34	17.71	15.64	12.97	12.33	12.07				M5	-14.4	
SCH J16091837-20073523		17.96	16.11	13.00	12.37	12.01				M7.5	-15.5	
SCH J16092137-21393452	18.71	16.96	14.98	11.98	11.38	11.02	2.25	1.43	0.92	M5.5	-24.5	
SCH J16093018-20595409		19.41	17.30	13.99	13.35	12.98	2.59	1.53	0.89	M6	-11.1	
SCH J16093707-20525337	19.50	17.80	15.86	12.90	12.25	11.97	2.28	1.33	0.91	M4.75	-5.7	
SCH J16095217-21362826	20.24	18.33	16.05	12.56	11.96	11.56	2.66	1.76	0.94	M7	-26.2	
SCH J16095307-19481704		18.12	16.00	12.80	12.16	11.76	2.58	1.60	0.91	M6	-21.7	
SCH J16095695-22120300		18.72	16.49	13.62	13.03	12.66	2.64	1.53	0.90	M5.5	-8.9	
SCH J16095991-21554293		19.84	17.50	14.30	13.64	13.30	2.49	1.57	0.89	M6.5	-17.4	
SCH J16100129-21522466[b]	19.75			12.63	12.06	11.70	2.53	1.55	0.91	M5.5	-12.0	
SCH J16100541-19193636		20.75	18.13	14.21	13.43	12.70	2.55	1.68	0.94	M6	-49.8	DENIS-P J161005.4-191936/M7[e]
SCH J16100751-18105666		18.34	16.06	12.74	12.15	11.75	2.82	1.74	0.90	M6	-15.9	DENIS-P J161007.5-181056/M6[e]

Table 5.1 (cont'd)

ID[a]	g	r	i	J[c]	H[c]	K_S[c]	TiO-7140	TiO-8165	Na-8195	SpType[d]	$W(H\alpha)$ [Å]	Otherid/Sptype
SCH J16101190-21015540	20.24	18.80	16.77	13.78	12.99	12.57	2.41	1.54	0.91	M5.5	-14.6	
SCH J16102990-24035024	18.97	17.42	15.59	12.92	12.33	12.01				M4.5	-10.0	
SCH J16103525-20291714	19.53	17.77	15.77	12.69	12.04	11.71	2.25	1.37	0.91	M5	-12.5	
SCH J16103876-18292353		19.87	17.63	13.96	13.16	12.64	2.29	1.57	0.96	M6	-80.3	
SCH J16104635-18405996	19.35	17.64	15.56	12.70	11.81	11.26	1.97	1.25	0.93	M4.5	-8.8	[PBB2002] USco J161046.3-184059/M4[f]
SCH J16105500-21261422	19.71	18.19	16.03	12.77	12.10	11.77	2.59	1.59	0.90	M6	-27	
SCH J16105727-23595416	18.68	17.31	15.57	12.86	12.21	11.91				M4	-7.4	
SCH J16110144-19244914		18.44	16.43	13.35	12.71	12.36	2.27	1.39	0.90	M5	-9.3	
SCH J16110739-22285027	19.26	17.64	15.44	12.31	11.72	11.32	2.29	1.54	0.92	M6.25	-139.1	
SCH J16111711-22171749		20.37	17.97	14.34	13.73	13.25	2.68	1.82	0.94	M7.5	-20.8	
SCH J16112629-23400611		18.33	16.42	13.44	12.82	12.47	2.32	1.49	0.90	M5.5	-7.1	
SCH J16112959-19002921		19.76	17.35	13.67	12.90	12.44	2.49	1.68	0.94	M6	-20.4	
SCH J16114735-22420649		18.46	16.41	13.49	12.82	12.53	2.33	1.37	0.89	M5	-13.1	
SCH J16115737-22150691		18.75	16.70	13.73	13.10	12.73	2.26	1.39	0.90	M5	-8.6	
SCH J16121044-19322708	19.03	17.19	15.30	12.23	11.59	11.23	2.31	1.38	0.92	M5	-12.8	
SCH J16121188-20472698		19.39	17.09	13.66	13.02	12.60	2.69	1.77	0.93	M6.5	-8.1	
SCH J16122764-24064850	19.54	17.85	15.88	12.89	12.29	11.93				M7	-13.5	
SCH J16123459-24583447	18.37	16.87	14.83	11.94	11.36	11.04	2.26	1.36	0.91	M4.75	-13.5	
SCH J16123758-23492340		19.10	17.00	13.93	13.28	12.91	2.47	1.51	0.87	M6	-15.8	
SCH J16124506-23053043		18.70	16.52	13.48	12.87	12.46	2.48	1.43	0.87	M5.5	-9.8	
SCH J16124692-23384086		19.25	16.98	13.65	13.02	12.62	2.66	1.70	0.90	M6	-14.7	
SCH J16125723-24280145		17.46	15.68	12.93	12.28	11.95				M4	-11.8	
SCH J16130306-19293234		18.85	16.75	13.45	12.76	12.35	2.60	1.54	0.92	M5.5	-7.3	
SCH J16130764-17035233		18.95	16.83	13.71	13.02	12.71	2.32	1.46	0.90	M5.5	-7.9	

Table 5.1 (cont'd)

ID[a]	g	r	i	J[c]	H[c]	K_S[c]	TiO-7140	TiO-8165	Na-8195	SpType[d]	$W(H\alpha)$ [Å]	Otherid/Sptype
SCH J16131212-23050329		19.87	17.43	14.05	13.44	13.00	2.62	1.73	0.90	M6.5	-13.4	
SCH J16131857-15293460	17.87	16.50	14.49	11.68	11.05	10.76	2.23	1.34	0.93	M4.75	-14.4	
SCH J16132576-17373542	17.98	16.48	14.83	12.32	11.69	11.40	1.72	1.14	0.91	M4	-5.3	
SCH J16132809-19245288	19.87	18.22	16.16	12.92	12.26	11.91	2.46	1.47	0.91	M6	-14.7	[PBB2002] USco J161328.0-192452/M5[f]
SCH J16141351-22445788		16.76	15.02	12.37	11.72	11.42				M4	-5.4	
SCH J16141484-24270844		17.83	15.60	12.47	11.85	11.48				M7	-17.6	
SCH J16141974-24284053		19.46	17.13	13.81	13.15	12.76	2.59	1.61	0.88	M6	-16.4	
SCH J16143286-22421358		20.54	17.87	14.23	13.66	13.24	2.77	1.75	0.98	M6.5	-23.6	
SCH J16150524-24593542		17.70	15.58	12.55	11.90	11.48	2.01	1.40	0.92	M5	-38.4	
SCH J16151115-24201556		19.68	17.46	14.23	13.58	13.17	2.33	1.43	0.90	M6	-10.9	
SCH J16151360-23042637		20.35	18.18	14.81	14.19	13.91	2.69	1.75	0.87	M6.5	-35.9	
SCH J16153915-191700073	19.03	17.32	15.09	11.68	10.84	10.43	2.11	1.31	0.93	M4.75	-9.3	
SCH J16155508-24443677		19.18	16.81	13.39	12.74	12.28	2.48	1.66	0.93	M6	-15.8	
SCH J16162396-24083016	19.69	17.67	16.02	13.15	12.51	12.13				M5	-17.5	DENIS-P J161624.0-240830/M5.5[e]
SCH J16162599-21122315		19.42	17.34	14.26	13.63	13.30	2.35	1.38	0.89	M5	-11.3	
SCH J16163504-20575551	19.04	17.26	15.29	12.22	11.63	11.29	2.38	1.47	0.91	M5.5	-17.6	
SCH J16164538-23334143		18.79	16.77	13.77	13.15	12.81	2.27	1.39	0.86	M5	-17.1	
SCH J16165160-20485398	18.13	16.49	14.78	12.11	11.43	11.13				M4	-5.0	
SCH J16171901-21371312		18.78	16.65	13.48	12.86	12.54	2.52	1.49	0.91	M5.5	-13.4	
SCH J16172504-23503799		19.40	17.20	13.74	13.01	12.63	2.25	1.44	0.87	M5	-12.0	
SCH J16173105-20504715		18.83	16.49	13.03	12.36	12.02				M7	-34.8	
SCH J16173238-20403653		20.83	18.18	14.34	13.68	13.19	2.60	1.70	0.92	M6	-24.6	
SCH J16173788-21191618	18.41	16.84	14.93	12.23	11.54	11.26				M4	-8.7	
SCH J16174368-21115536	20.36	18.67	17.04	14.47	13.68	13.35				M4	-4.7	

Table 5.1 (cont'd)

ID[a]	g	r	i	J[c]	H[c]	K_S[c]	TiO-7140	TiO-8165	Na-8195	SpType[d]	$W(H\alpha)$ [Å]	Otherid/Sptype
SCH J16174540-23533618		19.88	17.44	14.05	13.31	12.95	2.83	1.67	0.91	M6	-15.5	
SCH J16181201-24133263	19.29	17.77	15.70	12.69	11.93	11.59				M5	-21.7	
SCH J16181567-23470847		18.55	16.18	12.42	11.51	10.97	2.32	1.39	0.94	M5.5	-16.3	
SCH J16181601-24372688	18.54	16.75	14.70	11.67	10.92	10.59				M4	-16.1	
SCH J16181906-20284815	19.13	17.36	15.38	12.39	11.50	10.95	2.14	1.31	0.91	M4.75	-11.3	
SCH J16182501-23381068		19.50	17.19	13.72	12.88	12.44	2.06	1.32	0.91	M5	-9.2	
SCH J16183144-24195229		20.22	17.76	14.15	13.46	12.97	2.45	1.60	0.87	M6.5	-11.4	
SCH J16183620-24253332	18.36	16.60	14.75	12.03	11.31	10.95				M4	-7.5	
SCH J16185038-24243205		18.97	16.79	13.63	12.93	12.51	2.34	1.38	0.90	M5	-6.5	
SCH J16190473-23075283		18.50	16.30	13.00	12.34	11.98	2.36	1.47	0.91	M5.5	-12.1	
SCH J16191521-24172429	19.00	17.23	15.19	12.13	11.37	11.05				M4	-13.3	
SCH J16192994-24255414	18.55	16.41	14.53	11.53	10.63	10.22				M4	-6.5	
SCH J16193976-21453527		18.47	16.40	13.22	12.53	12.11	2.10	1.66	0.93	M6	-36.5	DENIS-P J161939.8-214535/M7[e]
SCH J16200756-23591522		19.14	16.75	13.21	12.48	12.05	2.49	1.58	0.92	M6	-24.2	
SCH J16201318-24250155		17.96	16.21	13.77	13.20	12.86				M4	-15.0	
SCH J16202127-21202923		19.14	16.61	13.39	12.74	12.40	2.61	1.62	0.89	M6	-23.9	
SCH J16202523-23160347		19.47	17.59	14.37	13.68	13.23	2.20	1.53	0.88	M5.5	-9.5	
SCH J16211564-24361173		15.86	14.50	12.44	11.81	11.59				M3.5	-5.0	
SCH J16211922-24255250		17.99	15.73	12.17	11.18	10.67				M4	-8.7	
SCH J16212490-24261446		18.24	16.14	12.87	11.86	11.41				M3.5	-6.8	
SCH J16213591-23550341		20.23	17.67	13.94	13.19	12.73	2.38	1.69	0.90	M6	-19.9	
SCH J16221577-23134936		18.87	16.80	13.71	13.14	12.80	2.52	1.55	0.87	M6	-9.2	
SCH J16222156-22173094		18.63	16.52	13.74	13.09	12.61	2.00	1.36	0.92	M5	-60.3	
SCH J16224384-19510575		17.54	15.88	12.35	11.61	11.15	2.42	2.13	0.98	M8	-62.1	

Table 5.1 (cont'd)

ID[a]	g	r	i	J[c]	H[c]	K_S[c]	TiO-7140	TiO-8165	Na-8195	SpType[d]	$W(H\alpha)$ [Å]	Otherid/Sptype
SCH J16235158-23172740		19.86	17.40	13.55	12.89	12.41	2.82	2.16	0.96	M8	-76.8	
SCH J16235474-24383211		19.77	17.21	13.31	12.49	11.92	2.34	1.61	0.95	M6	-12.8	
SCH J16252862-16585055		19.95	17.47	13.67	13.01	12.62	2.66	1.94	0.94	M8	-23.3	
SCH J16252968-22145448		18.64	16.40	13.19	12.49	12.11	2.25	1.41	0.94	M5	-16.2	
SCH J16253671-22242887		19.46	16.97	13.53	12.83	12.45	2.64	1.76	0.93	M7	-11.6	
SCH J16254319-22300300	19.35	17.22	15.84	13.02	12.40	12.09	2.19	1.37	0.90	M5	-9.2	
SCH J16255064-21554577		19.28	17.20	14.26	13.62	13.27	2.36	1.35	0.85	M4.75	-8.9	
SCH J16260630-23340375		19.31	16.85	13.14	12.27	11.75	2.28	1.41	0.93	M5.5	-5.4	
SCH J16262192-24444004		18.98	16.52	12.34	11.48	10.85	2.50	1.83	0.97	M8	-88.8	
SCH J16263026-23365552		19.51	17.48	13.75	12.82	12.21	2.51	1.69	0.94	M6	-32.1	
SCH J16265619-22135224		19.14	16.76	13.48	12.83	12.41	2.71	1.67	0.90	M6	-28.4	
SCH J16270940-21484591		18.39	16.29	12.97	12.15	11.71	1.85	1.27	0.92	M4.5	-11.1	
SCH J16274801-24571371		19.87	17.31	13.54	12.65	12.11	2.20	1.42	0.91	M5	-22.0	
SCH J16281810-24283619		19.19	16.55	12.69	11.81	11.29	2.43	1.49	0.93	M6	-20.1	BKLT J162818-242836[g]
SCH J16284706-24281413		18.71	16.59	13.24	12.53	11.95	2.16	1.72	0.94	M6	-182.7	BKLT J162847-242814[g]
SCH J16292211-17420937	19.23	17.48	15.46	12.58	12.02	11.72	2.17	1.36	0.88	M4.75	-13.0	
SCH J16293625-24565325		18.66	16.43	13.43	12.85	12.48	2.90	1.59	0.86	M6	-41.2	
SCH J16293664-17084094	18.39	16.74	14.82	12.01	11.31	11.01	2.16	1.31	0.91	M4.75	-11.3	
SCH J16293934-16145647	17.35	15.90	14.51	12.19	11.49	11.19				6.3	-3.1	
SCH J16294877-21370914	19.13	17.38	15.45	12.52	11.86	11.52	2.16	1.34	0.92	M5	-9.2	
SCH J16302675-23590905		18.26	16.02	12.61	11.93	11.47	2.39	1.64	0.96	M6	-34.7	
SCH J16303392-24280657		16.67	14.67	11.62	10.76	10.36				M4	-5.3	
SCH J16305349-24245439		17.51	15.51	12.27	11.46	11.04	2.21	1.41	0.97	M5.5	-34.8	
SCH J16310241-24084335		16.70	14.67	11.96	11.24	10.78				M5	-13.5	WSB 68[i]

Table 5.1 (cont'd)

ID[a]	g	r	i	J[c]	H[c]	K_S[c]	TiO-7140	TiO-8165	Na-8195	SpType[d]	$W(H\alpha)$ [Å]	Otherid/Sptype
SCH J16324224-23165644		16.77	14.70	11.76	11.17	10.87	2.60	1.48	0.87	M5.5	-12.9	
SCH J16324726-20593771		18.49	16.55	13.45	12.85	12.47	2.39	1.50	0.91	M6	-25.2	

[a]IDs given in J2000 coordinates.

[b]Two targets observed during the first spectroscopic observing run before the final photometric calibrations were finished do not have calibrated r, i magnitudes.

[c]Near-infrared photometry taken from 2MASS.

[d]Spectral type errors are ± 0.5 for M subclasses.

[e]Reference from: Martín et al. (2004).

[f]Reference from: Preibisch et al. (2002).

[g]Reference from: Barsony et al. (1997).

[h]Reference from: Ardila et al. (2000).

[i]Reference from: Wilking et al. (1987).

5.3 Discussion

5.3.1 HR Diagram for New USco Members

I combine each new member's spectral type and photometry to derive values for its luminosity and effective temperature and place it on a theoretical HR diagram. As described in chapter 2, the final Quest-2 photometry is not on a standard magnitude system. Thus, because of the reliability and uniformity of the 2MASS survey, I chose to use J-band magnitudes and $(J-H)$ colors to derive luminosities. An empirical fit to BC_J as a function of spectral type was determined from the observational data of Leggett et al. (1996) and Leggett et al. (2002) (spectral types M1-M6.5 and M6-L3, respectively). I adopted intrinsic colors, extinction, and effective temperatures using the methods described in Slesnick et al. (2004).

In figure 5.2 I present an HR diagram for the 145 identified low mass members of USco, shown with PMS model tracks and isochrones. The most commonly used PMS models for low mass stars and brown dwarfs are those derived by D'Antona & Mazzitelli (1997) (shown) and Baraffe et al. (1998) which differ primarily in their atmospheric approximations and treatment of convection. Both models suggest similar mass ranges for my data of $0.02M_\odot < M < 0.2M_\odot$, though predicted masses for individual objects can vary by up to $0.07M_\odot$. As illustrated in figure 5.2, I have identified a low mass stellar population of age roughly consistent with the 5 Myr age inferred in previous work on the intermediate mass ($6M_\odot > M > 0.1M_\odot$) members of USco (Preibisch et al., 2002). The mass and age distributions of this population will be discussed further in chapter 6. Among the PMS stars identified in my work, 56 have spectral types M6 or later, and are considered to be brown dwarfs based on theoretical models. Prior to this work, 34 spectroscopically confirmed USco members had been identified at these spectral types (Ardila et al. 2000, Preibisch et al. 2002, Martín et al. 2004), 10 of which are also presented here (see table 5.1). Thus, with this study I have more than doubled the number of known substellar objects in USco.

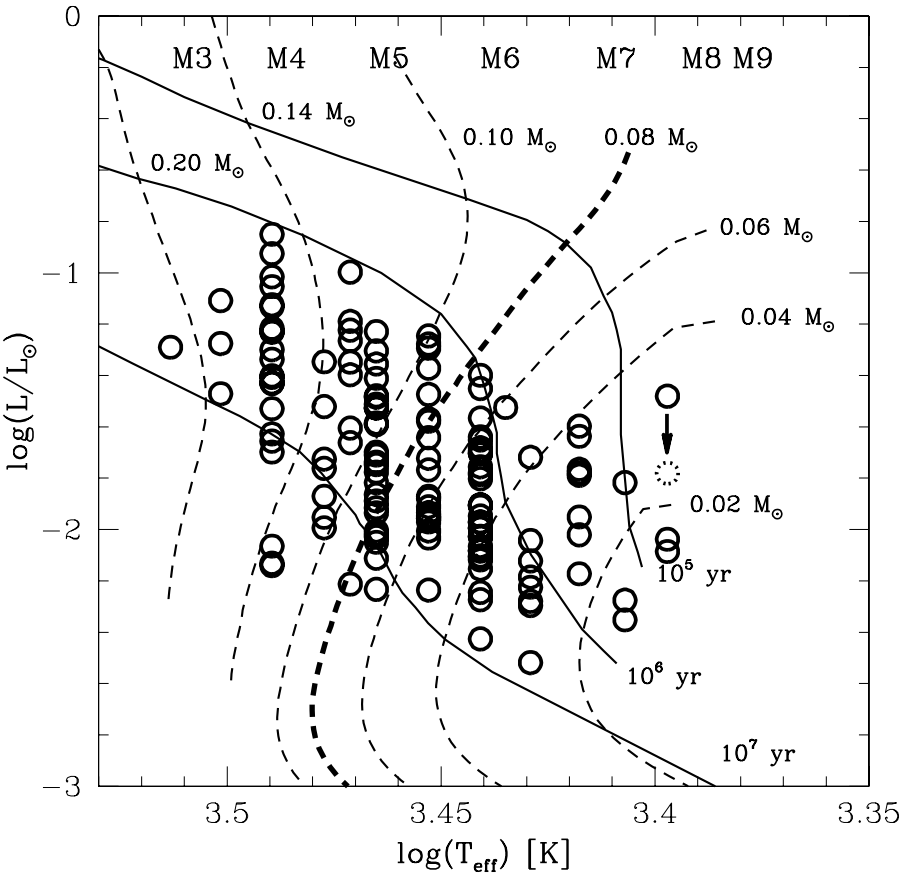

Figure 5.2 HR diagram for new PMS objects found in the USco region, shown with model tracks and isochrones of D'Antona & Mazzitelli (1997). The sample is consistent with an age of ∼5 Myr and contains masses spanning the brown dwarf to stellar regimes. The arrow plus dotted symbol indicates where that star would sit in the HR diagram as a single star if it is an unresolved binary (see §5.3.2).

5.3.2 A Possible Binary

The most luminous M8 brown dwarf (SCH16224384-19510575) is an obvious outlier to the main locus of stars in figure 5.2 appearing overluminous compared to the other sources. This object also has strong Hα emission (see §5.3.3) with a slightly asymmetric profile. It is unlikely that this object is a single, extremely young (<100,000 yr based on HR diagram placement) association member. The object could be a young, PMS-gravity foreground object that happens to fall within my line of sight. The simplest explanation is that SCH16224384-19510575 is an unresolved binary. Assuming typical seeing at Palomar under photometric conditions of $\sim$1.2", any pair with separations $\lesssim$175 AU would not be resolved in my data. If I assume SCH16224384-19510575 consists of 2 equal-luminosity objects, its placement in the HR diagram becomes more consistent with the main locus of association members. This effect is illustrated as an arrow plus dotted symbol in figure 5.2.

5.3.3 Emission Line Objects

The only prominent emission line observed in any of the spectra is Hα which, seen in the spectra of young stars and brown dwarfs, is predominantly created via one of two mechanisms. Weak, narrow Hα lines are presumed to originate from active chromospheres whereas strong, broad and/or asymmetric lines can be produced from high-velocity, infalling accretion or strong winds. Barrado y Navascués & Martín (2003) have proposed an empirical, spectral-type-Hα equivalent width ($W(\mathrm{H}_\alpha)$) relation to describe the upper limit of non-accreting stars and brown dwarfs based on the chromospheric saturation limit observed in young open clusters. Figure 5.3 plots measured Hα equivalent widths for all spectra as a function of spectral type, shown with the Barrado y Navascués & Martín (2003) empirical accretor/nonaccretor division. Many stars and brown dwarfs (see table 5.1) exhibit very strong Hα emission at levels substantially above the accretor/nonaccretor division and thus are possibly still undergoing active accretion.

Because errors on the accretor/nonaccretor division are not well defined (Barrado

y Navascués & Martín, 2003), I determined my own empirical criterion for identifying objects with Hα excess emission. I measured the median values of Hα emission as a function of spectral type (binned by 1 spectral type) using 1-sigma clipping. These values are shown as large magenta X's on figure 5.3. For most bins, I define a star to have an Hα excess if it exhibits emission at a level greater than 3-sigma above the median value for its spectral type (where sigma is defined as the dispersion about the median for all stars used to compute the median value at a given spectral type; shown as magenta –'s on figure 5.3). These sources are boxed in green on figure 5.3. The first and last bins only have 4 and 3 sources respectively. Thus, for these bins I do not have enough measurements to derive a statistically representative value for median Hα emission. Therefore I do not consider any stars in these bins in my sample of Hα excess sources, but note that two M8 stars (including the possible binary discussed in §5.3.2) sit above the Barrado y Navascués & Martín (2003) accretor/nonaccretor dividing line. In general, my empirical criterion for classifying a star as accreting is slightly more conservative (i.e., requires a higher W(Hα)) than the criterion defined by Barrado y Navascués & Martín (2003).

Based on the above criterion, I find 12 objects to exhibit very strong Hα emission. The blue half of the observed spectra for each accreting source is shown in either figure 5.4 or figure 5.5. Two accreting sources lie very close (within $\sim$1 deg) to the young ρOph molecular cloud. However, because ρOph and USco lie at approximately the same distance, if they were escaped, $\lesssim$1 Myr ρOph members we would expect to see them exhibit systematically higher luminosities than USco members of similar spectral type. Based on figure 5.2, this phenomenon is not observed and I include these two stars in my sample of accretors in USco. Thus, I find at an age of $\sim$5 Myr (see chapter 6), 12/145 (or $\sim 8^{+3}_{-2}\%$) of low mass association members (spectral type $\geq$M4) are observed to be accreting based on the strength of Hα emission present in their spectra. In comparison, Guieu et al. (2006) find $\sim 40^{+24}_{-16}\%$ of 1 Myr-old low mass objects in the known subclusters of Taurus to be actively accreting based on the strength of Hα emission observed in their spectra. Thus, a significant fraction of very low mass stars and brown dwarfs must actively stop accreting between 1 and 5

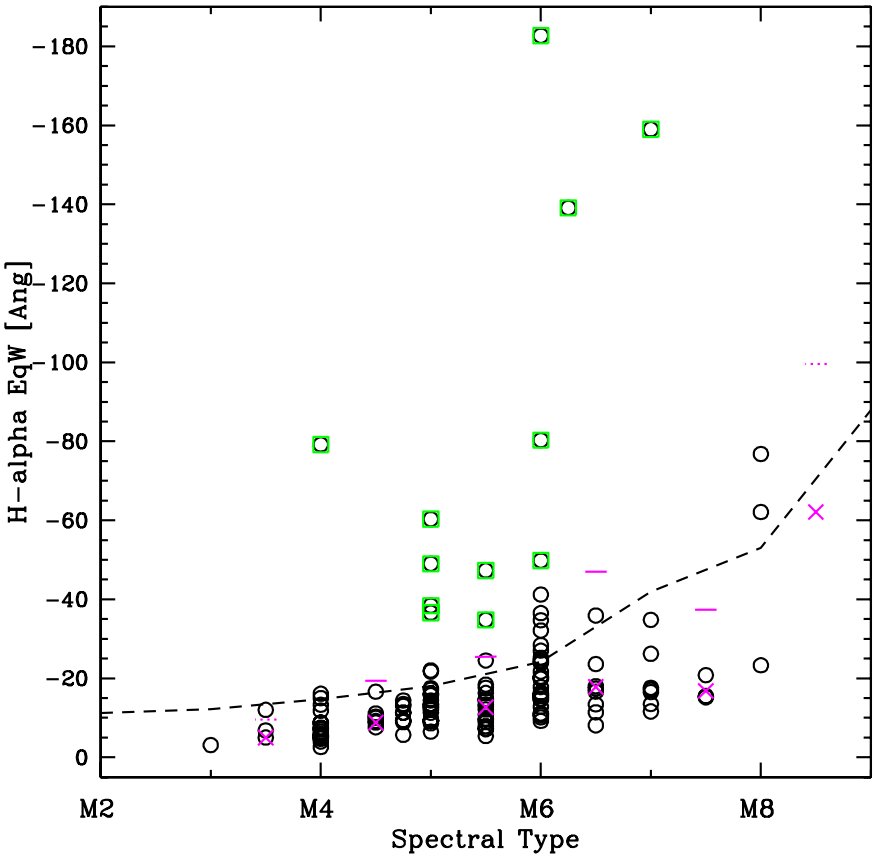

Figure 5.3 Measured Hα equivalent widths for all new USco members as a function of spectral type. The dotted line is the empirical accretor/nonaccretor upper limit derived by Barrado y Navascués & Martín (2003). Magenta X's represent the median $W(H\alpha)$ for each spectral type. Magenta -'s are 3 sigma upper limits above the median. Objects boxed in green are considered to be actively accreting.

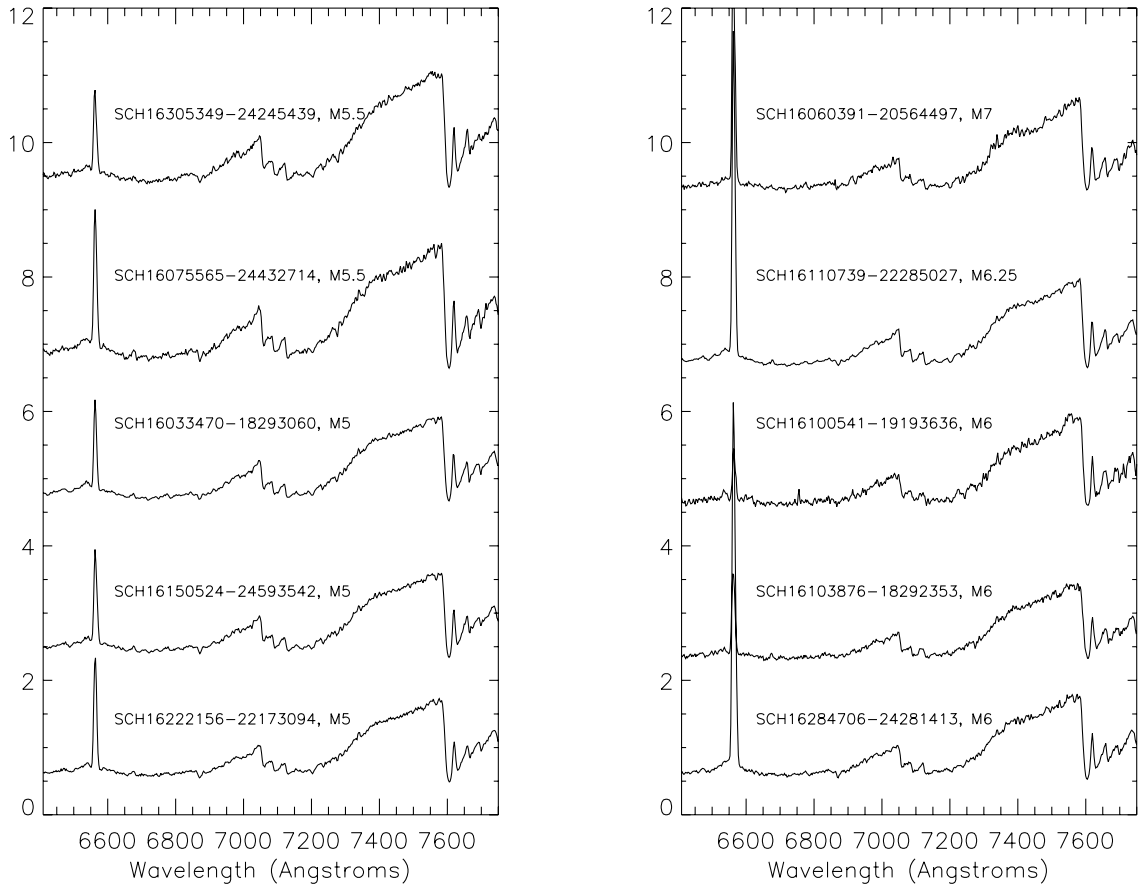

Figure 5.4 Spectra of the 10 stars determined to be accreting (as defined in §5.3.3) that were observed at Palomar, shown in order of spectral type.

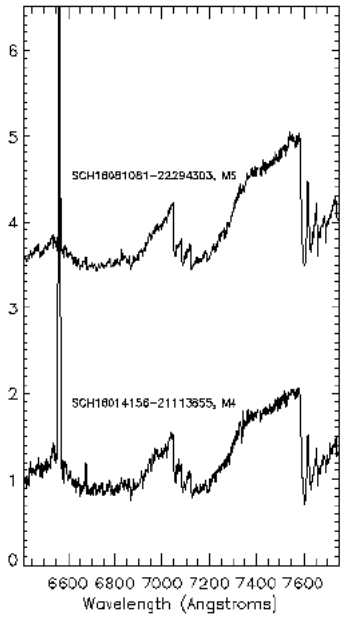

Figure 5.5 Spectra of the 2 stars determined to be accreting (as defined in §5.3.3) that were observed at CTIO, shown in order of spectral type.

Myr. This conclusion is consistent with a median accretion lifetime of ∼2–3 Myr for higher mass stars (Haisch et al. 2001, Hillenbrand 2005).

5.3.4 Spatial Distribution of Low Mass Stars

Figure 5.6 shows the 2D spatial distribution for the 120 known high mass members of USco dentified in the Hipparcos survey. This sample represents the complete population of known members more massive than ∼1 $M_{\odot}$. Thus, I define the boundaries of the Hipparcos stars to represent the boundaries of the USco high mass population. The density of high mass stars is roughly constant from $237 \lesssim \alpha \lesssim 249$ deg and peaks at $\delta \sim$ -24 deg. Contours show the percentage of the 243 spectroscopically observed candidates determined to be bona fide USco members. As can be seen, despite the large area of my Quest-2 survey (shown as a black box), it still only covered a minority of the total association. New members were identified only within the central $\sim 11^o$ in RA and the Northern $\sim 11^o$ in DEC.

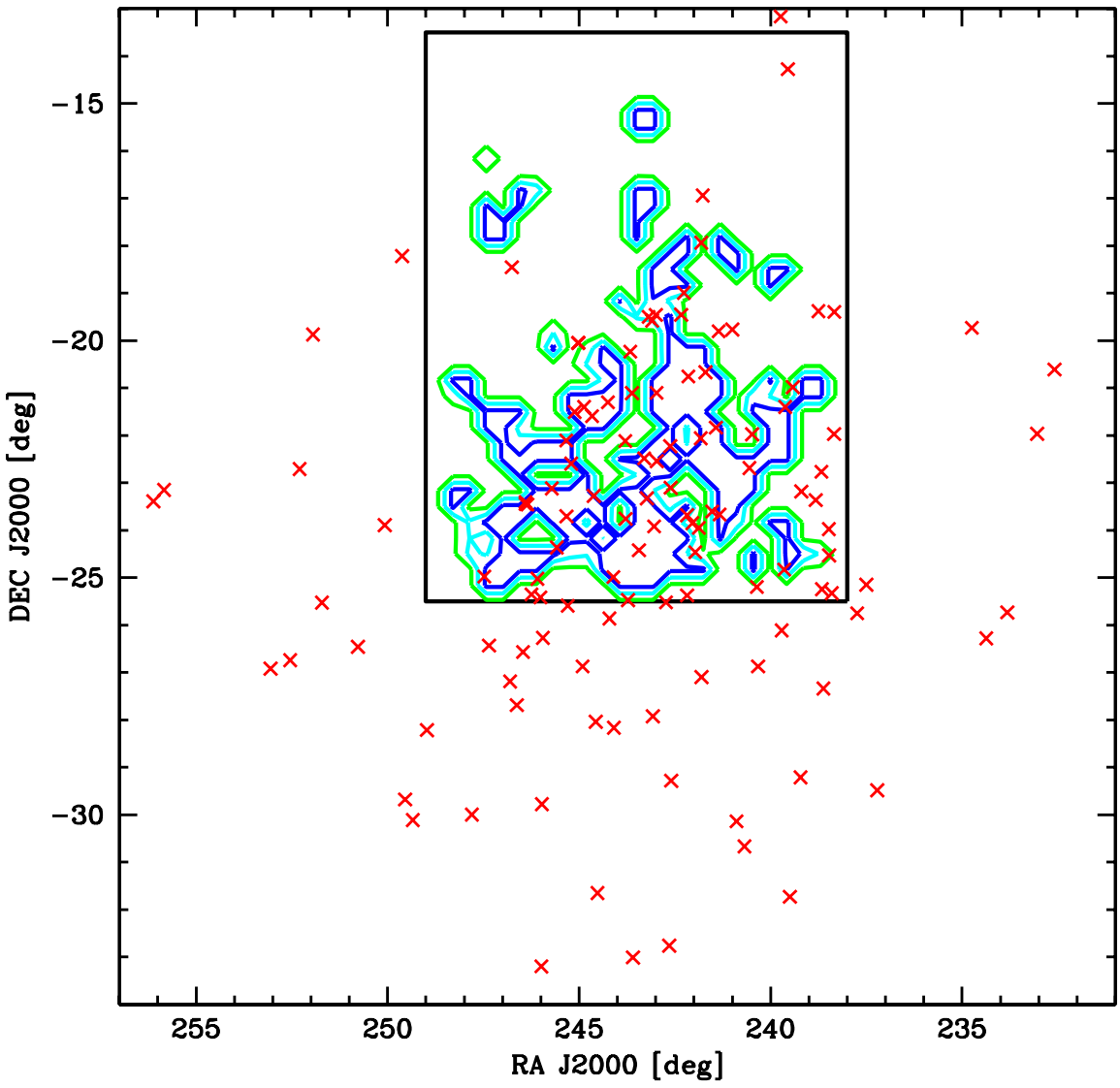

Figure 5.6 Spatial distribution of the 120 known Hipparcos members of USco (red X's) together with a contour plot showing the percentage of Quest-2 candidates observed spectroscopically that were determined to be new low USco members. Contours are shown at 90% (blue), 50% (cyan), and 10% (green) of the peak value. The Quest-2 survey area is shown in black.

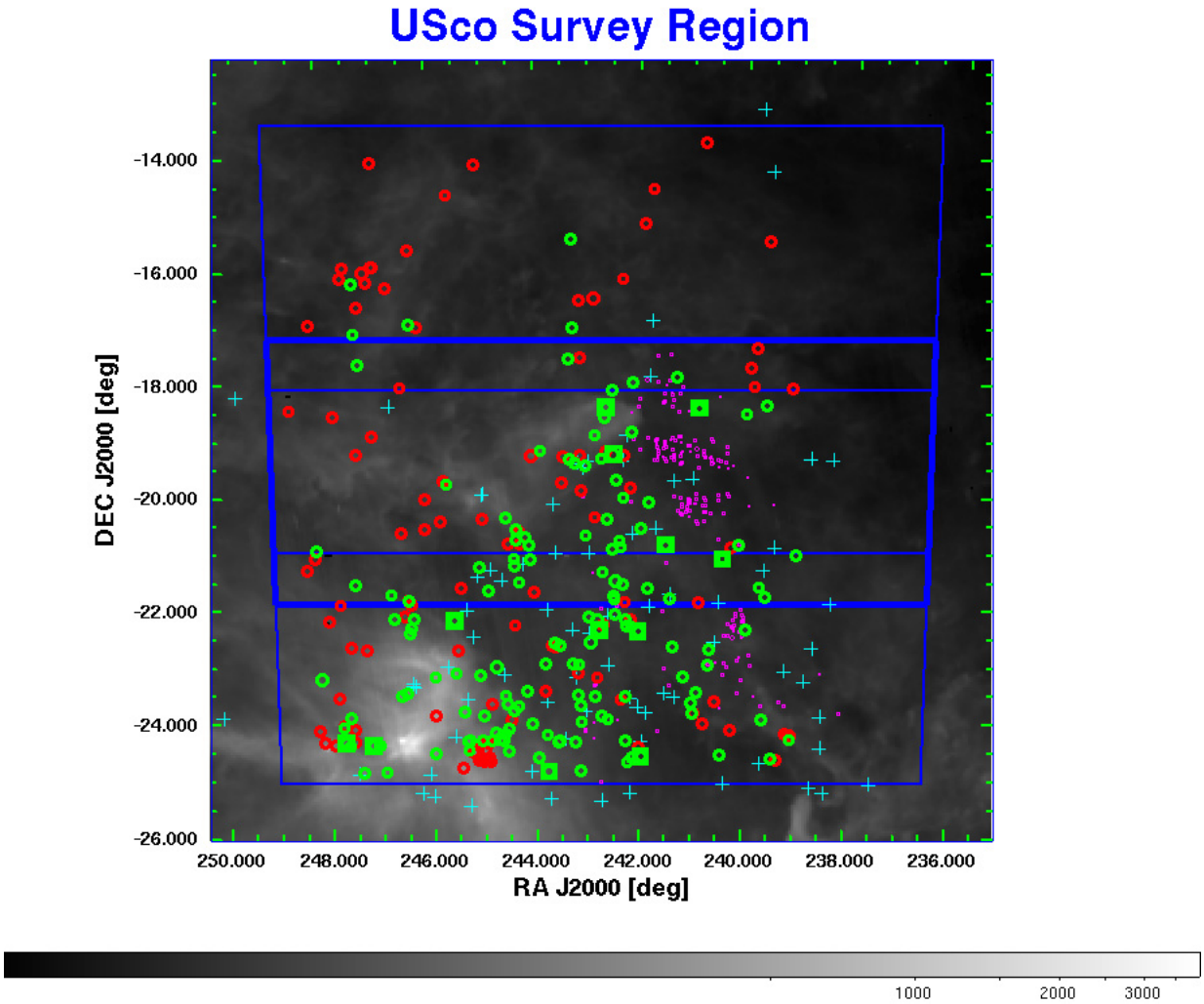

Figure 5.7 Spatial distribution of the USco survey area outlined in blue, overlaid on IRAS 100μm emission. The thicker blue line denotes the outline of the monitoring scan region which was repeated 24 times. New USco members identified from this work (145; green circles) are shown with previously known, spectroscopically confirmed low mass members (196; Sp Type $\geq$K7 corresponding to M $\leq$0.6 $M_{\odot}$ at 5 Myr; small magenta circles) from the literature (see text), high mass Hipparcos members (120; cyan pluses) and spectroscopic targets determined to be field dwarfs (98; red circles). The 12 new members which exhibit Hα excess emission are boxed.

Figure 5.7 shows the spatial distribution of observed spectral candidates overlaid on an IRAS 100μm emission map. New USco members identified from this work are shown with previously known, spectroscopically confirmed low mass members from the literature, high mass Hipparcos members and spectroscopic targets determined to be field dwarfs. The 12 new members that exhibit Hα excess emission are boxed. In general, the low mass PMS stars presented here share a common spatial distribution with the high mass Hipparcos members. Efforts to observe northwest of the Hipparcos stars largely yielded reddened field dwarfs rather than young association members. Figure 5.8 shows 1D spatial distributions for the 145 low mass association members discussed here (green line), together with those for the 56 Hipparcos stars that fall within my survey area (black line). The densities of both populations fall off sharply from -24^o at the association center to its northern edge. Figures 5.9 and 5.10 show histograms as a function of RA (figure 5.9) and DEC (figure 5.10) of the total number of candidates observed spectroscopically compared to the number determined to be bona fide USco members. Bottom panels show the percentage of observed candidates determined to be USco members as a function of RA and DEC. From figure 5.8, I conclude that the density of low mass association members found in the Quest-2 survey peaks at α $\sim$242^o and δ $\sim$ -25^o with stellar densities falling off beyond these values. Based on figures 5.6 and 5.10, my survey extended past the association's edge only at its northern boundary, which occurs at $\sim$-15^o (see figure 5.10).

5.4 Summary

I have completed a large-area *gri* photometric survey in and near the Upper Scorpius region of recent star formation. From these data I selected candidate new PMS association members based on their optical and near-infrared colors and magnitudes. I present in this chapter results from my spectroscopic follow-up campaign. I observed a total of 243 candidates at either Palomar or CTIO, and determined 145 ($\sim$60%) to be bona fide new Upper Scorpius members. I derive an HR diagram for new members and identify a possible unresolved binary. I measure Hα emission for all new members

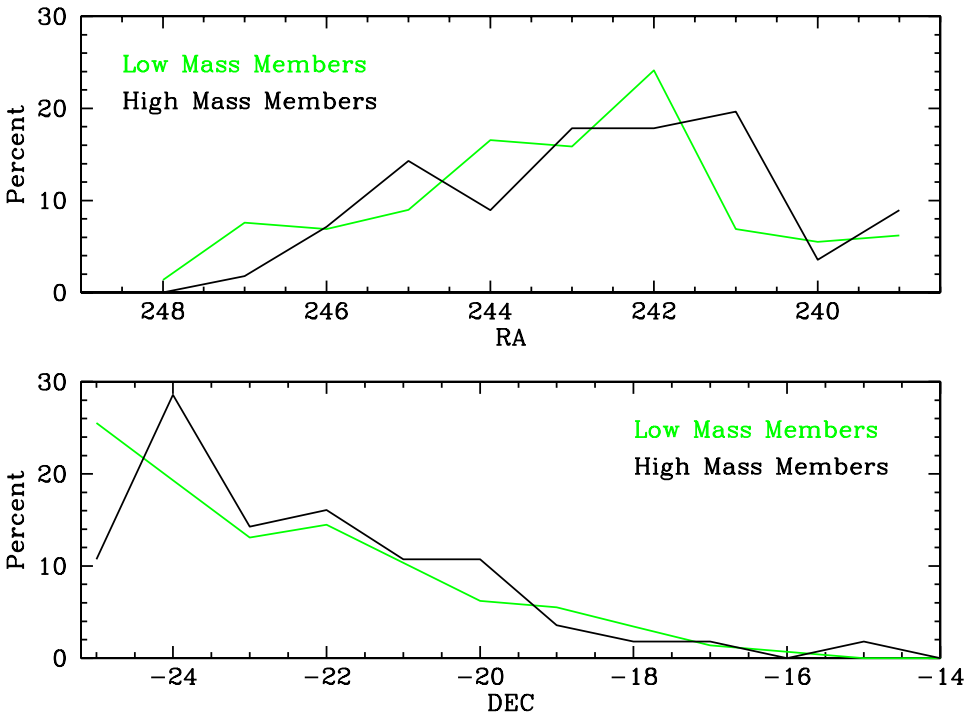

Figure 5.8 Top panel shows the percentage of the 145 low mass stars discussed in this work that lie at a given RA (green) together with same information for the 56 high mass Hipparcos stars found in the Quest-2 survey area (black). Bottom panel illustrates the same information as a function of DEC.

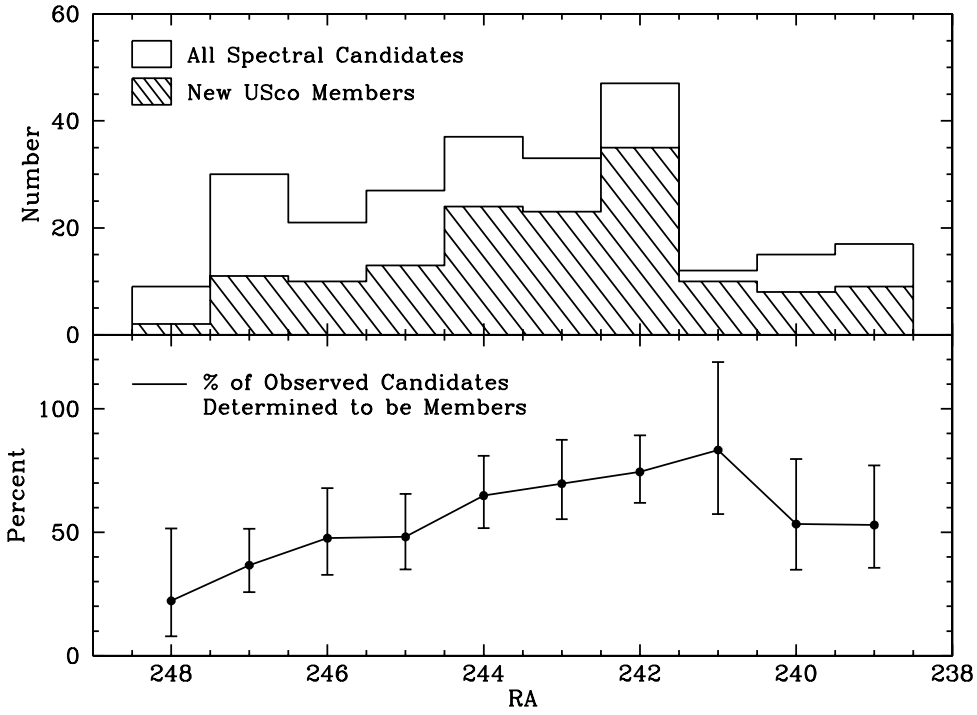

Figure 5.9 Top panel contains a histogram of RA values for all candidates in USco observed spectroscopically (open histogram) and for those observed candidates determined to be bona fide members (hatched histogram). Bottom panel shows the percentge of observed candidates determined to be USco members as a function of RA.

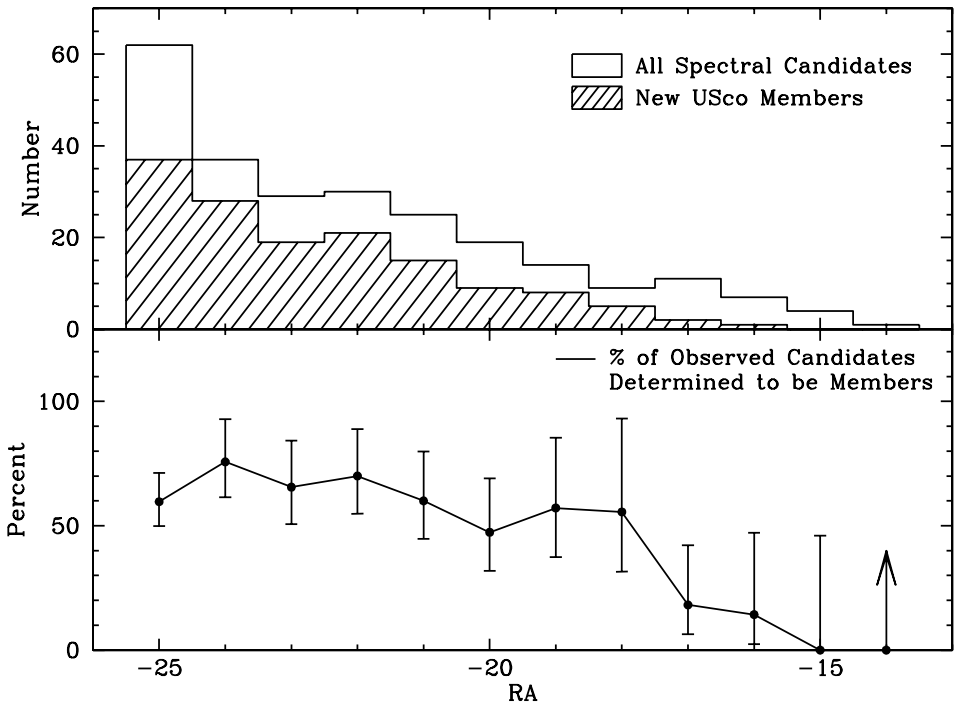

Figure 5.10 Top panel contains a histogram of DEC values for all candidates in USco observed spectroscopically (open histogram) and for those observed candidates determined to be bona fide members (hatched histogram). Bottom panel shows the percentage of observed candidates determined to be USco members as a function of DEC. The right-most point at DEC=-14 is drawn as an arrow because 0 out of 1 observed stars were determined to be PMS stars. Thus, due to small number statistics, the errorbar is larger than the plot.

and determine 12 of the 145 low mass stars and brown dwarfs in the 5 Myr USco association are still accreting. Based on comparison of the spatial distributions of low and high mass association members, I find no evidence for spatial segregation in USco within the northern portion of the association.

Part II:
Mass and Age Distributions in Young Associations

Chapter 6

Age and Mass Distributions for Low Mass Members of Young Clusters and Associations[1]

Much progress has been made within the past several decades towards our understanding how isolated stars are created. In its basic form, our current view today of isolated star formation is not substantially different from that put forth by Shu et al. (1987). However, as discussed in chapter 1, most stars do not form in isolation, they form in groups, and many details of this process remain unexplained. In particular, how and why do molecular clouds contract at particular sites to form stellar groups? What determines whether a particular star formation site will become a sparse Taurus-like association, a bound cluster such as the Orion Nebula Cluster, or an expanding OB association similar to USco? Do all members of a single star-forming group form in a single burst or is star formation a lengthy process?

In this chapter, I address some of these questions by assessing the age distributions of young star-forming regions. A useful tool in understanding the distribution of ages within a group of stars is the HR diagram. Once each object's spectral type and photometry is measured, those values can be combined to derive values for its luminosity and effective temperature and place it on a theoretical HR diagram. Using theoretical pre-main sequence evolutionary tracks, temperatures and luminosities can be transformed into ages and masses. Thus, I can use the HR diagram for USco

[1] A modified version of § 6.1 has been published previously as Slesnick, Hillenbrand, & Carpenter 2004, ApJ, 610, 1045.

derived in chapter 5 to derive the age distribution for low mass members of this OB association. My survey in Taurus identified tens of previously unknown intermediate-age PMS stars (several megayears older than the known Taurus population), but the relationship of these stars to the Taurus association remains ambiguous until follow-up studies can be completed (see §4.5). Therefore I can not use an HR diagram for this population to derive ages in an equivalent manner.

However, during my time at Caltech prior to my work on the Quest-2 surveys, I carried out a study to assess the star formation history of another young star-forming region, the Orion Nebula Cluster (hereafter ONC). The ONC is an ideal region in which to address questions relating to star formation in clusters because it contains >3000 members across a range of spectral types from O stars to brown dwarfs. It is also the nearest massive cluster to the sun (∼480 pc; Genzel et al. 1981). Thus, for the remainder of this chapter, I will assess and compare the star formation histories of the USco OB association and the embedded Orion Nebula Cluster. For the purpose of this discussion, I present only the analysis section of my work in the ONC, not the full study. Observational details for this survey can be found in Slesnick et al. (2004).

Another unanswered question fundamental to the theory of star formation within a stellar group is whether the distribution of stellar masses formed during a single epoch within an association or cluster, also known as the initial mass function (IMF), is universal or whether it varies with either star formation environment or time. We believe we understand the basic structure of the field star IMF at 'normal' stellar masses above ∼0.5 $M_\odot$ and below ∼10 $M_\odot$. In this mass range the field star IMF is generally well characterized by a power law slope $dN/dM \propto M^{-2.35}$, as derived originally by Salpeter (1955). However, while the shape of the *stellar* mass function is relatively well known, we are still struggling to understand the very low mass end of the distribution into the substellar regime. For stars and brown dwarfs less massive than ∼0.4–0.5 $M_\odot$, the shape of the mass function remains ambiguous and may be strongly dependent on the environment within the parental molecular cloud. Young stellar clusters and associations are particularly valuable for examining the shape of the low mass IMF because contracting low-mass pre-main sequence stars and brown

dwarfs are 2-3.5 orders of magnitude more luminous than their counterparts on the main sequence, and thus can be more readily detected in large numbers. Furthermore, the lowest mass members of young stellar groups have not yet been lost to dynamical evolution.

In addition to discussing the age distributions of the ONC and USco populations in this chapter, I use derived HR diagrams to examine the low mass IMFs of each star forming region. I will first discuss my work in the ONC. Second, I use the HR diagram derived in chapter 5 to determine an IMF for low mass stars and brown dwarfs in the USco region. Because I do not believe that all of the new PMS stars identified near Taurus are related to the known young subgroups, I do not attempt to use these stars to derive an IMF for Taurus from my data. Instead, I compare my results for USco and the ONC to results published in the literature for Taurus and for other young regions.

6.1 Age/Mass Distributions of the Low Mass Population in the ONC

The ONC is one of the nearest massive star-forming regions to the Sun and the most populous young cluster within $\sim$2 kpc. Thus, it has been observed at virtually all wavelengths over the past several decades. However, only recently have increased sensitivities due to near-IR detectors on larger telescopes allowed us to begin to understand and characterize the extent of the ONC's low mass stellar and brown dwarf population which, at $\lesssim$ 1-2 Myr, is just beginning to emerge from its giant molecular cloud.

Several recent studies have explored the ONC at substellar masses. Hillenbrand & Carpenter (2000) (hereafter HC00) present the results of an H and K imaging survey of the inner 5'.1 x 5'.1 region of the ONC. Observed magnitudes, colors, and star counts were used to constrain the shape of the ONC mass function across the hydrogen burning limit down to $\sim$0.03 $M_{\odot}$. They find evidence in the log-log

mass function for a turnover above the hydrogen-burning limit, then a plateau into the substellar regime. A similar study by Muench et al. (2002) (hereafter M02) uses J, H, K imaging of the ONC to derive an IMF which rises to a broad primary peak at the lowest stellar masses between 0.3 $M_\odot$ and the hydrogen burning limit before turning over and declining into the substellar regime. However, instead of a plateau through the lowest masses, M02 find evidence for a secondary peak between 0.03 and 0.02 $M_\odot$. Luhman et al. (2000) use H and K infrared imaging and limited ground-based spectroscopy to constrain the mass function and find a similar peak just above the substellar regime, but then a steady decline through the lowest mass objects.

Generally speaking, J, H, K photometry alone is insufficient for deriving stellar/substellar masses, though may be adequate in a statistical sense for estimating mass distributions given the right assumptions. The position of a young star in a near-IR color-magnitude diagram (CMD) is dependent on mass, age, extinction, and the possible presence of a circumstellar disk. These characteristics affect the conversion of a star's infrared magnitude and color into its stellar mass. Unless the distributions of these parameters are known a priori, knowledge of the cluster's luminosity function alone is not sufficient to draw definitive conclusions about its mass function. In addition, cluster membership is often poorly known and statistical estimates concerning the extent and characterization of the field star population must be derived. In the case of the densely populated ONC, it has been suggested that the field star contamination is small but negligible toward fainter magnitudes. HC00 used a modified version of the Galactic star count model (Wainscoat et al., 1992) convolved with a local extinction map (derived from a $C^{18}O$ molecular line map) to estimate the field star contribution, which they found to constitute $\sim$5% of the stars down to their completeness limit at $K \sim 17.5$.

In order to study a cluster's IMF in more than just a statistical sense, spectroscopy is needed to confirm cluster membership of individual stars and uniquely determine location in the HR diagram (see chapter 3). Candidate substellar objects were selected from the HC00 photometric survey for follow-up spectroscopy to determine if their temperatures and surface gravities are consistent with those of brown dwarf objects

at the age and distance of the ONC. I, along with Lynne Hillenbrand and John Carpenter, obtained new infrared spectra of 97 objects within the ONC; 81 selected from the HC00 work were observed using NIRSPEC and 16 selected from the optical magnitudes and colors of Hillenbrand (1997) (hereafter H97) were observed using CRSP. The sample included ∼50% of the stars in the HC00 survey area expected to be brown dwarfs based on their $K, (H-K)$ magnitudes and colors, down to the completeness limit of K ∼17.5. From the NIRSPEC data, I classified 71 objects in the inner ONC found to be of spectral type K7 or later, ∼50% of which are M6 or later. At an age of 1-2 Myr, all objects with spectral types later than M6 are substellar (M < 0.08 $M_\odot$) based on comparison with theoretical models (e.g., D'Antona & Mazzitelli 1997; hereafter DM97). In addition, 16 spectra of objects in the inner and outer parts of the nebula were taken with CRSP, 9 of which were classified M6 or later. A few spectral types from new optical LRIS data are also included in this analysis.

6.1.1 HR Diagram for Substellar Objects in the ONC

In figure 6.1 I present an HR diagram for those objects within the inner 5.'1 × 5.'1 of the ONC (survey area of HC00) for which new spectral types were obtained. Surface gravity assessment is indicated and a typical error bar for an M6±1.5 star is shown in the lower left corner. The pre-main-sequence model tracks and isochrones of DM97 are also shown. Figure 6.1 illustrates that this survey probes lower masses than previous spectroscopic studies have, down to 0.02 $M_\odot$.

From examination of figure 6.1, it appears that this survey explored two separate populations: the inner ONC at $\lesssim$1 Myr, and an older population at ∼10 Myr. None of the members of this apparently older population have gravity features which indicate they might be foreground M stars. Spectra of these objects indicate instead that they have low surface gravity consistent with young objects, and are therefore also candidate cluster members. For the remainder of §6.1.1, I discuss the possible explanations for this surprising population. First, I detail possible systematics in the data reduction/analysis which could, in principle, cause one to "create" older stars

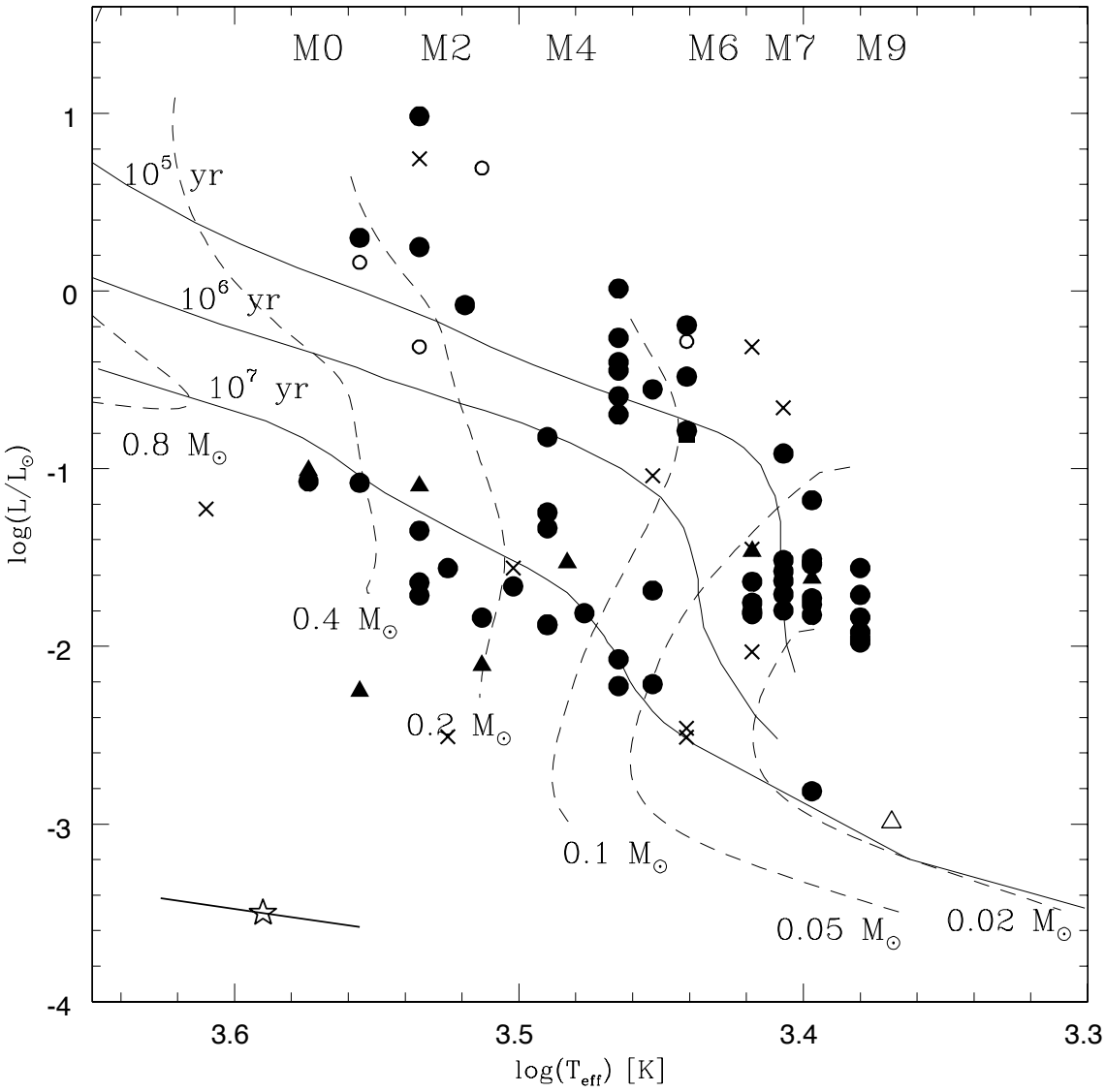

Figure 6.1 HR diagram of objects within the inner 5.'1 × 5.'1 of the ONC (survey area of HC00) for which I have new spectral types. Filled symbols correspond to stars classified using NIRSPEC and CRSP infrared observations which have good spectral types. Objects that were classified as "high" gravity (i.e., had strong absorption lines, similar in strength to dwarf stars of the same temperatures) are marked as open symbols and objects with less certain spectral types are marked as X's. Triangles represent objects which have new optical spectral types taken with LRIS. A typical error bar for an M6±1.5 star is shown in the lower left corner. The pre-main-sequence model tracks and isochrones of DM97 are also shown.

in the HR diagram. Next I discuss their possible origin if they are a real feature, and finally I determine why they may not have been detected in previous studies.

There are two possible reasons one might erroneously detect a bifurcation of the HR diagram: either the spectral types are in error and the objects are actually cooler than they are shown to be here, or their luminosities have been underestimated. A full description of how stars were placed in the HR diagram is given in Slesnick et al. (2004). The photometric uncertainties for these objects are <0.2 mag for both H, K in the HC00 data and < 0.4 mag for J, H, K in the M02 data. The two data sets agree to within 0.8 mag for all objects and variability, if present, is expected to be $\sim$0.2 mag (Carpenter et al., 2001). An object with spectral type M2 would need to be $\sim$3 magnitudes brighter in K, or have its extinction underestimated by >30 mag in order to move on the HR diagram from the 10 Myr isochrone to the 1 Myr isochrone. Even taking into account the above uncertainties and possible variability, errors of this magnitude are not possible. Moreover, if the photometry were in error, the expected result would be continuous scatter in the HR diagram, rather than two distinguishable branches.

The other way to account for the apparently older population through error is if the temperature estimates are too hot, i.e., the spectral types too early, in some cases by as much as 7 spectral subclasses. All spectra have been checked visually, by both me and my advisor Lynne Hillenbrand to ensure accurate classification, and I believe the spectral types are robust to $\pm$1 subtype. None of the possible biases resulting from assumptions made regarding veiling, extinction or gravity can have a large enough effect to produce a spectral type offset of this magnitude (see Slesnick et al. 2004). One possible exception is that a mid-M (M5) K-band spectrum with high reddening can have the same appearance and classification band index measurements as a later-M (M7) spectra with intermediate reddening. But this phenomenon could only affect a small subset of the lower branch population. Therefore, while it may reduce slightly the number of apparent older objects, it cannot correct for them entirely.

The accuracy of the spectral types is supported by the excellent agreement of the near-IR spectral classifications with existing optical spectral types, when present

(most agree to within 2 spectral subclasses). A significant fraction of the spectra taken with LRIS (filled triangles on figure 6.1), which were classified in a completely independent manner from the NIRSPEC and CRSP data, also resulted in several apparently 10 Myr old stars. If the older population arises from systematics in the reduction or spectral classification of the infrared spectra, it would not be expected that stars classified optically would fall on the same place in the HR diagram.

If we are to accept the bifurcation as a real feature in the HR diagram, several scenarios could, in principle, account for it. The first is contamination from foreground field stars. However, as mentioned, HC00 found the expected field star contribution to be only ∼5% down to the completeness limit of K∼17.5. whereas the apparent low luminosity population accounts for a much larger fraction ($\sim \frac{1}{3}$) of my sample. The second possibility is that there is contamination by a foreground population of M stars, however it does not originate from the field but from the surrounding OB association. The ONC (also known as Orion subgroup Id) is neighbored by three somewhat older subgroups of stars (Ia, Ib, & Ic; see Brown et al. 1994 for a detailed description of each) which are located at distances ranging from ∼360 to 400 pc and having ages (derived from high mass populations) from ∼2 to 11.5 Myr. The most likely subgroup which could contribute contamination to the survey data is subgroup Ic, which is located along the same line of sight as the ONC. However, its members are thought to be only ∼2 Myr old and therefore cannot account for the stars on the lower branch in the HR diagram unless their age estimate is in error. The only known part of the OB association which could be contributing ∼10 Myr old stars to the study is subgroup Ia, which is estimated to be ∼11.4 Myr.

While the known high mass population of the Ia subgroup does not extend spatially as far as the ONC, if there has been dynamical relaxation, it is possible that its lower mass members may occupy a more widespread area than the OB stars. Brown et al. (1994) found the initial mass function for the subgroups to be a single power law of the form $\xi(\log M) \propto M^{-1.7\pm0.2}$ based on the high mass population ($M > 4$ $M_\odot$). Since the lower mass members have not yet been identified or studied in detail, I extrapolate the high-mass IMF to determine the total number of stars in subgroup

Ia expected down to 0.02 $M_\odot$ and find there should be ∼3500 members. This number is an upper limit since I have not applied a Miller-Scalo turnover to the IMF but simply extended the power law form. The angular size of the Orion Ia subgroup as studied by Brown et al. (1994) corresponds to a linear size of ∼45 pc. From this information I calculate a relaxation time for the cluster

$$t_{relax} = n_{relax} \times t_{cross} = \frac{8 \ln N}{N} \times \frac{R}{\sigma}.$$

Assuming a gravitationally bound cluster and a velocity dispersion of σ ∼2 km s^{-1} consistent with the ONC (Jones & Walker, 1988), I find a crossing time for the Orion Ia cluster of ∼11 Myr and a relaxation time of ∼600 Myr. Clearly the cluster is not yet dynamically relaxed and it is unlikely that its low mass population would have spread significantly past its higher mass members. This calculation does not however, rule out the possibility that the lower mass population formed over a wider spatial area than the massive stars, given that primordial mass segregation has been suggested in other young clusters (Hillenbrand & Hartmann, 1998).

From the same IMF extrapolation I find the surface density of 0.5-0.02 $M_\odot$ objects in subgroup Ia to be ∼2.5 pc^{-2}. The areal extent corresponding to the angular size of our survey region (assuming a distance of 480 pc) is ∼0.5 pc^2. Assuming a constant surface density across this area, it is expected that <2 members of Orion Ia would be found in the current work. Even if I ignore previous age estimates, assume all three of the subgroups could be contributing to the observed lower branch of the HR diagram, and repeat the above calculation for subgroups Ib & Ic, I would expect to see < 10 stars total. Therefore, it is unlikely that the lower branch seen in the inner ONC HR diagram is purely due to contamination from surrounding populations. I cannot rule out that there may exist a foreground population of ∼10 Myr stars which is not associated with the ONC, but which was missed by the Brown et al. (1994) work due to its dirth of OB stars. However, the probability that this population would lie in exactly the same line of sight as the ONC is small.

Another possible cause of the older branch of the HR diagram is scattered light

from circumstellar disks and envelopes. Most of the objects in the lower branch of the HR diagram have $(J-H)$,$(H-K)$ near-infrared excesses consistent with their being young objects surrounded by circumstellar material which could result in their detection primarily in scattered light. If true, extinctions, and consequently luminosities for these objects would be underestimated, making them appear older than the bulk of the population. Similar arguments have been put forth by Luhman et al. (2003b) to explain low-lying stars on the HR diagram of IC 348. One uncertainty in this argument is that if scattered light is responsible for causing the apparently older population, it would have to be acting on the observations in such a way so as to create a dichotomy of object luminosities rather than a continuous distribution of stars at unusually faint magnitudes. This scenario could occur however, if the lower luminosities measured for this population are caused by a drop in observed light due to the objects being occulted by a disk. The relatively low luminosities of substellar objects would make such systems more difficult to detect and we may be observing the brighter end of a distribution of low mass scattered light sources. In support of this argument, one of these sources is coincident with an optically identified *Hubble Space Telescope* "proplyd" (which is known to be a photoevaporating circumstellar disk), and two with disks seen optically in silhouette only (Bally et al., 2000).

If the lower luminosity population in the inner ONC is real, rather than due to systematics in the data reduction/analysis or contamination from the surrounding older association, the question arises as to why it was not seen in previous surveys. The deepest optical photometric survey in this inner region is that by Prosser et al. (1994) which is reported complete to V≈20 mag and I≈19 mag, though no details are given on how these numbers were derived or how they might vary with position in the nebula. One can view the photometric data of H97, which is a combination of ground-based CCD photometry out to 15' from the cluster center and the Prosser et al. (1994) HST CCD photometry in the inner 3' or so, in terms of color-magnitude diagrams binned by radial distance from the cluster center. At all radial distances there are some stars which sit low in the color-magnitude diagram. However, it is only in radial bins beyond ∼7' that a substantial population (though still disproportionately small

compared to the current findings) of apparently 10 Myr old low mass (0.1-0.3 $M_\odot$) stars begins to appear, as might be expected if they are contaminants from the Orion Ic association. The inner radial bins do not display this population, though it should have been detected at masses larger than 0.15 $M_\odot$ *in the absence of extinction.* Notably the apparently 10 Myr old population in figure 6.1 does not lack extinction. Figure 6.2 shows a histogram of extinction for sources included in figure 6.1. The open histogram indicates all objects; the hatched and shaded histograms include only the 1 and 10 Myr old populations, respectively. I find all three populations to have similar, roughly constant distributions for $A_K \lesssim 0.6$ ($A_V \lesssim 10$) giving further evidence that the lower luminosity branch of the HR diagram is likely not a foreground population. Accounting for typical errors ($\sim$0.1 mag at K and $\sim$1.5 mag at V; see Slesnick et al. 2004) will not change my conclusions. For extinction values larger than $\sim$2 visual magnitudes the 0.15-0.5 $M_\odot$ stars at 10 Myr in figure 6.1 would have been missed by the optical Prosser et al. (1994) photometric survey but uncovered in later infrared surveys. Further, Walker et al. (2004) find from theoretical work a lower incidence of disk occultation for higher mass classical T Tauri stars ($\sim$20% of systems with disks) in comparison to lower mass substellar objects (up to $\sim$55% of systems with disks) due to smaller disk scale heights and less disk flaring. Therefore, if the low luminosity objects are a population of scattered light sources smaller numbers of them may be expected at higher masses.

6.1.2 The ONC's Low-Mass IMF

Currently, there are relatively few sets of pre-main-sequence (PMS) evolutionary models which extend into the substellar regime. The Lyon group (Baraffe et al. 1998 & Chabrier et al. 2000; hereafter BCAH98) calculations cover 0.001–1.2 $M_\odot$, but do not extend to the large radii of stars younger than 1 Myr. Thus, they must be applied to young low-mass star forming regions with caution. The other widely utilized set of low-mass PMS models are those by DM97. These models cover 0.017–3.0 $M_\odot$ over an age range of 7×10^4 yr to 100 Myr, and are therefore representative of even extremely

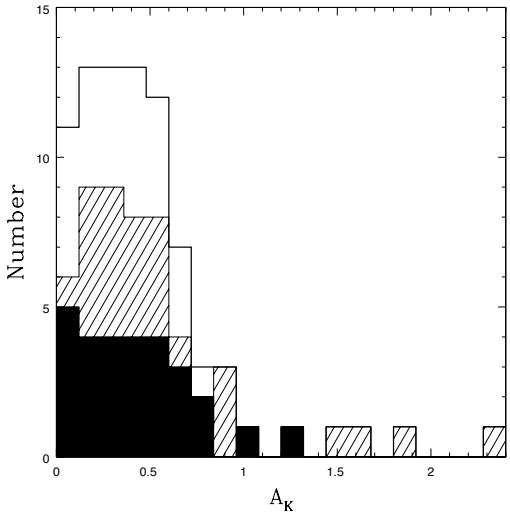

Figure 6.2 Histogram of extinction for sources included in figure 6.1. The open histogram indicates all objects; the hatched and shaded histograms include the two populations with apparent ages (as interpreted from the HR diagram) of ∼1 and ∼10 Myr old, respectively. Similar extinction distributions are found for all three populations.

young regions. A detailed analysis and comparison of the models is given by Hillenbrand & White (2004). For the purpose of the current work I use DM97 tracks and isochrones to determine masses and ages for stellar and substellar objects in our HR diagram.

Because the ONC is highly crowded and extremely nebulous, it is important to determine that the spectroscopic sample is representative of the population as a whole before using the sample to construct a cluster mass function. Figure 6.3 shows a histogram of completeness as a function of magnitude. Open and hatched histograms indicate the distribution of HC00 photometry and of sources for which I have spectral types, respectively. The hatched histogram includes not only sources for which I determined new spectral types, but also optically classified sources from the literature (H97 and references therein) which fall within the survey region and were determined to be of spectral type M0 or later. In combining the two data sets the goal is to assemble a statistically large sample of cool, spectroscopically confirmed ONC members down to extremely low masses (M ∼0.02 $M_{\odot}$) from which to create the IMF.

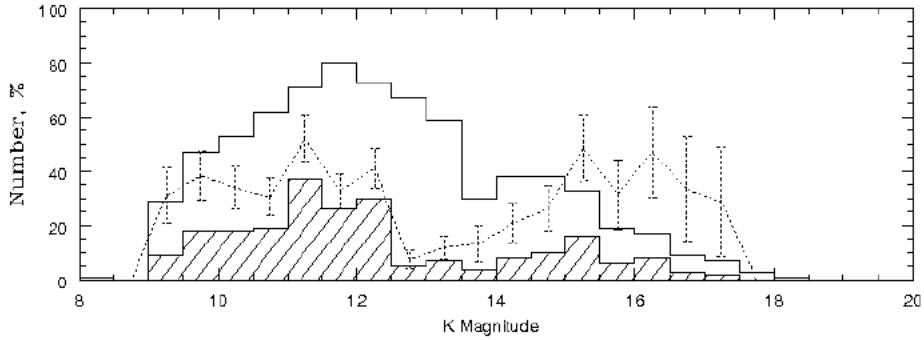

Figure 6.3 Histogram of HR diagram completeness as a function of magnitude. Open and hatched histograms indicate the distribution of all HC00 photometry and the subset for which we have spectral types, respectively. The dotted line in each panel indicates fractional completeness of the spectroscopic sample with $\sqrt{(N)}$ errorbars. Although the spectroscopic sample is ∼40% complete at bright and faint magnitudes, correction factors to the mass function are needed at intermediate magnitudes.

The dotted line in figure 6.3 indicates fractional completeness with $\sqrt{(N)}$ errorbars. I estimate that the stars included in figure 6.1 are ∼40% complete across the entire magnitude range with the exception of the $12.5 < K < 15$ bins. Undersampling at these intermediate magnitudes is caused by combing the sample of brighter, optically classified, mainly stellar objects with my sample of infrared-classified objects where the aim was to observe objects fainter than the substellar limit. Therefore, magnitude bins corresponding to masses near the hydrogen burning limit are underrepresented. I can correct for this deficiency by determining the masses which correspond to objects in the depleted magnitude bins. I then add stars to those mass bins according to the fractional completeness of the magnitude bins they came from, relative to the overall 40% completeness. I discuss both the corrected and corrected IMFs below.

Figure 6.1.2 shows the mass function for stars within the inner 5.'1 × 5.'1 of the ONC that have spectral types derived from either infrared or optical spectral data later than M0. The thick-lined open histogram, shown with $\sqrt{(N)}$ errorbars, includes all stars meeting this criteria which were not determined to have high surface gravity. In total, the IMF sample includes ∼200 stars and contains objects with masses as

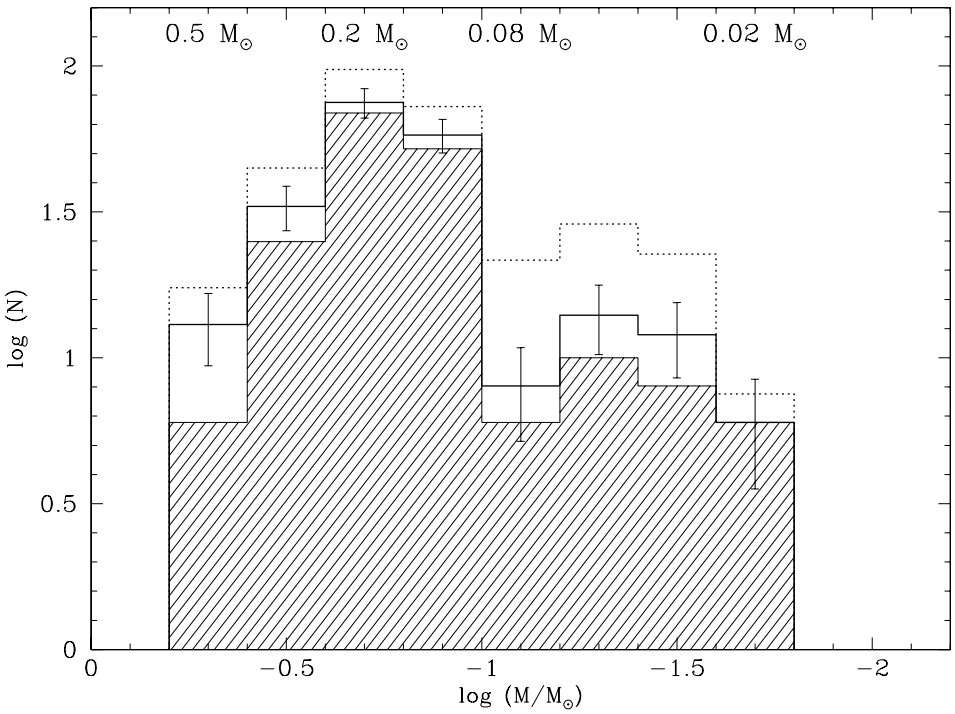

Figure 6.4 Mass function for all stars within the inner 5.'1 × 5.'1 of the ONC that have spectral types from the present work or the literature later than M0. Thick-lined open histogram shown with $\sqrt{N}$ errorbars indicates all stars; the dotted open histogram represents the same sample corrected for incomplete magnitude bins (figure 6.3). The hatched histogram indicates only stars younger than ∼5 Myr according to the HR diagram (figure 6.1).

high as ∼0.6 $M_\odot$ and as low as <0.02 $M_\odot$. Mass completeness (to the 40% level) extends from ∼0.4 $M_\odot$ (corresponding to an M0 star at 1 Myr; see figure 6.1) to the completeness limit of HC00, ∼0.03 $M_\odot$ for $A_V < 10$. The dotted open histogram indicates an IMF for the same sample, where I have corrected for the incomplete magnitude bins. The most substantial correction occurs right at the substellar limit as indicated above. The hatched histogram represents only those objects determined to be younger than 5 Myr from HR diagram analysis; thus, I remove any possible bias occurring by inclusion of the apparently older ∼10 Myr population which may or may not be a real part of the cluster. As can be seen, the apparently older stars constitute a relatively uniformly spaced population across the mass range I am exploring (see also figure 6.1), and including them in the IMF does not affect the interpretation.

The stellar-substellar IMF for the inner ONC in figure 6.1.2 peaks at ∼0.2 $M_\odot$ and falls across the hydrogen-burning limit into the brown dwarf regime. Using the observed IMF, I find ∼17% (39) of the objects in my sample to be substellar ($M <$ 0.08 $M_\odot$). Below ∼0.08 $M_\odot$ the mass distribution levels off through the completeness limit of ∼0.02 $M_\odot$. There may be a secondary peak at ∼0.05 $M_\odot$, but it is not statistically significant. Decreasing the bin size by 50% yields the same results, with the peak at 0.05 $M_\odot$ becoming even more pronounced. Increasing the binsize by 50% produces a steady decline into the substellar regime. The total mass inferred between 0.6 and 0.02 $M_\odot$ from these data is ∼41 $M_\odot$ which, corrected for the 40% completeness factor becomes ∼100 $M_\odot$. This value is a lower limit because, as I have already shown, the survey is not 40% complete at all magnitudes. I find an average mass of ∼0.18 $M_\odot$ corresponding to the peak in the data.

6.1.2.1 Comparison to Previous ONC IMF Determinations

The stellar/substellar IMF has been discussed in previous work on the ONC. A determination based on near-infrared photometric data was made by HC00 using H and K magnitudes and colors combined with star count data to constrain the IMF down to ∼0.03 $M_\odot$. They find a mass function for the inner regions of the ONC which rises to a peak around 0.15 $M_\odot$ and then declines across the hydrogen burning limit with

slope N($\log M$) $\propto M^{0.57}$. M02 transform the inner ONC's K-band luminosity function into an IMF and find a mass function which rises with decreasing mass to form a broad peak between 0.3 $M_\odot$ and the hydrogen-burning limit before turning over and falling off into the substellar regime. This decline is broken between 0.02 and 0.03 $M_\odot$ where the IMF may contain a secondary peak near the deuterium burning limit of ∼13 M_{Jup}. Luhman et al. (2000) combined near-infrared NICMOS photometry of the inner 140" × 140" of the ONC with limited ground-based spectroscopy of the brightest objects ($K < 12$) to determine a mass function which follows a power-law slope similar, but slightly steeper than the Salpeter value, until it turns over at ∼0.2 $M_\odot$ and declines steadily through the brown dwarf regime. H97 presents the most extensive spectroscopic survey of the ONC, combining optical spectral data with V and I-band photometry over a large area (∼2.5 pc^2) extending into the outer regions of the cluster. The IMF determination covers a large spectral range and appears to be rising from the high (50 $M_\odot$) to low (0.1 $M_\odot$) mass limits of that survey.

The peak in the IMF presented here, ∼0.2 $M_\odot$, matches remarkably well to those found from both the deep near-infrared imaging IMF studies (HC00 and M02) which cover similar survey areas, and the Luhman et al. (2000) study which covered only the very inner region of the cluster. My data also show a leveling off in the mass distribution through the substellar regime similar to that found by HC00. A significant secondary peak within the substellar regime has been claimed by M02. While I see some evidence for such a peak in my data, this result is not robust to within the errors. Furthermore, if real, I find the secondary peak to occur at a slightly higher mass than M02 (∼0.05 $M_\odot$ vs. ∼0.025 $M_\odot$). The primary difference between the observed IMF derived in the current work and those presented in previous studies of the substellar ONC population is the steepness of the primary peak and the sharpness of the fall-off at the hydrogen-burning limit (see for comparison figure 16 of M02). Most IMF determinations for this region exhibit a gradual turnover in the mass function around ∼0.2 $M_\odot$ until $\sim \frac{2}{3}$ the level of the primary peak is reached at which point the IMF levels off or forms a secondary peak. However, I find a sharp falloff beyond ∼0.1 $M_\odot$ to $\sim \frac{1}{2}$ the primary peak value.

6.1.2.2 Photometric vs. Spectroscopic Mass Functions

As mentioned in §6.1, spectroscopy is needed to study a cluster's IMF in more than a statistical sense. The fact that many of the fainter objects in my survey expected to be substellar based on their location in the K, $(H-K)$ diagram are in fact hotter, possibly older objects gives strong evidence in support of this statement. Independent knowledge of an individual star's age, extinction and infrared excess arising from the possible presence of a circumstellar disk is needed before definitive conclusions can be drawn about that object's mass. Despite the increasing numbers of brown dwarfs studied, both in the field and in clusters, details of their formation process remain sufficiently poorly understood that knowledge of near-infrared magnitudes and colors alone is not enough to accurately predict these characteristics for young low mass objects. Near-infrared magnitudes alone also cannot distinguish between cluster members and nonmembers, and field star contamination must be modeled rather than accounted for directly.

Previous studies of the ONC had spectroscopy available in general only for the stellar population, and relied on photometry alone to determine the mass function at substellar masses. This may have caused overestimates in the number of brown dwarfs for reasons discussed above. However, the more significant cause of the shallower peak in previous IMF determinations for the inner ONC as opposed to the sharply peaked IMF derived here is likely just the inherent nature of photometric vs. spectroscopic mass functions. Determining masses for stars in a sample from temperatures derived from spectral types necessarily discretizes the data. Conversely, photometric studies are by their nature continuous distributions, and deriving masses from magnitudes and colors or luminosity functions results in a smooth distribution of masses. I emphasize that while neither situation is ideal, mass functions derived for young objects from photometry alone represent only a statistically probable (given correct assumptions wer made) distribution of underlying masses. Spectroscopy is needed in order to derive cluster membership and masses for individual objects.

6.1.3 Summary of ONC Survey

I have identified for the first time a large sample of spectroscopically confirmed young brown dwarfs within the inner regions of the ONC, including five newly classified M9 objects. From this data I made an HR diagram and possibly discovered a previously unknown population of ∼10 Myr old low mass stars within the inner regions of the cluster. I examined this population in detail and determined that it is not an artifact arising from systematics in the spectral reduction/classification processes. I ruled out that this population consists primarily of "contaminants" from the surrounding OB1 association. If this population is real, I propose that it was not detected in previous works because of its intrinsic faintness, coupled with extinction effects. Another possible scenario is that these objects constitute a population of scattered light sources. If this hypothesis is correct, these objects provide indirect observational support for recent theoretical arguments indicating higher disk occultation fractions for young substellar objects in comparison to higher mass classical T Tauri stars (Walker et al., 2004).

From the HR diagram I used DM97 tracks and isochrones to infer a mass for each object and constructed the first spectroscopic substellar ($0.6 > M > 0.02$ $M_{\odot}$) IMF for the ONC. The mass function presented here peaks at ∼0.2 $M_{\odot}$ consistent with previous IMF determinations (M02; HC00; Luhman et al. 2000), however it drops off more sharply past ∼0.1 $M_{\odot}$ before roughly leveling off through the substellar regime.

6.2 Age/Mass Distributions of the Low Mass Population in USco

The details of my photometric/spectroscopic survey in USco were discussed extensively in chapters 2, 3 & 5. In this section I assess quantitatively the age and mass distribution of low mass association members. The discussion will proceed in a manner similar to that for the ONC (§6.1). I discuss first the age distribution as inferred from an HR diagram, and, subsequently, I derive a stellar/substellar mass function

for USco. In the next section (§6.3) I compare my results for both USco and the ONC to those in the literature for other young associations.

6.2.1 HR Diagram for Low Mass Members of USco

In figure 6.5 I present the HR diagram (originally shown as figure 5.2) for low mass PMS stars and brown dwarfs in USco. I have chosen to use DM97 tracks and isochrones for all analysis presented here for ease of comparison with results from the ONC survey. All derived quantities are given in table 6.1. Interpreting the ages literally, figure 6.5 reveals a population with a median age of ∼4.1 Myr and a continuous spread of ages over ∼10 Myr. While this result *may* be real, the continuous nature of the observed age distribution in USco is more likely to be produced from uncertainties in observed parameters than, for example, the bimodal distribution seen in my survey of the ONC (§6.1.1). Also suspicious is the fact that the surface gravity-sensitive spectral features do not show evidence for the same age spread. Figure 6.6 shows spectra of two stars with spectral type M5 identified in the USco survey. The top spectrum is of the 'youngest' M5 star observed spectroscopically at Palomar (SCH16054416-21550566), ∼2.6 Myr-old based on its location on the HR diagram (figure 6.5); the bottom spectrum is of a the 'oldest' M5 star observed at Palomar (SCH16162599-21122315), ∼14.4 Myr from the HR diagram. Recalling the discussion in §4.3, young stars less than a few megayears old exhibit systematically less Na I (λ8190 Å) absorption than do intermediate-age stars (∼5–10 Myr). Thus, if the derived ages from the HR diagram are correct, the spectrum of the 14.4 Myr-old star should have noticeably stronger Na I absorption. However, unlike the spectral sequence shown in figure 4.3 where the young and intermediate-age stars clearly show different surface-gravity spectral features, the spectra presented here are nearly identical (and have near-identical measured Na-8190 indices of 0.89 and 0.90). Based on analysis of spectral features, I classified these two stars as being roughly the same age. However, based on the differences in observed luminosity, interpreting the HR diagram literally, one would infer an age spread of >10 Myr between the two stars.

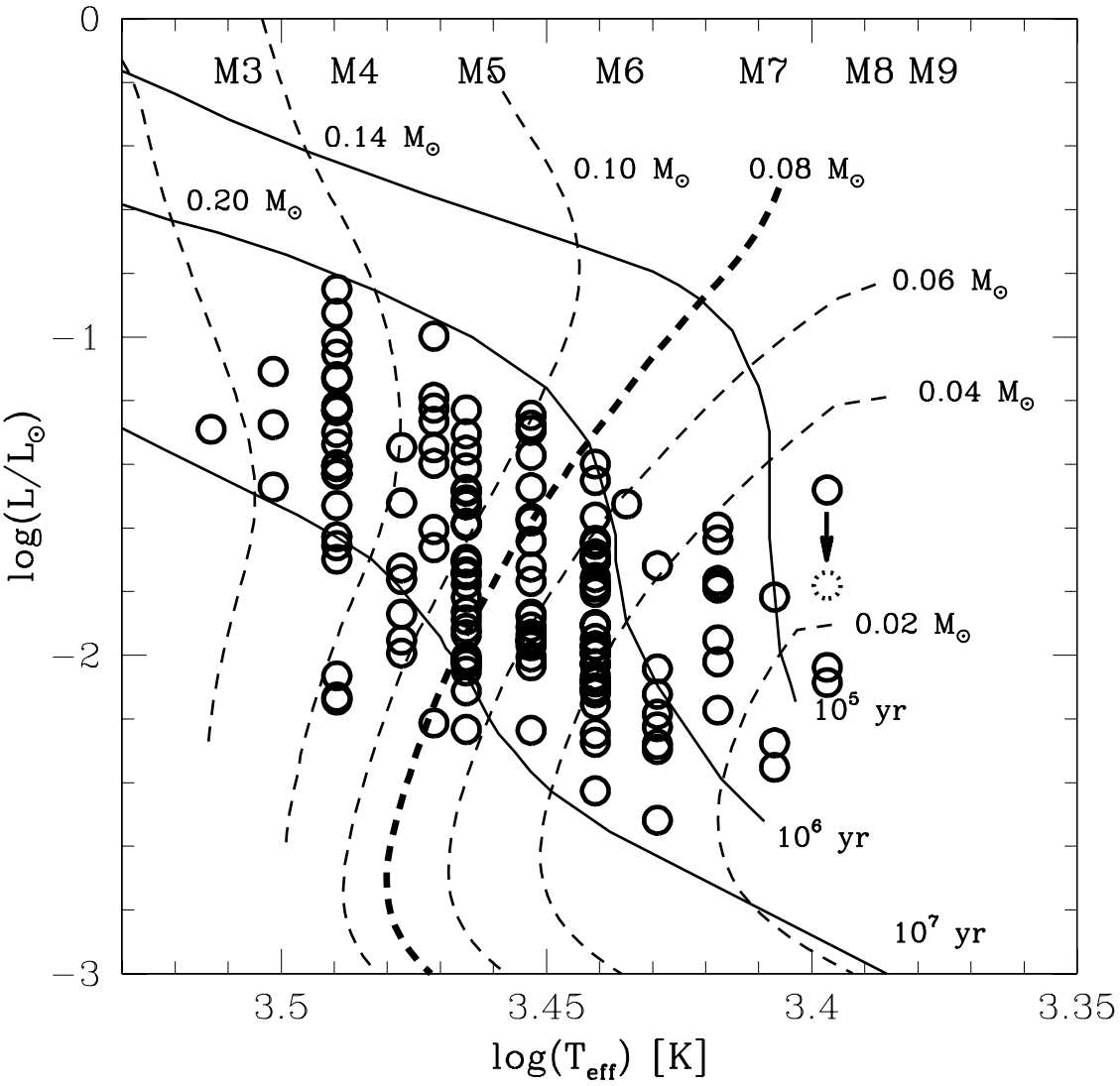

Figure 6.5 HR diagram for PMS objects discovered in my photometric/spectroscopic survey of the USco region. Literal interpretation of the HR diagram reveals a population with a median age of ∼4.1 Myr and an age spread from <1 Myr to >10 Myr.

Table 6.1. Derived quantities for new USco members

ID	$\log(T_{eff})$ [K]	$\log(L/L_\odot)$	$\log(age)$ [yr]	$M/M_\odot$
SCH15560497-21064632	3.41	-2.17	5.46	0.03
SCH15561978-24232936	3.47	-1.87	7.10	0.12
SCH15574757-24441236	3.49	-1.69	7.09	0.16
SCH15582337-21515908	3.47	-1.39	6.54	0.13
SCH15582566-18260865	3.44	-1.65	6.41	0.06
SCH15583162-24025411	3.47	-1.76	7.00	0.12
SCH15584812-21413426	3.45	-1.95	6.75	0.06
SCH15594802-22271650	3.40	-2.27	5.35	0.02
SCH15595868-18365205	3.45	-1.88	6.71	0.06
SCH16002669-20563190	3.47	-1.95	7.17	0.11
SCH16014156-21113855	3.49	-1.52	6.88	0.16
SCH16014768-24410152	3.46	-2.11	7.06	0.07
SCH16024143-22484204	3.45	-1.76	6.64	0.07
SCH16024576-23045102	3.46	-1.52	6.61	0.11
SCH16033470-18293060	3.46	-1.48	6.57	0.11
SCH16034029-23352386	3.49	-1.40	6.70	0.17
SCH16035651-23572517	3.47	-1.99	7.21	0.11
SCH16040453-23463795	3.49	-1.13	6.35	0.16
SCH16044303-23182620	3.42	-2.12	5.96	0.03
SCH16051829-17562092	3.49	-1.12	6.34	0.16
SCH16053077-22462016	3.44	-2.10	6.75	0.04
SCH16054416-21550566	3.46	-1.30	6.42	0.12
SCH16060391-20564497	3.41	-2.02	5.44	0.03
SCH16072239-20115852	3.45	-1.57	6.54	0.08
SCH16072640-21441727	3.44	-2.42	6.94	0.03
SCH16075565-24432714	3.45	-2.00	6.78	0.06
SCH16075850-20394890	3.44	-1.99	6.68	0.04
SCH16081081-22294303	3.46	-1.58	6.66	0.11
SCH16083646-24453053	3.50	-1.10	6.41	0.18
SCH16083658-18024994	3.42	-1.71	5.64	0.05
SCH16084058-22255726	3.49	-2.14	7.60	0.13
SCH16084170-18561077	3.44	-1.45	6.09	0.07
SCH16085870-24493641	3.49	-1.40	6.71	0.17
SCH16090451-22245259	3.41	-1.78	5.39	0.04
SCH16090511-24262843	3.49	-1.21	6.45	0.16
SCH16090771-23395430	3.46	-1.35	6.46	0.12
SCH16090883-22174699	3.46	-1.71	6.76	0.10

Table 6.1 (cont'd)

ID	$\log(T_{eff})$ [K]	$\log(L/L_\odot)$	$\log(age)$ [yr]	$M/M_\odot$
SCH16091837-20073523	3.40	-1.81	5.01	0.02
SCH16092137-21393452	3.45	-1.37	6.39	0.10
SCH16093018-20595409	3.44	-2.15	6.77	0.04
SCH16093707-20525337	3.47	-1.66	6.81	0.12
SCH16095217-21362826	3.41	-1.63	5.36	0.04
SCH16095307-19481704	3.44	-1.68	6.43	0.06
SCH16095695-22120300	3.45	-2.03	6.80	0.06
SCH16095991-21554293	3.42	-2.27	6.16	0.03
SCH16100129-21522466	3.45	-1.64	6.57	0.08
SCH16100541-19193636	3.44	-2.10	6.74	0.04
SCH16100751-18105666	3.44	-1.69	6.44	0.06
SCH16101190-21015540	3.45	-1.91	6.73	0.06
SCH16102990-24035024	3.47	-1.72	6.96	0.13
SCH16103525-20291714	3.46	-1.59	6.66	0.11
SCH16103876-18292353	3.44	-1.99	6.68	0.04
SCH16104635-18405996	3.47	-1.34	6.53	0.14
SCH16105500-21261422	3.44	-1.63	6.40	0.06
SCH16105727-23595416	3.49	-1.62	7.01	0.16
SCH16110144-19244914	3.46	-1.86	6.88	0.09
SCH16110739-22285027	3.43	-1.52	5.75	0.06
SCH16111711-22171749	3.40	-2.35	5.38	0.02
SCH16112629-23400611	3.45	-1.93	6.74	0.06
SCH16112959-19002921	3.44	-1.90	6.61	0.05
SCH16114735-22420649	3.46	-1.88	6.90	0.09
SCH16115737-22150691	3.46	-2.02	7.00	0.08
SCH16121044-19322708	3.46	-1.41	6.51	0.12
SCH16121188-20472698	3.42	-2.04	5.87	0.03
SCH16122764-24064850	3.41	-1.76	5.39	0.04
SCH16123459-24583447	3.47	-1.34	6.49	0.13
SCH16123758-23492340	3.44	-2.11	6.75	0.04
SCH16124506-23053043	3.45	-1.95	6.75	0.06
SCH16124692-23384086	3.44	-2.02	6.70	0.04
SCH16125723-24280145	3.49	-1.65	7.04	0.16
SCH16130306-19293234	3.45	-1.87	6.70	0.06
SCH16130764-17035233	3.45	-1.97	6.76	0.06
SCH16131212-23050329	3.42	-2.22	6.09	0.03
SCH16131857-15293460	3.47	-1.18	6.34	0.13

Table 6.1 (cont'd)

ID	$\log(T_{eff})$ [K]	$\log(L/L_\odot)$	$\log(age)$ [yr]	$M/M_\odot$
SCH16132576-17373542	3.49	-1.43	6.74	0.17
SCH16132809-19245288	3.44	-1.70	6.45	0.06
SCH16141351-22445788	3.49	-1.42	6.74	0.17
SCH16141484-24270844	3.41	-1.59	5.35	0.04
SCH16141974-24284053	3.44	-2.06	6.72	0.04
SCH16143286-22421358	3.42	-2.29	6.18	0.03
SCH16150524-24593542	3.46	-1.52	6.61	0.11
SCH16151115-24201556	3.44	-2.24	6.82	0.04
SCH16151360-23042637	3.42	-2.51	6.89	0.03
SCH16153915-19170073	3.47	-0.99	6.08	0.13
SCH16155508-24443677	3.44	-1.90	6.61	0.05
SCH16162396-24083016	3.46	-1.77	6.81	0.09
SCH16162599-21122315	3.46	-2.23	7.16	0.07
SCH16163504-20575551	3.45	-1.47	6.48	0.09
SCH16164538-23334143	3.46	-2.05	7.01	0.08
SCH16165160-20485398	3.49	-1.29	6.56	0.16
SCH16171901-21371312	3.45	-1.94	6.75	0.06
SCH16172504-23503799	3.46	-1.93	6.93	0.08
SCH16173105-20504715	3.41	-1.78	5.39	0.04
SCH16173238-20403653	3.44	-2.27	6.84	0.04
SCH16173788-21191618	3.49	-1.33	6.61	0.16
SCH16174368-21115536	3.49	-2.13	7.59	0.13
SCH16174540-23533618	3.44	-2.08	6.73	0.04
SCH16181201-24133263	3.46	-1.47	6.57	0.11
SCH16181567-23470847	3.45	-1.24	6.26	0.10
SCH16181601-24372688	3.49	-1.05	6.26	0.16
SCH16181906-20284815	3.47	-1.22	6.37	0.13
SCH16182501-23381068	3.46	-1.81	6.85	0.09
SCH16183144-24195229	3.42	-2.18	6.04	0.03
SCH16183620-24253332	3.49	-1.23	6.47	0.16
SCH16185038-24243205	3.46	-1.91	6.92	0.08
SCH16190473-23075283	3.45	-1.72	6.62	0.07
SCH16191521-24172429	3.49	-1.22	6.47	0.16
SCH16192994-24255414	3.49	-0.85	6.05	0.15
SCH16193976-21453527	3.44	-1.80	6.53	0.05
SCH16200756-23591522	3.44	-1.75	6.49	0.05
SCH16201318-24250155	3.49	-2.06	7.52	0.14

Table 6.1 (cont'd)

ID	$\log(T_{eff})$ [K]	$\log(L/L_\odot)$	$\log(age)$ [yr]	$M/M_\odot$
SCH16202127-21202923	3.44	-1.90	6.61	0.05
SCH16202523-23160347	3.45	-2.23	6.94	0.05
SCH16211564-24361173	3.50	-1.47	6.93	0.19
SCH16211922-24255250	3.49	-1.01	6.22	0.16
SCH16212490-24261446	3.50	-1.27	6.64	0.19
SCH16213591-23550341	3.44	-2.02	6.70	0.04
SCH16221577-23134936	3.44	-2.08	6.73	0.04
SCH16222156-22173094	3.46	-2.00	6.98	0.08
SCH16224384-19510575	3.39	-1.48	7.15	0.04
SCH16235158-23172740	3.39	-2.03	5.31	0.02
SCH16235474-24383211	3.44	-1.70	6.45	0.06
SCH16252862-16585055	3.39	-2.08	5.33	0.02
SCH16252968-22145448	3.46	-1.73	6.78	0.10
SCH16253671-22242887	3.41	-1.95	5.42	0.03
SCH16254319-22300300	3.46	-1.74	6.79	0.10
SCH16255064-21554577	3.47	-2.21	7.28	0.08
SCH16260630-23340375	3.45	-1.56	6.53	0.08
SCH16263026-23365552	3.44	-1.77	6.51	0.05
SCH16265619-22135224	3.44	-1.94	6.64	0.05
SCH16270940-21484591	3.47	-1.52	6.73	0.14
SCH16274801-24571371	3.46	-1.69	6.75	0.10
SCH16281810-24283619	3.44	-1.39	5.95	0.08
SCH16284706-24281413	3.44	-1.78	6.51	0.05
SCH16292211-17420937	3.47	-1.60	6.75	0.12
SCH16293625-24565325	3.44	-1.97	6.66	0.05
SCH16293664-17084094	3.47	-1.26	6.41	0.13
SCH16293934-16145647	3.51	-1.29	6.79	0.22
SCH16294877-21370914	3.46	-1.51	6.60	0.11
SCH16302675-23590905	3.44	-1.56	6.34	0.07
SCH16303392-24280657	3.49	-0.92	6.13	0.15
SCH16305349-24245439	3.45	-1.27	6.31	0.10
SCH16310241-24084335	3.46	-1.22	6.35	0.12
SCH16324224-23165644	3.45	-1.29	6.33	0.10
SCH16324726-20593771	3.44	-1.97	6.66	0.04

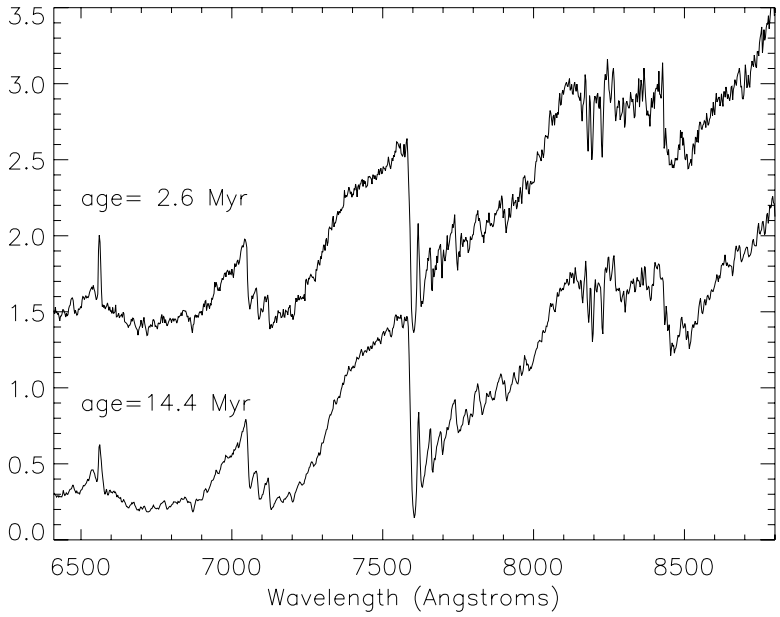

Figure 6.6 Spectra of two stars with spectral type M5 found in the USco survey. The top spectrum is of the 'youngest' (based on analysis of the HR diagram) M5 star observed spectroscopically at Palomar, ∼2.6 Myr-old; the bottom spectrum is of a the 'oldest' (based on analysis of the HR diagram) M5 star observed at Palomar, ∼14.4 Myr. These stars have near-identical spectra, and, based on analysis of the strength of the surface gravity sensitive Na I line (8190 Å), appear to be the same age. However, based on the differences in observed luminosity, interpreting the HR diagram literally, one would infer an age spread of >10 Myr between the two stars.

Due to the discrepancy between stellar ages derived from surface gravity analysis and HR diagram analysis, I sought to determine the statistical significance of the apparent spread in ages from the HR diagram. To assess this value quantitatively, I used Monte Carlo techniques to simulate a coeval 5 Myr-old population of stars at the mean distance (145 pc) of USco. The stars in my sample were placed onto the HR diagram in figure 6.5 based on observed J magnitudes, $J-H$ colors, and spectral types (see chapter 5). Once a star is placed onto the HR diagram from effective temperature and luminosity, age and mass are inferred using a set of theoretical isochrones and mass tracks. Thus, uncertainties in measured photometry or spectral types are propagated into uncertainties in mass and age. Variations in distance and

binarity can cause additional uncertainty in luminosity, and hence, quantities derived from the HR diagram.

I sought to explore if I could recreate the apparent age spread in the HR diagram using only known uncertainties. To accomplish this goal, I generated a population of 5 Myr-old stars and brown dwarfs at a distance of 145 pc. The input spectral type distribution was selected to mirror that of my observed distribution of stars, in that for every observed star of a given spectral type, 1000 stars of that starting spectral type were simulated. From my starting population I varied the J- and H-band magnitudes by adding random offsets drawn from a Gaussian distribution with a 1-sigma deviation of 0.025 mag, corresponding to the average uncertainty in the 2MASS photometry for observed stars. To mimic the magnitude-limited data sample, I did not allow any star to be simulated below the photometric survey limits (J=16 and H=15.5). Similarly, I added a random offset to the assumed spectral type selected from a Gaussian distribution with 1-sigma errors of 0.5 spectral subtypes corresponding to the qualitative error of the optical spectral type determinations. Using the new spectral type, for each simulated star I re-derived the expected effective temperature, bolometric correction and intrinsic $J-H$ color using the methods described in Slesnick et al. (2004).

The maximum distance spread (derived from secular parallax measurements) among members of the association with Hipparcos measurements is predicted to be 50 pc (Preibisch et al. 2002; de Bruijne 1999). In the simulation I assumed a uniform spatial distribution over a box of this depth centered at 145 pc. I assumed a 33% binary fraction for stars across all simulated spectral types (M3–M8), as derived by Kraus et al. (2005) from high resolution imaging observations. This study also finds all observed binaries to have near equal masses ($m_{secondary}/m_{primary} \gtrsim 0.6$) consistent with results for low mass stars in the field and in open clusters. For the purpose of this exercise, I made the assumption that all binaries were composed of two equal mass stars. This is assumption is somewhat conservative in that it will produce the largest possible dispersion in luminosity.

Figure 6.7 shows the same information as figure 6.5 with the addition of blue

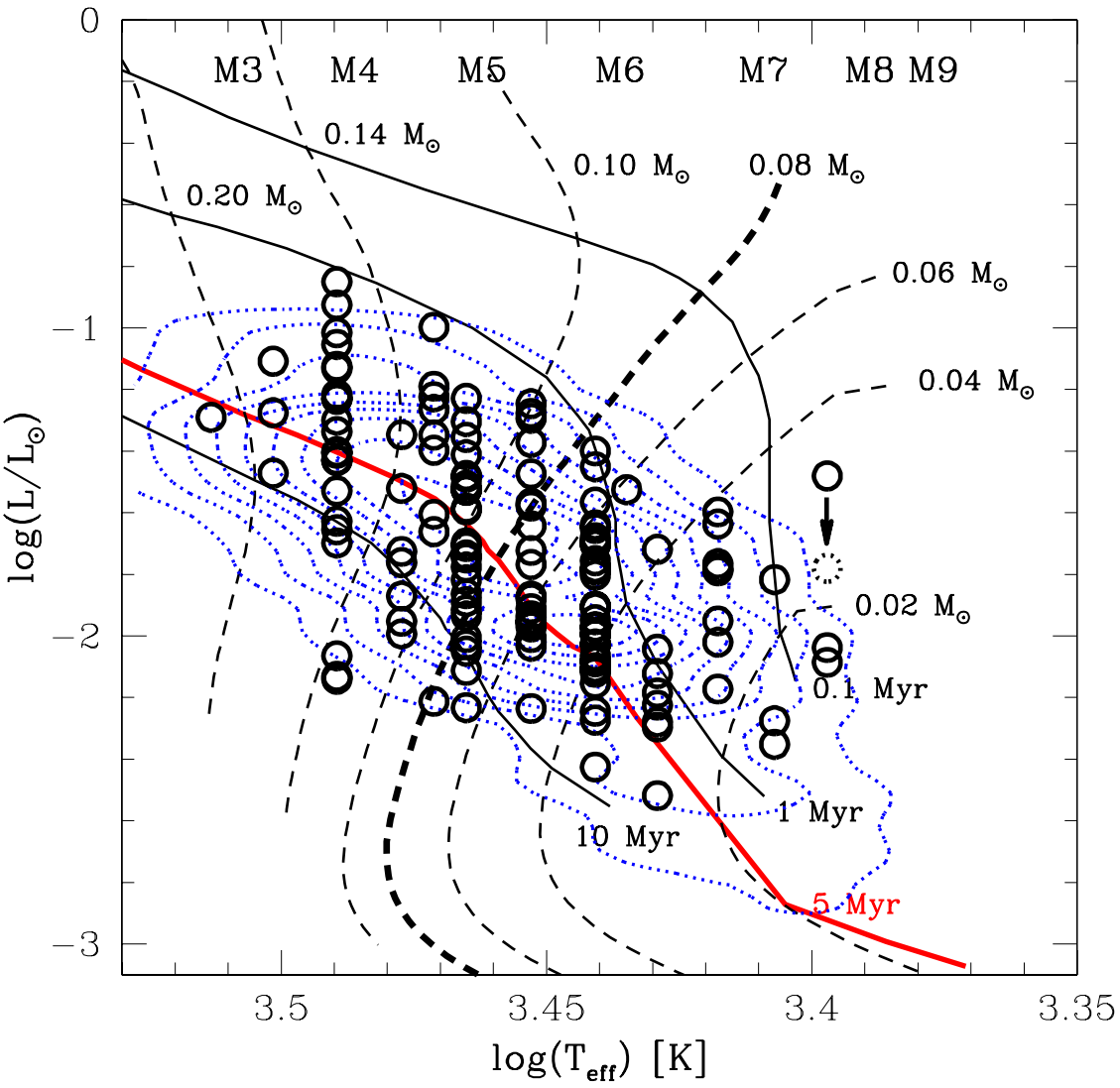

Figure 6.7 HR diagram for low mass members of USco. Blue contours are results from a numerical Monte Carlo simulation aimed at modeling the expected observed age spread given a coeval 5 Myr-old population with known observable uncertainties (see text for more details). Contours are shown at 90%–10% of the peak level.

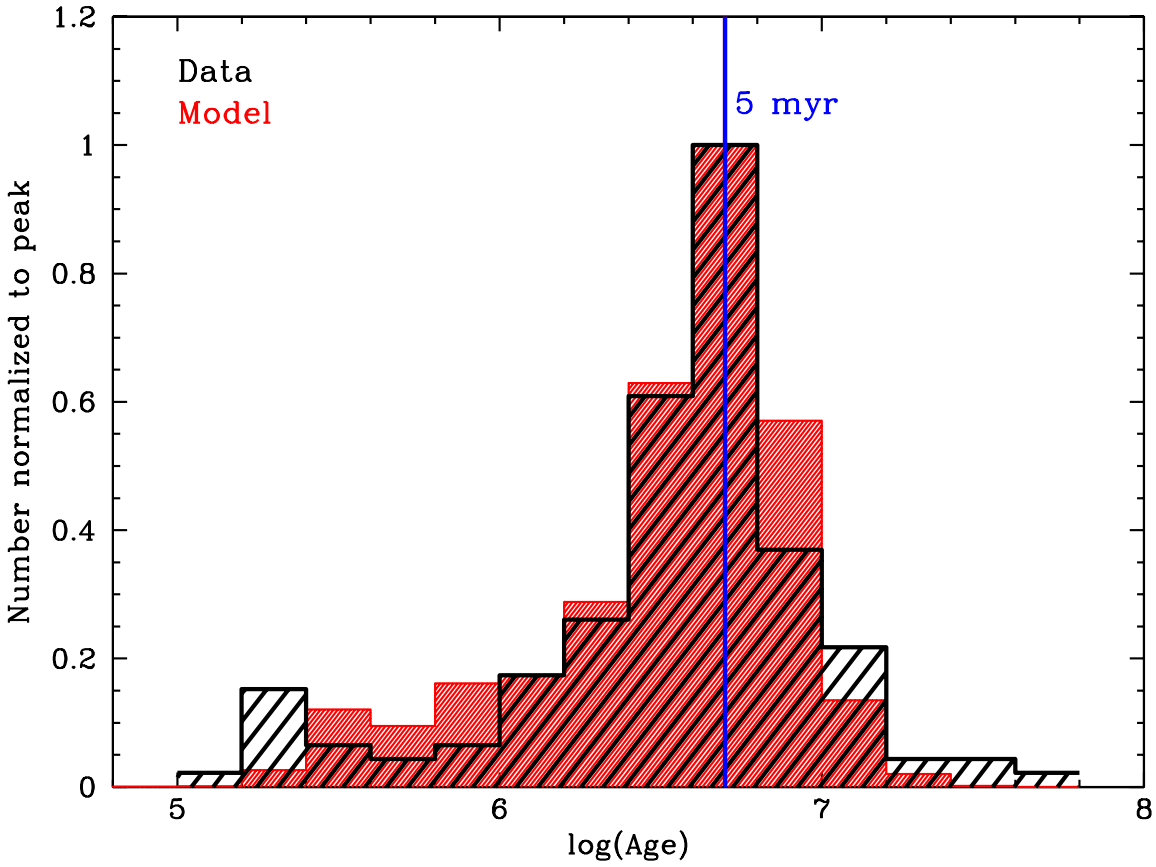

Figure 6.8 Red shaded histogram shows the age distribution derived from the Monte Carlo simulation, overplotted with a histogram of ages for the data (black hatched histogram). Both histograms have been normalized to one at the peak for comparison, and all stars having $\log(T_{eff})$ <3.4 (beyond which interpolation of the isochrones becomes unreliable) have been excluded from both the data and the model results. The widths of the distributions are remarkably similar, given the simplistic nature of the Monte Carlo simulation.

contours representing the model output. Contours are shown at 90%–10% of the peak. As can be seen, much of the age spread in the HR diagram *could* be caused by uncertainties in the data rather than by an intrinsic spread in ages. I examine this result further in figure 6.8. The red shaded histogram shows the age distribution derived from the Monte Carlo simulation, overplotted with a histogram of ages for the data (black hatched histogram). Both histograms have been normalized to one at the peak for comparison, and all stars with $\log(T_{eff})$ <3.4 (beyond which interpolation of the isochrones becomes unreliable) have been excluded from both the data and the model results. The widths of the distributions are remarkably similar, given the simplistic nature of the Monte Carlo simulation. For the simulated association I find a median apparent age of $\log(age)$=6.62±0.41 whereas for the data (not including the 3 M8 stars) I find a median age of $\log(age)$=6.62±0.47. While all input parameters were realistic assumptions, I did not vary the expected photometric uncertainty as a function of magnitude, and I assumed that the population of USco consists of a box of stars with a constant stellar density. Because the output from this simple simulation produced a reasonable match to the data, I did not find a need to try a more complicated set of initial assumptions. A KS test yields a 70% probability that the distributions from the model output and the data could be drawn from the same population. Thus, given the uncertainties, the data are consistent with most stars in USco forming via a single burst ∼5 Myr ago.

This result is somewhat surprising given the large extent of the association (∼35 pc across). Assuming a sound speed of c_S=0.2 km/s consistent with a T=10 K molecular cloud, and assuming the stars formed close to where they are observed today, the sound crossing time for the parental molecular cloud is ∼85 Myr. Thus, one end of the cloud could not have 'communicated' to the other in time to create a simultaneous burst of star formation. This result does not, however, rule out the possibility that star formation happened simultaneously throughout the extent of the cloud because every part independently reach the threshold for star formation at the same time. Another scenario is that the stars formed much closer together and have since spread to their current positions. However, this possibility can be ruled out from

simple arguments. The velocity dispersion of the Hipparcos members is ∼1.3 km/s (de Bruijne, 1999). Thus, in 5 Myr the furthest an association member is expected to travel is ∼6.5 pc, less than half the radius of the current association.

This discrepancy between the small observed age spread for USco's stellar members and the large spatial extent of the population has been noted previously in the literature. To explain the disparity, Preibisch & Zinnecker (1999) (and later Preibisch & Zinnecker 2007) proposed a scenario in which star formation in USco was triggered by an external event in the form of a supernova explosion in the neighboring Upper Centaurus-Lupus association (∼70 pc away and ∼17 Myr-old). They argue based on the structure and kinematics of large H I loops surrounding Sco Cen, that such an event is evidenced to have occurred ∼12 Myr ago. If true, the explosion would have driven a shock wave which would have reached USco about ∼5 Myr ago, consistent with the inferred age of USco's stellar population. My results imply a similar small age spread with an association age ∼5 Myr and large spatial extent (see §5.3.4) for USco's lowest mass stars and substellar members. While this conclusion in no way proves the Preibisch & Zinnecker (1999) hypothesis true, it does give support to its plausibility and extend its validity to even the lowest mass association members.

In figure 6.8 the model and data differ from each other most significantly at the distribution tails. Specifically, the data are composed of more very young and very old stars than expected. Deriving ages from the DM97 isochrones, I observed 8 stars with age <2.5×10^5 yr (log(age)<5.4) and 15 stars with age >10 Myr (log(age)>7). If I scale down the results from the model to match the total number of stars present in my dataset (142 stars with $\log(T_{eff}) > 3.4$), the predicted number of observed stars in these age ranges is 1.2 and 6.9 for the young and old tails, respectively. Assuming Poisson statistics, the probability that out of the 142 stars I would have observed 8 or more stars younger than 2.5×10^5 yr is

$$P = \sum_{k=0}^{8} \frac{e^{-1.2} 1.2^k}{k!} = 0.004\%.$$

Using a similar equation, the probability that I would have observed 15 or more stars

older than 10 Myr is 0.5%.

There is no systematic spatial correlation between stars within the young and old age bins (see table 6.1). The young tail is, however, comprised only of the lowest mass, latest spectral type stars. This result is suspicious of an observational bias in that for a magnitude limited sample, I expect to preferentially observe the brightest (i.e., youngest) stars at low masses. To test this possibility, I ran a second version of the Monte Carlo simulation but requiring all simulated stars to be brighter than the faintest spectroscopic target confirmed to be a USco member (J $\sim$15 mag). However, this constraint yielded little change in the overall shape of the modeled age distribution and did not recover any of the stars with $age<2.5\times10^5$ yr. Thus, *assuming the absolute validity of the model isochrones*, and assuming I made a correct assumption by using Poisson statistics, the group of young stars does appear to be real and may be evidence for recent star formation in USco. It should be noted, however, that the isochrones younger than $\sim$5 Myr begin to decrease sharply in luminosity at temperatures less than $\log(T_{eff})\sim3.45$ (see figure 6.7), while the data do not. Because my simulation input assumed a constant age of 5 Myr, the resulting distribution follows the 5 Myr isochrone, not the younger ones. Thus, the young group of stars may be illustrative of a systematic problem with the youngest isochrones at the lowest masses (i.e., perhaps the turnover in luminosity beyond $\log(T_{eff})\sim3.45$ is not accurate) rather than a real feature of the USco population.

Similar arguments could be made for the older group of stars. The old tail is comprised only of the earliest spectral type stars (spectral type $\lesssim$M5) where the DM97 isochrones at ages >5 Myr begin to get systematically closer together than they are for cooler stars. This fact leads to systematically larger numbers of hotter (<M5) stars to have derived ages $\gtrsim$10 Myr compared to later spectral types. A detailed test of the theoretical models is beyond the scope of this work. At this time I simply reiterate the point that theoretical isochrones for low mass PMS stars and young brown dwarfs are still not well understood, and results derived from these models must be used as a guideline for analysis only, rather than as literal truth.

6.2.2 USco's Low-Mass IMF

In this section I use the model tracks of DM97 to derive the first spectroscopic mass function for stars and brown dwarfs in USco less massive than ∼0.1 $M_\odot$. The study by Preibisch et al. (2002) derived an IMF for the *stellar* population in the association by combining the 166 spectroscopically confirmed low mass members (M∼0.8–0.1 $M_\odot$) discovered via their 2dF survey with the 120 known Hipparcos members (constituting a complete sample of members more massive than ∼1 $M_\odot$) and 84 X-ray selected members (M ∼0.8–2 $M_\odot$; Preibisch & Zinnecker 1999). The resultant mass function yielded a 3-segment power law function that was consistent with other recent field star and cluster IMF determinations above ∼2 $M_\odot$, but with a 2σ excess of stars at lower masses.

The only previous survey that has attempted to derive an IMF for USco's substellar members is the photometric study by Lodieu et al. (2007). This work observed ∼6.5 deg^2 of USco at $ZYJHK$-bands as part of the UKIRT Infrared Deep Sky Survey (UKIDSS) Galactic Cluster Survey. From these data, they used the J-band luminosity function to derive a *photometric* IMF in USco from 0.3–0.007 $M_\odot$. They derived a mass function that was significantly flatter ($dN/dM \propto M^{-0.3\pm0.1}$) than the IMF derived by Preibisch et al. (2002) for similar mass ranges ($dN/dM \propto M^{-0.9\pm0.2}$ for $0.1 \leq M/M_\odot < 0.6$). However, as noted in §6.1.2.2, great care must be taken when interpreting photometrically derived IMFs as they are based on incomplete knowledge of individual stellar ages, photometric excesses, and extinctions, and they cannot directly (only statistically) correct for field star contamination.

However, as was shown in §6.2.1, deriving quantities from an HR diagram has its own set of uncertainties. I have already shown that known uncertainties in observable magnitudes and spectral types can produce an apparent age spread of ∼10 Myr. I now wish to explore variation in the apparent mass distribution derived for stars in my sample. The top panel of figure 6.9 shows the apparent mass function derived for the 145 spectroscopically confirmed members shown in the HR diagram (figure 6.5). The bottom panel shows the derived mass function for a theoretical coeval population

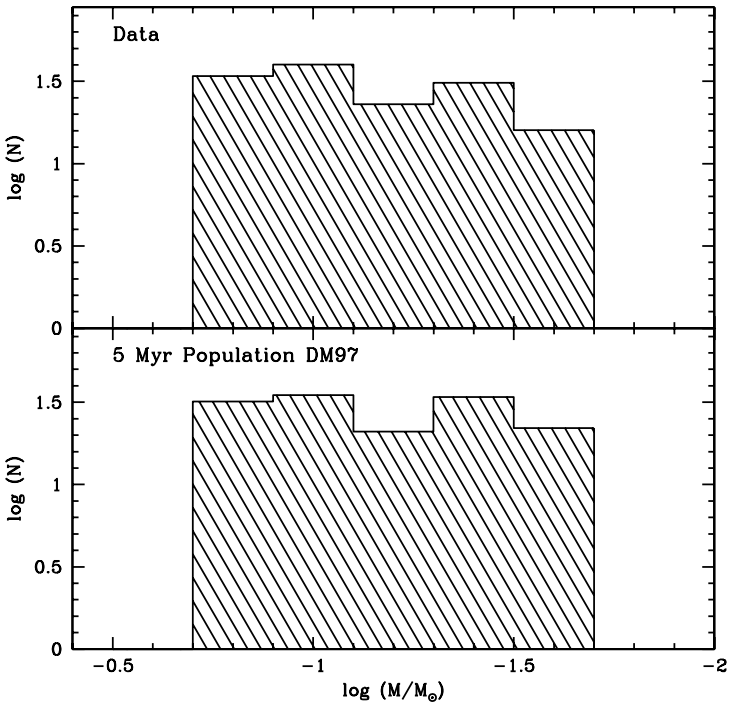

Figure 6.9 Top panel shows the apparent mass function derived for the 145 spectroscopically confirmed members shown on figure 6.5. Bottom panel shows the apparent mass function for a theoretical population of 145 stars with a uniform age of 5 Myr and a spectral type distribution consistent with that for the observed stars.

of 145 stars at an age of ∼5 Myr. To derive this IMF, I have assumed a spectral type distribution consistent with that for my observed population, and assigned each star the mass that it would have at that spectral type if it were 5 Myr-old. In both panels, data have been binned in steps of $\log(M)$=0.2. I have examined the difference between the two mass distributions using a KS test and find that the mass distributions derived from the real data and the theoretical 5 Myr-old population are statistically consistent with each other (probability=12%). Because the mass tracks are close to vertical for low mass stars (see figure 6.5), the dominant source of uncertainty in derived masses will come from uncertainties in temperature stemming from uncertainties in spectral type. My spectral type uncertainties are ±0.5 subtypes which is not enough to shift the derived mass by $\log(M)$=0.2 at any spectral type and the derived histograms will not change significantly. Presuming I am equally likely to misclassify a star 0.5 subtypes too early as I am to misclassify it 0.5 substypes too late, the mass distribution itself should not change significantly either. Thus, I conclude that the mass distribution derived from the HR diagram is more robust to observable uncertainties than I found the age distribution to be.

In figure 6.10 I show again the IMF derived from my spectroscopic survey of low mass stars and brown dwarfs, covering the mass range M ∼0.2–0.02 $M_{\odot}$. I have thus far observed spectroscopically only ∼15% of the photometric PMS candidates in the USco region. Therefore, before constructing a mass function, it is necessary to determine that the spectroscopic sample presented here is representative of the USco low mass population as a whole. I use a method similar to that employed in the ONC to determine the completeness of my sample. In the ONC, I binned the photometric and spectroscopic surveys as a function of magnitude and used this information to determine the relative completeness of the spectroscopic sample. This method was employed because at these masses in an $H, H-K$ diagram, the isochrones are almost vertical (see figure 1 of Slesnick et al. 2004). However, for the optical Quest-2 survey, I selected as candidate PMS stars all stars red-ward of the 1% data contour (see figure 3.3), and the selection cut was made along lines that depended on both r magnitude and $r-i$ color. Thus, to correct for incompleteness in the optical

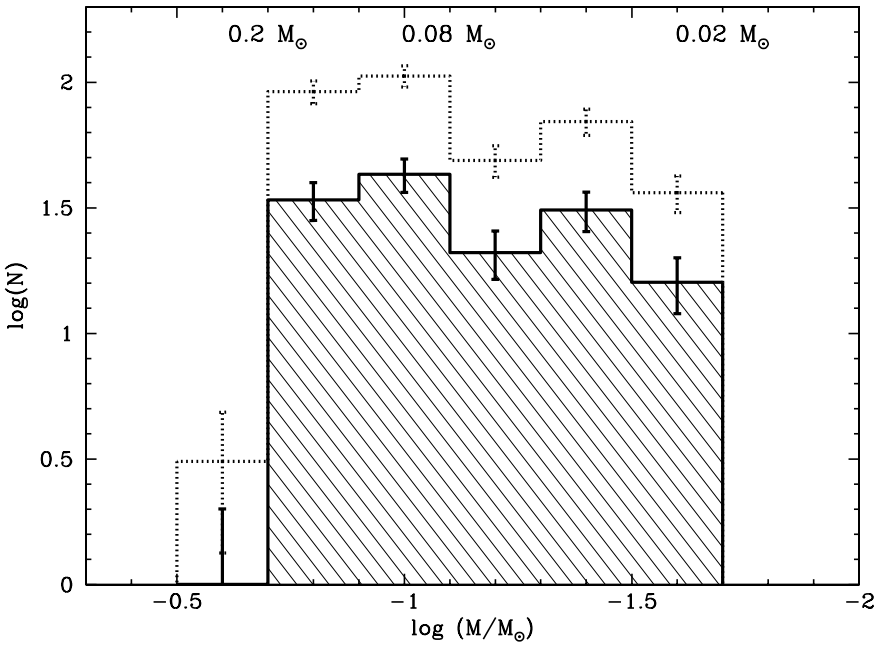

Figure 6.10 Mass function for all spectroscopically confirmed members presented in chapter 5. Thick-lined hatched histogram indicates all stars; the dotted open histogram represents the same sample corrected for incomplete selection bins (§6.2.2).

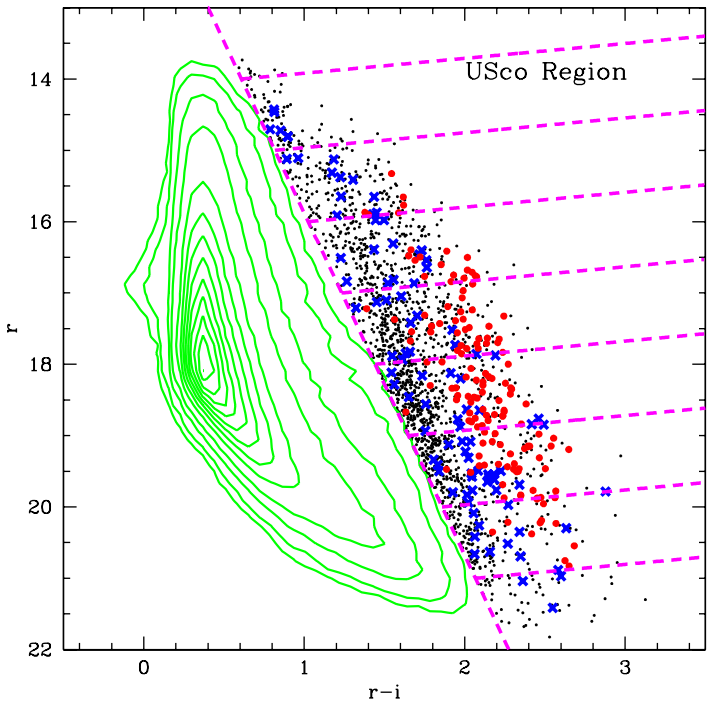

Figure 6.11 Optical Quest-2 $r, r-i$ CMD for the USco survey region. Photometric candidates (as defined in chapter 3) are shown as discrete points. Spectroscopic candidates are shown as large colored symbols: red circles are stars determined to be USco members based on spectral features. Blue X's are stars determined to be field dwarfs. The dashed, nearly vertical magenta line represents the 1% contour used in candidate selection (§3.1). Near horizontal magenta lines (perpendicular to the 1% contour line) delineate bins used to compute the spectroscopic completeness fraction.

photometric survey I computed the number of stars in bins perpendicular to the line of selection as shown in figure 6.11. The resulting histograms are shown in figure 6.12 for all photometric candidates (top panel) and for those observed spectroscopically (middle panel). Bin centers correspond to the middle of the bin in r magnitude at the selection line. The bottom panel in figure 6.12 shows the percentage of stars observed spectroscopically with $\sqrt{(N)}$ errorbars. As can be seen, priority in spectroscopic observations was given to faint stars, but with numbers of observed stars falling off considerably for stars fainter than r $\sim$19.5 which could be observed only under the best seeing conditions. The spectroscopic survey completeness peaks at $\sim$20%, and I followed the same method used in the ONC to correct all bins to this completeness level. The dotted histogram in figure 6.10 shows the IMF corrected to a uniform 20% completeness across all $r, r-i$ bins shown in figures 6.11 & 6.12. The derived mass function for USco is relatively flat across the mass range sampled and does not exhibit the sharp drop off at the substellar limit as seen for stars in the ONC.

In order to increase my sample size (improve statistics) and extend it to higher masses, I combined masses derived for my sample with those for stars from the Preibisch et al. (2002) survey. I chose to use this sample because 1) it constitutes the largest sample of spectroscopically confirmed low mass stellar members, and 2) candidates were selected from an $I, R-I$ CMD in an analogous manner to the methods employed to select my sample (chapter 3.1), and thus provide a complementary dataset. I specifically chose not to include the higher mass X-ray selected sources (Preibisch & Zinnecker, 1999) due to the large difference in selection techniques. To provide the most analogous samples possible, I re-derived masses for the 166 stars in the Preibisch et al. (2002) survey using the DM97 tracks and the same interpolation program used to generate masses for the sample of stars presented here. In combining samples from multiple sources one must be careful to account for relative completeness. Preibisch et al. (2002) estimate spectroscopic completeness levels of 87% for stars with $0.2 < M/M_{\odot} < 0.8$ and 67% for stars with mass <0.2 $M_{\odot}$, whereas, my corrected survey is only 20% complete across all sampled mass bins. The two surveys also cover very different areas. Preibisch et al. (2002) looked at 9 deg^2 whereas

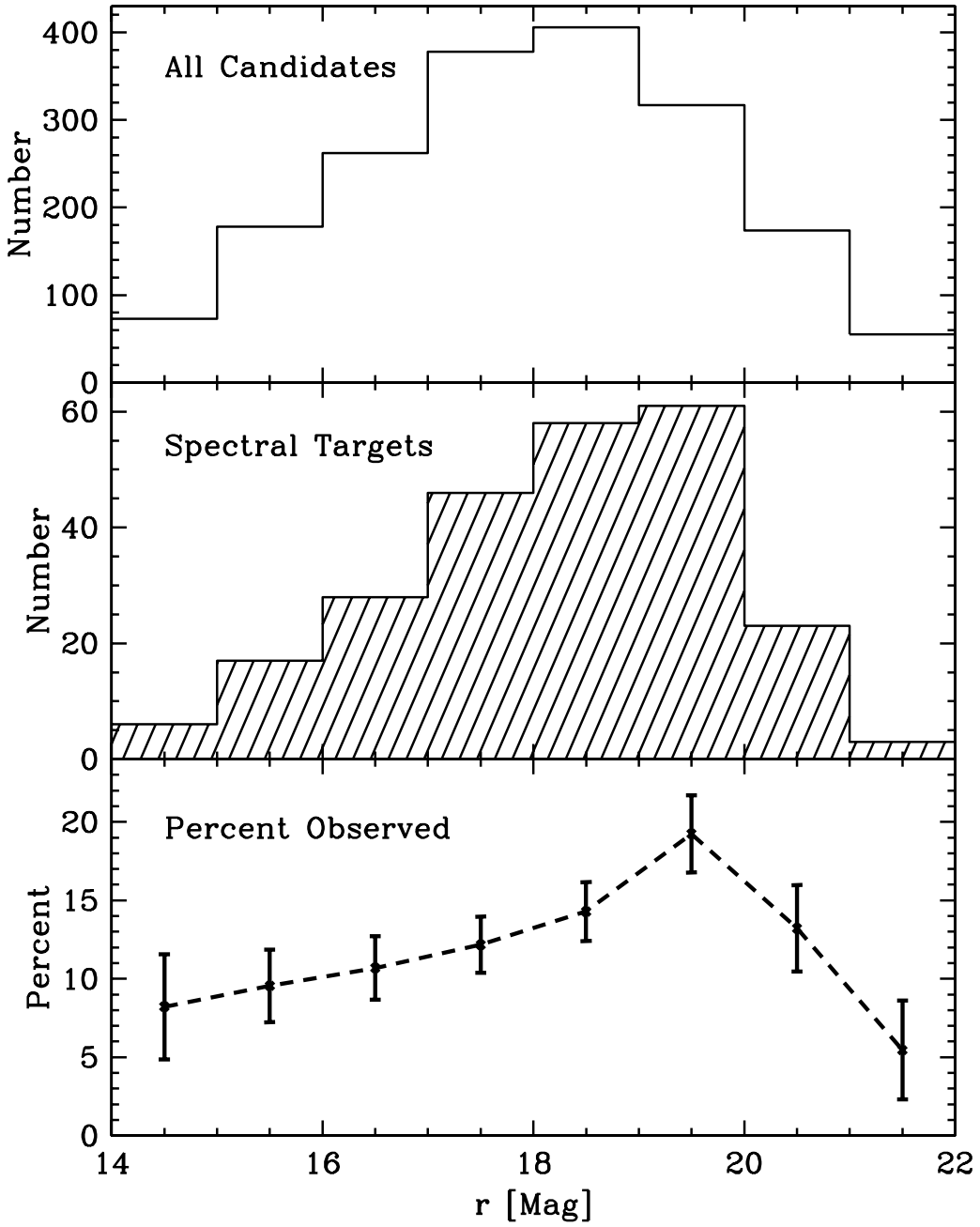

Figure 6.12 Histogram of optical CMD completeness as a function of r magnitude. Bin centers correspond to r magnitudes at the 1% contour line in figure 6.11. The top panel shows data for all photometric candidates and the middle panel shows data for all targets observed spectroscopically. As can be seen, faint targets were preferentially observed before brighter ones. The bottom panel shows the percent completeness with $\sqrt{(N)}$ errorbars. This quantity peaks at 20% near r=19.5 mag.

the Quest-2 survey looked at ∼150 deg^2. However, as mentioned in chapter 2, the Quest-2 survey coverage within this area is not complete due to several failed CCDs, gaps between the CCDs, and incomplete $r - i$ color coverage. Taking all of these factors into account, the total usable Quest-2 survey area is ∼100 deg^2. The number of stars in the Preibisch et al. (2002) survey were thus multiplied by either (100 deg^2/9 deg^2)×(20% complete/87% complete) for stars with $0.2 < M/M_\odot$ <0.8, or (100 deg^2/9 deg^2)×(20% complete/67% complete) for stars with M <0.2 M$_\odot$.

Figure 6.13 shows IMFs for the low mass stellar and substellar population of the USco association. The top panel shows separately IMFs derived from the Quest-2 survey (black hatched histogram) and the Preibisch et al. (2002) survey (blue hatched histogram). Both IMFs have been scaled to 20% completeness over 100 deg^2. All histograms are shown with $\sqrt{(N)}$ errorbars. The bottom panel shows the summed IMF for the combined samples. In total, the combined IMF contains ∼300 stars with masses as high as ∼0.8 M$_\odot$ and as low as <0.02 M$_\odot$. The derived mass function rises with a slope of $dN/dM \propto M^{-1.0}$, peaks at ∼0.16 M$_\odot$ and then gradually falls off through the substellar regime. Thus, I find the spectroscopic IMF for USco's low mass population to be very different from the photometric IMF derived by Lodieu et al. (2007) which had a flatter slope $dN/dM \propto M^{-0.3}$ from $0.3 < M/M_\odot$ <0.01, and peaked at M ∼0.01 M$_\odot$. The total mass inferred from the spectroscopic IMF over the mass range 0.8–0.02 M$_\odot$ is ∼156 M$_\odot$. If I correct this number to account for the fact that the IMF shown here is only 20% complete, the total mass inferred is ∼780 M$_\odot$. Brown dwarfs (M < 0.08 M$_\odot$) account for ∼20% of objects in the combined sample, but constitute only ∼4.5% of the total mass.

6.2.3 Summary of USco Survey

I have used the HR diagram to derive mass and age distributions for the new low mass members of USco discovered as part of my Quest-2 survey (chapter 5). I generated a Monte Carlo simulation aimed at modeling the expected observed age spread given a coeval 5 Myr-old population with known observable uncertainties. From quantitative

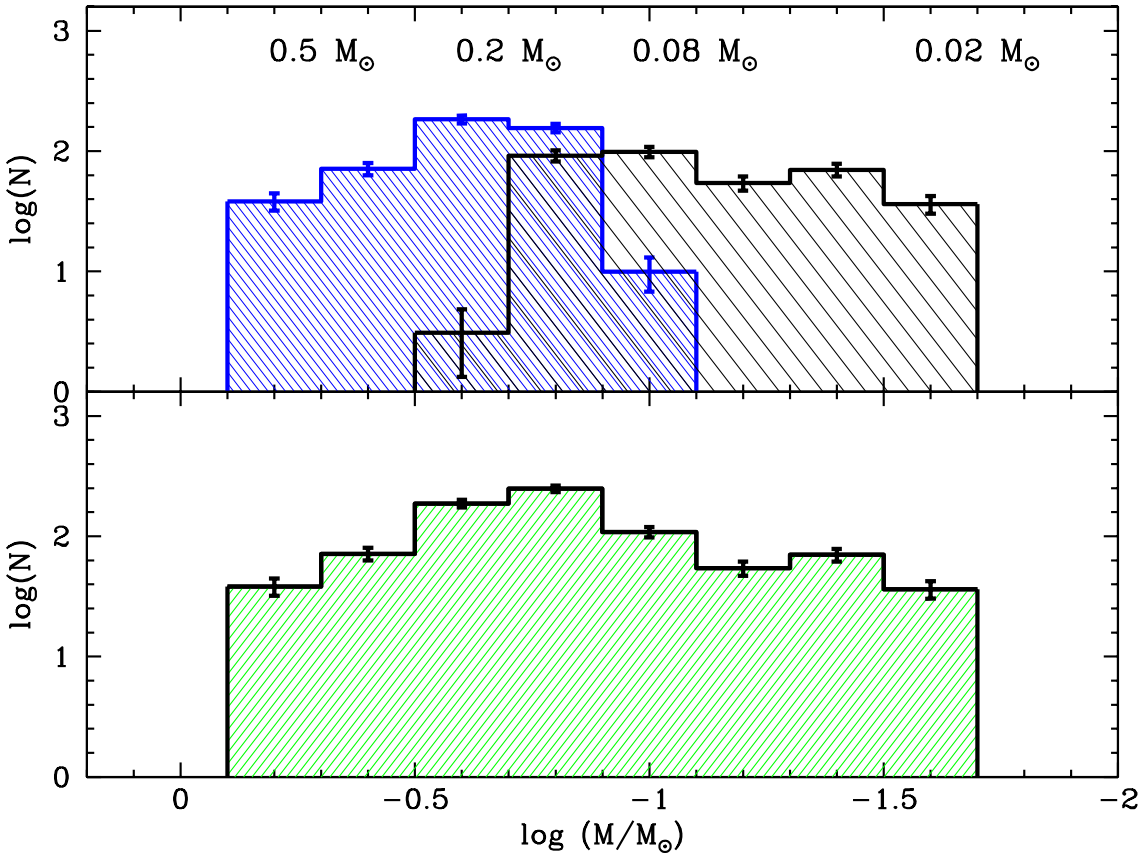

Figure 6.13 IMF for the USco association from ∼0.8–0.02 $M_\odot$. The top panel shows separately IMFs derived from the Quest-2 survey (black hatched histogram) and the Preibisch et al. (2002) survey (blue hatched histogram). Both IMFs have been scaled to a uniform 20% completeness over 100 deg^2 (see text). The bottom panel shows the cumulative IMF for the combined samples. All histograms are shown with $\sqrt{(N)}$ errorbars.

comparison of my data with simulated results I found that the data are consistent with all members of USco having formed in a single burst ∼5 Myr ago. However, if this scenario is true, the large spatial extent of the association suggests that star formation in USco was likely influenced by an external event.

I used DM97 tracks to construct the first spectroscopic IMF for USco that extends into the substellar regime. I combined my data with that from Preibisch et al. (2002) to derive a mass function with uniform completeness from ∼0.8 to 0.02 $M_{\odot}$. The derived mass function peaks at ∼0.16 $M_{\odot}$ and turns over into the brown dwarf regime.

6.3 Comparisons between Star-Forming Regions

Diagnostic studies of stellar populations in different locations and at varying stages of evolution are needed to explore the possibility of a universal mass function. While one might expect that the IMF should vary with star formation environment, we do not yet have enough evidence to determine if such a variation exists. Aside from work already mentioned in the ONC and USco, numerous studies have been carried out to characterize the low mass stellar and substellar mass functions of other young clusters in various environments. Because of the intrinsic faintness of these objects, most surveys are photometric. Authors then use a combination of theoretical models and statistical analysis to transform a cluster's color-magnitude diagram or luminosity function into an IMF which may or may not accurately represent the underlying cluster population (see §6.1.2.2).

However, the substellar populations of several other young star-forming regions have been studied spectroscopically using techniques similar to those presented here. Luhman et al. (2003b) studied the rich cluster IC 348 in Perseus, and Levine et al. (2006) studied the young cluster of NGC 2024 within the Orion Ib association. Aside from my work, there have been several additional studies of the Taurus region using similar techniques, namely those by Luhman (2000), Briceño et al. (2002), Luhman et al. (2003a), and Luhman (2004b), which together constitute a complete sample within a selected region. The data for IC 348 (Luhman et al., 2003b) and Taurus

(Luhman 2000, Briceño et al. 2002, Luhman et al. 2003a, and Luhman 2004b) are published as complete across all mass ranges within the areas surveyed. Data for NGC 2024 (Levine et al., 2006), are not complete in the magnitude range 11.25< K <14.75. These authors derived corrections in the same manner as I have employed in the ONC. The corrected values are not published; however, based on visual assessment of the published IMF from this work (see Levine et al. 2006, figure 9), the corrections appear to be uniform across all masses. Thus, for the purpose of this discussion I assume the IMF for NGC 2024 to be *relatively* complete across all masses considered. These three clusters are all young ($age \lesssim 3$ Myr), and, similar to the ONC and USco, have not yet had time to lose members through dynamical ejection. Therefore, if the IMF is universal, similar mass distributions should be observed for all five regions.

Direct comparison of the published data requires caution given that different mass tracks were used to derive masses for different studies. To avoid this problem, I have used published effective temperatures and luminosities from the studies listed above to re-derive masses for the three comparison regions with both the DM97 (D'Antona & Mazzitelli, 1997) and the BCAH98 (Baraffe et al., 1998) tracks using the same interpolation program used to derive masses for my samples in the ONC and in USco. Resultant IMFs are shown in figures 6.14 and §6.15. For the ONC and USco I have shown completeness-corrected IMFs as discussed in §6.1.2 & 6.2.2. Remarkably, for both sets of tracks I find a common turnover at the low mass end in all five regions. For the purpose of this study I will discuss only the DM97 comparative results consistent with my prior analysis, but note that varying conclusions can be drawn dependent upon which models one is using. This is a very important, but too often downplayed, caveat that must be kept in mind for any discussion regarding the low mass IMF.

From the DM97 models I find that all five star forming regions exhibit a common peak at $M \sim 0.16$ $M_{\odot}$. Note the varying scales on the y-axis (my samples in USco and the ONC have more stars than the comparison studies) and the fact that while the mass functions for USco or the ONC do not include the associated high mass stars, I have not cut these from the literature samples of IC 348 or Taurus. The Levine et al.

(2006) study in NGC 2024, similar to my work, concentrated only on the low mass stars and brown dwarfs despite the large number of high mass stars present in this cluster.

One method by which I can quantitatively examine differences between the mass distributions is to use KS tests. I ran a KS test between the mass distributions for each association. I limited the mass ranges to 0.02 $M_\odot < M <$0.5 $M_\odot$ to account for the lack of inclusion of high mass stars for some samples. I find that the derived mass functions for three associations, USco, the ONC and NGC 2024, are consistent with being drawn from the same distribution (probabilities $\gtrsim$5%–30%). These same three associations were highly inconsistent with the distribution found for IC 348 with probabilities of <0.02% in all cases. All four associations were borderline inconsistent with the Taurus distribution at the $\lesssim$1% probability level.

Another common method employed when comparing mass distributions for different star forming regions is to compute the relative numbers of brown dwarfs to stars. However, with the possible exception of the ONC, examination of figure 6.14 reveals nothing distinguishing about the distributions on either side of the substellar limit (M=0.08 $M_\odot$; Log($M/M_\odot$)=-1.1). Thus, I have chosen to use as a divisor the peak of the mass function, which is more physically significant in this case than the substellar limit. I will define my high mass bin to be limited to stars <0.5 $M_\odot$ because several of the mass functions presented here do not include high mass stars above this limit. All surveys are complete (within the area surveyed) through $M \sim$0.02 $M_\odot$. I have computed the ratio R_N defined as:

$$R_N = \frac{N(-1.7 \leq log(M/M_\odot) \leq -0.9)}{N(-0.9 < log(M/M_\odot) \leq -0.3)}$$

for each of the five mass distributions. I find relatively small R_N values for Taurus and IC 348, 0.24 and 0.17, respectively. For the other three associations I find much higher values of 0.53 (NGC 2024), 0.64 (ONC – corrected for uniform completeness), 0.58 (ONC – raw data), 0.49 (USco – corrected for uniform completeness), and 0.62 (USco – raw data). Using a two-tailed Fisher's Exact test on the raw data for all five

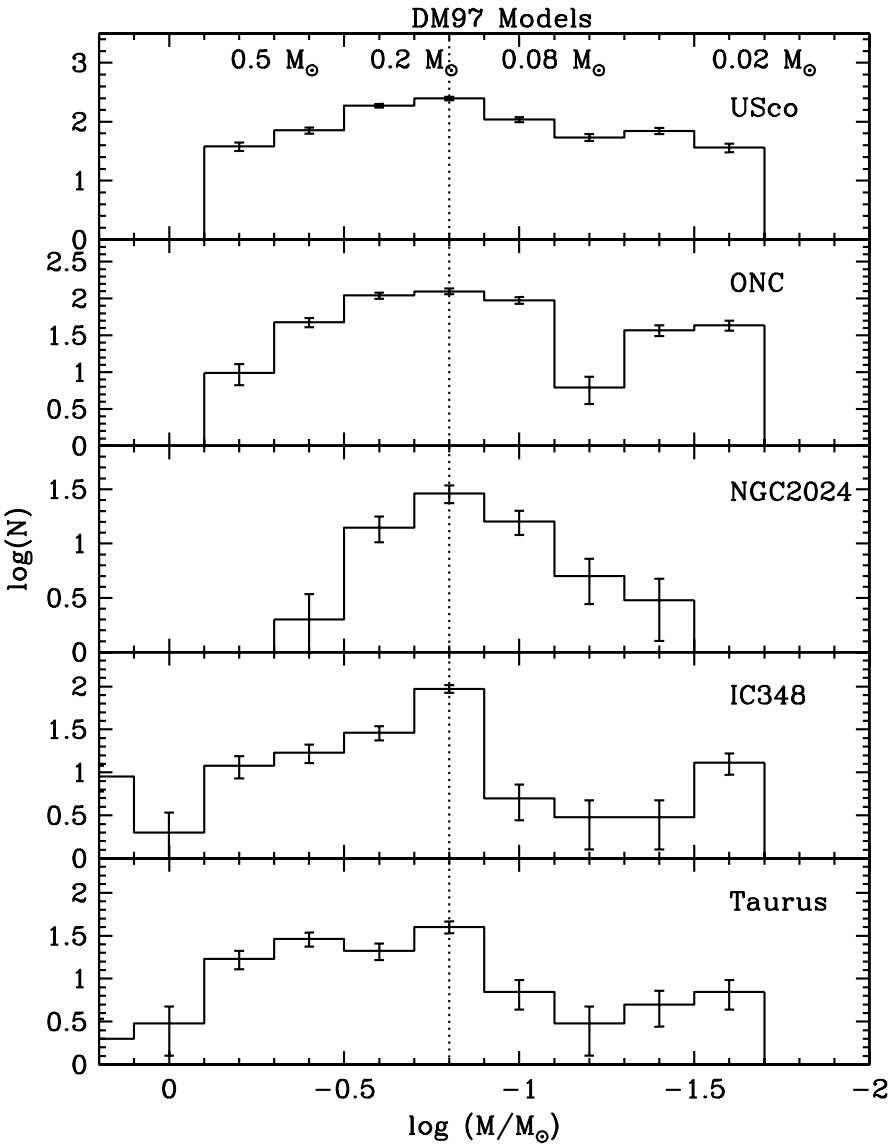

Figure 6.14 Low mass IMFs for USco, the ONC, NGC 2024, IC 348, and Taurus generated from DM97 mass tracks. Data for the latter three regions were taken from the literature (see text). I find a common peak a M $\sim$0.16 $M_{\odot}$ for all five regions and then a turn over into the substellar regime, the form of which may vary.

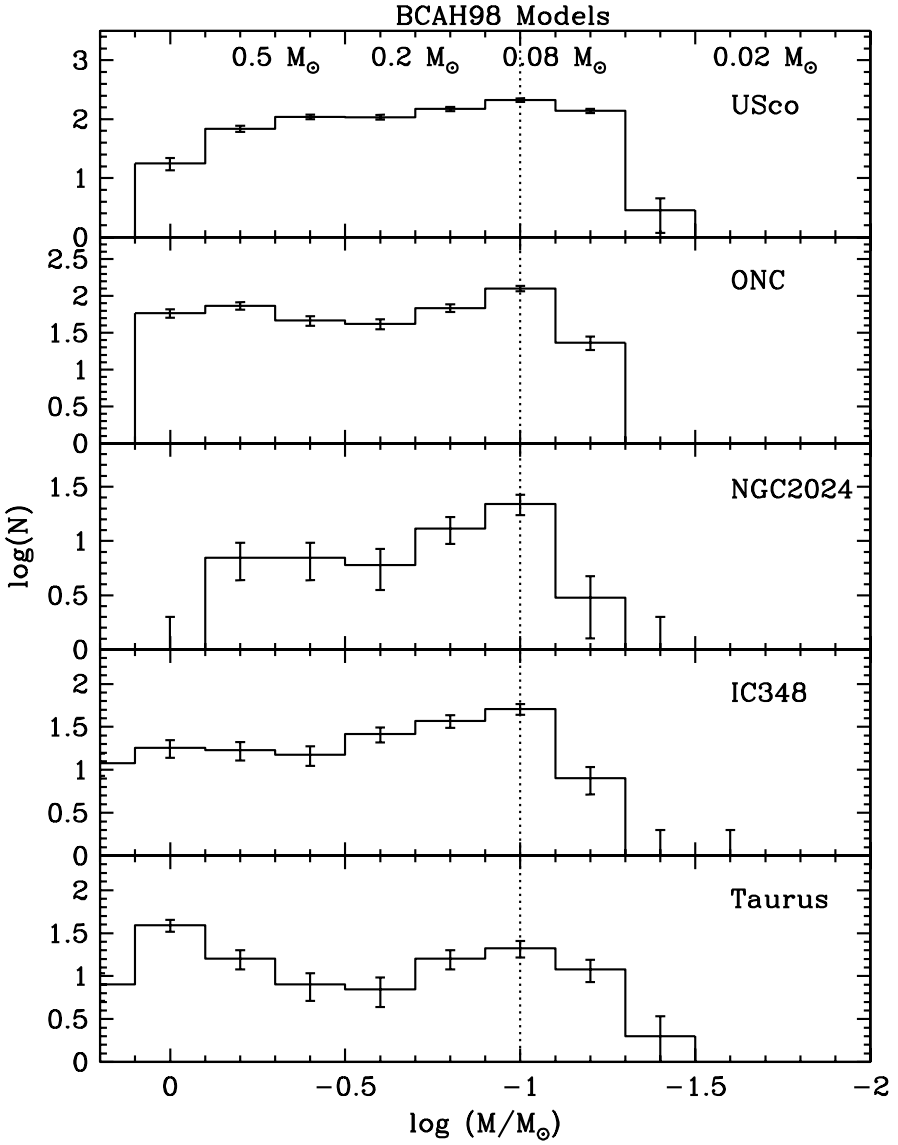

Figure 6.15 Low mass IMFs for USco, the ONC, NGC 2024, IC 348, and Taurus generated from BCAH98 mass tracks. Data for the latter three regions were taken from the literature (see text). As for the IMFs generated from DM97 tracks (figure 6.14), I find a common peak for all regions (though in Taurus this may be a secondary peak). However, using the BCAH98 tracks the peak is shifted to lower mass (M $\sim$0.1 $M_{\odot}$) than that found using the DM97 tracks.

mass functions, I compute that the measured R_N values for NGC 2024, USco, and the ONC are consistent with each other at the 70%–80% level, and different from the R_N values for IC 348 with $\lesssim$0.1% probability that the R_N values could have been drawn from the same distribution. Comparison of R_N values for NGC 2024, USco and the ONC with that for Taurus finds $\lesssim$4% probability of consistency in all cases. These correlations, together with results from the KS tests, strongly suggests that there is something similar about the mass distributions for NGC 2024, the ONC and USco that is not found for IC 348 and Taurus.

While the environments of the ONC and NGC 2024 are similar, they are different from that of USco in that USco is a low stellar-density, OB association rather than a high stellar-density embedded cluster. One factor, however, that all three former regions have in common which IC 348 and Taurus do not share is the presence of hot, ionizing stars. The young regions of NGC 2024 and the ONC, both have an O-type member. The older region of USco currently has 49 B-type stars and its most massive member, the O7-type progenitor of pulsar PSR J1932+1059 exploded as a supernova $\sim$1.5 Myr ago (de Geus, 1992). Conversely, neither Taurus nor IC348 have (or show any evidence for having once had) a member earlier than $\sim$B5 (Briceño et al. 2002, Luhman et al. 2003b). It is possible that a prestellar core in the presence of an ionizing OB (i.e., with spectral type earlier than $\sim$B0) star may ultimately become a lower mass star than it otherwise would have because much of its surrounding material is eroded away by ionizing radiation before it can be accreted. This scenario has been discussed previously in the literature both through observational arguments (e.g., Robberto et al. 2004; Luhman 2004b) and through quantitative theoretical analysis (e.g., Whitworth & Zinnecker 2004; Kroupa & Bouvier 2003). However, this process for generating low mass stars can only take place during the first $\sim10^5$ yr of a protostar's lifetime when most of its material in still in an accretion envelope, and will only significantly affect cores close to ($\lesssim$1 pc, dependent on the mass of the ionizing star) the source of ionization (Kroupa & Bouvier, 2003). Thus, this mechanism may be responsible (at least in part) for the larger numbers of low mass stars and brown dwarfs seen in the two clustered regions of the ONC and NGC 2024,

however, it likely can not have affected protostellar cores across the entire ∼35 pc expanse of USco. These arguments do not, however, exclude the possibility that some other mechanism inherent to regions with high mass stars in some way causes larger numbers of associated low mass stars. For example, Adams et al. (2006) have shown through numerical simulation that disks around lower mass stars are more susceptible to destruction (further out than ∼10 AU) from interactions with surrounding stars of higher mass. It is possible that in a similar manner, low mass cores moving through a giant molecular cloud are more susceptible to being stripped of their accretion envelope in the presence of higher mass cores.

In conclusion to this section, I have re-derived mass functions for the low mass stellar and substellar populations of five recently star forming regions using a consistent set of mass tracks and a common interpolation scheme. Remarkably, I find a common peak for all five regions using either the DM97 or the BCAH98 tracks, implying the IMF turnover may be independent of environment. Based on masses derived from the DM97 tracks, I find that mass distributions for the three regions containing high mass stars, the ONC, NGC 2024 and USco, are statistically consistent with each other, but significantly different from the mass distributions for the two regions Taurus and IC 348 which do not contain OB stars. This result is supported by the finding that the three former associations contain several times more very low mass stars and brown dwarfs compared to stars with masses greater than the IMF turnover than do the latter two. Both results suggest that, within a star forming region, the presence of very massive stars may play a large role in determining the low mass IMF.

Part III:
Circumstellar Properties of Intermediate-Age PMS Stars

Chapter 7

Spitzer Observations of 5 Myr-old Brown Dwarfs in Upper Scorpius

7.1 Introduction

Ground-based infrared studies have found that while disks are commonplace around stars in the most recently formed clusters ($\lesssim$1 Myr; Kenyon & Hartmann 1995; Skrutskie et al. 1990), by an age of $\sim$10 Myr, dust is removed from the inner few AU of circumstellar disks for most stars (Mamajek et al., 2004). Since the launch of the *Spitzer Space Telescope* in 2003, studies aiming to probe circumstellar disks have extended to longer wavelengths and hence larger disk radii. Sicilia-Aguilar et al. (2006) used IRAC and MIPS observations to probe inner circumstellar disks from $\sim$0.1 to 20 AU for stars in the $\sim$10 Myr-old NGC 7160 association and found that $<$4% of stars in this region still retain disks at these radii. Silverstone et al. (2006) used IRAC to survey 45 nearby sunlike stars with ages 10–30 Myr and found that only 1/45 stars ($<$3%) had mid-infrared excess emission indicating the presence of an inner disk. Between the ages of $\sim$1 and 10 Myr, stars must be in the process of actively clearing circumstellar material, presumably through a combination of accretion, photoevaporation or planet-formation.

Observational evidence (e.g., Guieu et al. 2007, Allers et al. 2006) has found that even the lowest mass pre-main sequence stars and young brown dwarfs form with a circumstellar disk in a manner analogous to solar-type stars. However, the evolution

of material around such extremely low mass objects may not follow the same path as that for their higher mass stellar counterparts. Disks are heated via a combination of irradiation and accretion. The much lower temperatures and masses of brown dwarfs compared to solar-type pre-main sequence stars may cause differences in the evolution of accretion, disk composition and grain size. The standard photoevaporative model (e.g., Hollenbach et al. 1994) of high mass disk destruction requires a high flux of EUV Lyman continuum photons from a hot central object to ionize and heat the disk surface. In the absence of an outside source of ionizing radiation, the photoevaporative disk destruction rate decreases with decreasing stellar mass due to much lower levels of EUV photons produced, possibly leading to longer disk lifetimes with corresponding effects on the potential of brown dwarfs and low mass stars to form planetary systems.

Rapidly increasing knowledge garnered from *Spitzer* observations has been suggestive that the lifetime of circumstellar disks is, in fact, dependent on the mass of the central object. Carpenter et al. (2006) took IRAC 4.5μm and 8μm observations of $\sim$200 stars ranging from $\sim$20 to 0.1 $M_{\odot}$ in the 5 Myr-old USco association. This study found the frequency of stars which still harbored a mid-infrared excess at 5 Myr to be strongly spectral type dependent, with the coolest stars (K-M types) preferentially retaining their inner disks longer than those stars at intermediate temperatures (F-G types). A similar study by Dahm & Hillenbrand (2007) used IRAC observations to explore the 5 Myr-old NGC 2362 association across all stars from spectral type B2 to M5, and found that no star more massive than $\sim$1.2 $M_{\odot}$ exhibited a significant mid-infrared excess short-ward of 8.0μm. These results are supported by similar findings in the $\sim$3 Myr-old σOri cluster (Hernández et al., 2007), the $\sim$3 Myr-old IC 348 cluster (Lada et al., 2006), the $\sim$5–9 Myr-old η Chameleontis association (Megeath et al., 2005), and the 25 Myr-old NGC 2547 cluster (Young et al., 2004).

In this chapter I present a mid-infrared study of brown dwarf members of the 5 Myr-old USco association, thus extending the work by Carpenter et al. (2006) into the substellar regime. I use results from these observations to probe circumstellar disk evolution as a function of mass at 5 Myr, and as a function of age for substellar mass objects.

7.2 Observations

I obtained 3.6, 4.5, 5.8, 8.0, and 24 μm images with IRAC (Fazio et al., 2004) and MIPS (Rieke et al., 2004) cameras on the *Spitzer Space Telescope* for 27 low mass members of USco identified originally from my first set of Palomar spectroscopic observations (Slesnick et al. 2006, hereafter SCH06; see also chapters 2, 3, & 5). The sources in the *Spitzer* sample were selected first as candidate members based on optical/near-infrared colors and magnitudes, and confirmed spectroscopically to have cool temperatures and low surface gravity consistent with low mass USco members. These objects therefore represent an unbiased sample in that they were identified independent of any circumstellar signatures. All targets have spectral type M6–M8, where spectral types M6 and later correspond to substellar masses ($\lesssim$0.08 $M_{\odot}$) at the age of the association ($\sim$4–5 Myr). The *Spitzer* sample discussed here represents 32% of all spectroscopically confirmed brown dwarf members of USco.

IRAC data for 24 of the objects were obtained on 20, 21 and 24 Aug. 2005. Exposure times were set for each source by requiring detection of photospheric emission at S/N $\sim$10 in a single pointing in all four bands (3.6, 4.5, 5.8 & 8 μm). For approximately half of the sources a 2 sec pointing was sufficient to achieve the desired S/N; for the other half a 12 sec exposure was required. All observations were taken in a five-point Gaussian pattern with medium scale factor, thus providing ample coverage for cosmic ray rejection. Three of the targets were sufficiently close to the young ρ Ophucius cluster (16:25:35.12, -23:26:49.8) that they were observed serendipitously as part of the C2D Legacy program. The observing strategy for this project is given in Evans et al. (2003).

Observations using the MIPS camera in the 24 μm band were obtained in Photometry mode between Sept. 2005 and Sept. 2006. Each cycle resulted in 14 dithered exposures providing enough redundancy for cosmic ray rejection even when relatively few cycles were requested. When possible, exposure times were determined to detect *photospheric* emission with S/N $\sim$5. A maximum exposure time of 2240 seconds was imposed which was estimated to allow us the ability to detect photospheric emission

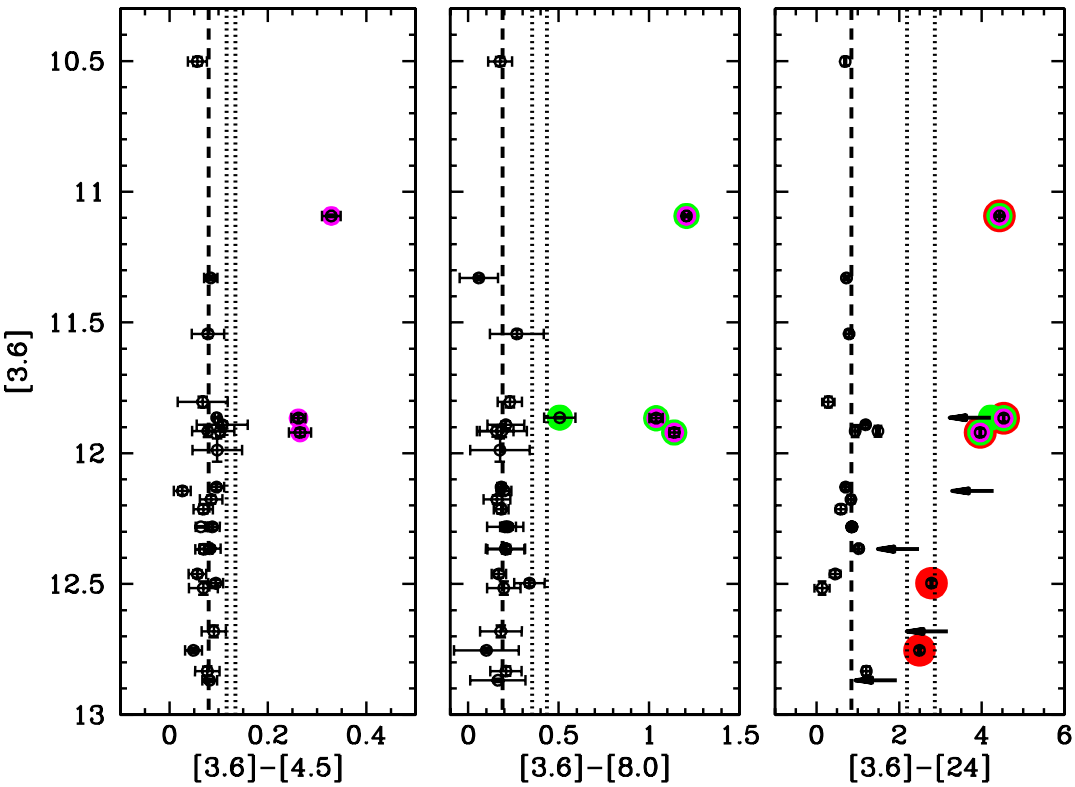

Figure 7.1 Color-magnitude diagrams for the 27 brown dwarfs observed in the *Spitzer* survey. All data have been dereddened using extinction values derived in SCH06 (chapter 5), and photometric errorbars are shown. The dashed line in each panel represents the median value of all data computed using 2σ clipping of outliers. Dotted lines represent 2σ and 3σ deviations about the median. Objects which have an excess of $> 2\sigma$ red-ward of the [3.6]-[4.5] color median are denoted with a large magenta circle in all panels. Objects which have an excess of $> 2\sigma$ red-ward of the [3.6]-[8.0] color median are denoted with a large green circle, and objects which have an excess of $> 2\sigma$ red-ward of the [3.6]-[24] color median are denoted with a large red circle. Arrows in the right panel denote five objects for which we were able only to derive upper limits at 24μm.

at S/N ∼3, for even the faintest objects. However, due to highly structured, strong nebulosity present in this region, five sources were detected only as upper limits at 24μm.

Data analysis was performed on the basic calibrated data images produced by the S14 pipeline for both IRAC and MIPS. Processing of all data (including that obtained by the C2D team) was carried out primarily by my collaborator, John Carpenter, using a modified version of IDLPHOT. Details are given in Carpenter et al. (2006) and Carpenter et al. (2008, in prep.). For the IRAC data, he performed aperture photometry using a radius of 3 pixels (1".22) and a sky annulus between 10 and 20 pixels. Due to the inherently higher levels of structured background contamination at longer wavelengths, we chose to use point-spread function fitting (PSF) photometry for the MIPS data using a 5-pixel fitting radius. Photometry was calibrated to the scale given in the IRAC and MIPS manuals by applying aperture corrections of 1.109, 1.110, 1.107, 1.200, and 1.600 to the IRAC 3.6 μm, IRAC 4.5 μm, IRAC 5.8 μm, IRAC 8.0 μm, and MIPS 24 μm flux densities, respectively. Adopted photometric zeropoints were 277.52, 179.53, 116.58, 63.14, (IRAC; Reach et al. 2005) and 7.16 Jy (MIPS; Engelbracht et al. 2007). Photometry for all sources is given in table 7.1.

Figure 7.1 shows color-magnitude diagrams for the 27 brown dwarfs observed with *Spitzer*. All data have been dereddened using extinction values derived in SCH06 (and chapter 5; extinctions were derived using the reddening law by Cohen et al. 1981), and photometric errorbars are shown. The dashed line in each panel represents the median value of all data (computed using 2σ clipping of outliers), presumed to represent photospheric colors. Dotted lines represent 2σ and 3σ excess levels above the defined median photosphere. I find median photospheric colors of 0.08 mag ([3.6]-[4.5]), 0.19 mag ([3.6]-[8.0]), and 0.85 mag ([3.6]-[24]), with 1σ deviations of 2%, 8%, and 85% above photospheric levels. Objects which have an excess of $> 2\sigma$ red-ward of the color median in each panel are shown as large colored circles. Five sources represented as arrows in the right panel denote objects for which we were able only to derive upper limits at 24μm. I identify from this figure four sources which have a $> 3\sigma$ excess above the median photosphere at [3.6]-[8.0] colors. Three of these sources

Table 7.1. *Spitzer* photometry for brown dwarfs in USco

ID	[3.6][a]	error	[4.5]	error	[5.8]	error	[8.0]	error	[24]	error[b]	A_V
SCH15594802-22271650	12.697	0.023	12.602	0.008	12.586	0.068	12.506	0.113	9.502	-1.000	0.332
SCH16044303-23182620	12.284	0.011	12.196	0.009	12.164	0.057	12.062	0.042	11.428	0.095	0.053
SCH16053077-22462016	12.366	0.011	12.283	0.018	12.231	0.028	12.159	0.107	11.341	0.088	0.035
SCH16093018-20595409	12.516	0.011	12.416	0.009	12.386	0.081	12.165	0.083	9.718	0.016	0.390
SCH16095991-21554293	12.889	0.006	12.801	0.013	12.779	0.085	12.711	0.152	10.931	-1.000	0.426
SCH16103876-18292353[c]	12.008	0.014	11.716	0.017	11.411	0.018	10.812	0.022	7.985	0.004	1.780
SCH16111711-22171749	12.833	0.017	12.756	0.017	12.733	0.076	12.624	0.084	11.626	0.093	0.000
SCH16112959-19002921	11.965	0.013	11.835	0.049	11.802	0.101	11.709	0.101	10.722	0.068	1.517
SCH16121188-20472698	12.141	0.011	12.042	0.010	12.023	0.024	11.951	0.019	11.428	0.078	0.235
SCH16123758-23492340	12.485	0.014	12.421	0.011	12.367	0.060	12.300	0.036	12.013	0.131	0.480
SCH16124692-23384086	12.228	0.016	12.155	0.010	12.115	0.042	12.036	0.037	11.626	0.123	0.290
SCH16131212-23050329	12.516	0.025	12.447	0.013	12.392	0.034	12.319	0.089	12.379	0.179	0.000
SCH16141974-24284053	12.308	0.003	12.236	0.010	12.207	0.033	12.086	0.100	11.428	0.070	0.544
SCH16151115-24201556	12.774	0.009	12.719	0.013	12.636	0.075	12.660	0.178	10.266	0.024	0.417
SCH16155508-24443677	11.828	0.020	11.753	0.046	11.731	0.084	11.582	0.063	11.523	0.147	0.490
SCH16174540-23533618	12.429	0.016	12.340	0.005	12.312	0.076	12.180	0.100	9.904	-1.000	1.262
SCH16200756-23591522	11.601	0.014	11.505	0.029	11.355	0.033	11.294	0.147	10.770	0.085	1.180
SCH16202127-21202923	11.935	0.020	11.826	0.019	11.764	0.143	11.765	0.091	10.433	0.039	0.408
SCH16213591-23550341	12.212	0.014	12.165	0.009	12.131	0.009	11.970	0.037	7.880	-1.000	1.380
SCH16224384-19510575	10.538	0.017	10.470	0.009	10.450	0.065	10.338	0.063	9.815	0.008	0.748
SCH16235158-23172740[c]	11.864	0.002	11.768	0.003	11.650	0.112	11.358	0.086	7.646	-1.000	0.000
SCH16235474-24383211	11.431	0.009	11.316	0.009	11.291	0.009	11.306	0.105	10.631	0.063	2.071
SCH16252862-16585055	12.178	0.015	12.093	0.016	12.056	0.027	12.018	0.072	11.341	0.072	0.021
SCH16253671-22242887	11.948	0.023	11.860	0.022	11.862	0.105	11.740	0.136	10.988	0.064	0.665
SCH16263026-23365552[c]	11.240	0.004	10.866	0.018	10.585	0.055	9.937	0.011	6.706	0.002	3.017
SCH16265619-22135224	12.007	0.044	11.904	0.024	11.864	0.136	11.819	0.158	0.000	0.000	0.390
SCH16324726-20593771[c]	11.869	0.013	11.606	0.005	11.343	0.031	10.828	0.034	7.336	0.003	0.062

[a]All photometry given in magnitudes with associated error.

[b]An error on MIPS 24μm photometry of -1.000 indicates the magnitude given is a 3σ upper limit.

[c]This brown dwarf has a [3.6]-[8.0] color excess as defined in §7.2.

have a confirmed $> 3\sigma$ excess at [3.6]-[24] colors. The fourth may also have a [3.6]-[24] excess; however, it was detected only as an upper limit at 24 μm. Two additional sources exhibit an excess at [3.6]-[24] color at the $> 2\sigma$ level. These stars do not have a [3.6]-[8.0] color excess and *may* represent disks that have begun to clear material from the inside out; however, without data at longer wavelengths I cannot draw any definitive conclusions. The four brown dwarfs with [3.6]-[8.0] color excess emission at $> 3\sigma$ levels (i.e., $\gtrsim$25% above photospheric levels) are listed as excess sources in table 7.1. I note at this time that the RMS residual about the median [3.6]-[8.0] color, $\sim$8.3%, is slightly *lower* than the average $([3.6]\text{-}[8.0])_{error}$, $\sim$8.6%. Thus, the photometric uncertainties given in table 7.1 are likely overestimated.

Because the *Spitzer* observations began before the spectroscopic follow-up program in USco was complete, only one of the five brown dwarfs (spectral type$\geq$M6) determined in §5.3.3 to be accreting was included in the *Spitzer* target list. That source, SCH16103876-18292353, does have mid-infrared excess emission above photospheric colors at all IRAC and MIPS wavelengths (see table 7.1). SCH16235158-23172740, the M8-type brown dwarf that exhibited the strongest Hα emission, significantly above the accretor/nonaccretor division defined by Barrado y Navascués & Martín (2003), is also observed to have a mid-infrared excess.

7.3 The Evolution of Circumstellar Disks with Mass

In order to place my results into context, I have compared my data to those for 1) similar age stars at higher masses, and 2) similar mass brown dwarfs at different ages. To allow robust conclusions to be drawn, I have re-derived the disk frequency for my sample in §7.3 and §7.4 using criteria which takes into account both my data and the appropriate comparison sample. Thus, differences in computed disk frequencies between §7.2, §7.3, and §7.4 reflect changes in the criteria adopted to define a source with a mid-infrared excess, *not* changes in the data.

Figure 7.2 shows a 2MASS-IRAC color-color diagram for the sample of brown dwarfs presented here (circles) together with observations from Carpenter et al. (2006)

for higher mass stellar members of USco with spectral types B–M5 (triangles). The red solid line indicates a linear fit to the data, computed with 3σ clipping of outliers and presumed to represent photospheric colors. RMS residuals of the fit are dominanted by small uncertainties measured for the stellar photometry; thus, the limiting uncertainties are not fit residuals but the photometric uncertainties of the low mass brown dwarfs. I therefore adopt a threshold to define an excess source corresponding to 3× the average $([4.5]\text{-}[8.0])_{error}$ for the brown dwarfs, or ∼24% above photospheric colors. The four brown dwarfs with a [3.6]-[8.0] color excess also have an excess at [4.5]-[8.0] colors, and exhibit similar [4.5]-[8.0] colors to those computed for K- and M-type stars with disks identified by Carpenter et al. (2006). Based on the adopted criteria listed above to identify infrared excess sources, the disk frequency for M stars (M0–M5) in the study by Carpenter et al. (2006) is 16/101 ($\sim 16^{+5}_{-4}\%$). I measure a disk frequency for brown dwarfs of $15^{+12}_{-7}\%$. Using a two-tailed Fisher's Exact test, these frequencies are indistinguishable from each other implying a near-constant frequency in USco of stars with disks compared to stars without disks spanning a mass range from ∼0.5 $M_\odot$ to ∼0.02 $M_\odot$. Thus, the observations I presented here add to the growing evidence that substellar formation and early evolution must proceed through very similar physical processes as those that form and shape low mass stars.

The measured disk frequency for my sample is lower than the value of 37±9% (measured using different criteria — see below) reported by Scholz et al. (2007) for substellar members of USco. This study took MIPS 24μm photometry and 8–12μm IRS spectroscopy of 35 brown dwarfs in USco that had been identified in the literature prior to my Quest-2 surveys. The reason for the discrepancy in measured disk frequencies is not obvious. However, one difference between our two works is that Scholz et al. (2007) used K-[24] colors to identify sources with excess emission at 4× the photospheric value calculated from theoretical blackbody colors, whereas I have used empirical IRAC colors. In order to assess the significance of the difference between our two results, I have recomputed the disk frequency for both data sets adopting consistent criterion to identify sources with infrared excess emission. In figure 7.3 I show the 2MASS K_S vs. K_S-[24] color magnitude diagram for the 27 brown dwarfs

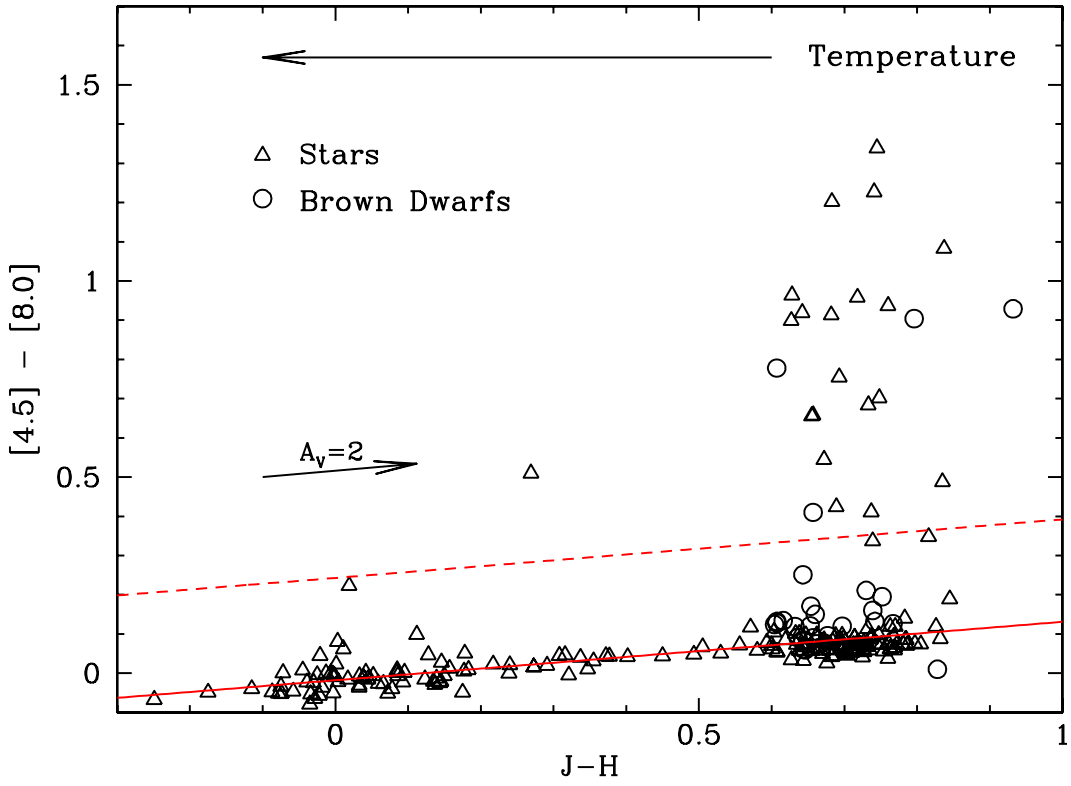

Figure 7.2 $J - H$ vs. [4.5]-[8.0] color-color diagram for substellar (circles; presented here) and stellar (triangles; taken from Carpenter et al. 2006) members of USco. Solid line indicates a linear fit to the data and dashed line indicates the threshold adopted to identify excess sources corresponding to a color excess of 24% above the photosphere.

in my USco survey (black), together with data from Scholz et al. (2007). I have included only the 27 brown dwarfs from the Scholz et al. (2007) work with spectral types M6–M8, so as to compare a consistent samples. Black and red triangles represent upper limits. Note that Scholz et al. (2007) report the *survey* upper limit, but not the upper limit for individual sources. Thus, I have used the survey upper limit in each case causing the linear line of red triangles. As in figure 7.1, the dashed line represents the median value of all data in my sample (computed using 2σ clipping of outliers), presumed to represent photospheric colors. Dotted lines represent 2σ and 3σ deviations about the median. As can be seen, using this criteria I do not identify any additional sources (beyond the four identified in §7.2) with measured K_S-[24] in excess of 3σ ($\sim$500%) above the photospheric color (K_S-[24]=1.34 mag), and actually measure a lower disk frequency of $3/27 = 11^{+11}_{-6}$%. Adopting the same criterion to calculate the disk frequency from the Scholz et al. (2007) dataset, I measure a disk frequency of $8/27 = 30^{+14}_{-11}$%. Thus, the two results are consistent, but only at the 1σ level.

7.4 The Evolution of Circumstellar Disks with Age

The second method by which I can place into context the results from my mid-infrared study of 5 Myr-old brown dwarfs in USco, is to analyze them in comparison to results from similar observations of brown dwarfs at different ages. Mid-infrared *Spitzer* observations have been carried out for several other nearby associations, including IC 348 (3 Myr, 320 pc; Lada et al. 2006, Luhman et al. 2005), Chameleon I (2 Myr, 165 pc; Luhman et al. 2005), and the young Taurus subclusters (1 Myr, 140 pc; Hartmann et al. 2005, Luhman et al. 2006, Guieu et al. 2007). I have compiled measured IRAC photometry for brown dwarfs in these associations from three of the studies that extended to substellar masses (Luhman et al. 2006, Lada et al. 2006, Luhman et al. 2005), together with extinctions and/or spectral types from Luhman (2004a) (Chameleon I), Luhman et al. (2003b) (IC 348), and Briceño et al. (2002), Luhman et al. (2003a), Guieu et al. (2006) (Taurus). I limited my literature search

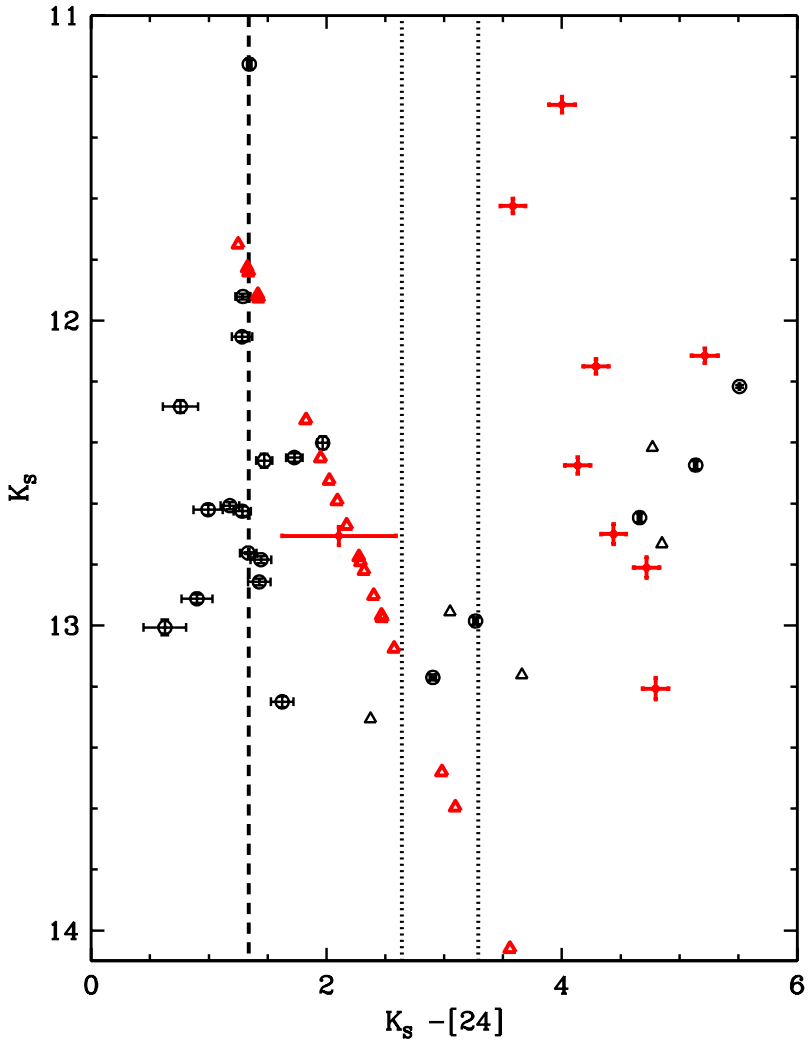

Figure 7.3 2MASS K_S vs K_S-[24] color magnitude diagram for the 27 brown dwarfs in my USco survey (black), together with data for M6-M8 brown dwarfs from Scholz et al. (2007) (red). Black and red triangles represent upper limits. Dashed and dotted lines are as defined in figure 7.1.

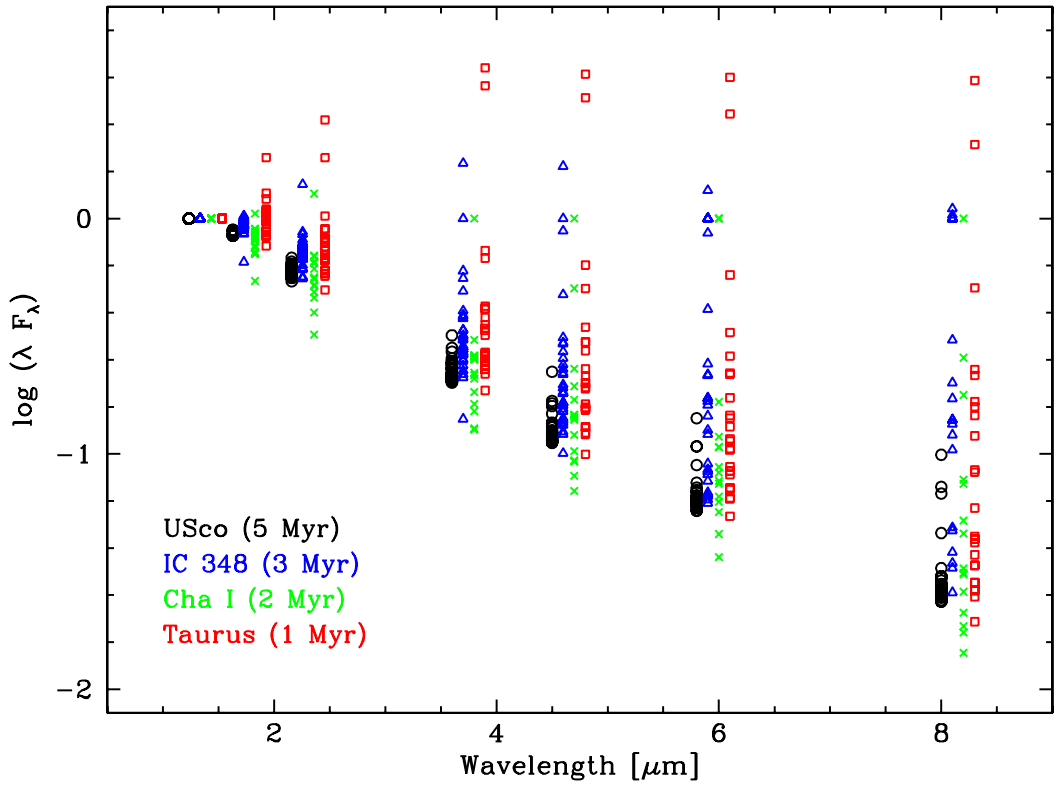

Figure 7.4 Dereddened SEDs for brown dwarfs with spectral types M6–M8 from 1 to 5 Myr. Data for IC 348 (3 Myr; blue), Chameleon I (2 Myr; green), and Taurus (1 Myr; red) are taken from the literature (see text). All stars have been normalized to unity at J-band and an offset has been applied to the wavelength data for stars in associations other than USco for ease of comparison.

to include only those brown dwarfs in the surveys listed above with spectral types M6-M8, thus providing samples analogous to the one presented here for USco. In total, I find 25 brown dwarfs in Taurus, 12 in Chameleon I, and 24 in IC 348 to have measured IRAC photometry and spectral types M6-M8.

In figure 7.4 I show dereddened spectral energy distributions (SEDs) for these brown dwarfs together with SEDs for the brown dwarfs observed in USco. Flux for all objects has been normalized to unity at J-band. As can be seen, the SEDs for the brown dwarfs in USco (black) that exhibit an [8.0] excess have systematically lower flux than the brown dwarfs with an excess in the three younger clusters or associations. In figure 7.5 I have computed the percentage of objects with a [3.6]-

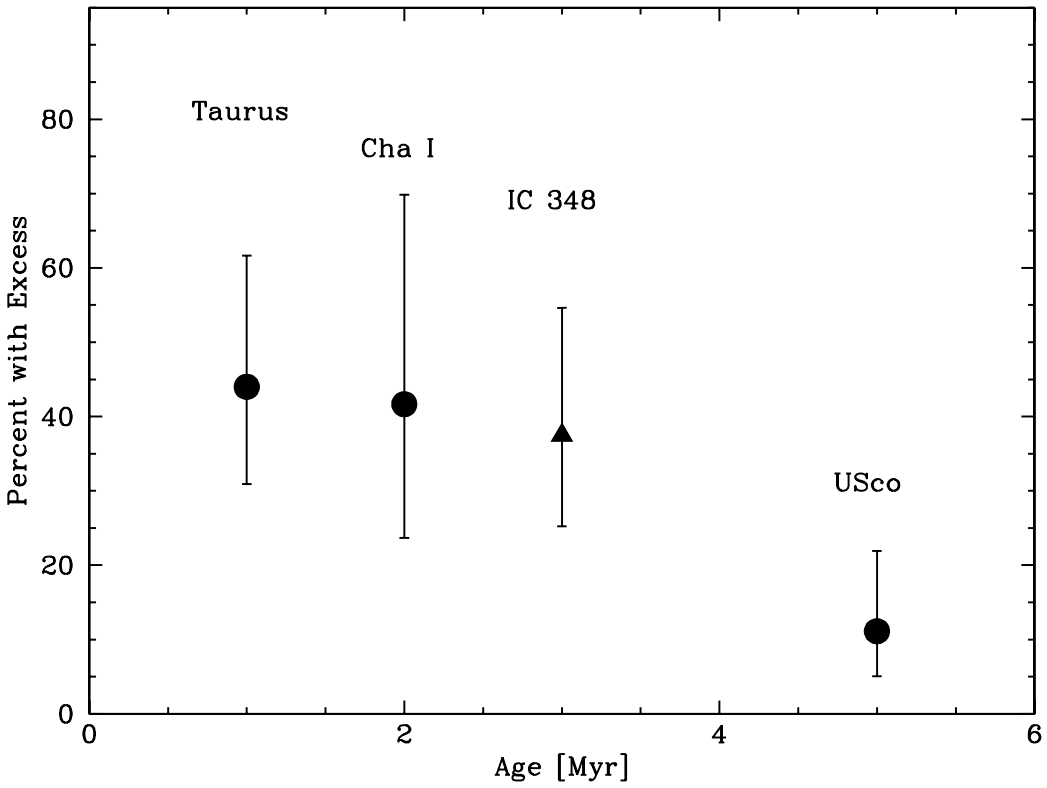

Figure 7.5 Percentage of brown dwarfs in the USco and comparison samples (see text) as a function of mean cluster age. IC 348 is shown as a triangle because only 14/24 brown dwarfs were detected at 8μm in the Lada et al. (2006) survey. Thus, the value shown is a lower limit.

[8.0] color excess using the same method that I used to define an excess source in USco. Median photometric uncertainties for the three comparison samples are 0.058 mag (Taurus), 0.036 mag (Chameleon I), and 0.16 mag (IC 348). Thus, the limiting uncertainty is that for the IC 348 stars. Therefore, for the purpose of this comparison, I take 1σ=0.16 and define a source to have an excess if it has [3.6]-[8.0] colors >56% (i.e., $>3\sigma$) above the photospheric level of 0.19 mag. The disk frequency for IC 348 is shown in figure 7.5 as a triangle because only 14/24 brown dwarfs were detected at 8μm in the Lada et al. (2006) survey. Thus, the value shown is a lower limit. I find disk frequencies of 44^{+18}_{-14}% (11/25) for Taurus, 42^{+28}_{-18}% (5/12) for Chameleon I, and 38^{+17}_{-12}% (9/24) for IC 348. While the measured disk frequencies do decline with increasing age from 1 to 3 Myr for these regions, considering the large associated errors, these values are statistically indistinguishable from each other. Thus, to increase the size of the sample analyzed, I combine data for the three associations younger than ∼3 Myr and derive a disk frequency of 41^{+10}_{-9}% (25/61). For my sample of brown dwarfs in USco I measure a disk frequency of 11^{+11}_{-6}% (3/27) (one source did not have a large enough excess to be considered to exhibit a mid-infrared excess when I used the larger sigma cutoff). Using a two-tailed Fisher's Exact test I find the disk frequencies for the associations younger than ∼3 Myr to be different from that for the 5 Myr-old brown dwarfs in USco with ∼94% confidence.

Based on results of comparison between these four star forming regions, I infer that about half of brown dwarfs clear the inner regions of their circumstellar material within the first ∼1 Myr (i.e., by an age of Taurus). The other half do not begin to dissipate circumstellar material until ∼3 Myr, but then this process must proceed rapidly for most objects through ∼5 Myr. One caveat to this argument which must be mentioned is that Taurus, IC 348, Chameleon I, and USco all represent different environments. As discussed in previous chapters, Taurus is an example of an isolated, low density star forming region whereas USco is a large OB association. Neither IC 348 nor Chameleon I contain stars hot enough to ionize material; however, they are much more dense star-forming environments than either Taurus or USco. Thus, until we have a better understanding of the role environment may play in circumstellar disk

lifetime, we cannot draw definitive conclusions about the rate at which circumstellar evolution proceeds around the lowest mass stars and brown dwarfs.

7.5 Summary and Conclusions

I have observed 27 brown dwarfs identified as part of my thesis work using the IRAC and MIPS mid-infrared cameras on the *Spitzer Space Telescope*. From these data I have identified four brown dwarfs (15^{+12}_{-7}%) that possess an infrared excess. Based on comparison with work by Carpenter et al. (2006) of higher mass association members, I find the disk frequency in USco to be near-constant for M-type objects from M ∼0.5 to 0.02 $M_{\odot}$. I have also compared my results for 5 Myr-old brown dwarfs in USco to those for 1,2, and 3 Myr-old brown dwarfs at similar masses in the young Taurus subclusters, and the star forming regions of Chameleon I and IC 348. I measure a disk frequency of ∼40% for brown dwarfs from 1–3 Myr, declining sharply by the age of USco (5 Myr). Thus, assuming environmental factors do not play a large role in the lifetimes of disks around the lowest mass stars and brown dwarfs (which does not have to be true!), the evolution of circumstellar material must proceed rapidly around such objects between 3 and 5 Myr. Larger samples spanning a range of both environment and age are needed to confirm this result.

Chapter 8

Research in Progress

While I have thus far carried out several in-depth studies utilizing the Quest-2 photometric and follow-up spectroscopic surveys, I have only begun to scratch the surface of the analysis that this vast dataset is capable of producing. In this chapter, I highlight some of the projects that I have already begun to pursue beyond the work presented in this thesis.

8.1 Hydra Spectroscopic Observations

In chapter 3, I present spectroscopic observations taken with the Hydra multifiber spectrograph at CTIO as follow-up to the photometric survey in USco. As mentioned, in total the observations produced ∼1150 spectra (of varying quality) yet I only discussed results for ∼100 stars in chapter 5. The reason for lack of inclusion of the remaining spectra was twofold. 1) Because I ultimately wished to derive the age and mass distributions for this region, I needed a data set selected in a manner consistent with itself. Thus, I chose to include only those stars observed with Hydra that met the same selection criteria as that applied to stars observed spectroscopically at Palomar. The remaining Hydra targets met less strict selection criteria in an attempt to place as many fibers on stars as possible during a single pointing. 2) We applied for time with Hydra early during analysis of the Quest-2 observations. As such, the photometry changed several times both before and after these observations were made, and several candidates thought to be 'top tier' candidates (i.e., those meeting all of the selection

criteria applied to the single slit Palomar observations) at the time of observation would no longer have made the cut. Additionally, at the time of the proposal, I did not have a full appreciation for the spatial density of top tier candidates. Because the photometric survey region is so large, while I have >1000 top tier candidates in this region, perhaps only ∼5 could be observed in each 40'×40' field of view. These observations were still *extremely* beneficial to this work in that I was able to observe at ∼5 times the rate of the Palomar observations; however, they did not yield as many new PMS stars as expected.

Of the stars with Hydra spectra not discussed in chapter 5, ∼400 have spectral types late-K through M-types, which I will refer to as 'late-types'. Another ∼650 have spectral types late-F through mid-K which I will refer to as 'mid-types.' I show histograms of magnitudes for these two samples at r-band (figure 8.1) and at J-band (figure 8.2) along with the range of magnitudes expected for members of USco at these spectral types. I have assumed for this calculation that all members of USco are 5 Myr-old, 145 pc away, and have $0 \leq A_V \leq 2$. As can been seen from figures 8.1 & 8.2, most of the stars classified as late-type *could* be bona fide members of USco. However, since most of the spectral types are earlier than ∼M3, I cannot use the strength of the Na I doublet (λ8190 Å) to determine surface gravity and must therefore rely on an alternative criteria for youth. Most of the stars classified as mid-type, do not appear to be members of USco based on their observed magnitudes and spectral types. This sample is likely dominated by reddened field dwarfs and background giants.

I intend to analyze the spectra of all stars observed with Hydra (not already presented in chapter 5) more thoroughly. Based on initial classification, ∼100 stars exhibit Hα emission, most of them late-type objects. I do not see evidence of significant Li (λ6707 Å) absorption for more than a handful of stars, despite the fact that the spectra are of high enough resolution to detect it for mid-type stars. This result provides further evidence that most of the stars in the mid-type sample are field stars. For late-type stars with strong TiO molecular absorption, Li absorption becomes diluted with TiO absorption and much higher resolution is required for detection. This project will be my first priority when I begin my postdoc position, and I intend to

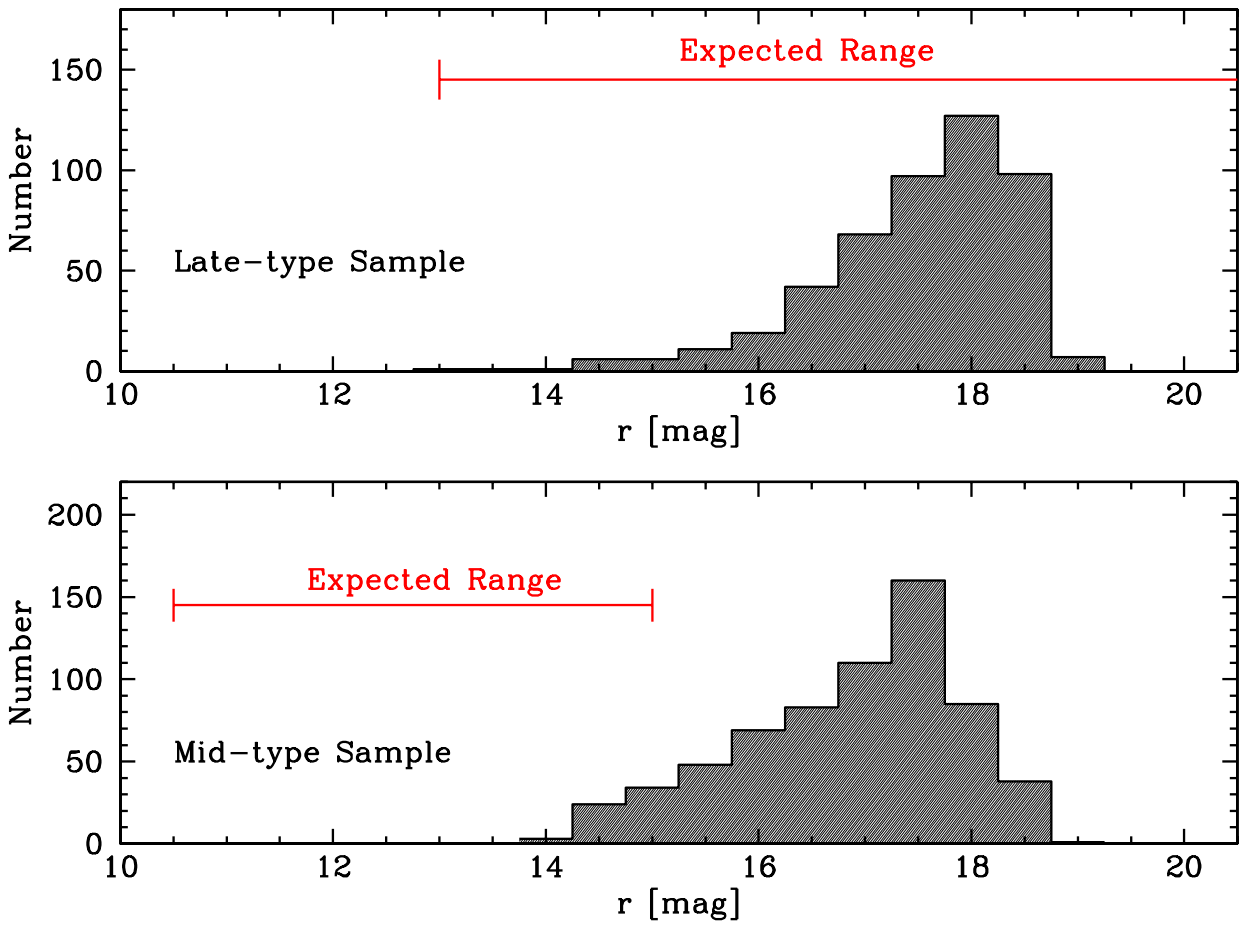

Figure 8.1 Histograms of r-band magnitudes for targets of the Hydra spectral observations not discussed in chapter 5. The top histogram shows data for stars classified as spectral type late-K to M; the bottom histogram shows data classified as spectral type late F to early-K. Shown in both panels is the expected range of magnitudes for 5 Myr-old stars of those spectral types at the distance of USco.

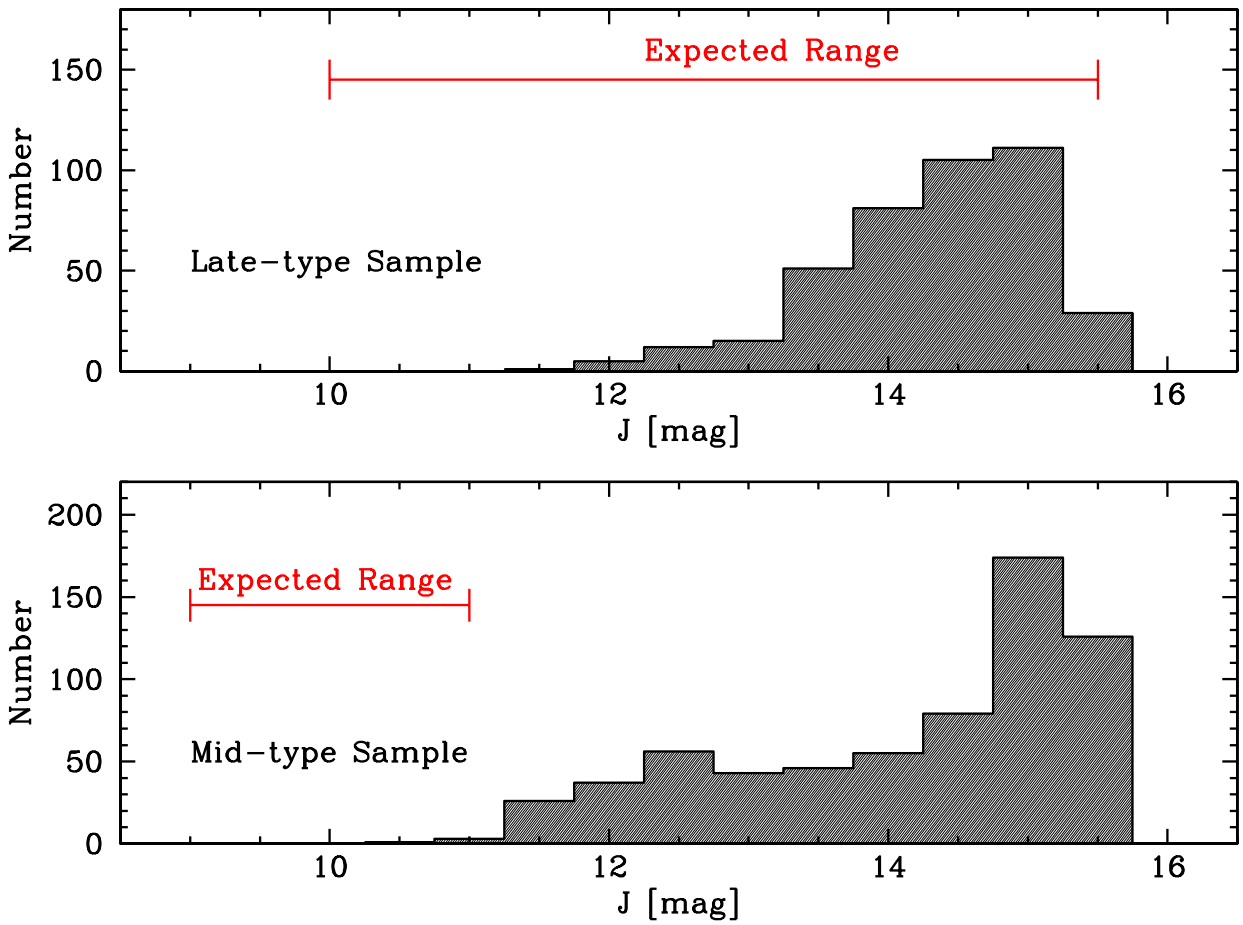

Figure 8.2 Histograms of J-band magnitudes for targets of the Hydra spectral observations not discussed in chapter 5. The top histogram shows data for stars classified as spectral type late-K to M; the bottom histogram shows data classified as spectral type late F to early-K. Shown in both panels is the expected range of magnitudes for 5 Myr-old stars of those spectral types at the distance of USco.

present the results along with results from remaining Palomar spectra (chapter 5) in an upcoming publication (chapter 9, last paragraph).

8.2 Palomar Spectra of High-Variability Stars

The ultimate form of the Quest-2 survey to look for new PMS stars near USco and Taurus was/is quite different from that envisioned when the proposal to obtain the observations was written. The original intent had been to identify candidate PMS stars based on their colors and magnitudes *and* photometric variability. Thus the reason for taking 12 to 24 monitoring observations in each region. As described in chapter 1, young PMS stars have systematically more magnetic activity than do older stars at equivalent masses. This activity causes increased photospheric activity in the form of cool star spots which can be observed as photometric variability. This technique has been successfully used by Briceño et al. (2005) to identify ∼200 new members of the ∼5–10 Myr-old regions of Orion OB 1a and Orion OB 1b using Quest-1 in Venezuela.

However, because the CCDs used in Quest-2 are not scientific grade, at the time we initially received the photometric data, repeatability was not sufficient to identify low mass PMS variable stars. The Briceño et al. (2005) survey finds an average value of $< \Delta V >\sim 0.26$ mag for non-accreting PMS stars. These stars were identified above a noise of $< \Delta V >\sim 0.005$ at $V < 17$ to $< \Delta V >\sim 0.09$ at $V < 20$. The Quest-2 data had average repeatability at several times this level at the time when the spectroscopic follow-up program began. Because the photometry for each source (in the monitoring regions) was an average of multiple observations, the colors and magnitudes in the photometric catalog were much more accurate than any single measurement. Thus, the photometry for a given star was relatively accurate, even when its magnitude had a high RMS (i.e., photometric repeatability). The RMS value, however, was artificially high because I had not yet worked out all the bugs in the photometry (see chapter 2 for more details). Therefore I chose to select candidate PMS stars only from colors and magnitudes listed in the source catalog and largely ignored a star's

photometric variation.

During the past 3–4 years that I have been working on this project, the photometry reduction and calibration has gone through several iterations. The results discussed in §2.3 are for the final version of the photometry and are at a precision where I could now begin to select candidate PMS stars based on photometric variability. To this end, I was awarded 3 nights at Palomar to begin taking spectra of variable stars newly identified in the USco region. Because photometric precision was determined to be *very* CCD dependent, I assessed the repeatability plot of each CCD separately before deciding which stars to include in the variability sample.

In figures 8.3 & 8.4 I show photometric repeatability as a function of r-magnitude for the 28 r-band CCDs. Only stars observed in more than half of the 24 monitoring scans (i.e., >12 times) are considered as variable candidates. Red lines indicate the empirical boundary between variable and non-variable stars in each column. I did not consider any stars in column 19 as variables. This procedure produced ∼1300 candidate variable stars. Of these, ∼250 were red in all colors and thus, possible young PMS stars. During the three nights at Palomar in May 2007, I was able to observe ∼20% of this list. Because these data were taken only a few months before my defense, I have not yet analyzed the spectra. However, I am hopeful that they will yield tens of additional PMS stars in this region.

8.3 HIRES Spectra of PMS Stars near Taurus

In chapter 4, I presented results from my photometric/spectroscopic survey of ∼200 deg^2 in and near the Taurus molecular clouds. As part of this work, I identified 42 new low mass PMS stars of which approximately half have spectral signatures that indicate they are as young as members of the known ∼1 Myr-old Taurus subclusters while the other half was determined to be slightly more evolved, ∼5–10 Myr-old. From assessment of the spatial and proper motion distributions, I argued in chapter 4 that the new pre-main sequence stars identified far from the clouds cannot have originated from the vicinity of the 1–2 Myr-old subclusters which contain the bulk of

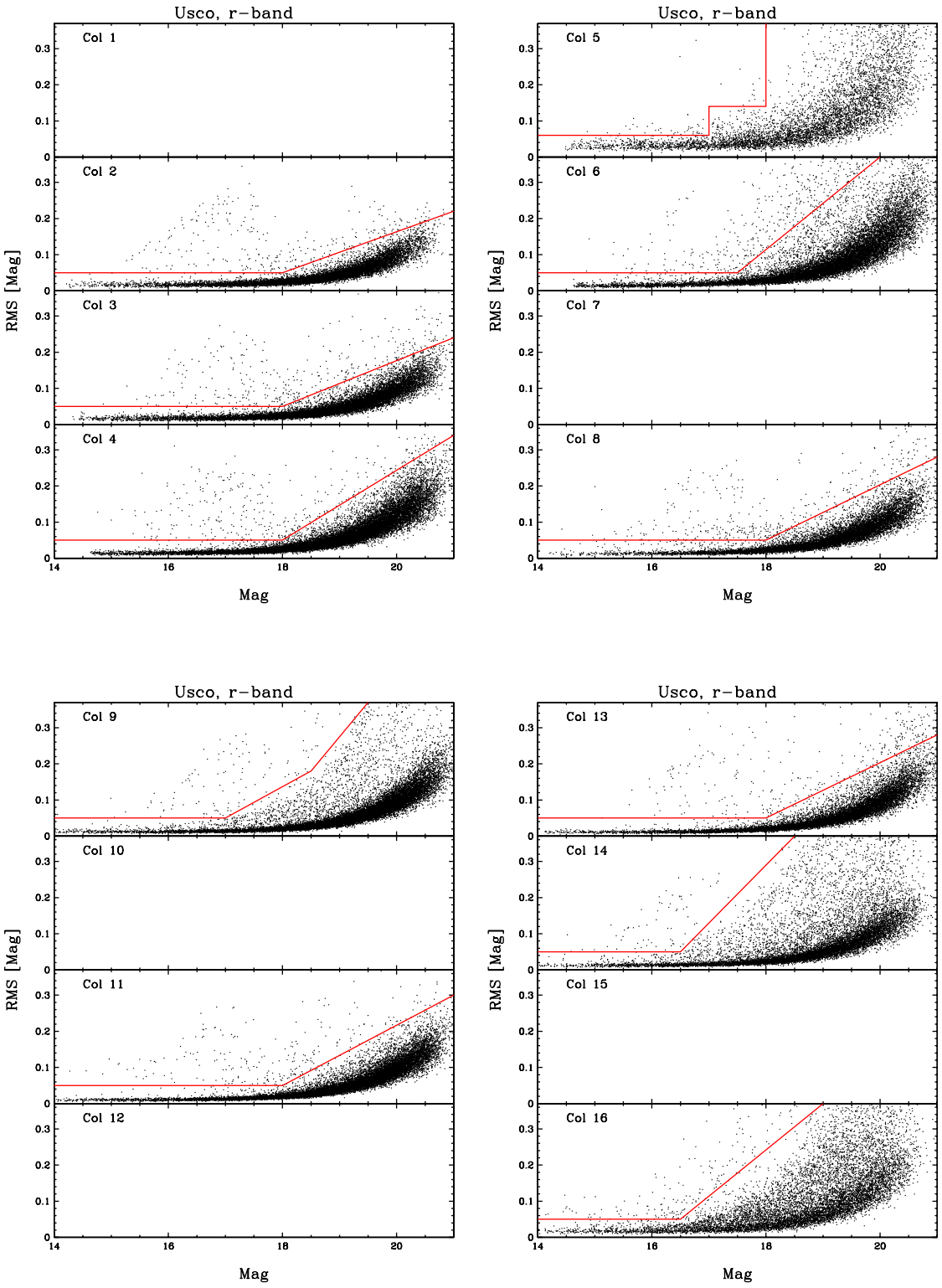

Figure 8.3 Photometric repeatability as a function of magnitude for all stars detected in more than half of the monitoring scans (i.e., >12) in USco.

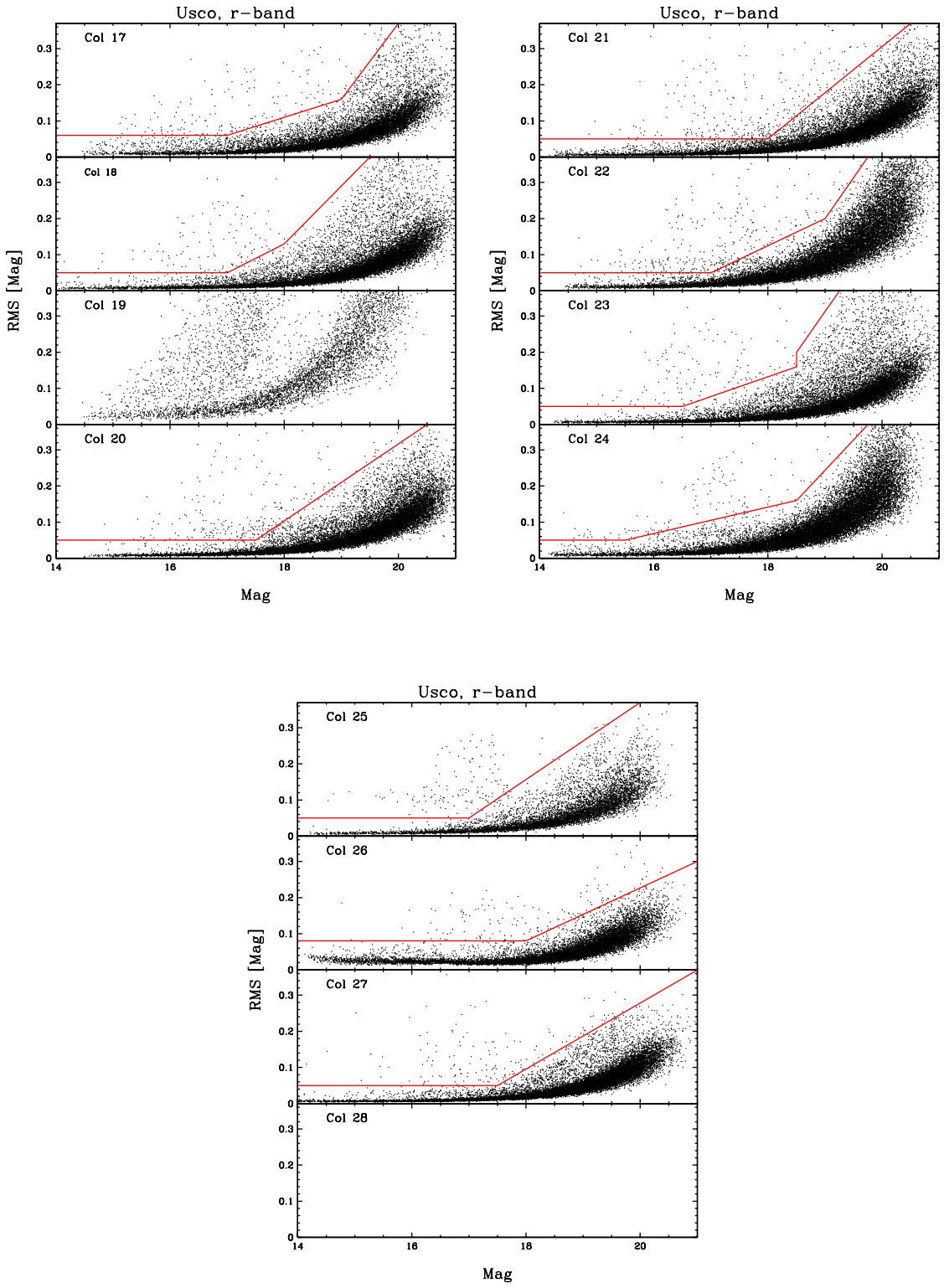

Figure 8.4 Photometric repeatability as a function of magnitude for all stars detected in more than half of the monitoring scans (i.e., >12) in USco.

the identified Taurus members, but instead represent a newly identified area of recent star formation near the clouds.

I was awarded 3 nights on Keck with HIRES in the 2006B season to take high-resolution spectral observations of these stars. Thus far, I have observed $\sim$2/3 of the sample in this manner, and have time this fall to observe the remaining stars using the Magellan Inamori Kyocera Echelle (MIKE) on the Magellan Clay Telescope. Once the observations have been completed, I will use the high resolution spectroscopic data to derive additional information on the kinematics (i.e., radial velocities) and ages (i.e., Li equivalent widths) of the newly identified PMS stars which will help solidify their origin and relationship to Taurus. The radial velocity distribution of Taurus is tightly peaked at V_R $\sim$-18.7 km/s with a small dispersion of $\sim$1.7 km/s (e.g., Frink et al. 1997). I will use high resolution spectroscopy to measure the radial velocities for new PMS stars at a precision of $\lesssim$1 km/s which I will combine with more robust measurements of proper motion (derived from existing catalogs). Following the methods of Frink et al. (1997), I will assess whether the space motions and distances of the sources can simultaneously be consistent with stars in Taurus, thus providing a compelling argument for or against these stars being part of the 'missing' PTTS population.

In addition to kinematic information I will also measure Li equivalent widths. Li depletion occurs slowly over >100 Myr for F and G type stars and is therefore not suitable for distinguishing PTTSs from older Pleiades-age objects. For K to mid-M type stars that are fully convective, Li depletion occurs over much faster timescales ($\sim$10 Myr; D'Antona & Mazzitelli 1994) and is a more robust indicator of youth. In this spectral range Li can only be measured with high resolution spectroscopy due to broad molecular absorption features present in the spectra. Detecting Li in these objects will serve as an independent check of the surface gravity assessment and further confirm youth. I will also investigate secondary indicators of youth such as rapid rotation and weak accretion (i.e., broad wings in the Hα emission line) which are known to evolve on timescales of $\sim$10 Myr.

Chapter 9

Thesis Summary

My thesis research focused primarily on identifying and characterizing pre-main sequence (PMS) stars in nearby star-forming regions. I carried out wide-field (∼150–250 deg^2) optical photometric and spectroscopic surveys in and near the nearby Taurus and Upper Scorpius associations. These two regions represent very different star-forming environments. Known members of Taurus are primarily very young (1–2 Myr-old) and very low mass (M >1 M$_\odot$). The intermediate-age, ∼5 Myr-old region of USco is a massive OB association. The spatial coverages of my optical surveys in both Taurus and USco were chosen specifically to extend to regions well beyond areas previously explored in a similar manner.

In Taurus, the aim of my optical photometric/spectroscopic survey was specifically to probe for a distributed population of intermediate-age PMS (∼5–10 Myr-old) stars outside of the young subclusters that are known to contain most of the young Taurus population. Because stars continue to move with the velocity of their parent cloud after they are born, in 3–10 Myr, the intermediate-age PMS stars could have traveled significantly far from their birth sites. The area I surveyed was sufficient to detect stars of $\lesssim$10 Myr old that originated in the current young regions of Taurus and subsequently drifted away.

From this work I found tens of young (∼1–3 Myr) and intermediate-age (∼5–10 Myr) stars both near the known Taurus population and to the east, but relatively few PMS stars of any age to the west. Based on this result and assessment of the proper motion distributions, I argued that the new PMS stars identified far from

Taurus cannot have originated from the vicinity of the 1–2 Myr-old subclusters. I proposed instead that they comprise a new, previously undiscovered region of recent star formation which *may* have formed out of a different part of the same molecular cloud that is forming the current Taurus population. Because the new PMS stars exhibit a range of ages from 1 to ∼10 Myr, if they do share a common parental cloud with Taurus, this new population would provide definitive evidence that the Taurus cloud has been forming stars for at least 10 Myr.

In USco, the aim of my optical photometric/spectroscopic survey was to probe beyond previously explored regions to identify large numbers of intermediate-age, 5 Myr-old low mass stars which had not yet been uncovered due to the inherent challenges of surveying an association that spans >200 deg^2 on the sky. From the spectroscopic data I have discovered 145 new low mass members of USco and over-doubled the number of previously known 5 Myr-old brown dwarfs. I used photometry and spectral types to derive effective temperatures and luminosities, and placed newly identified association members onto a theoretical HR diagram. These data were combined with pre-main sequence evolutionary models to derive a mass and age for each star. Using Monte Carlo simulations I showed that, taking into account known observational errors, the observed age dispersion for the low mass population in USco is consistent with all stars forming in a single burst ∼5 Myr ago. I also derived the first spectroscopic mass function for USco that extends into the substellar regime and compared these results to those for four other young clusters and associations. For the five regions considered, I find the low mass IMF to be dependent on environment in that associations that contain a significant number of O- and B-type stars produce more very low mass stars and brown dwarfs.

As follow-up to the optical surveys in USco, together with my collaborator John Carpenter, I have completed a program to measure mid-infrared photometry using *Spitzer* for 27 new substellar members. I have compared my 3.6–8 μm IRAC photometry for brown dwarfs in Upper Sco to similar observations by Carpenter et al. (2006) for higher mass stellar association members and find from this comparison that the frequency of brown dwarfs with disks at 5 Myr is indistinguishable (∼15%) from the

fraction of 5 Myr-old low mass stars with disks. Thus, these observations add to the growing evidence that substellar formation and early evolution must proceed through very similar physical processes as those that form and shape low mass stars. I have additionally compared my *Spitzer* IRAC results to those from similar studies in the younger regions of IC 348, Chameleon I, and Taurus. I found a disk frequency of $\sim$40% for brown dwarfs from 1 to 3 Myr, declining sharply by 5 Myr. Thus, assuming environmental factors do not play a large role in the lifetimes of disks around the lowest mass stars and brown dwarfs (which does not have to be true), the evolution of circumstellar material must proceed rapidly around such objects between 3 and 5 Myr.

In total, my thesis worked produced two published papers on the photometric and spectroscopic surveys in USco (Slesnick et al. 2006a) and Taurus (Slesnick et al. 2006b), and I anticipate an additional two papers to be submitted by the fall. One will present the additional spectroscopic data in USco (chapter 5 and §8.1), and will include the analytical discussion of the age distribution in USco and the low mass IMF (chapter 6). The other paper will discuss results from *Spitzer* observations discussed in chapter 7. In addition to the papers that have (or will) come out of the surveys in USco and Taurus, I undertook two separate projects early during my time at Caltech, both resulting in publications. I completed a near-infrared spectroscopic survey in the ONC and derived the first spectroscopic substellar mass function for this cluster (Slesnick et al., 2004). Discussion of this work was given in chapter 6. I also worked on a project to characterize the star formation history and mass function of the high mass population in h and χ Persei (Slesnick et al., 2002). Results from this work are presented in appendix A.

Appendix A

High Mass End of the Mass Function: The Star Formation History and Mass Function of h and χ Persei[1]

As discussed in chapter 6, our somewhat limited understanding of the intermediate mass stellar IMF is greatly overshadowed by our relative non-existent understanding of the lowest mass stellar and substellar end of the mass function. Almost as problematic is the high mass end of the IMF. Garnering a full census of high mass stars is difficult, due to the fact that they form, evolve, and die within just a few to tens of megayears, often before their lower mass counterparts have even reached the main sequence. Thus, deriving a field star IMF that extends to tens of solar masses is meaningless as the included high mass stars will necessarily be gigayears younger than the local intermediate and low mass field star population. A less biased view of the high mass IMF can be derived by examining a young, high mass cluster for which the highest mass stars have not yet evolved into supergiants. In this appendix I illustrate analysis of how an HR diagram can be used to assess the age and mass distributions of high mass clusters by describing a study I completed of the massive double cluster h & χ Persei. This work was carried out very early during my time at Caltech, prior to my work with the Quest-2 surveys of Taurus and USco and prior to

[1]A modified version of this appendix has been published previously as Slesnick, Hillenbrand, & Massey 2002, ApJ, 576, 880, and all work was done in collaboration with Phil Massey and Lynne Hillenbrand.

my work in the ONC. In this appendix, I summarize the results of this work only. A full analysis is given in Slesnick et al. (2002).

A.1 Motivation

The "double cluster" h and χ Persei (hereafter h/χ Per; also known as NGC 869 and NGC 884, respectively) is among the brightest, densest, and closest of the open clusters containing moderately massive stars. The double cluster has been studied extensively over the last century (e.g., Oosterhoff 1937, Bidelman 1943, Wildey 1964, Schild 1965, Crawford et al. 1970, Vogt 1971, Tapia et al. 1984, Waelkens et al. 1990) with resulting mean reddenings of $E(B-V) = 0.5$-0.6, and distance moduli in the range 11.4-12.0 mag (1.9-2.5 kpc). The clusters contain several tens of Be stars (e.g., Slettebak 1968, Bidelman 1947; see also Keller et al. 2001). Wildey's (1964) HR diagrams suggested several distinct episodes of star formation (7 Myr, 17 Myr, and 60 Myr), which would imply a spread of >50 Myr in the formation times of OB stars in a single (double) cluster! This age spread is larger than that claimed for any other well-studied open cluster, and was one of the primary motivations of my investigation in this region.

Most work prior to my study on h/χ Per has used photographic or single-channel photoelectric photometry with little emphasis on spectroscopy. Several very recent papers have used CCDs but consisted of photometric analysis only ($UBVI$/Hα, Keller et al. 2001; $ubvy/\beta$, Marco & Bernabeu 2001). Distance moduli in the range 11.6-11.8 mag and ages of 10-20 Myr have been found, with Marco & Bernabeu (2001) arguing (like Wildey 1964) for three distinct episodes of star formation, while Keller et al. (2001) find instead a single age. There is significant disagreement between various authors as to whether the reddenings, distances, and ages of the two clusters are identical or substantially (30%-50%) different. It is especially important to understand in detail the star formation history of h/χ Per as these clusters are widely used from professional review papers to basic introductory astronomy textbooks to illustrate stellar evolution at the high mass end of the main sequence. My main goals in this

study were to re-determine the age, and age spread in the double clusters, and to explore for the first time the mass function and the evidence for mass segregation.

My modern study of h/χ Per consisted of wide-field CCD *UBV* photometry for 4528 stars obtained from observations with the 0.9-m telescope at Kitt Peak National Observatory using the Mosaic CCD camera. Several hundred spectral types complement the photometric database. For hot stars, spectral data are needed to obtain accurate effective temperatures and consequently accurate extinction estimates and bolometric corrections (Massey 1998b, Massey 1998a) all necessary for locating a star in the HR diagram. Stars were selected for spectroscopy based on their brightness and colors, and blue optical spectroscopy was taken for 196 of the stars presumed to be the most massive (i.e., the brightest blue and red stars). The most luminous stars identified in the vicinity of h/χ Per are M, A, and B supergiants.

A.2 HR Diagram for h/χ Per

Figure A.1 is the HR diagram resulting from this study. Post-zero-age main sequence evolutionary tracks and isochrones are transformed from the log $T_{\rm eff}$ and M_{bol} values calculated by Schaller et al. (1992). All stars with MK spectral classifications of luminosity class I or III, and stars earlier than B5 with luminosity class IV or V were placed spectroscopically (larger, filled circles) while most other stars were placed photometrically (open circles). It is expected that stars near the cluster cores predominantly will be members, while stars further afield will be a mixture of both members and nonmembers. I constructed a contour plot of the spatial distribution of stars within the imaging field, and found that the stellar densities were enhanced by 2σ at identical radii of 7 arcminutes from each of the cluster cores. Thus, I use this radial criterion when describing stars near the nuclei. I also determined accurate centers for the two cores (α_{2000}=2:19:22.2, δ_{2000}=+57:09:00 for h Per, and α_{2000}=2:22:12.0, δ_{2000}=+57:07:12 for χ Per) by examining mass and number density contours. The left panel shows data for the entire imaging area while the right panel contains only stars within 7 arcmin of the cluster nuclei. No corrections for field star contamination

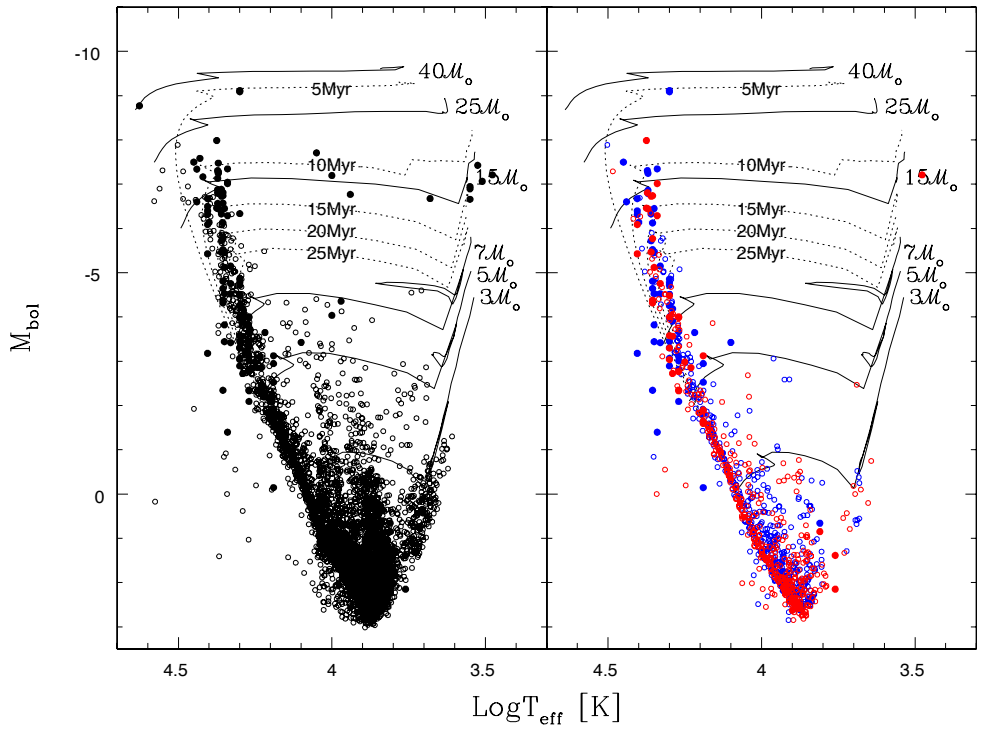

Figure A.1 The HR diagrams of h/χ Per are shown. On the left is shown all of the data: filled circles represent stars placed by means of spectroscopy and open circles represent stars for which only photometric data are available. On the right is shown only the stars within a 7 arcminute radius of the center of h (blue dots) and χ (red dots).

have been applied and the HR diagrams for the central regions of the clusters contain significantly less field star contamination, especially above the main sequence.

From these HR diagrams it is immediately seen that the high mass stars in the h/χ Per clusters are slightly evolved from the zero-age main sequence and that the most massive stars are only $\sim$20 to 30 $\mathcal{M}_\odot$. The data extend down to about $3\mathcal{M}_\odot$ before field star contamination becomes substantial.

A.3 Stellar Ages and the Age Distribution within h/χ Per

The dereddened CMD (figure A.2) is used to determine cluster ages. Data are shown in figure A.2 with a grid of isochrones computed at intervals of 0.1 Myr from 5 to 30 Myr.[2] Age determination is restricted to only the most luminous stars ($M_V < -3$) where the isochrones are substantially far apart to yield meaningful results. Obvious foreground contaminants were filtered out, e.g., $(B-V)_o > -0.2$ for $-3 > M_V > -5$. Red supergiants (RSGs) cannot be used for our age determinations, unfortunately, since the evolutionary tracks do not actually extend that far to the red. However, it is noted that the location of the RSGs in the CMD are consistent with the ages derived if the isochrones are extrapolated. For each of the clusters an essentially identical age was found: 12.8 Myr and 12.9 Myr for h and χ respectively. The formal errors of the mean on these determinations are 1 Myr, and the scatter is <0.01 mag level.

I do not find evidence for multiple distinct episodes of star formation despite the remarkable similarities between the dereddened CMD presented here and that of Wildey (1964). This difference in interpretation likely occurs because Wildey in his original analysis did not consider the possibility of field star contamination from G and

[2]The CMD was used rather than the HRD to determine ages in order to avoid the quantization problem introduced by spectral types. The ages of hot stars are very sensitive to $\log T_{\rm eff}$ (or $(B-V)_o$), and thus this quantization would introduce a spurious age spread. The spectral types *have* been employed in the CMD in order to derive $E(B-V)$. In a subsequent section the HRD is used to derive the mass function. The masses are primarily sensitive to an accurate determination of $M_{\rm bol}$, which is expected to be better determined using the bolometric corrections determined from spectral types.

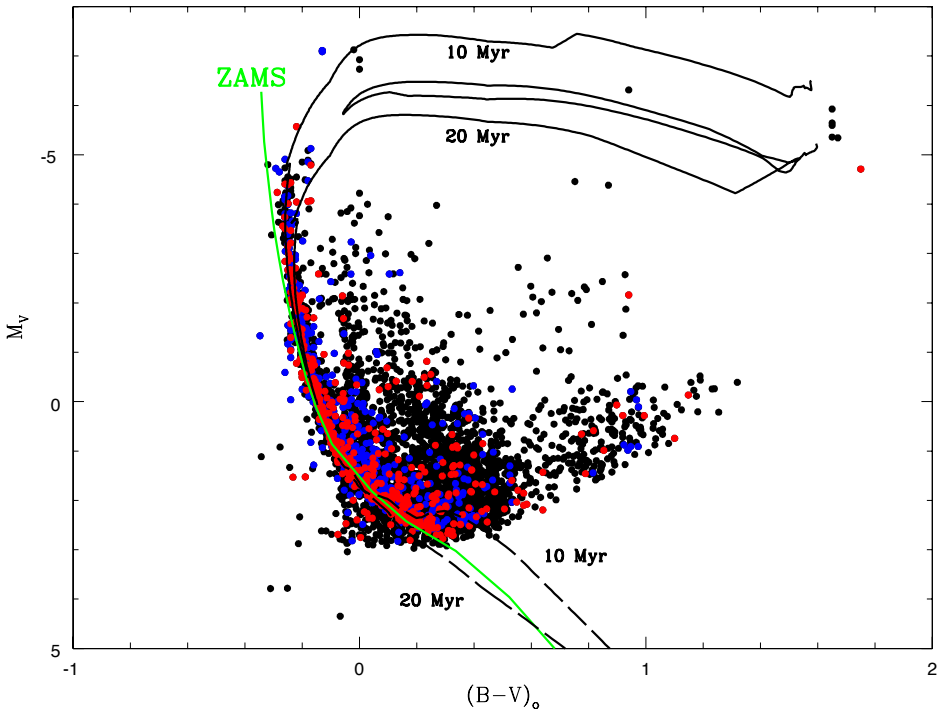

Figure A.2 The dereddened CMD for stars within 7 arcminutes of the center of h (blue) and χ (red) Per are shown now with the ZAMS and post-main-sequence isochrones of 10 and 20 Myr indicated. Corresponding 10 and 20 Myr pre-main-sequence isochrones are shown as dashed lines. The black points represent the rest of the stars in the full $0.98^\circ \times 0.98^\circ$ field.

K giants seen to large distances through the Galaxy. It is clear from the right panel of figure A.1 that when just the cluster nuclei are considered any apparent branching in the HR diagram is significantly diminished. There do exist several high-mass stars with uncharacteristically young ages as compared to the rest of the cluster. However, in most cases these stars are either not in the central regions of the clusters or their spectroscopically derived distance is inconsistent with their being cluster members.

A.4 Mass Function and Mass Segregation in h/χ Per

Masses are inferred for individual stars by interpolating between the mass tracks on the HR diagram. By counting the number of stars found in each mass bin, the "present day mass function" (PDMF) is derived. To the extent that star formation may be coeval, this is equivalent to the initial mass function (IMF) except for the depopulation of the highest mass bin.

In order to minimize the effect of field star contamination, PDMFs have been constructed only for the two regions within 7 arcmin of the cluster cores. In addition, a few stars found red-ward of the main-sequence, and presumed to be foreground contaminants, were excluded by eliminating stars in the region constrained between $M_{\rm bol} < -20.5 \times \log T_{\rm eff} + 82.5$ and $M_{\rm bol} > -5$. A lower mass cutoff of 4 $\mathcal{M}_{\odot}$ was used below which field and pre-main sequence star contamination dominate. At the high-mass end, it is expected that evolution through the supernova phase will have depleted stars above ∼15-20 $\mathcal{M}_{\odot}$, and so only the mass bins below this value have been used to compute the slope of the IMF. All of the higher-mass stars were combined into one mass bin. Following Scalo (1986), the quantity ξ is defined as the number of stars per mass bin divided by the difference in the base-ten logarithm of the upper and lower bin masses, and also by the surface area in kpc. The run of $\log \xi$ with log mass then provides the slope, Γ, of the IMF/PDMF. Values for the number of stars and for ξ are given in table A.1.

Table A.1. Mass function data for h/χ Per

Mass Range	h Per		χ Per	
$[\mathcal{M}_\odot]$	N	log ξ	N	log ξ
4.0-5.0	45	6.80	37	6.71
5.0-6.3	33	6.66	23	6.50
6.3-7.9	28	6.59	26	6.56
7.9-10.0	25	6.54	13	6.26
10.0-12.6	11	6.18	9	6.10
12.6-15.8	10	6.14	10	6.14
15.8-40.0	7	5.39	2	4.84

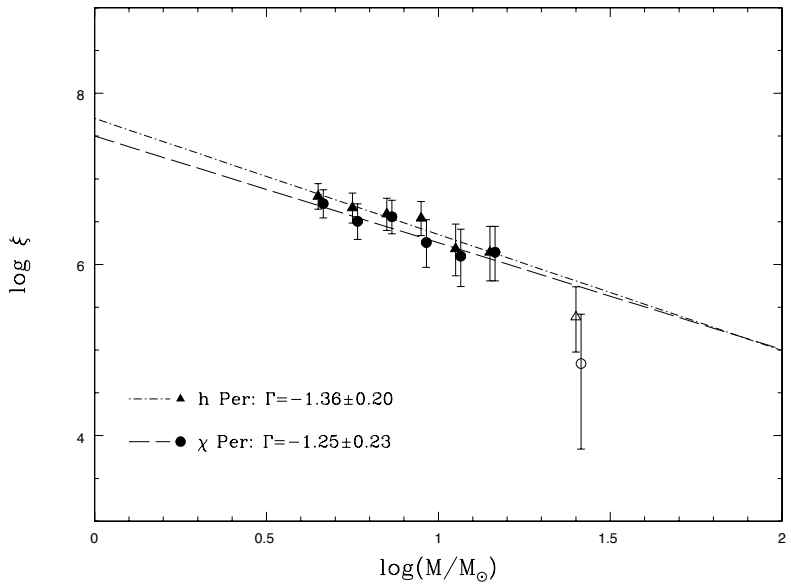

Figure A.3 The mass function is shown for the two clusters. Open symbols indicate an incomplete bin.

Figure A.3 shows PDMFs in the 4-16 $\mathcal{M}_\odot$ range for stars within 7 arcmin of the cluster centers. Error bars are based on $\pm\sqrt{N}$ statistics. Values are obtained of $\Gamma = -1.36 \pm 0.20$ for h Per and $\Gamma = -1.25 \pm 0.23$ for χ Per. Within the errors of the fits, both slopes are in good agreement with each other and also with the Salpeter value of $\Gamma = -1.35$. This result can be compared with what is known of the IMF in other young OB associations and clusters, where a weighted average yields $\Gamma = -1.1 \pm 0.1$ for the Milky Way and $\Gamma = -1.3 \pm 0.1$ for the LMC/SMC (Massey, 1998b) for similar mass stars. Thus, an IMF slope of $\Gamma = -1.3 \pm 0.2$ for h and χ is in no way unusual.

Based on extrapolation of the measured PDMFs to 120 $\mathcal{M}_\odot$, I estimate that $\sim$40 supernovae have occurred in the past in the central regions of the h/χ Per clusters. From this information, and assuming a constant mass function from 1 to 120 $\mathcal{M}_\odot$, I estimate the total stellar mass within each of the cluster centers down to 1 $\mathcal{M}_\odot$ to be 3700 $\mathcal{M}_\odot$ and 2800 $\mathcal{M}_\odot$ for h Per and χ Per , respectively. This is about 8-10 times that of the mass in >1 $\mathcal{M}_\odot$ stars in the younger Orion Nebula cluster ($\sim$450 $\mathcal{M}_\odot$) or the older Pleiades ($\sim 320\mathcal{M}_\odot$). For comparison, a "supercluster" like R136 in the LMC has a mass of roughly 3–4$\times 10^4 \mathcal{M}_\odot$ in >1 $\mathcal{M}_\odot$ stars (Hunter et al., 1996), about a factor of 10 greater than either h or χ and a factor of almost 100 greater than Orion or the Pleiades.

Figure A.4 explores the evidence for concentration and mass segregation in the two clusters. Only those stars satisfying the criteria for inclusion in the PDMF are considered in this figure. The top and middle panels of figure A.4 show that inside of 7 arcmin (i.e., the 2σ surface density contour), both the mass surface density and the number surface density begin to rise noticeably above the field star surface density, and then steepen considerably at $\sim$3 arcmin. The increase in density at smaller cluster radii is evidence of higher central concentration.

The histograms of the total mass/pc^2 as a function of radial distance (top panels of figure A.4) show that h Per is about twice as dense at its core compared to χ Per. This occurs both because h Per has $\sim$25% more stars at its center (as can be seen in the middle panels of figure A.4) and because it contains several high mass ($>$30

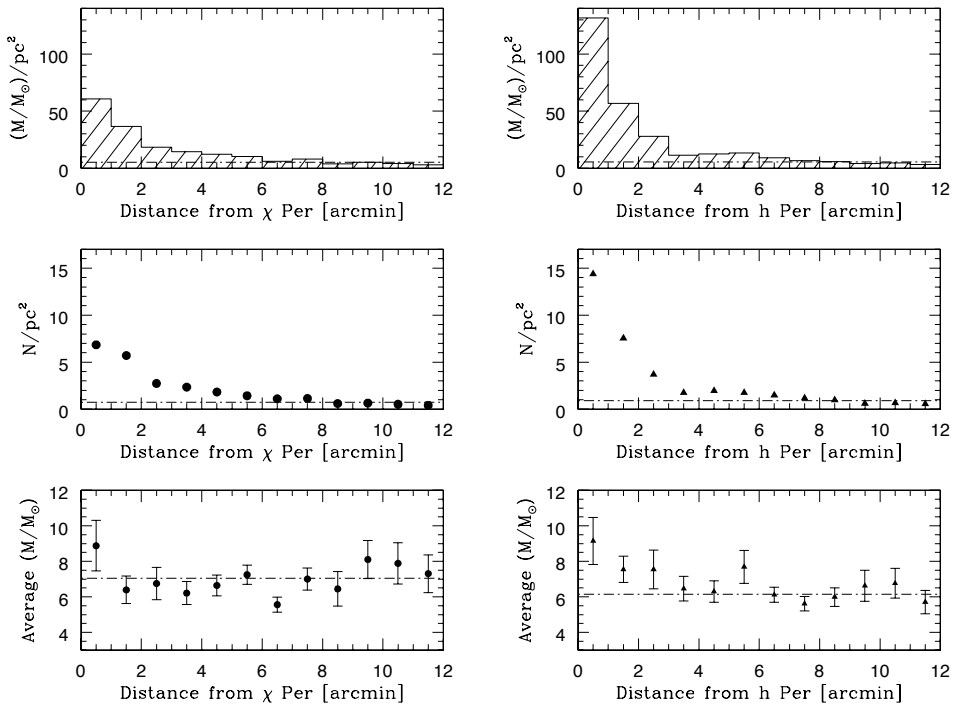

Figure A.4 The total mass per unit area (top panels), the number of stars per unit area (middle panels), and the average stellar mass per unit area (bottom panels) are shown as a function of radial distance for h Per (left) and χ Per (right). The data have been binned in 1 arcmin rings from the respective cluster centers. Horizontal dashed lines indicate the average of the values from 6 to 12 arcmin. Within the 2σ surface density enhancements (r = 7 arcmin), there is clear evidence in both h and χ Per for central concentration within 3 arcmin (top and middle panels), and also some evidence for mass segregation within 1-2 arcmin (bottom panels).

$\mathcal{M}_{\odot}$) B supergiants. However, the density profile of h Per falls off more rapidly than that of χ Per and the two clusters are roughly equivalent in mass density at a radius of $\sim$3 arcmin.

The bottom panels of figure A.4 show the average mass as a function of radial distance from the cluster centers. For h Per, we find a significant gradient inside of $\sim$7 arcmin in the mean mass vs. radial distance, suggestive of mass segregation. The data for χ Per is less convincing, yet we still find the mean stellar mass to be higher by $\sim$1.5–2σ within the central 1 arcmin. This phenomenon has been claimed with varying degrees of strength in other open clusters in the Galaxy (e.g., the Orion Nebula Cluster; Hillenbrand & Hartmann 1998 and references therein) and in the Magellenic Clouds (e.g., R136; Hunter et al. (1995), and NGC 1805 and NGC 1818; de Grijs et al. 2002). However, unlike their younger counterparts, the mean mass gradient in h/χ Per may not be primordial, i.e., associated with the formation of the clusters. Assuming a velocity dispersion of σ_v $\approx$3 km/s and a 7 arcmin (4.79 pc) cluster radius, each of the cluster nuclei has a crossing time of $\sim$1.56 Myr. Given that the clusters are $\sim$13 Myr old, the age/t_{cross} $\approx$8 and hence dynamical relaxation may indeed play some part in the observed mass segregation.

A.5 Summary of the h/χ Per Survey

I have studied the h and χ "double cluster" using modern imaging and spectroscopic techniques. My conclusions differ with those of previous studies such as Wildey's (1964) largely due to my recognition of the significant effect that field star contamination has on the determination of cluster ages. Inclusion of foreground younger stars and GK giants can easily lead to apparent branching in the HR diagram which has been misinterpreted in the past as an age spread. I find mean ages of 12.8 Myr for each of the two clusters and no evidence for multiple epochs of star formation.

The present day mass function yields a slope consistent with that found in other well-studied Galactic OB associations and clusters ($\Gamma \sim -1.1 \pm 0.1$, see Massey (1998b)), and is essentially Salpeter ($\Gamma = -1.35$). In addition, I do find some evidence

of mass segregation. The total masses are 3700 $\mathcal{M}_{\odot}$ for h Per and 2800 $\mathcal{M}_{\odot}$ for χ Per, for stars with $> 1\mathcal{M}_{\odot}$.

Bibliography

Adams, F. C., Hollenbach, D., Laughlin, G., & Gorti, U. 2004, ApJ, 611, 360

Adams, F. C., Proszkow, E. M., Fatuzzo, M., & Myers, P. C. 2006, ApJ, 641, 504

Allers, K. N., Kessler-Silacci, J. E., Cieza, L. A., & Jaffe, D. T. 2006, ApJ, 644, 364

Andrews, P. A. 2003, Ph.D. thesis, Yale University

Andrews, S. M., & Williams, J. P. 2005, ApJ, 631, 1134

Ardila, D., Martín, E., & Basri, G. 2000, AJ, 120, 479

Ballesteros-Paredes, J., & Hartmann, L. 2007, Revista Mexicana de Astronomia y Astrofisica, 43, 123

Bally, J., O'Dell, C. R., & McCaughrean, M. J. 2000, AJ, 119, 2919

Baraffe, I., Chabrier, G., Allard, F., & Hauschildt, P. H. 1998, A&A, 337, 403

Barrado y Navascués, D., & Martín, E. L. 2003, AJ, 126, 2997

Barsony, M., Kenyon, S. J., Lada, E. A., & Teuben, P. J. 1997, ApJS, 112, 109

Basri, G., Marcy, G. W., & Graham, J. R. 1996, ApJ, 458, 600

Bidelman, W. P. 1943, ApJ, 98, 61

Bidelman, W. P. 1947, ApJ, 105, 492

Blitz, L., & Shu, F. H. 1980, ApJ, 238, 148

Bok, B. J. 1934, Harvard College Observatory Circular, 384, 1

Briceño, C., Calvet, N., Hernández, J., Vivas, A. K., Hartmann, L., Downes, J. J., & Berlind, P. 2005, AJ, 129, 907

Briceño, C., Calvet, N., Kenyon, S., & Hartmann, L. 1999, AJ, 118, 1354

Briceño, C., Hartmann, L., Stauffer, J., & Martín, E. 1998, AJ, 115, 2074

Briceño, C., Luhman, K. L., Hartmann, L., Stauffer, J. R., & Kirkpatrick, J. D. 2002, ApJ, 580, 317

Briceño, C., et al. 2001, Science, 291, 93

Briceno, C., Hartmann, L. W., Stauffer, J. R., Gagne, M., Stern, R. A., & Caillault, J.-P. 1997, AJ, 113, 740

Brown, A. G. A. 1996, PASP, 108, 459

Brown, A. G. A., de Geus, E. J., & de Zeeuw, P. T. 1994, A&A, 289, 101

Carpenter, J. M. 2000, AJ, 120, 3139

Carpenter, J. M., Hillenbrand, L. A., & Skrutskie, M. F. 2001, AJ, 121, 3160

Carpenter, J. M., Mamajek, E. E., Hillenbrand, L. A., & Meyer, M. R. 2006, ApJ, 651, L49

Chabrier, G., Baraffe, I., Allard, F., & Hauschildt, P. 2000, ApJ, 542, 464

Cohen, J. G., Persson, S. E., Elias, J. H., & Frogel, J. A. 1981, ApJ, 249, 481

Crawford, D. L., Glaspey, J. W., & Perry, C. L. 1970, AJ, 75, 822

Dahm, S. E., & Hillenbrand, L. A. 2007, AJ, 133, 2072

Dame, T. M., Hartmann, D., & Thaddeus, P. 2001, ApJ, 547, 792

D'Antona, F., & Mazzitelli, I. 1994, ApJS, 90, 467

D'Antona, F., & Mazzitelli, I. 1997, Memorie della Societa Astronomica Italiana, 68, 807

de Bruijne, J. H. J. 1999, MNRAS, 310, 585

de Geus, E. J. 1992, A&A, 262, 258

de Grijs, R., Gilmore, G. F., Johnson, R. A., & Mackey, A. D. 2002, MNRAS, 331, 245

de la Reza, R., Jilinski, E., & Ortega, V. G. 2006, AJ, 131, 2609

de Zeeuw, P. T., Hoogerwerf, R., de Bruijne, J. H. J., Brown, A. G. A., & Blaauw, A. 1999, AJ, 117, 354

Desch, S., & Ouellette, N. 2005, in Protostars and Planets V, 8467

Engelbracht, C. W., et al. 2007, ArXiv e-prints, 704

Evans, N. J., II, et al. 2003, PASP, 115, 965

Fazio, G. G., et al. 2004, ApJS, 154, 10

Feigelson, E. D., & Decampli, W. M. 1981, ApJ, 243, L89

Frink, S., Röser, S., Neuhäuser, R., & Sterzik, M. F. 1997, A&A, 325, 613

Fukugita, M., Ichikawa, T., Gunn, J. E., Doi, M., Shimasaku, K., & Schneider, D. P. 1996, AJ, 111, 1748

Genzel, R., Reid, M. J., Moran, J. M., & Downes, D. 1981, ApJ, 244, 884

Gomez, M., Hartmann, L., Kenyon, S. J., & Hewett, R. 1993, AJ, 105, 1927

Guieu, S., Dougados, C., Monin, J.-L., Magnier, E., & Martín, E. L. 2006, A&A, 446, 485

Guieu, S., et al. 2007, A&A, 465, 855

Guillout, P., Sterzik, M. F., Schmitt, J. H. M. M., Motch, C., & Neuhaeuser, R. 1998, A&A, 337, 113

Haisch, K. E., Jr., Lada, E. A., & Lada, C. J. 2001, ApJ, 553, L153

Hartmann, L. 2000, in ESA SP-445: Star Formation from the Small to the Large Scale, ed. F. Favata, A. Kaas, & A. Wilson, 107

Hartmann, L. 2002, ApJ, 578, 914

Hartmann, L., Ballesteros-Paredes, J., & Bergin, E. A. 2001, ApJ, 562, 852

Hartmann, L., Hewett, R., Stahler, S., & Mathieu, R. D. 1986, ApJ, 309, 275

Hartmann, L., Megeath, S. T., Allen, L., Luhman, K., Calvet, N., D'Alessio, P., Franco-Hernandez, R., & Fazio, G. 2005, ApJ, 629, 881

Herbig, G. H. 1978, Can Post-T Tauri Stars Be Found? (Problems of Physics and Evolution of the Universe), 171

Hernández, J., et al. 2007, ApJ, 662, 1067

Hillenbrand, L. A. 1997, AJ, 113, 1733

Hillenbrand, L. A. 2005, ArXiv Astrophysics e-prints

Hillenbrand, L. A., & Carpenter, J. M. 2000, ApJ, 540, 236

Hillenbrand, L. A., & Hartmann, L. W. 1998, ApJ, 492, 540

Hillenbrand, L. A., & White, R. J. 2004, ApJ, 604, 741

Hollenbach, D., Johnstone, D., Lizano, S., & Shu, F. 1994, ApJ, 428, 654

Hunter, D. A., O'Neil, E. J., Jr., Lynds, R., Shaya, E. J., Groth, E. J., & Holtzman, J. A. 1996, ApJ, 459, L27

Hunter, D. A., Shaya, E. J., Holtzman, J. A., Light, R. M., O'Neil, E. J., Jr., & Lynds, R. 1995, ApJ, 448, 179

Jones, B. F., & Walker, M. F. 1988, AJ, 95, 1755

Keller, S. C., Grebel, E. K., Miller, G. J., & Yoss, K. M. 2001, AJ, 122, 248

Kenyon, S. J., Dobrzycka, D., & Hartmann, L. 1994, AJ, 108, 1872

Kenyon, S. J., & Hartmann, L. 1995, ApJS, 101, 117

Kirkpatrick, J. D., Henry, T. J., & McCarthy, D. W., Jr. 1991, ApJS, 77, 417

Kraus, A. L., White, R. J., & Hillenbrand, L. A. 2005, ApJ, 633, 452

Kraus, A. L., White, R. J., & Hillenbrand, L. A. 2006, ApJ, 649, 306

Kroupa, P., & Bouvier, J. 2003, MNRAS, 346, 369

Ku, W. H.-M., & Chanan, G. A. 1979, ApJ, 234, L59

Lada, C. J., & Lada, E. A. 2003, ARA&A, 41, 57

Lada, C. J., et al. 2006, AJ, 131, 1574

Lada, E. A., & Lada, C. J. 1995, AJ, 109, 1682

Lebreton, Y., Fernandes, J., & Lejeune, T. 2001, A&A, 374, 540

Leggett, S. K., Allard, F., Berriman, G., Dahn, C. C., & Hauschildt, P. H. 1996, ApJS, 104, 117

Leggett, S. K., et al. 2002, ApJ, 564, 452

Levine, J. L., Steinhauer, A., Elston, R. J., & Lada, E. A. 2006, ApJ, 646, 1215

Lodieu, N., Hambly, N. C., Jameson, R. F., Hodgkin, S. T., Carraro, G., & Kendall, T. R. 2007, MNRAS, 374, 372

Luhman, K. L. 2000, ApJ, 544, 1044

Luhman, K. L. 2004a, ApJ, 602, 816

Luhman, K. L. 2004b, ApJ, 617, 1216

Luhman, K. L. 2006, ApJ, 645, 676

Luhman, K. L., Briceño, C., Stauffer, J. R., Hartmann, L., Barrado y Navascués, D., & Caldwell, N. 2003a, ApJ, 590, 348

Luhman, K. L., et al. 2005, ApJ, 631, L69

Luhman, K. L., Rieke, G. H., Young, E. T., Cotera, A. S., Chen, H., Rieke, M. J., Schneider, G., & Thompson, R. I. 2000, ApJ, 540, 1016

Luhman, K. L., Stauffer, J. R., & Mamajek, E. E. 2005, ApJ, 628, L69

Luhman, K. L., Stauffer, J. R., Muench, A. A., Rieke, G. H., Lada, E. A., Bouvier, J., & Lada, C. J. 2003b, ApJ, 593, 1093

Luhman, K. L., Whitney, B. A., Meade, M. R., Babler, B. L., Indebetouw, R., Bracker, S., & Churchwell, E. B. 2006, ApJ, 647, 1180

Mamajek, E. E., Meyer, M. R., Hinz, P. M., Hoffmann, W. F., Cohen, M., & Hora, J. L. 2004, ApJ, 612, 496

Marco, A., & Bernabeu, G. 2001, A&A, 372, 477

Marino, A., Micela, G., Peres, G., & Sciortino, S. 2003, A&A, 406, 629

Martín, E. L., Delfosse, X., & Guieu, S. 2004, AJ, 127, 449

Massey, P. 1998a, ApJ, 501, 153

Massey, P. 1998b, in Astronomical Society of the Pacific Conference Series, Vol. 142, The Stellar Initial Mass Function (38th Herstmonceux Conference), ed. G. Gilmore & D. Howell, 17

Massey, P., Strobel, K., Barnes, J. V., & Anderson, E. 1988, ApJ, 328, 315

Megeath, S. T., Hartmann, L., Luhman, K. L., & Fazio, G. G. 2005, ApJ, 634, L113

Meyer, M. R., Calvet, N., & Hillenbrand, L. A. 1997, AJ, 114, 288

Monet, D. G., et al. 2003, AJ, 125, 984

Muench, A. A., Lada, E. A., Lada, C. J., & Alves, J. 2002, ApJ, 573, 366

Myers, P. C. 1998, ApJ, 496, L109

Neuhaeuser, R., Sterzik, M. F., Schmitt, J. H. M. M., Wichmann, R., & Krautter, J. 1995, A&A, 295, L5

Neuhaeuser, R., Torres, G., Sterzik, M. F., & Randich, S. 1997, A&A, 325, 647

Oosterhoff, P. T. 1937, Annalen van de Sterrewacht te Leiden, 17, 1

Ortega, V. G., de la Reza, R., Jilinski, E., & Bazzanella, B. 2004, ApJ, 609, 243

Palla, F., & Stahler, S. W. 2000, ApJ, 540, 255

Podosek, F. A., & Cassen, P. 1994, Meteoritics, 29, 6

Preibisch, T., Brown, A. G. A., Bridges, T., Guenther, E., & Zinnecker, H. 2002, AJ, 124, 404

Preibisch, T., Guenther, E., & Zinnecker, H. 2001, AJ, 121, 1040

Preibisch, T., Guenther, E., Zinnecker, H., Sterzik, M., Frink, S., & Roeser, S. 1998, A&A, 333, 619

Preibisch, T., et al. 2005, ApJS, 160, 401

Preibisch, T., & Zinnecker, H. 1999, AJ, 117, 2381

Preibisch, T., & Zinnecker, H. 2007, in IAU Symposium, Vol. 237, IAU Symposium, ed. B. G. Elmegreen & J. Palous, 270

Prosser, C. F., Stauffer, J. R., Hartmann, L., Soderblom, D. R., Jones, B. F., Werner, M. W., & McCaughrean, M. J. 1994, ApJ, 421, 517

Rabinowitz, D., et al. 2003, in Bulletin of the American Astronomical Society, 1262

Reach, W. T., et al. 2005, PASP, 117, 978

Rieke, G. H., et al. 2004, ApJS, 154, 25

Robberto, M., Song, J., Mora Carrillo, G., Beckwith, S. V. W., Makidon, R. B., & Panagia, N. 2004, ApJ, 606, 952

Robichon, N., Arenou, F., Mermilliod, J.-C., & Turon, C. 1999, A&A, 345, 471

Salpeter, E. E. 1955, ApJ, 121, 161

Scalo, J. M. 1986, Fundamentals of Cosmic Physics, 11, 1

Schaller, G., Schaerer, D., Meynet, G., & Maeder, A. 1992, A&AS, 96, 269

Schild, R. E. 1965, ApJ, 142, 979

Schlegel, D. J., Finkbeiner, D. P., & Davis, M. 1998, ApJ, 500, 525

Scholz, A., Jayawardhana, R., & Wood, K. 2006, ApJ, 645, 1498

Scholz, A., Jayawardhana, R., Wood, K., Meeus, G., Stelzer, B., Walker, C., & O'Sullivan, M. 2007, ApJ, 660, 1517

Shu, F. H., Adams, F. C., & Lizano, S. 1987, ARA&A, 25, 23

Sicilia-Aguilar, A., et al. 2006, ApJ, 638, 897

Silverstone, M. D., et al. 2006, ApJ, 639, 1138

Skrutskie, M. F., et al. 2006, AJ, 131, 1163

Skrutskie, M. F., Dutkevitch, D., Strom, S. E., Edwards, S., Strom, K. M., & Shure, M. A. 1990, AJ, 99, 1187

Slesnick, C. L., Carpenter, J. M., & Hillenbrand, L. A. 2006, AJ, 131, 3016

Slesnick, C. L., Carpenter, J. M., Hillenbrand, L. A., & Mamajek, E. E. 2006, AJ, 132, 2665

Slesnick, C. L., Hillenbrand, L. A., & Carpenter, J. M. 2004, ApJ, 610, 1045

Slesnick, C. L., Hillenbrand, L. A., & Massey, P. 2002, ApJ, 576, 880

Slettebak, A. 1968, ApJ, 154, 933

Spitzer, L. J. 1958, ApJ, 127, 17

Tachibana, S., & Huss, G. R. 2003, ApJ, 588, L41

Tapia, M., Roth, M., Costero, R., & Navarro, S. 1984, Revista Mexicana de Astronomia y Astrofisica, 9, 65

Vogt, N. 1971, A&A, 11, 359

Waelkens, C., et al. 1990, A&AS, 83, 11

Wainscoat, R. J., Cohen, M., Volk, K., Walker, H. J., & Schwartz, D. E. 1992, ApJS, 83, 111

Walker, C., Wood, K., Lada, C. J., Robitaille, T., Bjorkman, J. E., & Whitney, B. 2004, MNRAS, 351, 607

Walter, F. M., Vrba, F. J., Mathieu, R. D., Brown, A., & Myers, P. C. 1994, AJ, 107, 692

White, R. J., & Hillenbrand, L. A. 2004, ApJ, 616, 998

Whitworth, A. P., & Zinnecker, H. 2004, A&A, 427, 299

Wichmann, R., et al. 1996, A&A, 312, 439

Wildey, R. L. 1964, apjs, 8, 439

Wilking, B. A., Meyer, M. R., Robinson, J. G., & Greene, T. P. 2005, AJ, 130, 1733

Wilking, B. A., Schwartz, R. D., & Blackwell, J. H. 1987, AJ, 94, 106

York, D. G., et al. 2000, AJ, 120, 1579

Young, E. T., et al. 2004, ApJS, 154, 428